Ionothermal Carbon Materials: Advanced Synthesis and Electrochemical Applications

Dissertation

zur Erlangung des akademischen Grades
Doktor der Naturwissenschaften (Dr. rer. nat.)
in der Wissenschaftsdisziplin „Kolloidchemie"

eingereicht an der
Mathematisch-Naturwissenschaftlichen Fakultät
der Universität Potsdam

von

Jonas Pampel

geboren am 17.02.1989 in Dresden

Potsdam-Golm, im August 2016

Acknowledgment

Table of Contents

1 Motivation and Background

1.1 Population Growth, Energy Demand, and Renewable Energies

In the last five years (2010 − 2015) the global population has grown by 6.06 % corresponding to an average growth of 84 million people per year or 160 people per minute. Furthermore, the population is expected to grow up to 9.16 billion people in 2040 according to the United Nations.[1] These numbers alone indicate how much more energy will be needed in the future: A lot! Furthermore, the life standard is improving in most countries, which is associated with higher consumption of goods and energy. According to the International Energy Outlook 2016, the global energy demand will grow to a value of 239,000 TWh in 2040 reflecting a 48 % increase from 2012.[2] In 2012, 84 % of the total energy was produced either by liquid fuels (mostly oil), coal, or natural gas, all fossil fuels. Energy production using fossil fuels is critically discussed nowadays. The scarcity and uneven distribution of these resources causes international conflicts and wars. The energy production based on the use of fossil fuels is always coupled with carbon dioxide (CO_2) emission. To tackle the increased CO_2 values in the atmosphere and the resulting global warming, the general thinking towards energy has to be changed. More and more efforts are focusing on the generation of electricity from renewable resources, primarily solar, wind, geothermal and hydropower.[2] The energy share by renewables was estimated to grow from 12 % in 2012 to 16 % in 2040, the biggest increase of all energy sectors. Nevertheless, this value is still small compared to expected shares of 30 % for liquid fuels, 26 % for natural gas, and 22 % for coal still leading to a total value of 78 % for fossil fuels in 2040. Due to improved technologies, the carbon intensity of the energy use will be reduced in the future. Nonetheless, even with the current policies and regulations, the total energy-related CO_2 emissions will further rise to 43 billion tons in 2040 reflecting a 34 % increase in only 28 years. Thus, renewable and sustainable (herein called "green") energy production schemes have to be further enhanced, promoted, and finally applied.

The most attractive approach is to gain electricity directly from sustainable, CO_2-neutral resources such as wind, solar radiation, and water. The latter is very appealing because hydroelectric power stations can provide a constant energy, and further allow the compensation of energy peak loads.[3] Unfortunately, hydropower is restricted to certain locations, and cannot be expanded arbitrarily. In contrast, wind and solar power plants can be installed almost everywhere, which enables widespread renewable energy production

leading the way to a greener future. However, their usage involves another big challenge, which is the time discrepancy between energy production and energy demand. Naturally, solar power plants produce the most energy during midday, whereas the peak loads occur in the morning and evening hours. The power produced by wind is generally irregular. However, the average values for Western Europe show a larger power production during the day than during the night, which is more agreeable with the power demand.[4] Nonetheless, the needed expansion of the renewable energy sector is only possible if the energy storage systems are also promoted and expanded. Nowadays, energy can be stored in various ways, such as flywheels, supercapacitors, (lithium ion) batteries, compressed air, and pump storage stations.[5] The latter is especially promising due to a high overall efficiency of $75 - 80\%$ and the lack of energy loss during storage. To put it in battery terms, pump storage stations show no self-discharge. However, their investment costs are very high and they are restricted to specific local conditions. The need to consider the self-discharge of possible energy storage systems gets even more pronounced if the yearly mismatch of energy production by renewables and final user demand is taken into account.
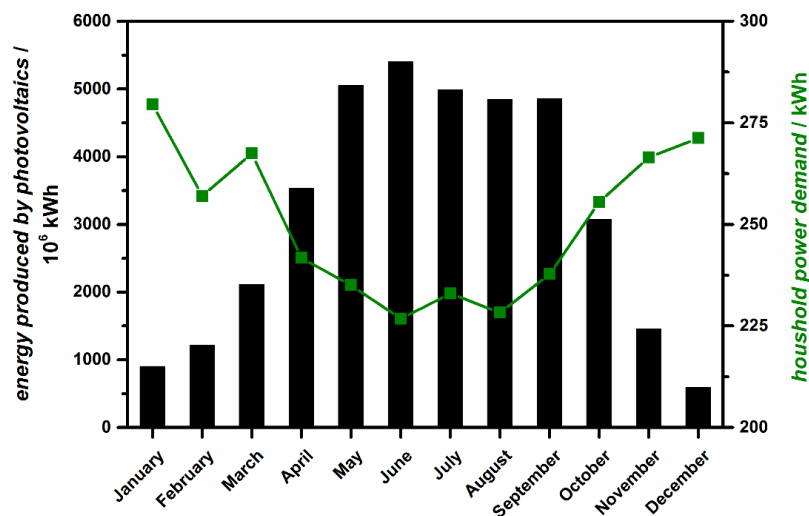
Figure 1.1 Mismatch between energy produced by photovoltaics (data for Germany, 2015) and household power demand (calculated on the basis of a yearly consumption of 3000 kWh using the average values for the years 1992-2008, Germany).[4,6]

Figure 1.1 depicts the difference between the monthly energy produced by solar power and consumed by the average German household in 2015. An appealing solution is to transfer the electrical energy, generated by wind or solar power, into chemical energy (chemical bonds). Chemical energy cannot only be stored without any energy loss but can also provide the solution to another rising problem: the effective transport of energy. Among different options, hydrogen is a very attractive chemical energy reservoir. It can be

produced by the electrolysis of water, possesses a very high gravimetric energy density of ~ 140 MJ kg^{-1}, and transferred again into electrical energy by fuel cells.[7] If renewable energy concepts are used for hydrogen production, the whole pathway is decoupled from any direct CO_2 emissions. Of course, the described concept is idealized and other factors have to be considered such as the overall energy loss of the process and the production expenses of the materials needed. Furthermore, it is highly unrealistic that one concept alone will solve all the energy related problems.[8] The future lies in the combination of different energy production/storage concepts, all aiming to reduce the amount of fossil fuels needed and CO_2 emitted. The energy efficiency of the different concepts can be further enhanced by the optimization of already existing or the development of new catalyst materials.[9] Generally, the materials implemented in next generation energy storage/conversion devices need to be cost-efficient and producible in an economic fashion. One material class, which plays a very important role in almost all energy storage/conversion approaches, is porous (heteroatom doped) carbons. They are applied as electrode material, catalyst support, conductive additive and even as the catalyst itself. Porous carbon materials will be introduced in detail in the following section 1.2, and the energy related applications (especially, the ones, which are applied in the present thesis) will be explained in section 1.3.

1.2 Porous (Heteroatom Doped) Carbon Materials

Although carbon is only ranked 17th regarding the abundance of the terrestrial elements, it is one of the most important.[10] It exhibits the second largest library of known chemical compounds, only beaten by the omnipresent hydrogen. Among all elements, carbon exhibits the strongest affinity to form covalent bonds with similar atoms. It can be combined with more or less electronegative elements as seen by its position in the periodic table of elements. While there are a lot of carbon containing compounds discussed in organic chemistry, the number of carbon containing substances relevant for materials science is rather limited. Nevertheless, even "simple" elemental carbon plays a major role for material science due to its allotropic versatility and widespread application. The importance of carbon is further evinced by the fact that an entire, highly regarded scientific journal is dedicated to it ("*Carbon*", published by Elsevier Science).

The generally known carbon allotropes, diamond and graphite, demonstrate the versatile properties of elemental carbon. The rather soft graphite (Mohs' hardness ~ 1.5) exhibits a high (in-plane) electrical conductivity, a black appearance, and is made up of sp^2

3

hybridized carbon atoms.[11] In contrast, diamond is the hardest existing material on earth (Mohs' hardness = 10), possesses a wide bandgap with an accompanied optically transparent character, and is composed of a sp^3 hybridized carbon framework.[12] The interest in carbon materials has extensively grown since the recent discovery of nanostructured carbon allotropes, such as graphene (a single sp^2 carbon layer), carbon nanotubes (CNTs), and fullerenes, leading to the expression of "the new carbon age" (Figure 1.2).[13-16] Graphene combines outstanding properties, e.g., very high electrical conductivity, very high tensile strength and an extraordinary (theoretical) specific surface area of 2965 m^2 g^{-1}.[17] Furthermore, graphene can be considered the basic building block of intrinsically porous carbon materials, whose structure can be simplified as highly disordered and defective graphite. The highly defective nature does not show any ordering causing the typically observed amorphous microstructure of porous carbon materials. Regarding applications, amorphous carbons are of high interest because they can be obtained by inexpensive synthesis approaches and their properties can be easily adjusted.
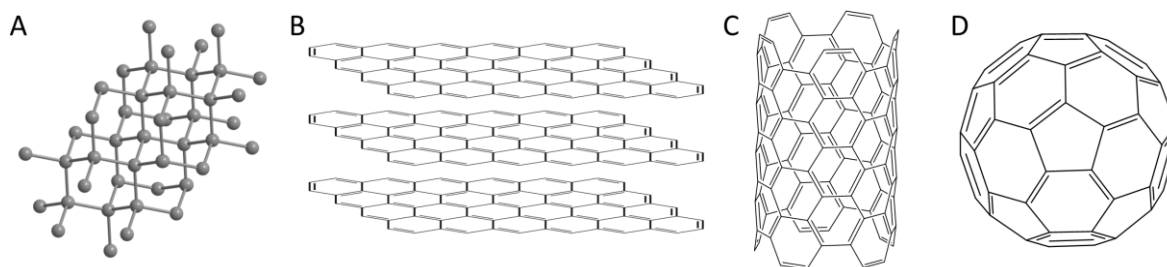
Figure 1.2 Structure of different carbon allotropes: A) diamond, B) graphite, C) carbon nanotube, and D) fullerene.

As aforementioned, porous carbon materials play a crucial role in various applications, for instance catalysis, adsorption, energy conversion, and energy storage.[18-24] This is due to the high thermal, chemical, and mechanical stability, the high abundance and the low specific weight of carbon.[25] The latter is especially beneficial for energy storage devices which are typically evaluated by their specific energy (or power) output with respect to their mass. Porous materials comprise pores of various sizes which are generally categorized according to their diameter (d), applying the IUPAC conventions:[26]

- micropores: d < 2 nm
- mesopores: 2 nm < d < 50 nm
- macropores: d > 50 nm

There is no such thing as a universal optimal porosity for carbon materials. Different applications demand different porosity characteristics. Three parameters derived from nitrogen physisorption measurements are herein mainly used to characterize/describe porosity properties: specific surface area (SSA), total pore volume (TPV) and pore size distribution (PSD). The SSA defines the interfacial area between carbon and the surrounding phase. Therefore, the SSA can be directly related to the performance-to-price ratio regarding surface dependent applications such as catalysis or adsorption. A large total pore volume (TPV) is especially important for absorption processes. However, this may lead to a low measure of performance per volume. The pore size distribution (PSD) and the related pore structure can be connected to the accessibility of the surface sites thereby defining the transport properties. The significance of each parameter varies with the desired application. Thus, the investigation of synthesis approaches, which allow the preparation of carbon materials with tailored porosity, is clearly relevant.

1.2.1 Porous Carbon Materials Synthesized by Activation

Various approaches are applied to generate porosity (herein called porogenesis) in carbon materials. On an industrial scale, the porosity is mostly introduced by activation methods, which can be divided into physical and chemical activation.[27,28] Physical activation is a two-step procedure. First, the raw carbon material is transformed into char with rudimentary porosity by pyrolysis under inert gas atmosphere, and, second, the char is treated with the activation agent at high temperatures. Typically applied activation agents are water (called steam activation) and CO_2. It is generally accepted, that physical activation leads to etching of carbon atoms from the amorphous carbon framework resulting in porosity. The porogenesis during CO_2 activation is based on the well-known Boudouard equilibrium, shown in Equation (1.1). At high temperatures, the equilibrium is enthalpically and entropically shifted towards gaseous carbon monoxide (CO) causing carbon etching. In the case of steam activation, water etches carbon atoms due to the formation of CO and hydrogen, according to the water-gas reaction (Equation (1.2)). Furthermore, the formed CO undergoes the water-gas shift reaction creating CO_2, which serves as an additional activation agent (Equation (1.3)).

$$x \, CO_2(g) + C_y(s) \rightleftarrows 2x \, CO(g) + C_{y-x}(s) \qquad (1.1)$$

$$x \, H_2O(g) + C_y(s) \rightleftarrows x \, CO(g) + x \, H_2(g) + C_{y-x}(s) \qquad (1.2)$$

$$CO(g) + H_2O(g) \rightleftarrows CO_2(g) + H_2(g) \qquad (1.3)$$
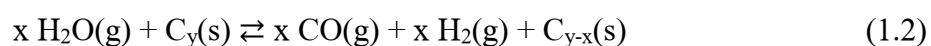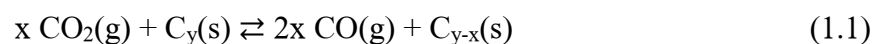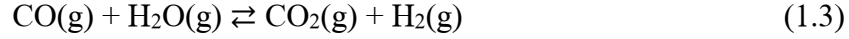
Due to its simplicity and broad applicability, physical activation is regarded as a rather economically friendly, as well as a benign, process. However, its drawbacks include the large energy consumption, the requirement of two different furnaces (one for the pyrolysis, one for the activation), and, especially, the very low yield caused by the porogenesis mechanism. Chemical activation is classically characterized by the reaction of a carbon precursor with a chemical agent, e.g., potassium hydroxide (KOH), phosphoric acid (H_3PO_4), or zinc chloride ($ZnCl_2$).[27,29-31] Typically, the precursor is impregnated with a highly concentrated, aqueous solution of the activation agent. After drying, the resulting composite is pyrolyzed under an inert gas atmosphere. Finally, the activation agent is removed by washing to yield the porous carbon material. The obtained porosity can be adjusted by altering the precursor to activation agent ratio and the conditions of the thermal treatment. Even though the process may require different heating steps, it can be executed in one furnace.

Carbon materials activated with KOH can possess very high SSA up to $\sim 3000 \, m^2 \, g^{-1}$.[32] The process was developed from researchers at *AMOCO CO.*, USA, in the 1970s, and the occurring reactions were described in detail by Otawa *et al.* (Equation (1.4) to (1.7)).[30] At lower temperatures (T < 700 °C), KOH undergoes dehydration, yielding H_2O and potassium oxide (K_2O). The formed H_2O creates porosity according to the steam activation process. The resulting CO_2 reacts with K_2O forming potassium carbonate (K_2CO_3). At temperatures higher than 700 °C, K_2O can be reduced either by H_2 or carbon to form elemental potassium. Hence, the amount of etched carbon atoms, ergo the porosity, further increases. Additionally, the liquid potassium is mobile, and may intercalate in between the carbon layers causing layer separation. After removal of the activation agent, the space between the carbon layers results in a high internal microporosity.

$$2 \, KOH(s) \rightleftarrows K_2O(s) + H_2O(g) \qquad (1.4)$$

$$CO_2(g) + K_2O(s) \rightleftarrows K_2CO_3(s) \qquad (1.5)$$

$$K_2O(s) + H_2(g) \rightleftarrows 2 \, K(l) + H_2O(g) \qquad (1.6)$$

$$x \, K_2O(s) + C_y(s) \rightleftarrows 2x \, K(l) + x \, CO(g) + C_{y-x}(s) \qquad (1.7)$$
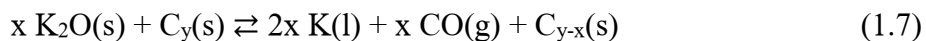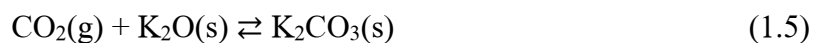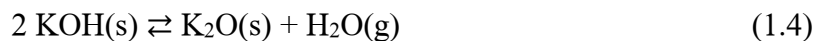
The exact mechanism of activation using dehydrating agents, such as H_3PO_4 and $ZnCl_2$, is still under debate. However, it is generally accepted that those activation agents promote a

dehydration reaction, e.g., polycondensation, thus enhancing the crosslinking of the precursor. Hence, tar formation is suppressed, and volatile byproducts can be efficiently bound generating higher product yields. Due to the general simplicity, scalability, and low costs of physical and chemical activation, these approaches are highly interesting for industry, which is reflected by a yearly production for activated carbon materials of more than 500,000 tons.[33] However, the obtained pores mainly exhibit a microporous character, which is often coupled with a worm-like or bottleneck pore structure, both restricting the mass transport of the materials.[34,35] Furthermore, activation methods rarely allow control over the morphology of the materials. These drawbacks can be overcome by templating methods, which allow the synthesis of carbon materials with defined (meso- and macro-) pores, and distinct morphology.

1.2.2   Porous Carbon Materials Synthesized by Templating

Generally, templating can be defined as the synthesis of a substance in the presence of a structure-directing agent, ergo a template. The removal of the template leads to voids, resulting in a porous structure. Therefore, the template defines the pore size and pore structure obtained. Templating methods can be classified according to different parameters, such as the mechanism of templating or the nature of the template. The material can be synthesized either inside or around the template structure, called exotemplating or endotemplating, respectively.[36] Endotemplated structures always result in a continuous phase of the porous material, whereas exotemplating can also lead to separated structures, e.g., particles or rods. The most common classification concerns the nature of the template leading to the expressions: soft templating and hard templating.

Soft templating is based on the self-assembly of soluble, amphiphilic molecules into micelles or liquid crystals. The molecules typically are surfactants, e.g., cetyltrimethyl-ammonium bromide (CTAB), or block co-polymers such as the poly(ethylene oxide)-based Pluronics®. The self-assembly is driven by a combination of non-covalent, mostly weak interactions such as Coulomb and van-der-Waals forces. The desired porous material is obtained by polymerization of precursors molecules, which self-assemble around the building blocks, i.e., micelles or liquid crystals (Figure 1.3). The understanding and the general importance of the soft templating approach was strongly promoted by the discovery of the hexagonal ordered mesoporous silica by researchers from Mobil in the beginning of the 1990s.[37] Next to the hexagonal MCM-41 (Mobil Composition of Matter),

7

the most famous silica materials are probably the hexagonal SBA-15 (Santa Barbara Amorphous Type Material) as well as the cubic MCM-48 and KIT-6 (Korea Advanced Institute of Science and Technology).[37-39]
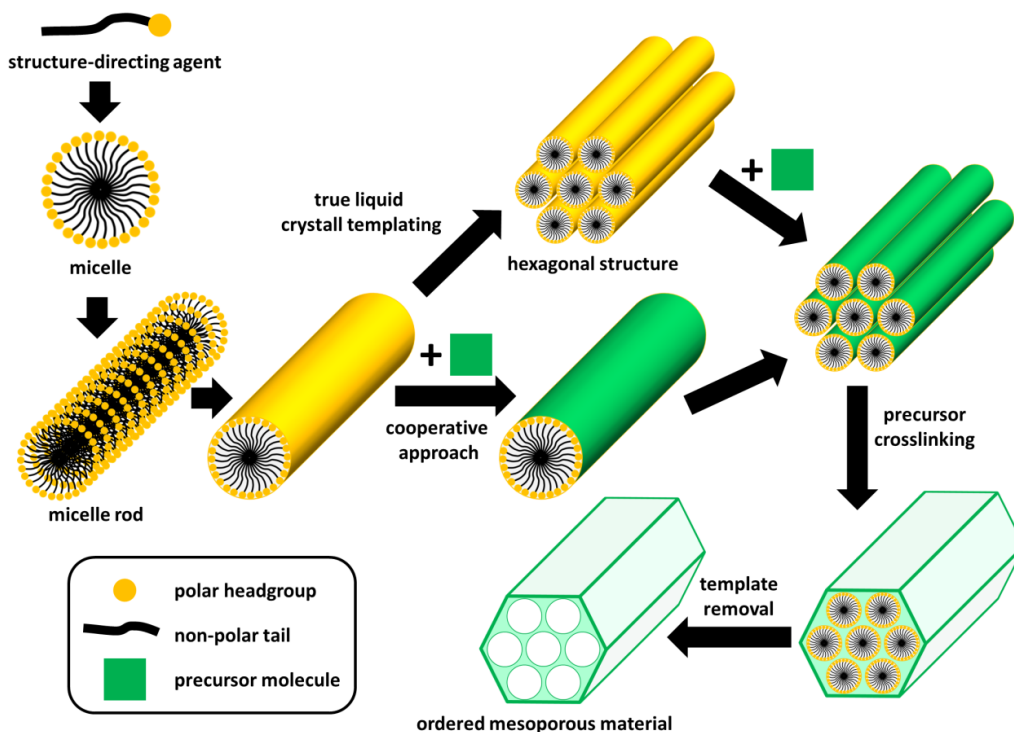
Figure 1.3 Schematic illustration of the synthesis of ordered mesoporous materials (e.g., MCM-41) *via* soft templating.

Detailed studies on the structure formation mechanism revealed that the first assumed theory of true liquid crystal templating only occurs at very high surfactant concentrations, whereas lower concentrations result in a cooperative mechanism.[36,40,41] In the latter, both substances, surfactant and precursor molecules, self-assemble, thereby forming the ordered structure. In contrast, true liquid crystal templating would first require the formation of an ordered structure only composed of the surfactant molecules, which are subsequently covered by the precursor molecules.

The direct synthesis of soft templated carbon materials is still rather difficult. There are four general requirements:[21] A) The used precursors have to be able to self-assemble into nanostructures. B) A pore-forming and a carbon-yielding phase have to be present. C) The pore-forming substance has to be stable during the curing (crosslinking) of the carbon precursor, but should yield negligible amounts of carbon during its decomposition. D) The curing of the carbon-yielding component needs to result in a highly crosslinked, thermally stable framework, ensuring its stability during the decomposition of the pore-forming agent. Moriguchi *et al.* created different (also ordered) mesophases using CTAB as the

8

pore-forming substance and a phenolic resin as carbon-yielding component.[42] The thermally induced crosslinking of the carbon component led to the collapse of the mesophases only yielding non-porous carbons. In contrast, the application of amphiphilic block co-polymers (mainly from the Pluronic® family) as structure-directing agents allowed the successful synthesis of a large family of soft-templated carbon materials with defined and homogenous mesopores.[43] The topology and size of the mesopore system can be easily adjusted by the choice of the precursor, as well as the ratio of the precursor to the block co-polymer. However, the obtained SSAs usually do not exceed $1000 \, \mathrm{m^2 \, g^{-1}}$ restricting the performance-to-price ratio of soft templated carbons. Furthermore, the polymer template is typically removed by a thermal treatment, which always induces a compaction of the material leading to a shrinkage of the pore system. The latter drawback can be overcome by hard templating methods.

Hard templating can be compared to a casting process on the nanoscale, giving rise to the expression "nanocasting".[44] Typically, a precursor is infiltrated into a porous solid template which acts as a space confinement ("casting mold"). Heat treatment and subsequent template removal yields the product ideally representing the exact inverse replica of the void space of the template. Hence, the pore size, pore structure, and pore connectivity are directly dictated by the template used, and therefore, can be easily adjusted. Due to the control over the final structure, hard templating is very appealing for the synthesis of highly ordered mesoporous carbon materials, employing the aforementioned ordered mesoporous silica as a template. Certain requirements have to be fulfilled to ensure a successful nanocasting:[44] A) All template pores have to be infiltrated with the precursor. B) The template itself and its mesoporous structure have to be stable during precursor carbonization. C) The precursor needs to possess low volatility, and negligible volume shrinkage during carbonization. The complete infiltration of the template can be achieved by the application of a liquid precursor which, however, stands in contrast to the low volatility requested. The most commonly used solid precursors can be infiltrated as a solution using an appropriate solvent. The subsequent solvent evaporation leads to volume loss, thus requiring multiple infiltration steps to ensure complete pore filling. Depending on the precursor, melt infiltration can sometimes be used to overcome the drawback of multiple impregnation steps.

The first successful nanocasted carbon material was reported by Gilbert *et al.* in 1982.[45] A silica gel was impregnated with a phenol-formaldehyde resin mixture, and

heated to 1000 °C in an inert gas atmosphere. The silica was subsequently removed with an alkali solution yielding the porous carbon. The first ordered porous carbon material synthesized by nanocasting used the aforementioned MCM-48 and yielded a cubic mesoporous carbon which was named CMK-1 (carbon mesostructured by KAIST[I]).[46] The synthesis of a self-supported porous carbon material was possible due to the bicontinuous gyroid mesopore system present in MCM-48. Generally, the preservation of the 3D shape requires an interconnected pore structure of the template. The probably most prominent hard templated carbon material is the hexagonal ordered CMK-3 representing the inverse replica of SBA-15.[47] The mesopore channels of SBA-15 are connected by micropores, allowing the synthesis of hexagonal ordered, interconnected carbon nanorods which exhibit mesopores between them (Figure 1.4).
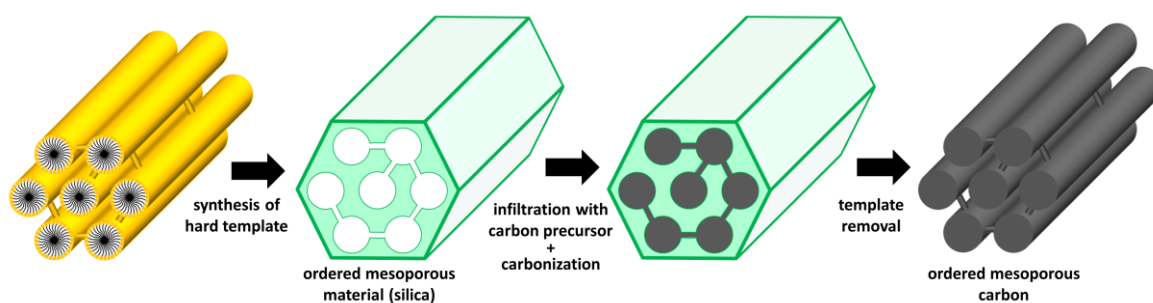
Figure 1.4 Schematic illustration of the synthesis of an ordered mesoporous carbon (e.g., CMK-3) *via* hard templating employing a mesoporous template (e.g., SBA-15).

Despite the hard templating method's great control over the obtained pore structure, it is hardly applied on an industrial scale. This is, for example, due to the cost, time, and materials needed to synthesize the hard template prior to the whole process. Another major drawback lies in the harsh conditions needed for the silica removal, which is typically conducted by washing with highly toxic hydrofluoric acid.[48] A different approach uses sacrificial templates, such as polymer spheres, which decompose directly during the thermal treatment of the precursor.[49,50] However, the sphere diameter usually exceeds 100 nm leading to solely macroporous carbons. The surface areas of hard templated carbons are typically larger than of soft templated carbons but are still distinctly lower than of activated carbons.

The three different synthesis approaches for porous carbon materials discussed so far (activation, soft templating, and hard templating) all exhibit advantages and disadvantages. Activation yields carbon with high SSAs but only allows limited control over the porosity.

[I] KAIST stands for Korea Advanced Institute of Science and Technology

Templating methods deliver the desired control over the (meso)porosity. However, soft templated carbons are still rather difficult to synthesize and hard templating is a cost-intensive, multistep approach. The challenge lies in the development of facile, inexpensive and sustainable synthesis approaches of porous carbons materials with high SSAs and controllable (meso-)porosity.

The porosity requirements can be fulfilled by carbide derived carbons (CDCs).[51] Chlorine treatment of metal carbides at high temperature causes the selective etching of the metal, yielding a mainly microporous carbon with SSAs up to 3000 $m^2 g^{-1}$. The micropore size can be carefully adjusted, even in the sub-Ångström region, by the variation of chlorination temperature and the type of (semi-)metal carbide.[52] The approach was further extended by using hard templated, mesoporous metal carbides as starting materials, allowing the synthesis of ordered mesoporous CDCs.[53,54] These materials combine the desired (meso-)porosity control with high SSAs. Furthermore, the obtained carbons possess a hierarchical porosity ensuring fast access to the surface sites. However, the synthesis consists of multiple steps, is still rather expensive, and results in low yields.

Recently, Fechler *et al.* introduced the synthesis of highly porous carbon materials using $ZnCl_2$-containing salt mixtures as the reaction medium.[55] The process combines simplicity with high SSA and a hierarchical pore structure of the obtained carbon material, indicating its high potential. The materials were obtained in a high yield and the morphology of the carbon was clearly influenced by the type of salt mixture used, both rather pointing to a templating effect than to an activation. Regarding the clear differences between classical activation (with H_2O and CO_2) and templating approaches, it is questionable if chemical activation with $ZnCl_2$ should be really discussed as an activation procedure. In 1992, Rodriguez-Reinoso *et al.* already pointed out that the incorporated $ZnCl_2$ prevents the contraction of the carbon framework during carbonization.[29] It was further stated that the porosity of $ZnCl_2$ "activated" carbons was initiated though the removal of the salt, and that the created pore volume could be linked to the used salt volume. It has to be considered that $ZnCl_2$ is in the liquid state ($T_{melt} = 318 \,°C$) at the typically applied activation temperatures. The liquid, mobile $ZnCl_2$ could migrate in between the carbon layers, thereby causing layer separation. All these factors indicate that $ZnCl_2$ "activation" also may rather be discussed as a templating method. Accordingly, Fechler *et al.* introduced the term "salt templating" for the synthesis of highly porous carbon inside a molten eutectic mixture. The application of salt melts as reaction mediums

(herein called ionothermal synthesis) is highly interesting and will be discussed in the following section 1.2.3.

1.2.3 Porous Carbon Materials Obtained by Ionothermal Synthesis („Salt Templating")

The term ionothermal synthesis indicates a reaction which is conducted in a solvent made up of ionic species. Hence, any reaction carried out in a molten salt (independent on the reaction temperature) can be regarded as an ionothermal process. Rather high temperatures are needed if classical salts are used to ensure the liquid state of the solvent. The rising interest in ionic liquids (ILs), typically defined as organic salts, which are liquid at temperatures lower than 100 °C, led to a further extension of the ionothermal approach.[56] ILs can serve as the solvent, template, and/or structure directing agent during the formation of solid materials.[57] Another material class, regarded as molten salts, is deep eutectic solvents (DES), delivering an inexpensive alternative to ILs.[58,59] The final temperature needed to obtain "real" carbon materials by pyrolysis is rather high (T > 800 °C). Thus, neither ILs nor DES can be used as reaction mediums due to their lower decomposition points.

Material synthesis is a chemical transformation, which can be conducted in a gaseous, liquid or solid medium. Solid-state synthesis usually exhibits limited reaction kinetics, requiring high temperatures and long reaction times. Apart from the high energy needed, this makes it difficult to obtain kinetically stable intermediates, such as many nanomaterials.[60-62] Contrarily, reactions in solution deliver (reversible) dynamics, homogenous heat distribution, and high reaction control. However, typical solution chemistry is restricted to temperatures below ~ 200 °C. Solvothermal approaches or the application of high-boiling solvents can extend the range up to 400 °C, but at higher temperatures almost all of the solvents decompose or turn supercritical. As aforementioned, these temperatures do not trigger the carbonization process. The application of salt melts as the reaction medium combines the advantages of the high mobility of the reactants with the high thermal stability of the solvent.

There are three general parameters which have to be considered for the ionothermal synthesis regarding an ideal precursor – salt systems:[63] A) The operating temperature should be higher than the melting point of the used salt or salt mixture. B) The precursor should be adequately soluble in the salt melt because the solubility determines the rate of reaction. C) The salt melt should be inert under the reaction conditions (not directly

involved in the reaction) to ensure a "typical" solvent-like behavior. Metal halides (e.g., $ZnCl_2$ and KCl) are especially interesting due to their inertness as reflected by their large electrochemical window. Moreover, the melting point can be adjusted (lowered) by the use of eutectic mixtures allowing the application of precursors that decompose at relatively low temperatures such as inexpensive and sustainable glucose.

The possibility of obtaining porous carbon materials by applying molten salts as a reaction medium was introduced by Liu *et al.* and their pyrolysis of glucose inside a eutectic LiCl/KCl mixture.[64] The two salts were simply mixed with the precursor and the resulting powder was heated under an inert gas atmosphere. The salt, which was still present in the obtained composite, was removed by aqueous washing, yielding the porous carbon material. The amount of salt used had a clear influence on the resulting carbon structure/porosity, indicating a templating effecting (Figure 1.5).
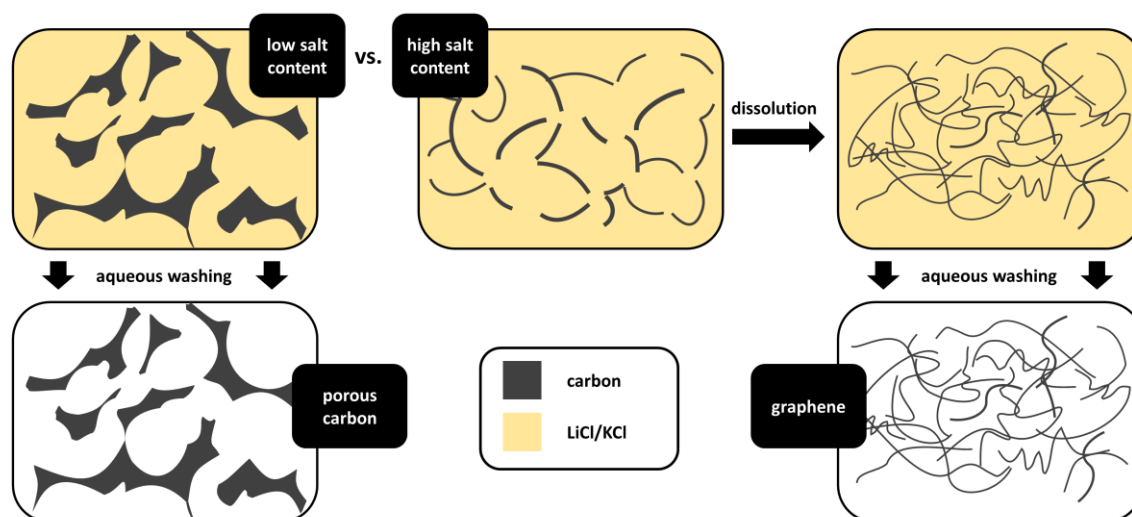
Figure 1.5 Schematic illustration of the formation of porous glucose derived carbon in molten LiCl/KCl at low salt content and the formation of graphene at high salt content (adapted from[64]).

At the lower salt to precursor ratios investigated (10:1), the product exhibited an irregular, hierarchical morphology consisting of randomly interconnected microporous carbon domains. An increased synthesis temperature led to enlarged SSA values, which reached a maximum at 700 °C showing a value of 600 m^2 g^{-1}. At higher temperatures the SSA decreased again probably due to an enhanced stacking of the carbon layers. Contrarily, very high salt to precursor ratios (100:1) lead to the synthesis of a graphene like material that still possessed similar SSA. The different morphologies were linked to different carbonization mechanisms. High salt content results in a solution process producing graphene sheets whereas low salt content causes precipitation yielding larger, interconnected carbon domains. The method was extended by intentionally adding reactive

salt species to the reaction mixture, which led to highly porous carbon materials (SSA ~ 3200 $m^2\,g^{-1}$) and allowed the introduction of heteroatoms.[65,66] The structure of the porous sheet-like carbons was very recently described as assembled sp^2 carbon nanoribbons.[67]

The templating effect of salt mixtures during the synthesis of highly porous heteroatom doped carbon materials was discussed in more detail by Fechler *et al.*[55] Inorganic $ZnCl_2$ containing salt mixtures were mixed with carbonizable ILs in a 3:1 wt.-ratio and heat treated under high temperatures (T = 1000 °C) in an inert gas atmosphere. The compatibility of the inorganic salt and the organic IL ensured molecular mixing of the two phases during the whole process, and only nanoseparation of the inorganic salt and the carbonizing precursors occurred. After heat treatment the salt phase (the template) was removed by aqueous washing yielding highly porous carbon materials with SSAs up to 2000 $m^2\,g^{-1}$. The morphology/pore structure of the ionothermal carbon was mainly dependent on the eutectic salt mixture and not on the type of ionic liquid, which was applied as a precursor (Figure 1.6). This effect was explained by different properties of the eutectic salt mixtures, such as melting point, viscosity and polarity.
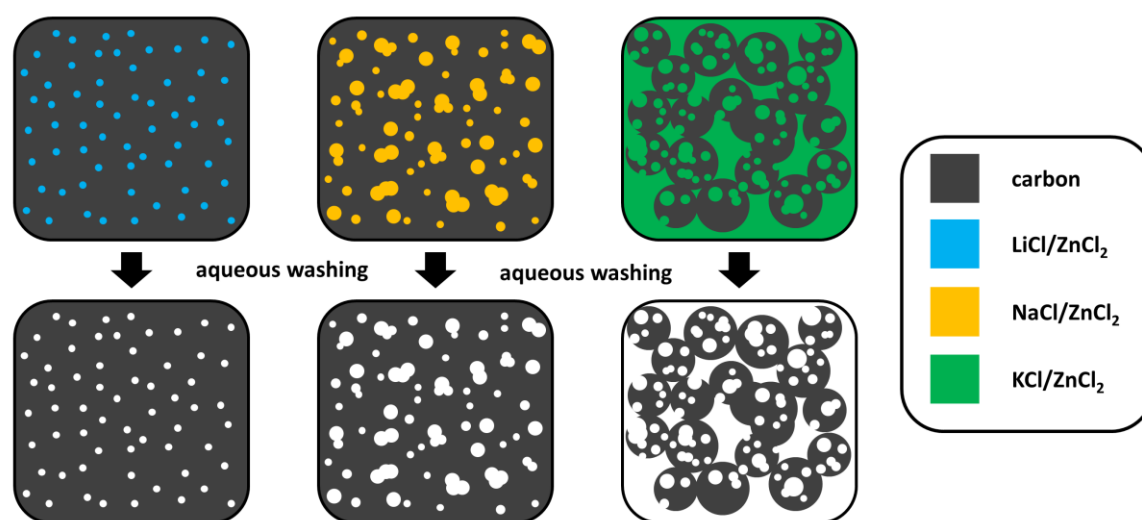
Figure 1.6 Schematic illustration of the obtained carbon morphology/porosity depending on the used salt mixture during the ionothermal synthesis of ionic liquid derived carbon materials (adapted from[55]).

The application of $LiCl/ZnCl_2$ led to a continuous carbon phase possessing mainly micropores, which indicated a "molecular templating" role of the salt system. Replacing LiCl with NaCl also resulted in a continuous carbon phase but additional supermicropores and small mesopores were formed. The effect was linked to the lower melting point of $NaCl/ZnCl_2$ in comparison to $LiCl/ZnCl_2$ and to larger salt clusters caused by phase demixing in the later stage of carbon condensation. The $KCl/ZnCl_2$ mixture, possessing the

lowest melting point of the three salt systems investigated, resulted in a continuous salt phase and micro- and mesoporous spherical carbon particles. The morphology was explained by an enhanced phase separation in the earlier stages of the crosslinking reactions.

The discussed results indicate that the application of molten salts as reaction mediums for carbonization reactions is not only interesting from a scientific point of view, but also entails appealing factors for a "greener" production of highly porous carbon materials, such as morphology control and the very easy template removal. Moreover, the used ILs contained nitrogen and/or boron atoms which were incorporated into the carbon framework upon carbonization leading to heteroatom doped carbons. The introduction of different heteroatoms into to the carbon framework opens up new possibilities in tailoring the properties towards distinct applications. The present thesis will concentrate on nitrogen doped carbons which are further discussed in the following section 1.2.4.

1.2.4 Porous Nitrogen Doped Carbon Materials

The introduction of nitrogen atoms into a carbon framework not only alters surface properties but also the electronic structure of the material. The resulting nitrogen doped carbon (NDC) can exhibit changed sorption properties, a varied work function, and even clearly improved catalytic activities when compared to the non-doped material.[68-70]

The introduced nitrogen species can be divided into surface functionalities (e.g., amine) and structural modifications (e.g., graphitic nitrogen) (Figure 1.7). The former hardly changes the original characteristics of the carbon itself while the latter is assumed to cause the observed change in intrinsic properties.[71] One possible effect is an enhanced electrical conductivity, as seen by the N-induced metal like behavior of N-doped CNTs.[72] Furthermore, structural nitrogen introduces more charge carriers also leading to a reduced work function.[73] This is believed to be one of the reasons for the greatly increased activity of NDCs in electrocatalytic applications. Regarding supercapacitor applications, surface N-sites can store additional energy due to Faradaic reactions (called pseudocapacitance) causing an increased overall capacitance of the device.[74] The special role of porous and nitrogen doped carbons in electrochemical applications will be discussed in more detail in chapter 1.3.
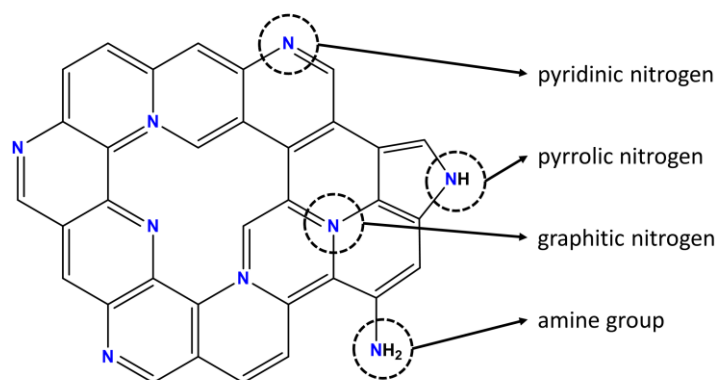
Figure 1.7 Schematic illustration of different possible nitrogen functionalities present in nitrogen doped carbons.

The synthesis approaches of porous NDCs can be generally separated in two different classes: A) The nitrogen functionalities are introduced by a post-treatment of already porous carbons, which is typically accomplished by heat treatment in ammonia (NH_3) atmosphere. B) Nitrogen containing precursors are used for the aforementioned synthesis methods of porous carbons which leads to N-incorporation into the carbon framework upon pyrolysis. The latter pathway usually leads to structurally incorporated N-sites and simplifies the process by eliminating the treatment under NH_3-atmosphere. If the ionothermal approach is used, NDCs can be synthesized in a one-pot reaction only requiring aqueous washing as post-treatment.

1.3 Energy Storage and Conversion

Among different approaches to store energy, batteries and supercapacitors are very promising devices, as presented in section 1.1.[75,76] The former is more interesting regarding high energy devices and the latter for high power applications. The general concept of supercapacitors will be discussed in section 1.3.1. Fuel cells represent one of the most promising technologies for energy conversion. One of the main challenges, that is necessary to overcome for their widespread commercialization, is reducing the high amount of platinum needed as the catalyst, especially for the oxygen reduction reaction occurring on the cathodic site of a fuel cell.[77] The activity of the oxygen reduction reaction of different materials can be measured by the rotating (-ring) disk electrode and will be introduced in detail in section 1.3.2.

1.3.1 Supercapacitors as Energy Storage Devices

The charge storage in supercapacitors (also denoted as ultracapacitors or electrochemical double layer capacitors) is based on the potential driven adsorption of ions on the surface of the electrode materials. Thus, the charge storage process in SCs is of purely physical character in contrast to the one of batteries which is based on rather slow redox reactions.[78] Consequently, SCs possess a high efficiency, a high cyclability, and a fast charge/discharge process accompanied by a high power density compared to batteries.[78] Porous carbon materials are a very promising candidate for SC-electrodes due to their high SSA, electrical conductivity, and electrochemical stability.[18,79] Due to their unique properties, SCs can close the gap between classical capacitors and batteries regarding energy and power density (Figure 1.8A). In comparison to batteries, the increase in performance and the decrease in production costs of SCs was significantly faster over the last decade.[80] Nonetheless, classical SCs still show lower energy densities than batteries. The overall capacitance of SCs can be further enhanced by so-called pseudocapacitive effects based on rapid and reversible surface redox-reactions. Pseudocapacitance can be introduced, for example, by the employment of metal oxides, conductive polymers, or the introduction of redox-active heteroatoms, such as nitrogen, into the carbon framework.[81-83]
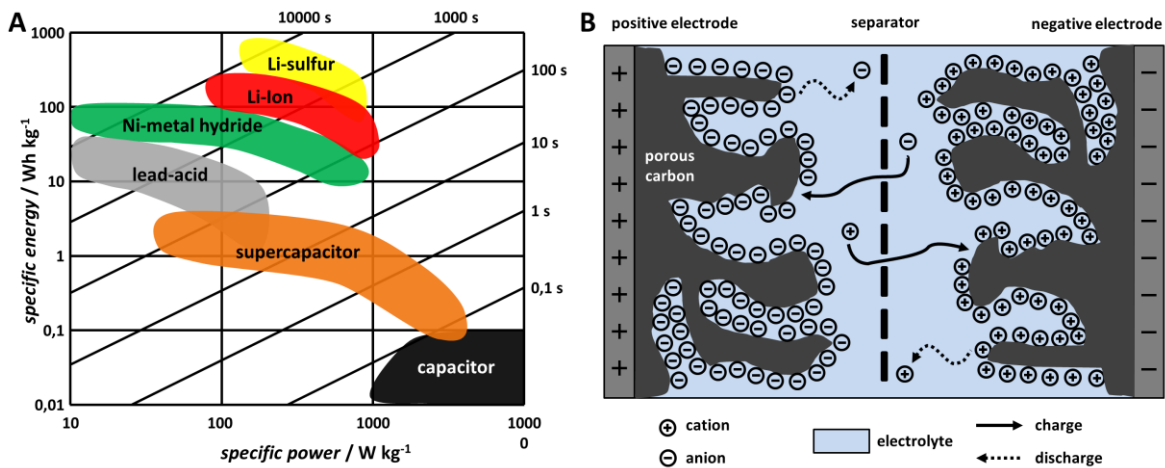
Figure 1.8 A) Ragone plot of selected energy storage devices, adapted from[84]. B) Schematic illustration of the charged state of a supercapacitor using porous electrodes.

In the simplest case, a SC is made up of two porous electrodes (contacted by current collectors) which are separated by an electrically insulating membrane and immersed in an ion containing electrolyte (Figure 1.8B). If a voltage is applied at the current collectors, electrolyte ions will accumulate according to their charge at the electrodes and energy can be stored. The reversible adsorption of electrolyte ions on the electrode surface coupled with charge separation at the electrolyte-electrode interface can be described by the

classical Helmholtz-theory which was later expanded by Gouy, Chapman, and Stern.[85] The amount of stored energy with respect to the applied voltage is denoted as capacitance (C) and is determined by the area (A) of the electrodes, the dielectric constant of the electrolyte (ε_r), the dielectric constant of the vacuum (ε_0), and the charge separation distance (d), as described in Equation (1.8).

$$C = \varepsilon_r \, \varepsilon_0 \, \frac{A}{d} \tag{1.8}$$

In SCs, d is determined by the thickness of the Helmholtz double layer, which is in the monadic Ångstrom region, giving rise to high capacitance values. The characteristic values of energy storage devices, i.e., specific energy (E) and the specific power (P), can be determined by Equation (1.9) and (1.10), respectively.

$$E = \frac{1}{2 \cdot m} \cdot C \cdot U^2 \tag{1.9}$$

$$P = \frac{1}{4 \cdot ESR \cdot m} \cdot U^2 \tag{1.10}$$

Here, m is the total mass of the electrode material, U the applied voltage, and ESR the equivalent series resistance.

The porosity of the used carbon material plays a major role regarding the achievable energy and power density in SCs. Certain pore sizes can be linked to different functions.[86,87] Micropores cause a high SSA to accomplish a high double-layer capacitance. In the case of ultramicropores, the capacitance can be even further increased due to a desolvation/intercalation mechanism. Present meso-/and macropores act as "ion-highways" promoting the ion supply. Generally, the ion diffusion kinetics are determined by the pore size distribution, thus, influencing the maximum power densities of the device.[18,78,80,85,88]

1.3.2 The Oxygen Reduction Reaction

As aforementioned, the oxygen reduction reaction (ORR) takes place at the cathodic site of fuel cells which are classically operated under acidic conditions. In acidic media, oxygen (O_2) can either be reduced in a four electron process to H_2O or in a two electron process to hydrogen peroxide (H_2O_2), as described in Equation (1.11) and (1.12), respectively.

$$O_2 + 4\,H^+ + 4\,e^- \rightarrow 2\,H_2O \tag{1.11}$$

$$O_2 + 2\,H^+ + 2\,e^- \rightarrow H_2O_2 \tag{1.12}$$
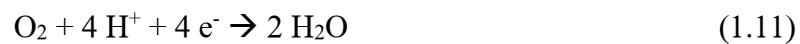
In fuel cell applications, the favored reaction is the four electron process due to the higher current per molecule oxygen and the avoidance of H_2O_2 which is a known degradation source.[89]

Due to the high activation energy needed for the cleavage of the O_2 bond, a catalyst has to be employed to accelerate the reaction. Most of the commercial applications still focus on platinum (Pt) based catalysts (typically dispersed on a porous carbon support, Pt/C) despite their high costs and their limited performance due to a moderate lifetime and the methanol crossover effect.[90] During the last years, it has been shown that NDCs can deliver the catalytic properties needed, especially, in alkaline media.[68,91-94] Under alkaline conditions (pH > 12), the four electron reduction of O_2 leads to the formation of hydroxide ions whereas the two electron process yields (next to the hydroxide ion) the hydrogen peroxide anion (Equation (1.13) and (1.14)).

$$O_2 + 2\,H_2O + 4\,e^- \rightleftharpoons 4\,OH^- \qquad (1.13)$$

$$O_2 + H_2O + 2\,e^- \rightleftharpoons HO_2^- + OH^- \qquad (1.14)$$
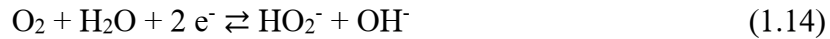
The introduction of additional non-noble metals (such as iron and cobalt) can further enhance the alkaline ORR activity and even leads to promising activities under acidic conditions.[95,96] Furthermore, the porosity of the used NDC material plays an important role since the catalytic reactions take place on (or close to) the surface of the catalyst material. Thus, a high SSA should in principal lead to a high activity per mass catalyst. Moreover, the porosity should enable a fast transport of O_2 to (and a fast transport of the products from) the active sites indicating the importance of the presence of relatively large pores in the meso- and macropore range. Indeed, literature results show that hierarchical pore systems containing micro-, meso- and macropores can lead to high ORR performances, especially, in the kinetically limited region.[97,98] Next to the porosity features, the nitrogen content and the type of nitrogen sites also play an important role. It is believed that higher N-contents can enhance the activity to a certain extend and highly active catalysts show a N-content of approximately 5 to 10 wt.%.[99,100] However, the findings are only of empirical nature and it is not possible to identify a general optimal N-content for the ORR. Regarding different N-sites, the ORR activity of NDCs is usually connected to the presence of pyridinic, pyrrolic, and/or graphitic N species.[101-106] However, the obtained correlations between the ORR activity and a specific N-site are contradicting. One commonly faced challenge during the investigation of the relation between the ORR activity and a varied parameter (e.g., SSA, N-content, N-site etc.) is the co-dependence of

these parameters. Different synthesis temperatures, for example, can be used to vary the N-content, but will/can also lead to different porosity characteristics. Thus, it is important to develop methods that allow the variation of only one parameter to gain more insights on the effect/importance of a certain parameter on the ORR performance. Nonetheless, four main features of NDCs appear to be reasonable to link to a high ORR activity: a) a high SSA ensuring a high activity to mass ratio, b) transport porosity enhancing the kinetics, c) a sufficient N-content (~ 5 - 10 wt.%), and d) a high electrical conductivity of the material.

The rotating disk electrode (RDE) is a convenient tool for analyzing different catalysts regarding their ORR-performance. The applied rotation rate induces a controlled and well-defined convection of the solution allowing the collection of information about reaction kinetics *via* mathematical modelling.[107-109] The ORR activity is typically studied by linear sweep voltammetry. Thereby, the potential is swept at a constant rate (sweep rate) from an initial to a final value and the current response is measured.[107] A similar method is cyclic voltammetry (CV), in which the potential is repeatedly swept back-and-forth between two boundary values. The ORR-activity of a catalyst is usually analyzed by the application of a cathodic sweep starting at a potential at which no reaction is occurring. During the LSV, a cathodic (negative) current arises when the potential is negative enough to introduce the reduction of O_2. The further negative polarization of the electrode increases the cathodic current till a maximum value is reached (limiting current, i_{lim}). At this stage, every oxygen molecule is immediately converted (reduced) and the current is only determined by the mass transport of the oxygen towards the electrode, which is related to the thickness of the diffusion layer (δ_F). The δ_F on a RDE can be adjusted by the applied angular rotation rate (ω) according to Equation (1.15).

$$\delta_F = 1.61 \cdot D_F^{1/3} \cdot v^{1/6} \cdot \omega^{-1/2} \qquad (1.15)$$

Here, D_F and v are the diffusion coefficient of oxygen (in the employed electrolyte) and the kinematic viscosity of the electrolyte, respectively. If the saturation concentration of oxygen in the electrolyte (c_O) is known, the Levich-equation delivers the connection between the applied rotation rate and the theoretically obtained i_{lim} which is also called Levich current (i_{lev}) (Equation (1.16)).[110]

$$i_{lim} = 0.62 \cdot n \cdot c_O \cdot A \cdot F \cdot D_F^{2/3} \cdot v^{-1/6} \cdot \omega^{1/2} \qquad (1.16)$$

Here, n, A, and F are the number of transferred electrons (per molecule oxygen), the geometric area of the electrode, and the Faradaic constant, respectively. In a Levich-

analysis, the i_{lim} is studied in relation to the applied rotation rate. The slope of the resulting linear plot of i$_{lim}$ vs. $\omega^{1/2}$ can be used to determine the apparent electron transfer number of the ORR. During the ORR, the i_{lim} value for n = 4 defines the maximum current value which can be obtained at a certain rotation rate (in the used electrolyte) and depends on the geometric area of the electrode but is independent of the SSA of the catalyst. However, the catalytic activities do not always reach limiting currents due to kinetic limitations. Therefore, the Levich-equation was later extended to also describe kinetic limitations by the Koutecky-Levich (KL) equation presented in Equation (1.17).[107,109]

$$\frac{1}{i} = \frac{1}{i_{kin}} + \frac{1}{i_{lim}} = \frac{1}{i_{kin}} + \frac{1}{0.62 \cdot n \cdot c_O \cdot A \cdot F \cdot D_F^{2/3} \cdot v^{-1/6}} \cdot \omega^{-1/2} \qquad (1.17)$$

Here, i_{kin} stands for the kinetic current which is the potential dependent current that would be observed in the absence of any mass transport (diffusion) limitation. The plot of the reciprocal, measured current (i^{-1}) vs. the reciprocal angular rotation rate ($\omega^{-1/2}$) yields a straight line. The slope of the line and the intercept can be used to determine the apparent n and for the calculation of the (potential dependent) i_{kin}, respectively.

Especially if highly porous electrodes are studied, it is important to correct the obtained LSVs in O$_2$-saturated electrolyte for the capacitive current. This is accomplished by subtracting the current response in N$_2$-saturated electrolyte, representing the capacitive current, from the measured current response in O$_2$-saturated electrolyte (applying in both cases the same sweep rate). The resulting curve represents only the Faradaic current of the ORR, needed for the Levich or KL-Analysis.

The RDE set-up consists of the rotating working electrode (typically a glassy carbon), a reference electrode and a counter electrode (e.g., a Pt-wire or a graphite rod). The three electrode RDE set-up and is schematically presented in Figure 1.9A. Additionally, a photograph of the set-up is shown in Figure 1.9B.

To compare different catalysts, the halfwave potential ($E_{1/2}$, the potential at which 50 % of the i_{lim} is reached) can be used, providing a characteristic, rotation rate independent value for the activity and the kinetic performance of the catalyst. In literature, it is very common to compare the activity of the investigated catalyst with the performance of the commercial Pt/C catalyst by the LSVs at 1600 rpm resulting in a more figurative comparison.[II] However, literature studies reveal that such a comparison can be misleading due to the high sensitivity of the noble metal catalysts on the reaction conditions. The Pt/C

[II] To show the LSVs obtained with 1600 rpm, is actually typical for Europe whereas in the USA the rotation rate of the usually depicted LSVs is 900 rpm.

catalyst should be applied in sufficient loading and measured with an anodic scan.[111] In the case of a chloride containing electrolyte of the reference electrode, a salt bridge should be used to avoid poisoning of the Pt/C catalyst. This is especially important during long-term (stability) measurements. The mentioned issue of different Pt/C activities, which could lead to a false judgement of the investigated catalyst's activity, is illustrated in Figure 1.9C by the comparison of two Pt/C LSV curves (both obtained in 0.1 M KOH with a rotation rate of 1600 rpm).[112,113] To avoid such discrepancies, a *webplot tool* can be used allowing the direct (figurative) comparison of different LSV curves including literature plots, and will be applied in the present thesis.[III]
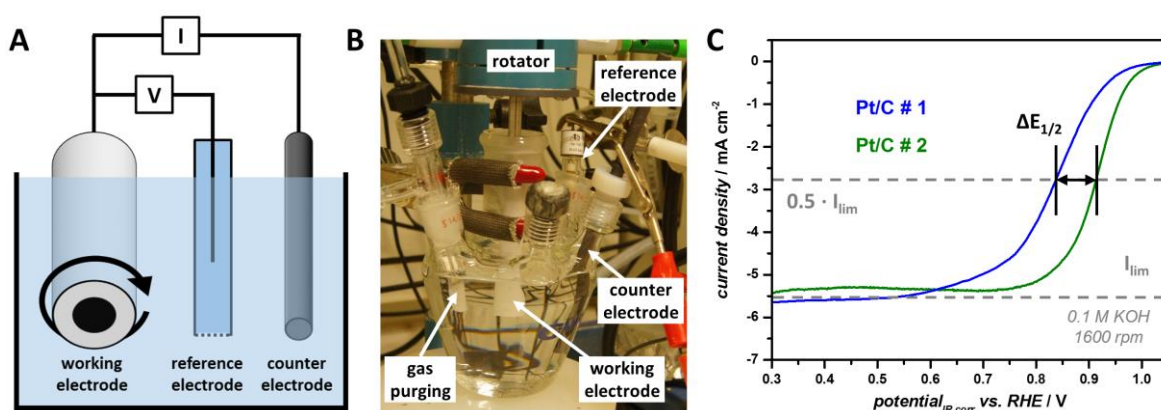
Figure 1.9 A) Schematic illustration and B) image of the three electrode RDE set-up. C) Polarization curves of the commercial Pt/C catalyst from two different literature sources with indicated limiting current and $E_{1/2}$ (both measured in 0.1 M KOH with a rotation rate of 1600 rpm).[112,113]

The rotating-ring disk electrode (RRDE) is a further expansion of the already described RDE and involves a ring electrode which is placed around the disk electrode.[114] The overall axial flow first brings the molecules (O_2 in the case of the ORR) to the disk electrode. The subsequent outward radial flow transports a fraction of those molecules to the ring. Thus, the products of the reaction occurring on the disk electrode can be *in-situ* detected and quantified on the ring electrode. In the case of the ORR, H_2O_2 as a side product can be detected by a positive polarized Pt-ring *via* oxidation. For quantification, the collection efficiency (N) has to be determined first experimentally, which represents the fraction of the molecules from the disk subsequently flowing past the ring electrode. With the measurement of the disk current (i_D) and the ring current (i_R) during a RRDE experiment, the yield of hydrogen peroxide ($H_2O_2(\%)$) and the transfer electron number (n) can be calculated with Equation (1.18) and (1.19), respectively.

[III] The used *webplot tool* is called WebPlotDigitalizer (http://arohatgi.info/WebPlotDigitizer).

$$H_2O_2(\%) = 200\,\frac{i_R/N}{i_R/N+i_D} \tag{1.18}$$

$$n = 4\,\frac{i_D}{i_R/N+i_D} \tag{1.19}$$

Here, at the end of the introduction, it has to be mentioned that, of course, the present thesis will not be able to deliver a universal solution for the energy related issues/challenges described in section 1.1. However, it can possibly pave the way towards the application of pore tailored carbon materials, prepared by cheap and sustainable pathways, in energy related fields, thereby, enforcing the expansion of renewable energy sector. The general outline of the thesis will be presented in chapter 2.

2 Outline

To fulfill the dream of a fossil-independent energy economy, alternative concepts for energy storage and conversion have to be developed, optimized and employed. One material, which plays a major role in many of those concepts, is porous carbon. Research groups all over the world work on the development of new synthesis routes of porous carbon materials. The tailoring of the porosity features is especially interesting due to the direct relation between porosity characteristics and the performance/activity obtained in electrochemical applications. Moreover, the introduction of heteroatoms can alter the properties of the carbon enhancing the activity and even leading to the exploration of new application fields. Indeed, nitrogen doped carbons show very promising activities towards the oxygen reduction reaction in fuel cells rating them as inexpensive alternative to the cost-intensive platinum based materials commercially employed. However, one challenge to overcome, scientifically and in respect of targeted catalyst optimization, is the not yet unraveled ORR-mechanism of NDC materials.

The aim of the present thesis is to gain a deeper understanding of the ionothermal approach which uses inexpensive salt mixtures as combined porogen/solvents for the synthesis of highly porous carbon materials. Throughout the work, biomass derived precursors will be employed to go along with the aim of sustainability. Depending on the precursor, either carbons or nitrogen doped carbons can be obtained. In chapter 3, a new pore tuning tool of ionothermal carbons will be introduced leading to precisely pore tailored but chemically equivalent materials. The results not only deliver deeper insights into the porogenesis but also allow the precise study of porosity/activity relations in electrochemical applications. The electrochemical results of the pore tailored NDC materials will mainly focus on the ORR revealing a strong effect of the pore shape on the activity and performance. To tackle the unknown ORR mechanism, a new methodology for mechanistic investigations will be introduced in chapter 4. The so-called H_2O_2 crossover test represents a facile approach to analyze if a catalyst intermediately produces H_2O_2. The results of different catalyst materials will be discussed, delivering new insights, especially, regarding the pH-dependence of the ORR-mechanism and -activity. Chapter 5 will extend the ionothermal approach towards the employment of hydrated salts as combined solvent/porogen. The so-called extended ionothermal synthesis is highly interesting due to the possibility of introducing a secondary templating effect which leads to structured highly porous NDC materials. The discussions will focus on the porosity features and the

understanding of the origin of the secondary templating effect. Moreover, the materials will be used to introduce the concept of facile metalation of NDCs to improve their ORR-activity. The results will be discussed in the context of the initial properties of the NDC, the active sites present after metalation, and the measured ORR-activity delivering further insights in the (pH-dependent) ORR-mechanism.

3 Ionothermal Carbons with Tailored Porosity

3.1 Background and State-of-the-Art

The ionothermal approach allows the synthesis of highly porous carbon materials with different morphologies as presented in section 1.2.3. It is aimed to carbonize in an all-liquid medium which can lead to nanoseparation of the carbonizing precursor and liquid salt phase thus giving rise to increased SSA and TPV of the obtained carbon material. The carbonizing precursor phase can be either the dispersing or the dispersed phase in the carbon-salt system. The salt domains are removed after the synthesis by (aqueous) washing resulting in the observed porosity. Assuming homogenous reaction conditions, the mixing/demixing of salt and carbonizing precursor phase is one of the main parameters influencing the porosity obtained. The PhD-thesis of Fechler and the work of Elumeeva *et al.* revealed that the ionothermal carbonization in molten salts, especially at high salt to precursor ratios, can be described as a sol-gel carbonization.[115,116]

Sol-gel carbonization classically requires an all liquid reaction mixture consisting of precursor and solvent molecules in the beginning. Partial polymerization of the precursor molecules forms the intermediate sol which can be described as a colloidal precursor dispersion. Further crosslinking reactions of the primary particles leads to the gel representing a (bi)continuous system consisting of the solid, crosslinked precursor and the liquid solvent phase (Figure 3.1). The solid phase can be described as a continuous network of interconnected carbon particles leading to aerogel-like structures.[117] The removal of the solvent results in a porous solid material, ergo a carbon aerogel.
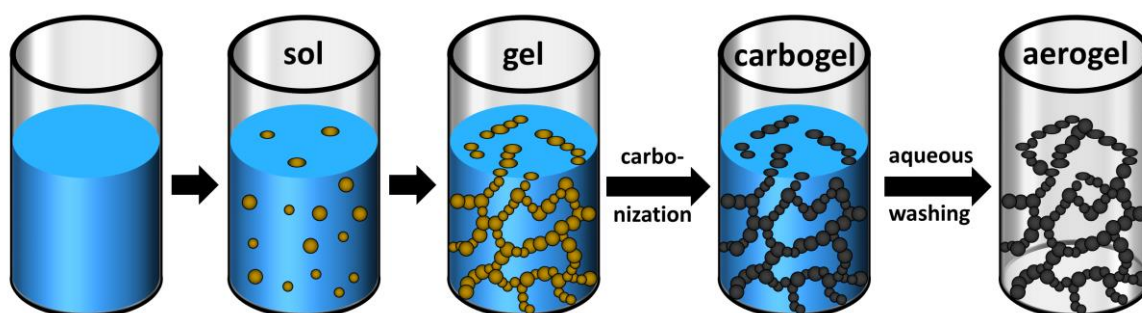
Figure 3.1 Schematic illustration of the sol-gel carbonization (adapted from[118]).

The first carbon aerogels were obtained by the pyrolysis of organic aerogels which were introduced by Pekala in 1989.[119,120] The organic aerogels were synthesized by the acid or base catalyzed condensation of resorcinol-formaldehyde and the obtained structure could

be tuned by the amount of catalyst used.[121] Higher catalyst amounts lead to an accelerated reaction rate. An increased reaction rate quickly leads to a critical supersaturation of the polymerized species causing a large number of seed particles (the sol) during the nucleation according to the LaMer-model.[122] A large number of seeds results in smaller particles during the growth phase yielding larger SSAs in the final material. The method was later expanded to the hydrothermal carbonization of biomass derived precursors, such as dissacharides or glucose, allowing the synthesis of biomass based carbon aerogels.[123,124] One advantage of the sol-gel carbonization is the hierarchical porosity obtained due to the micro- (or even meso-) porous character of the primary carbon particles and the interstitial pores in the macropore range. Another advantage lies in the possibility to specifically influence the sol-gel process by adding substances acting as moderators or catalysts which allows the facile tailoring of the porosity obtained.[125-127] In later work Fechler *et al.* introduced supersaturated, aqueous mixtures of $ZnCl_2$ (or $ZnCl_2$-containing salt mixtures) as reaction mediums for the hydrothermal carbonization of carbon aerogels.[128] The hypersaline conditions allowed the surface stabilization of the primary carbon nanoparticles thereby hindering particle growth and Ostwald ripening. After surpassing a critical particle concentration, spontaneous spinodal phase separation coupled with further crosslinking reactions occurred leading to the porous carbon structure. It was stated that higher salt contents led to higher SSAs showing the easy tunability of the porosity. The drawback of hydrothermal carbons, especially considering electrochemical applications, is the rather poorly developed π-system restricting the overall electrical conductivity. Hence, the application of pure molten salts as reaction mediums is highly interesting because it delivers the facile tunability of the porosity, according to the sol-gel principles, and a stable liquid reaction medium at high temperatures, as already introduced in section 1.2.3. As aforementioned, later work successfully showed that the principles of sol-gel carbons could be expanded to the ionothermal carbonization delivering not just a facile one-step reaction towards highly porous carbons, but also allowing the usage of the typical "sol-gel-toolbox" to tailor the porosity obtained.[115,116] According to the sol-gel principle, the porosity of ionothermal carbons can be easily tuned by adjusting the solvent (salt) to precursor ratio. Higher salt amounts lead to an increased separation of the carbon particles during the crosslinking which will lead, at least to a certain extent, to higher SSAs and TPVs. Furthermore, the type of salt mixture used will influence the morphology showing the already high variability of the ionothermal approach. Elumeeva *et al.* used those facile pore tuning tools to optimize the porosity regarding the mass transport of IL-derived highly

porous NDCs thereby achieving highly active (noble) metal free electrocatalysts.[95,116] To expand the range of precursors, Schipper presented in his PhD-thesis glucose and glucosamine as sustainable precursors for the ionothermal synthesis of carbon materials starting, however, in an aqueous solution of precursor and $ZnCl_2$, guaranteeing the all liquid initial reaction conditions.[129] The porosity could again be tailored by the simple adjustment of the salt to precursor ratio supporting a porogenesis mechanism according to the sol-gel principles.

Regarding the literature results, the ionothermal approach already delivers two major tools to tune the porosity/morphology of the final carbon material. A) The ratio of salt to precursor influences the separation of the primary carbon particles leading (to a certain extent) to higher SSAs coupled with higher TPVs if higher salt amounts are applied. B) The type of eutectic can be used to influence the properties of the salt melt, thereby, adjusting the general mixing/demixing behavior of precursor and salt phase. The right combination of those two parameters already allows for a great variation of the pore system. However, an increased salt amount is usually also linked to higher SSAs and the change of the eutectic results in a rather drastic change of the obtained morphology/porosity. Moreover, different eutectics could lead to chemically varied carbon materials complicating the investigation of porosity-performance relations in electrochemical applications. Thus, the development of methods which allow the synthesis of ionothermal carbon materials with tailor-made porosity features such as predictable SSAs and finely adjustable pore sizes but very similar chemical properties are of high interest.

In the present chapter, the variation of the molar composition of binary salt mixtures will be introduced as a new pore tuning tool allowing the desired synthesis of (heteroatom doped) highly porous carbon materials with tailor-made porosity. Moreover, the obtained materials show the desired chemical equivalence allowing the distinct investigation of porosity-performance relation in different application fields. To go along with the principles of Green Chemistry, biomass derived precursors will be investigated.[130] In section 3.2, the employed precursors will be introduced and the porosity obtained with the different $ZnCl_2$-containing salt mixtures (LiCl/$ZnCl_2$, NaCl/$ZnCl_2$, and/or KCl/$ZnCl_2$) will be discussed. Section 3.2.1 will concentrate on the ionothermal synthesis of (nitrogen doped) porous carbons derived from glucose or glucosamine expanding the work of

Schipper towards an all-solid reaction mixture in the initial state.[129] The herein developed approach supports the scalability allowing a batch yield of up to 130 g for the mesoporous NDC material. In section 3.2.2, nucleobases (i.e., guanine hydrochloride and adenine) will be introduced as a new precursor class for the ionothermal approach leading to highly porous NDCs. The ability to obtain glucose derived ionothermal carbons with tailor-made porosity by simply changing the molar composition of the $KCl/ZnCl_2$ mixture and the performance of the pore tailored carbon materials as SC-electrodes will be presented in section 3.3. The new pore tuning tool will be expanded to adenine as precursor and $NaCl/ZnCl_2$ as the salt system in section 3.4. The thereby obtained, pore tailored NDCs not only show outstanding porosity features such as SSAs up to 2900 $m^2\ g^{-1}$ and TPVs of up to 5.19 $cm^3\ g^{-1}$, but also reveal an immense influence of the pore structure on the ORR-performance. Moreover, electron microscopy data of the pore tailored NDCs contradicts the previously observed colloidal carbonization, especially at high salt to precursor ratios, leading to the expression of a high internal salt phase ionothermal carbonization.

3.2   Precursor Systems

3.2.1   Glucose and Glucosamine Derived Ionothermal Carbons

The glucose and glucosamine hydrochloride derived ionothermal carbons obtained by Schipper *et al.* showed promising activities as the matrix material in lithium sulfur (LiS) batteries and as electrodes for the capacitive deionization.[131,132] As mentioned before, the synthesis procedure started from an aqueous solution of precursor and salt. Upon heat treatment accompanied by water evaporation, the carbon was formed in a $ZnCl_2$ hydrate melt. During the subsequent pyrolysis at 900 °C, the salt was removed *in-situ* due to the relatively low boiling point of $ZnCl_2$ (T_{boil} = 732 °C). However, the evolution of a high amount of gaseous $ZnCl_2$ limits the scalability due to its corrosivity and the risk of exhaust line blockage due to $ZnCl_2$ solidification while cooling. Furthermore, the existing water can lead to the formation of ZnO in the final material, resulting in the need of an additional acidic work-up. The idea, herein, is the application of eutectic salt melts which should allow the synthesis to start in an all-solid powder mixture (avoiding additional water) and lead to less salt evaporation during the reaction, simplifying a possible scale-up.[IV] The scalability of the ionothermal synthesis is especially interesting due to the possibility to


[IV] The unwashed materials obtained at 900 °C with pristine $ZnCl_2$ and the eutectic $KCl/ZnCl_2$ mixture contained ~ 5 wt.% and ~ 55 wt.% of the initially employed salt, respectively.

obtain carbon materials with hierarchical porosity (containing micro-, meso-, and even macropores) in a much simpler approach compared, e.g., to hard templating. Moreover, the industrial knowledge regarding processes involving $ZnCl_2$ already exists from the production of carbons by classical $ZnCl_2$-activation recipes.[133] However, the worldwide production of this facile process is downsized. The reason therefor is mainly the high costs needed to ensure an environmentally friendly production which do not equal the product value. However, this could/would change if high-performance materials are synthesized.

The eutectic $KCl/ZnCl_2$ was chosen as the salt mixture due to its relatively low melting point of 231 °C. The freshly prepared salt mixture was thoroughly mixed with the precursor (either glucose or glucosamine hydrochloride) using a precursor to salt wt.-ratio of 1:3 or 1:5. The ionothermal synthesis was conducted under N_2-atmosphere by heating the sample at a rate of 2.5 K min^{-1} to 900 °C, and the final temperature was kept for 1 h. The obtained material was washed with water yielding the porous (heteroatom) doped ionothermal carbon. The sample name is defined by Glu-X (glucose derived samples) or $GluNH_2$-X (glucosamine derived sample) in which X stands for the 1:X wt.-ratio of precursor to salt. The N_2-physisorption data of the different samples clearly show that glucose and glucosamine derived ionothermal carbons can be synthesized starting from an all solid mixture of precursor and salts (Figure 3.2A, Table S4). These findings are in line with the concurrently conducted work of Ma et al.[134] All materials show high N_2 uptake in the low pressure region and correspond to type IV isotherms coupled with H3 hysteresis implying the presence of micro- and mesopores.[26] Scanning electron microscopy (SEM) images show spherical like particles exhibiting interstitial pores in the meso- to macropore range (Figure 3.2D). The findings point to a hierarchical pore structure of the materials possessing primary carbon particles with micro- (or even small meso-) pores and interstitial pores in the meso- to macropore range. Among the three samples, Glu-5 exhibits the largest SSA and TPV with values of 1180 m^2 g^{-1} and 1.59 cm^3 g^{-1}, respectively (Figure 3.2C). The reduced salt amount in Glu-3 resulted in decreased SSA and TPV, both ~ 82 % of the values of Glu-5. Application of glucosamine as the precursor led to a porous NDC material with moderate N-content of 4.7 wt.%. The isotherm of $GluNH_2$-3 could be described as an intermediate stage between Glu-3 and Glu-5. This is also reflected in the SSA and TPV obtained for $GluNH_2$-3, corresponding to ~ 95 % and ~ 91 % of the values of Glu-5, respectively. The larger SSA and TPV values of $GluNH_2$-3, in comparison to Glu-3, could be connected to different interactions of salt and precursor phase caused by the nitrogen present in the case of glucosamine. However, this should also cause a different

isotherm shape which is not the case. The most probable explanation is the different actual precursor to salt ratio. Glucosamine was used as a hydrochloride salt aiming towards a higher miscibility with the inorganic salt melt due to enhanced Coulomb interactions. Thus, the actual ratio between precursor carbon content and salt is lower for GluNH2-3 than for Glu-3. All the results agree with the materials obtained by Schipper using aqueous ZnCl2 solution as the reaction medium.[129] Interestingly, the isotherms suggest that a hypothetical Glu-4 sample should have almost the same isotherm shape as GluNH2-3, which would lead to samples with equivalent porosity but different chemical composition (one material is N-doped). Regarding the employment as, e.g., SC-electrodes or host matrix material in LiS-batteries, such kinds of systems are of high interest because they allow the clear differentiation between porosity-induced and N-doping-induced effects. All findings (morphology, effect of higher salt contents) support the predicted sol-gel model of carbon formation indicating a liquid state of the salt during carbonization.
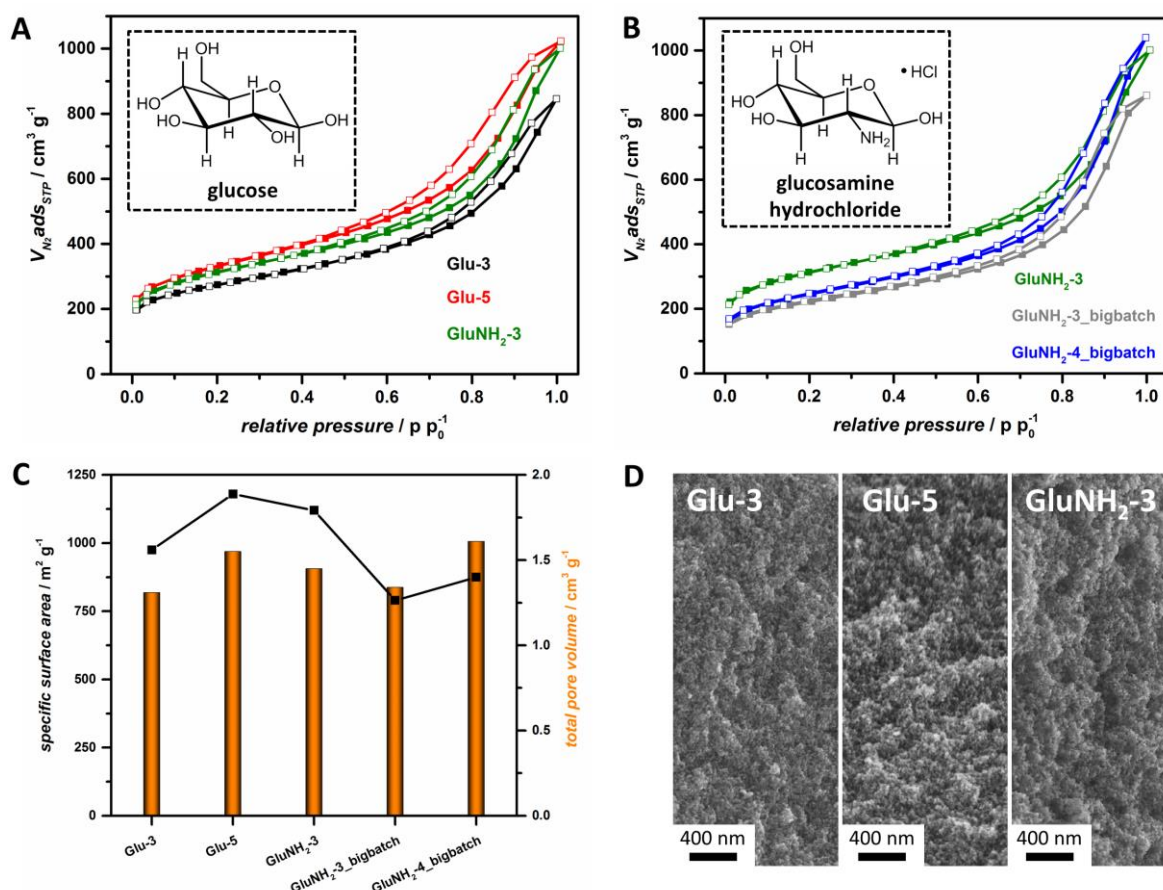
Figure 3.2 A+B) N2-physisorption isotherms, C) SSA and TPV, and D) SEM images of the glucose and glucosamine derived samples. Additionally, the structure of the used precursors is shown as inset.

The scalability of the procedure was tested for glucosamine hydrochloride using a precursor to salt ratio of 1:3. The amount of starting material was increased by a factor of

500, and the product was named GluNH2-3_bigbatch. The isotherm of the obtained material possesses a very similar shape to GluNH2, indicating similar porosity, but is shifted to lower pressures (Figure 3.2C). The latter can be connected to lower SSA and TPV caused by the upscale. However, GluNH2-3_bigbatch still exhibits 71 % SSA and 92 % TPV with respect to GluNH2-3 (Figure 3.2C, Table S4). Porosity characteristics similar to the small batch were obtained when the salt ratio in the starting mixture was increased from 75 to 80 wt.% (Figure 3.2B+C). The resulting GluNH2-4_bigbatch sample exhibits a TPV of 1.61 cm^3 g^{-1} and a SSA of 875 m^2 g^{-1}, and could be obtained with an absolute yield of approximately 130 g NDC per batch. Moreover, the high carbon yield of ~ 65 % has to be highlighted (Table S4). To put those values in better context, Figure 3.3 compares the SSAs and TPVs of the herein synthesized materials, commercially available activated carbons (Carbon Blacks), and mesoporous carbons from literature (detailed information of the reference materials is summarized in Table S5).[46,135-140]
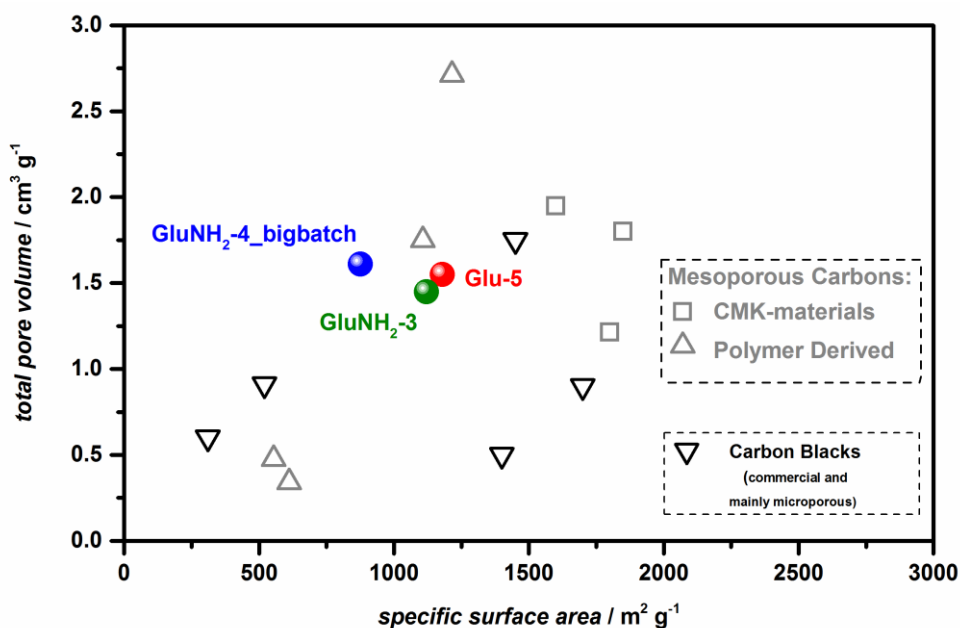
Figure 3.3 SSAs and TPVs (obtained by N2-physisorption) of the herein synthesized mesoporous ionothermal carbons (Glu-5, GluNH2-3 and GluNH2-4_bigbatch), mesoporous carbons from literature (including the CMK-materials), and commercially available activated carbons (Carbon Blacks).

The ionothermal (mesoporous) carbons exceed the TPVs and show similar SSAs compared to most of the (microporous) Carbon Blacks. Moreover, the TPVs of the herein synthesized materials approach the values of the well-known (hard-templated) CMK-materials, however, at lower SSA. Generally, the comparison shows the compatibility/advantage of the herein synthesized materials in comparison to the commercially available products. Furthermore, the GluNH2-4_bigbatch showed promising properties as host matrix material

in LiS-batteries as discussed in the doctoral thesis of Alen Vižintin (National Institute of Chemistry Slovenia).[141]

Further information was collected using a high temperature heating mantel set-up. Glucose was mixed in a 1:5 wt.-ratio with eutectic KCl/ZnCl$_2$, and heated to 550 °C in a quartz flask under argon atmosphere. Thus, macroscopic changes could be visually observed through the transparent flask. The initially white mixture of glucose and salt started to turn light brown at ~ 150 °C. A further increase in temperature led to a darkening of the color. At approximately 220 °C, a foaming process was initiated through the intense evolution of gas (most probably H$_2$O originating from polycondensation reactions).[V] The resulting brown-black monolithic structure can be described as a *pre-carbon cake* (Figure 3.4). Despite the additional evaporation of water at higher temperatures, the macroscopic appearance of the monolithic structure was hardly influenced. Nearly no changes were observed, neither at the melting point of the eutectic mixture, nor up to a temperature of 550 °C. The findings indicate that no complete liquid stage of the reaction mixture is reached if an all-solid precursor-salt mixture is employed. Interestingly, the porosity and morphology of the final carbon material nonetheless indicate the presence of a sol-gel type carbonization mechanism as it was previously reported employing aqueous starting conditions.[129] This could be due to the different size ranges which are ascertained by observation in a flask, in contrast to SEM and porosity measurements. The following paragraph will give a possible explanation for the observations made.

The evaporation of water at ~ 220 °C causes the formation of a foamed *pre-carbon cake*. It consists of relatively thick *cake-walls* containing the salt, partially polymerized precursor, and very large pores due to the formed gaseous products (i.e., water). Moreover, this effect produces a general separation of the reaction mixture. Carbon/salt domains (herein called secondary particles) of a certain size are separated by large macropores formed by gas bubbles. If the melting temperature of the eutectic is passed, the ionothermal (sol-gel) carbonization can take place inside the *cake-walls* of the *pre-carbon cake*. Figure 3.4 summarizes the proposed model of the ionothermal synthesis of glucose (and glucosamine) derived carbons. This implies that the interplay between the liquid salt melt and the partially polymerized glucose molecules, such as the formation of carbon primary particles and/or phase separation between carbon and salt phase, takes place in the *cake-walls*. These results also explain the superficies observed by SEM (Figure 3.4B+C). The

---

[V] The Lewis-acidic ZnCl$_2$ can as a catalyst for the dehydration of fructofuranose to hydroxymethylfurfural enhancing the cross-linking reactions as described in the PhD-thesis of Schipper.

interface between the gaseous phase and the carbon/salt phase will first solidify creating a rather dense film. When the electron beam faces the breaking edge of the secondary particle, the porous structure is visible. It has to be considered that the liquid salt phase may not "just" dilute the partially polymerized glucose molecules, thereby representing the liquid solvent/reaction medium needed for the ionothermal carbonization but could also break the already formed macromolecules resulting again in monomeric structures for the carbon formation.
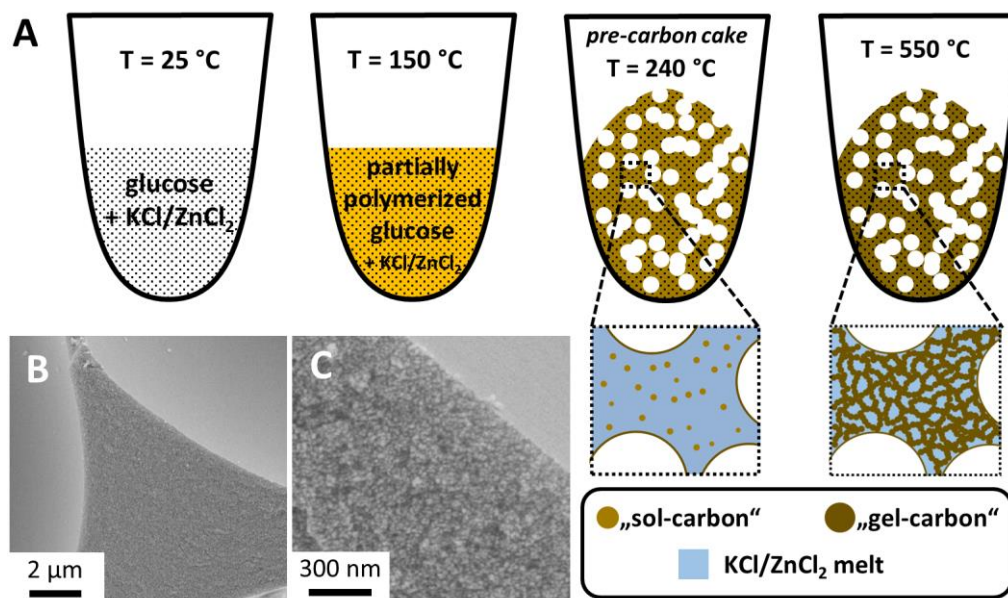
Figure 3.4 A) Schematic illustration of the occurring macroscopic changes during the heat treatment of a glucose-KCl/ZnCl$_2$ mixture and the resulting morphology of the *pre-carbon cake*. B+C) SEM images of the resulting material at 550 °C depicting the different superficies.

The results demonstrate the possibility to start with a solid – solid mixture of precursor and salt and, nevertheless, obtaining typical porosity and morphology characteristics of ionothermal carbon materials. However, the obtained materials show relatively low surface area and total pore volume compared to IL derived carbons (SSA ~ 1800 m^2 g^{-1}, TPV ~ 2.7 cm^3 g^{-1}).[116] Additionally, the ORR-performance of the glucosamine derived NDC is rather poor (especially, regarding the number of transferred electrons delivering a number of ~ 3.4) which could be speculated to be due to the relatively low N-content of 4.7 wt.% (Figure S3). It has to be considered that the correlation between the absolute N-content and the ORR-activity is "only" of empirical nature, and, of course, other reasons (e.g., type of N-site) could cause the low electron transfer number measured (cf. section 1.3.2). The application of nucleobases as sustainable and N-rich precursors for the ionothermal synthesis of NDCs will be discussed in the following section 3.2.2.

3.2.2 Nucleobase Derived Ionothermal Carbons

Nucleobases have a high nitrogen content, an aromatic structure, and are biomass derived, all very promising characteristics for their use as sustainable precursors for NDCs. Furthermore, nucleobases are thermally relatively stable showing melting/decomposition at temperatures higher than 320 °C. Concerning the results in chapter 3.2.1, this should allow the onset of carbonization (solidification) in a complete liquid salt phase.

In previous investigations, it was already shown that nucleobases can be used as additives during the synthesis of IL derived mesoporous carbons using silica spheres as hard templates.[142] The obtained NDCs showed promising activity for the ORR in alkaline conditions. Furthermore, the nucleobase adenine has served as the nitrogen source in glucose derived, iron and nitrogen doped ORR catalysts.[143] Concurrent to the present work, the possibility of obtaining ORR catalysts using adenine as the single nitrogen/precursor source was shown by Shen *et al.* synthesizing a cobalt doped NDC using a uniform cobalt-adenine assembly as starting material.[144] All these results indicate the high potential of nucleobases as starting material. In the present work, the nucleobases adenine and guanine hydrochloride (GuaHCl) were chosen as precursors, both decomposing at temperatures higher than the melting point of the typically applied eutectic salt mixtures, e.g. KCl/ZnCl$_2$, NaCl/ZnCl$_2$, and LiCl/ZnCl$_2$ showing melting points of 230 °C, 250 °C, and 294 °C, respectively.[145-147] The stability of the nucleobases is confirmed by the overlay of their decomposition curves, derived from thermogravimetric analysis (TGA), with the melting points of the eutectic salt mixtures (Figure S4). The mass decrease of GuaHCl at low temperatures of $T \sim 250$ °C indicates the elimination of hydrochloric acid. Nonetheless, the TGA measurement confirmed the high stability of the nucleobase itself revealing a decomposition temperature of ~ 500 °C.

In preliminary experiments, GuaHCl was mixed in a 1:3 wt.-ratio with the eutectic mixture of KCl/ZnCl$_2$. The mixture was heated to 550 °C under inert gas atmosphere, and changes were directly monitored using a quartz flask as reaction vessel equipped with a glass protected stirring rod (as also conducted for the glucose derived carbon in section 3.2.1). At $T \sim 250$ °C, a temperature slightly higher than the melting point of KCl/ZnCl$_2$, partial melting occurred. Further increase in temperature accelerated the melting of the mixture. However, no complete liquid reaction mixture was obtained at this point. At 300 °C, the mixture started to turn slightly brown. This temperature is clearly below the decomposition temperature of GuaHCl ($T_{decomposition} \sim 500$ °C) indicating the

catalytic effect of $ZnCl_2$ towards the crosslinking of the precursor units.[VI] At higher temperatures, the reaction mixture darkened further but slowly became less viscous. The whole process was accompanied by the formation of gaseous species. Interestingly, the viscosity reached a minimum at 360 °C representing at this stage a dark brown, but homogeneous, melt. This points to a homogeneous solution of partially polymerized precursor molecules in the complete liquid salt melt which can be described as the sol state of the sol-gel carbonization. Higher temperatures lead to an increase in viscosity and at 400 °C a brown-black monolithic structure was obtained, representing the gel. The monolith formation was accompanied by an increase in volume caused by trapped gas bubbles. The macroscopic appearance of the monolith hardly changed during further heating up to 550 °C. The results indeed indicate that the employment of nucleobases as precursor can lead to the onset of carbon solidification in a complete liquid reaction mixture, pointing to the desired sol-gel process as carbonization mechanism.

Motivated by the preliminary results, GuaHCl and adenine were mixed with different salt mixtures ($LiCl/ZnCl_2$, $NaCl/ZnCl_2$, and $KCl/ZnCl_2$) in different precursor to salt ratios (1:6, 1:10, and 1:14). The molar ratio of the two salts forming the salt mixture was either the eutectic composition (22 mol% LiCl) or very close to the eutectic (42 mol% NaCl, 50 mol% KCl). The aim, herein, was to gain a better understanding of the interplay between the nucleobase-salt-system used and the porosity obtained. The general sample preparation and the heat treatment was conducted as described for the glucose derived samples in section 3.2.1. The obtained materials were studied by N_2-physisorption and SEM (Figure 3.5, Table S6, Figure S5). All obtained materials possess very large SSA (1800 $m^2 g^{-1}$ to 2800 $m^2 g^{-1}$), showing the high compatibility of the used nucleobases with the ionothermal approach. These values are distinctly larger than the SSAs of glucose or glucosamine derived materials (~ 1000 $m^2 g^{-1}$) presented in section 3.2.1. This may be linked to a change in crosslinking of the precursor. The crosslinking of glucose (and glucosamine) starts at relatively low temperatures, already leading to larger partially polymerized precursor domains before the onset of the sol-gel carbonization. Hence, the resulting carbon-salt interface after pyrolysis is restricted, generally, generating smaller SSAs. Furthermore, the formation of the *pre-carbon cake* results in many gas-liquid/solid interfaces (foaming effect), which is accompanied by the formation of dense carbon layers

---

[VI] The exact mechanism of the crosslinking of GuaHCl is not unraveled yet. However, *in-situ* FTIR measurements during the thermal decomposition of pristine GuaHCl revealed the formation of HCN (results not shown). Hence, one could assume a $ZnCl_2$ catalyzed crosslinking mechanism similar to the known Gattermann-reaction.[148] This would also cause the fixation of the volatile HCN giving rise to the high yields observed.

(Figure 3.4). In contrast, the solidification of nucleobases starts in an all liquid reaction mixture, as studied with GuaHCl and KCl/ZnCl$_2$. This points to the presence of still small, partially polymerized precursor moieties which are adequately miscible with the liquid salt phase. Thus, the precursor and the salt phase only undergo nanoseparation during the carbon solidification, resulting in a large carbon-salt interface and the accompanied large SSA. Furthermore, the foaming effect, during the monolith formation, was less pronounced for GuaHCl in comparison to glucose, possibly leading to less non-porous carbon layers at the gas-liquid/solid interface for the former precursor.

The TPV of the nucleobase derived samples ranges from 1.3 cm^3 g^{-1}, comparable with typical TPVs of activated carbon, up to an outstanding value of 5.3 cm^3 g^{-1}. Hence, the facile ionothermal approach delivers the possibility to synthesize carbon materials with similar (or even higher) SSAs compared to activated carbons, however, possessing 4 - 5 times higher TPVs at the same time. The N-content of the obtained NDC materials is almost independent of the type and the amount of the salt mixture used. Furthermore, the approximate value of ~ 7 wt.% nitrogen is relatively high regarding the applied synthesis temperature of 900 °C and the high SSA of the materials. Additionally, all samples were obtained in a high carbon yield of ~ 45 to ~ 60 % (Table S6). Generally, the reached porosity by means of SSA and TPV clearly exceed the values of activated carbon but also the ones of the CMK-materials and other mesoporous carbons from literature (Figure 3.5C, Table S5). Moreover, the ionothermal NDCs show higher TPVs and similar SSAs as high-performance, micro- and mesoporous CDC-materials derived from mesoporous carbides (detailed information of the CDCs is summarized in Table S7).[54,149,150]

The general porosity of the GuaHCl derived NDCs follow the trends of the IL-derived materials.[55,95,116] Especially, the obtained morphologies in respect of the used salt mixture are in line with the ones which were presented in Figure 1.6 (cf. section 1.2.3). As seen in a typical sol-gel process, the solvent characteristics, in this case the salt mixture properties, will change the initial carbonization behavior leading to different amounts of seed particles and seed particle separation. The separation, thereby the miscibility, between the precursor (or partially crosslinked precursor molecules) and the molten salt strongly influences the morphology and porosity of the final product. The miscibility changes depending on the type of salt mixture applied as indicated by the pronounced variation in morphology/porosity at a constant precursor to salt wt.-ratio (obtained herein and in

literature).[VII] LiCl/ZnCl$_2$ can be regarded as the most miscible, followed by NaCl/ZnCl$_2$ and, finally, KCl/ZnCl$_2$. It has to be considered that the high Lewis acidity of ZnCl$_2$ should generally lead to bond formation between electron donating precursor groups and electron accepting Zn^{2+}-ions thus increasing the miscibility of precursor and salt phase. The morphology trend of the different salt mixtures could be linked to the higher amounts of the "secondary" salt (if ZnCl$_2$ is regarded as the "primary" salt) following the order of 22 mol%, 42 mol%, and 50 mol% for LiCl, NaCl, and KCl, respectively. Higher amounts of the secondary salt can shield the Lewis acidity of ZnCl$_2$ more efficiently thereby lowering the miscibility. However, the amount of secondary salt in the case of NaCl and KCl is very similar, but the morphology obtained was very different (Figure 3.5B). Hence, it can be assumed that not only the amount of the secondary salt, but also the nature of the secondary salt plays an important role. The polarity of the secondary salt is, of course, an important feature if mixing/demixing phenomena are discussed. The polarity correlates with the dielectric constant which can be directly linked to the refractive index (n) of the respective salt.[151] Hence, the reported n-values of the single molten salts can be used as (simplified) polarity descriptors.[VIII] The refractive index (n) of the single liquid salts are given as 1.59, 1.50, 1.42, and 1.38 for ZnCl$_2$, LiCl, NaCl, and KCl, respectively.[146] Thus, the polarity of the different salt mixtures can be described in the order LiCl/ZnCl$_2$ > NaCl/ZnCl$_2$ > KCl/ZnCl$_2$ which is in line with the observed morphologies. The salt mixture exhibiting the highest polarity (LiCl/ZnCl$_2$) results in a micro- and supermicroporous carbon if applied in a six-fold excess with respect to the precursor mass, as indicated by the type I(b) isotherm (Figure 3.5A). An increase of the salt ratio to 10:1 leads to the development of a high amount of mesoporosity, as seen by the apparent hysteresis and the type IV isotherm. Even higher salt ratios (14:1) cause a shift of the hysteresis to higher pressures, implying the further widening of the pore system. These observations are in line with the sol-gel principle that an increased volume fraction of salt leads to higher porosity. The effect is confirmed by the SEM images of the materials prepared with different salt to precursor ratios (Figure S5).

[VII] Different salt mixtures of the same mass, nevertheless, have different (molten) volumes which, actually, are the more relevant values which should be constant when discussing porogenesis according to sol-gel principles. However, the maximum volume difference of the herein discussed molten salt (at the same mass) is less than 4 %.[146]

[VIII] It has to be considered that the refractive index is typically measured at 589 nm, ergo at a very high frequency. However, the dielectric constant (which would be the better polarity descriptor) strongly depends on the frequency and is typically determined at much lower frequencies. Unfortunately, there are (to the best of the authors knowledge) no measured literature values of the dielectric constant of the herein used molten salts. Nonetheless, the refractive indices can be used assuming a similar frequency dependence of the (different) dielectric constants which is supported by the general similarity of the studied salts.
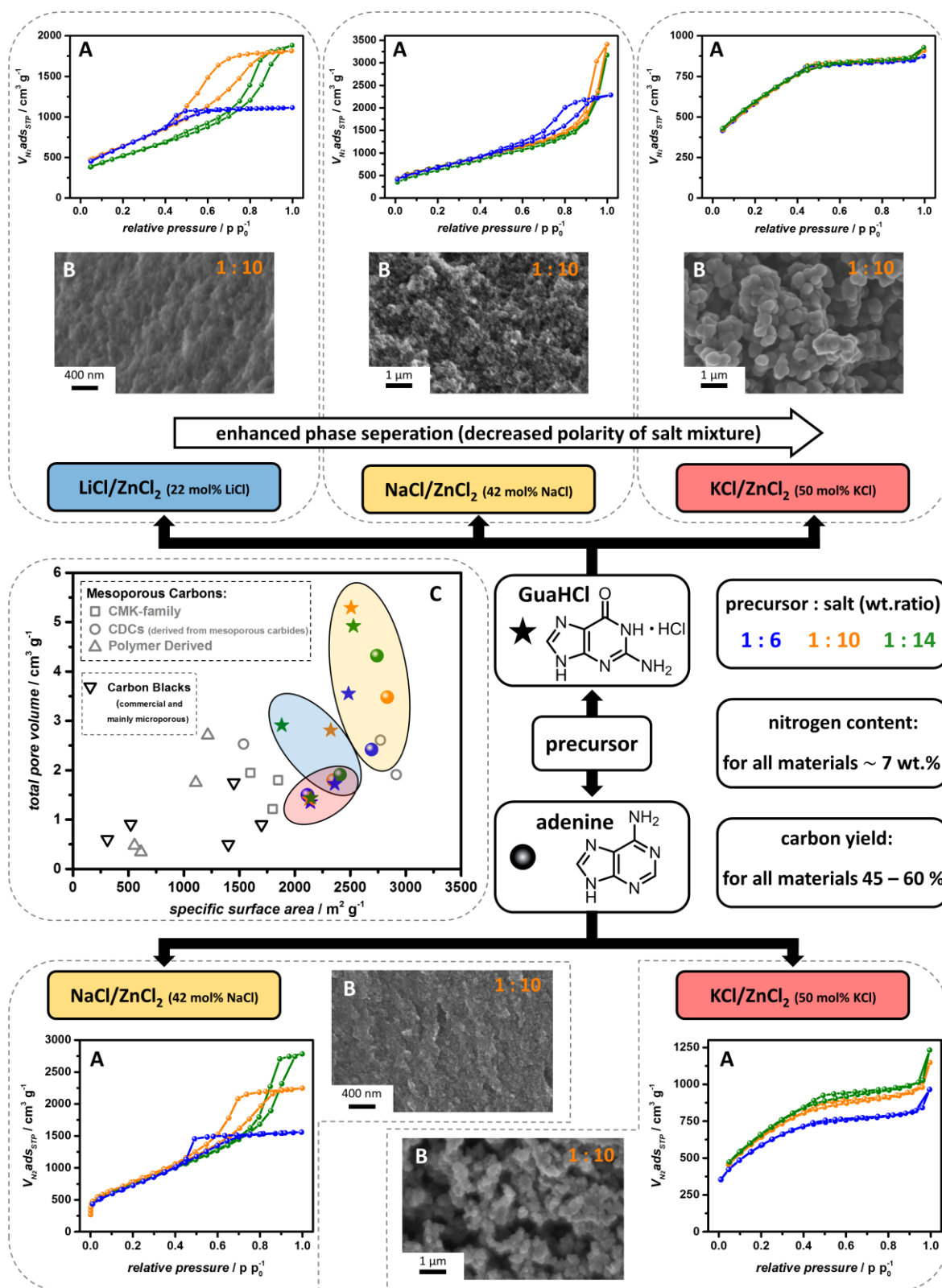
Figure 3.5 Summary of different characteristics of GuaHCl and adenine derived ionothermal NDCs with different salt mixtures and various precursor to salt wt.-ratios. A) N_2-physisorption of the NDCs synthesized with a precursor to salt ratio of 1:6, 1:10, and 1:14. B) SEM-image of the NDC prepared with a precursor to salt ratio of 1:10. C) SSAs and TPVs (calculated from N_2-physisorption measurements) of the nucleobase derived NDCs compared with mesoporous carbons from literature (including CMK-materials as well as micro- and mesoporous CDCs), and commercially available activated carbons (Carbon Blacks).

The application of the less-polar $NaCl/ZnCl_2$ results in a micro- and mesoporous material already if used in a six-fold excess (Figure 3.5A). The corresponding type IV isotherm shows a well-developed hysteresis in the high pressure region ($0.7 < p \, p_0^{-1} < 0.9$). The application of higher salt ratios causes the same trend as observed for the $LiCl/ZnCl_2$ system, i.e., promoted separation of the primary carbon particles. This is indicated by a shift of the hysteresis to higher pressures. The SEM images of the GuaHCl materials obtained with a 1:10 salt to precursor ratio further confirm the influence of the polarity of the salt systems. The $LiCl/ZnCl_2$ sample appears rather dense and only small pores are visible, whereas the $NaCl/ZnCl_2$ material exhibits an open structure of clearly separated carbon particles (Figure 3.5A+B). A further decrease in polarity of the salt should lead to stronger demixing causing larger carbon domains, which can be clearly seen by the morphology of the $KCl/ZnCl_2$ sample (Figure 3.5B). The morphology of the latter also explains why the isotherm shape and position of the $KCl/ZnCl_2$ materials are hardly influenced by the salt amount used. The interstitial pores created (possibly influenced by the salt ratio) are simply exceeding the range of the pores detectable by N_2-physisorption (Figure S5).

The porosity/morphology of the adenine samples synthesized with $NaCl/ZnCl_2$ and $KCl/ZnCl_2$ show very similar trends regarding the salt type and salt amount used in comparison to the GuaHCl derived materials (Figure 3.5A+B). The SEM images of the materials synthesized using a 1:10 salt to precursor ratio indicate, however, an even higher miscibility of salt phase with adenine than with GuaHCl. Adenine leads to smaller particle sizes and a clearly denser structure than GuaHCl, when comparing, both the $KCl/ZnCl_2$ and the $NaCl/ZnCl_2$ samples (Figure 3.5B). This effect is further supported by the generally larger SSAs of the adenine derived NDCs. Additionally, the carbon yields of the GuaHCl and the adenine derived samples are very similar showing, for example, for the materials synthesized with $NaCl/ZnCl_2$ values of ~ 50 % and ~ 60 %, respectively (Table S6). This is especially interesting for adenine which completely sublimes in the absence of salt as shown by the TGA-measurement (Figure S4). The effect is in line with the general statement that $ZnCl_2$ can enhance crosslinking.[IX] Thus, volatile species can be incorporated in the carbon framework causing higher yields which is known from $ZnCl_2$ "activated" carbons (section 1.2.1). The step-wise pore opening of the adenine derived samples, caused

---

[IX] Mechanistic studies regarding the crosslinking of adenine are hampered due to the subliming nature of adenine upon heat treatment. However, due to the very similar structure of GuaHCl and adenine, it can be assumed that the crosslinking reactions of both nucleobases are similar. Hence, also in the case of adenine, one could assume a mechanism similar to the Gattermann-reaction.[148]

by higher amounts of NaCl/ZnCl$_2$, is clearly depicted by the corresponding PSDs of the mesopore region (Figure 3.6). However, it has to be considered that PSDs are only derived from mathematical models which are applied to the measured isotherm and thus should be handled with care. A model which is widely employed in the carbon community is the equilibrium QSDFT (quenches solid density functional theory) model for slit pores based on the typical slit pore shape of activated carbons. The term "equilibrium" implies that the desorption branch is used for the calculation which is reasoned by the occurrence of metastable adsorption states and hindered nucleation of liquid bridges during the adsorption.[26] Nonetheless, it has to be considered that this is only valid for parallel hysteresis branches. "Real" carbon materials show very often non-parallel desorption and adsorption branches induced by irregular pore connectivity and/or the presence of bottleneck pores. Furthermore, every hysteresis should theoretically close at pressures between $0.4 < p\,p_0^{-1} < 0.5$ due to cavitation induced pore emptying which leads to the artefact of an apparent pore size contribution of ~ 3 - 4 nm. Hence, the use of the typically applied equilibrium QSDFT model is sometimes not only inaccurate, but leads to wrong information. A perfect example is the adenine derived sample synthesized with NaCl/ZnCl$_2$ in a 1:6 ratio. Figure 3.6 depicts the strong influence of the branch and model chosen on the PSD. Figure 3.6A shows the mesopore range derived from the in literature, often applied QSDFT model. Contrarily, Figure 3.6B depicts the PSD calculated with the (at least more) accurate model for the porous materials discussed in the present thesis.
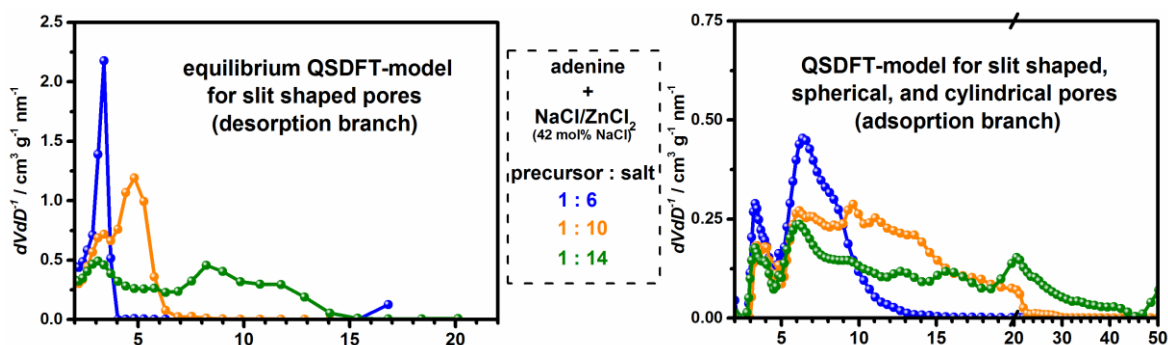
Figure 3.6 Mesopore size distributions of the adenine derived samples with different amounts of NaCl/ZnCl$_2$ using A) the equilibrium QSDFT model for slit shaped pores, and B) the QSDFT model for slit shaped, spherical and cylindrical pores calculated from the adsorption branch.

The equilibrium QSDFT model indicates an amazingly monomodal mesoporosity with a pore diameter of 3.4 nm (Figure 3.6A). If pores of this monomodality were actually present, a steep rise of the adsorption branch should be present, which is, however, not the case (Figure 3.5A). Therefore, all the PSDs shown in the present thesis were calculated

using the adsorption branch. Furthermore, due to the possible presence of "salt templated" pores, which differ from the typical observed slit shaped pores of activated carbons, the allowed pore shape of the used QSDFT model includes slit shaped, spherical and cylindrical pores.

Generally, the nucleobase derived ionothermal carbon materials demonstrate promising porosity features and high N-contents. It has to be highlighted that both precursors resulted in NDCs with outstanding SSAs, when combined in a 1:10 mass ratio with NaCl/ZnCl$_2$, of 2510 m^2 g^{-1} and 2830 m^2 g^{-1} for GuaHCl and adenine, respectively. The porosity can be tailored according to the "sol-gel-toolbox" which allows the synthesis of a hierarchical porous system that is especially appealing for electrochemical applications (cf. section 3.4.2). Hence, nucleobases can be regarded as highly interesting, sustainable alternatives to the previously used ILs. Moreover, the herein studied precursors (nucleobases, glucose, glucosamine) can serve as model substance for biomass leading, in the best-case scenario, to the employment of waste or industrial byproducts as precursor materials in the future. This is supported by the results of the experiment in the flask set-up which revealed an intermediate state, in which solid crosslinked precursor molecules and partially molten salt coexist, but an all liquid homogenous state of the reaction mixture at higher temperatures. Hence, molten salt presumably shows the ability to cleave existing bonds which can also lead to (biomass) liquefaction allowing the employment of biomass or waste materials (e.g, tires) as precursors for high performance porous carbons in the future.[152] As a matter of fact, the gathered knowledge allowed the employment of modified lignin as precursor for the ionothermal synthesis of porous NDCs.[153] Lignin is largely available at low costs as a byproduct of the paper and pulp industry.[154] The topic was investigated in a department internal collaboration and will be discussed in the thesis of Micaela Graglia. Briefly, nitrated and aminated lignin were used as N-containing precursors which could be transferred into highly porous NDCs using a KCl/ZnCl$_2$ salt mixture resulting in lignin derived ORR-catalysts with very promising performance (E$_{1/2}$ = 0.85 V (vs. RHE), number of transferred electrons = 4.0).[153]

The obtained morphology/porosity of the ionothermal carbon materials, presented in chapter 3.2, can be directly linked to the polarity of the used salt system. Thus, phase demixing, of precursor and salt phase, can be labeled as the main parameter determining the final porosity characteristics of the product. It could be concluded that the carbon formation follows the principles of spinodal phase separation. However, it has to be

considered that the carbon solidification is far more complicated, for example, due to the non-isothermal condition, and the changing properties of the precursor phase caused by the ongoing crosslinking reactions. The classical nucleation and growth theory (LaMer), nevertheless, plays a role as it occurs in the metastable region between the binodal and spinodal line. Due to the complexity of the present system, the effects will be addressed as general mixing/demixing properties of precursor and salt phase, and the steps of carbon formation will be discussed according to the sol-gel carbonization as described in literature.[117] The findings imply that a differed ratio between the two salts forming the salt mixture should have a great influence on the overall polarity of the liquid salt phase, consequently, introducing a new possibility to (also continuously) tune the porosity of ionothermal carbons. Hence, the influence of different KCl to $ZnCl_2$ molar ratios on the porosity of glucose derived ionothermal carbons will be discussed in section 3.3.

3.3 Glucose Derived Carbons with Tailored Porosity

As discussed in chapter 3.1, the polarity of the salt melt seems to be one of the main factors dictating the pore morphology of the final carbon material. For example, different polarities can be realized by using different type of eutectic mixtures. A change of the used eutectic mixture usually results in a rather drastic change of the morphology which was already discussed in chapter 3.2 and the thesis of Fechler.[115] Moreover, different eutectics could also lead to differed reaction mechanisms of the precursor crosslinking thereby influencing the final carbon structure which complicates the comparability of the obtained materials. Therefore, it is of high interest to explore new ways how the properties (mainly the polarity) of the salt melt can be continuously varied allowing a detailed study of the porosity in dependence of a differed polarity of the salt mixture. In previous work either single salts or eutectic mixtures were applied all showing a distinct polarity. The phase diagram of the often used KCl/$ZnCl_2$ system reveals a rather big region of low melting salt compositions ($T_m < 320\ °C$) for KCl-contents between 0 and 54 mol% (Figure 3.7). The refractive index of a certain salt mixture, which can be directly related to its polarity, can be simplified as the molar-weighted average of the refractive indices of the two salts forming the salt mixture.[151] Therefore, a steady increase of the KCl-content in the used KCl/$ZnCl_2$ mixture should lead to a continuous change of the polarity speculatively allowing a defined tailoring of the porosity.
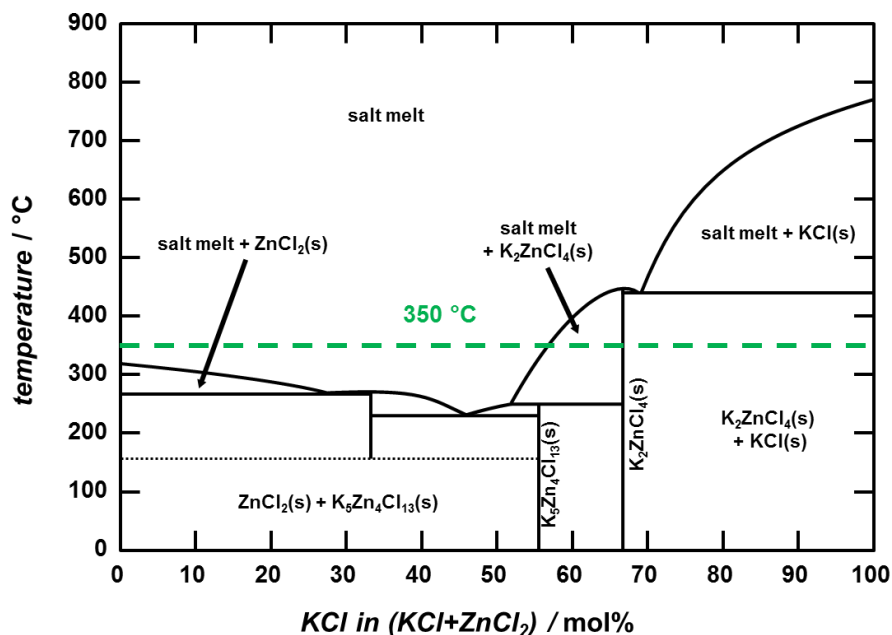
Figure 3.7 Phase diagram of KCl/ZnCl2.[145] The dashed green line visualizes the temperature of the isothermal heating step.

Hereby, glucose was used as precursor and KCl/ZnCl$_2$ as combined solvent/porogen. The weight ratio of precursor to salt was fixed to 1:5 for all experiments and the influence of a varying molar ratio of KCl and ZnCl$_2$ was investigated.[155] The general sample preparation and the heat treatment was conducted as described for the glucose derived samples in section 3.2.1. To support the homogenization of the reaction mixture, an additional isothermal annealing at 350 °C for 2 h was introduced during the heat treatment. The different samples are named Glu_XX where XX stands for the molar amount of KCl present in the KCl-ZnCl$_2$ mixture. In section 3.3.1, the porosity obtained in dependence of the molar KCl-content will be elaborately investigated by N$_2$-physisorption, SEM, transmission electron microscopy (TEM), powder X-ray diffraction (PXRD) and mercury (Hg) intrusion. Chapter 3.3.2 will discuss the SC performance of the obtained carbons with tailored porosity which was measured by Thomas Berthold (MPIKG).

3.3.1   Pore Tailored Carbons Synthesized with Non-Eutectic KCl/ZnCl$_2$ Mixtures

A homogeneous solution/dispersion of the precursor (or partially polymerized precursor molecules) within the also homogeneous salt melt is a basic requirement for a defined porogenesis. It is necessary to mention that with regard to the observations made with the eutectic mixture, the macroscopic appearance does not reach a liquid appearance during the reaction, allowing a sol-gel carbonization mechanism (section 3.2.1). In a preliminary

experiment, two different salt mixtures (30 mol% and 46 mol% KCl) were chosen to study the influence of the additional isothermal heating on the obtained porosity. The temperature of this step was set to 350 °C and the dwelling time to 2 h, ideally ensuring the homogenization, especially, of the non-eutectic mixture. The corresponding N_2-physisorption results are shown in Figure S6 and Table S8, and a detailed discussion of the results can be found in the supporting information. Briefly, the annealing step promotes the evaporation of the water *in-situ* formed by polycondensation reactions. Hence, the properties of the molten salt correspond rather to a water free salt mixture than to a hydrated salt, which seems to support the mixing of precursor and salt phase. The findings are supported by the work of Fischer *et. al* who reported that the solubility of cellulose in $ZnCl_2 \cdot X\ H_2O$ decreases with increasing water content.[156] Moreover, the general increased miscibility is in line with the concurrent work of Ma *et al.* who showed that, in the case of a ratio close to the eutectic mixture (51 mol% KCl), isothermal heating at 240 °C led to improved porosity with higher SSA and mesopore volume.[134]

For a detailed investigation of the influence of varying KCl-content in the $KCl/ZnCl_2$ mixture, different samples were synthesized with the isothermal annealing step at 350 °C. The KCl-content in the $KCl/ZnCl_2$ mixture was increased stepwise from 0 to 80 mol% and the resulting samples were first characterized by N_2-physisorption measurements (Figure 3.8, Figure 3.9, Table S8). The isotherms depict a strong influence of the KCl-content on the obtained pore structure. It is important to mention that the chemical composition was hardly influenced by the salt composition (Table S8). The application of pristine $ZnCl_2$ as solvent/porogen led to a high SSA of 2160 $m^2\ g^{-1}$ and a type I isotherm with almost no N_2 uptake for $p\ p_0^{-1} > 0.5$. The respective PSD of Glu_00 shows a high amount of micropores and some small mesopores (d < 10 nm). These values suggest a high miscibility of the (partially polymerizing) precursor phase with pure $ZnCl_2$.

Interestingly, the porosity characteristics of Glu_00 clearly differ from the properties of the carbon material previously synthesized in a very similar fashion by Schipper.[129] The biggest difference in the procedure of Schipper is the fact that the starting materials were dissolved in water leading to the formation of $ZnCl_2$-hydrate as salt phase. The obtained carbon of the previous work showed a type IV isotherm combined with a high N_2-uptake at high pressures indicating the presence of large mesopores, but, a lower SSA of 1385 $m^2\ g^{-1}$.[129] Those findings indicate a stronger phase separation between carbonizing phase accompanied by the formation of larger pores if $ZnCl_2$-hydrate instead of pristine $ZnCl_2$ is employed as salt. This supports the aforementioned influence of water

(either intentionally added or *in-situ* formed due to polycondensation of glucose) on the salt melt characteristics and, thus, on the obtained porosity.
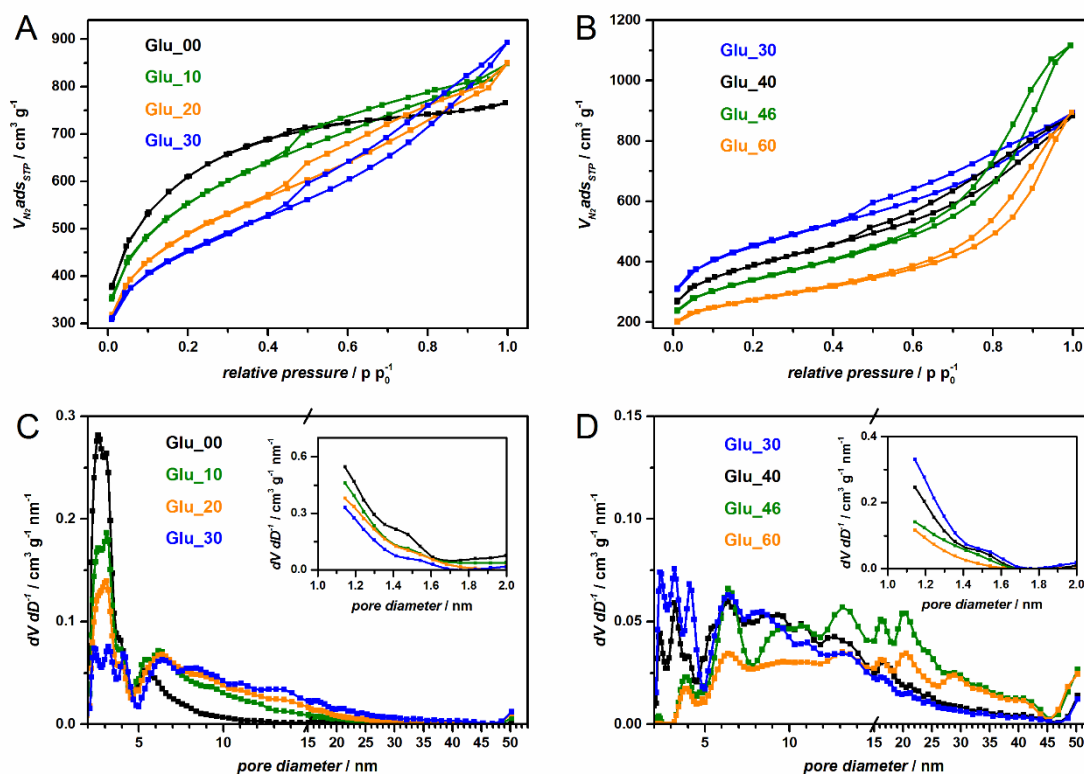
Figure 3.8 A+B) Nitrogen physisorption isotherms and C+D) mesopore and micropore (inset) size distribution of the samples prepared with different amounts of KCl in the KCl/ZnCl$_2$ mixture

The introduction of 10 mol% KCl caused an increased N$_2$ uptake in the high pressure region, but a decreased uptake in the low pressure region. A further rising KCl-content enforced those two effects leading to a consecutive shift of the isotherm from a composite type I - type IV (Glu_10) to a type IV (Glu_46). This process was accompanied by a hysteresis shift from H4 to H3 pointing to the transformation of narrow slit pores into larger mesopores.[26] These results indicate that a higher KCl-content led to a decreased polarity of the salt phase enforcing the demixing of the two phases. The resulting larger salt domains led to greater pore sizes in the final material and a stepwise opening of the pore system. Simultaneously, the interface between salt and precursor phase decreased leading to a reduced SSA (Figure 3.9A). Importantly, the obtained carbon yield was hardly influenced by the used salt ratio (Figure 3.9B). This indicates that the different porosities were caused by the changed properties (e.g., a changed templating behavior) of the salt mixture, and not by the intensity of chemical activation due to the amount of ZnCl$_2$ present. The validity of the term "templating" is further supported by the discrepancy in the total

yield values between the carbons synthesized herein and KOH activated carbons (27 wt% vs. 10 - 15 wt%, respectively).[157]
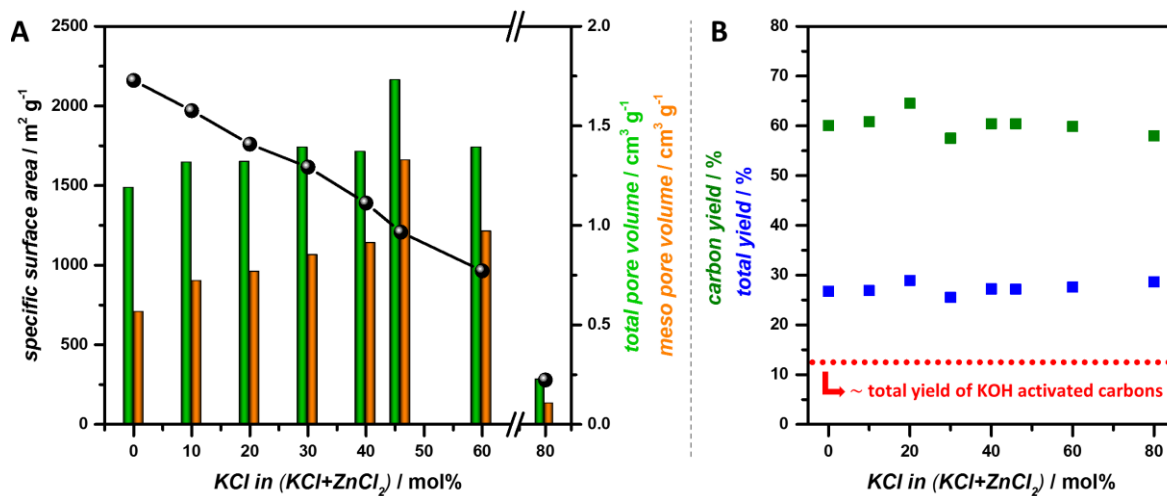
Figure 3.9 Influence of the amount of KCl used in the KCl/ZnCl$_2$ mixture on A) the specific surface area, total, and meso pore volume and B) the carbon yield and total yield of the obtained samples (for comparison the typical total yield for KOH activated carbons is also shown).[157]

Larger pores were mainly formed at the cost of smaller pores pointing to the coalescence of salt droplets caused by the enforced phase separation (Figure 3.8C+D). Glu_60 shows the same isotherm shape as Glu_46, but it is shifted to lower adsorbed volumes. This indicates a high qualitative similarity of the pore systems, at least in the pore range accessible by N$_2$-physisorption. Starting from 57 mol%, some salt will remain solid even at 350 °C (Figure 3.7). Hence, the liquid volume fraction of the salt is reduced leading to a decreased precursor to solvent (liquid salt) ratio. Very high amounts of KCl led to a large amount of solid salt during the process of carbon solidification explaining the comparatively poor porosity of Glu_80. The plot of SSA, TPV and mesopore volume vs. the molar content of KCl clearly depicts the strong influence of molar composition of the salt mixture on the porosity characteristics (Figure 3.9A). The maximum total pore volume of 1.73 cm^3 g^{-1} was obtained for Glu_46 which exhibited a SSA of 1210 m^2 g^{-1}. It has to be considered that activated carbons usually show high SSAs but seldomly exhibit pore volumes larger than 1 cm^3 g^{-1}.[27,158] The mesopore volume increased stepwise with rising KCl-content due to pore opening from Glu_00 (0.56 cm^3 g^{-1}) to Glu_40 (0.91 cm^3 g^{-1}). The maximum mesopore volume of 1.33 cm^3 g^{-1} is reached for the eutectic sample representing, however, an erratic increase of the pore volume. Possible explanation for this will be discussed later on in the present chapter together with the Hg-intrusion results. Glu_60 shows again a decreased mesopore volume which can be explained by the presence of solid macro templates which exceed the pore range detectable by N$_2$-physisorption.

Interestingly, the correlation between increasing KCl-content and decreasing SSA can be described in a linear fashion. The SSA for the samples with total pore volumes higher than $1 \, cm^3 \, g^{-1}$ can be expressed as a linear function of the KCl-content by Equation (3.1) showing a high coefficient of determination of $R^2 = 99.49 \, \%$ (Figure S7).

$$SSA = [-20.1 \, x + 2170] \, m^2 g^{-1}; \; x = mol\% \, KCl \qquad (3.1)$$

The derived correlation allows the synthesis of carbon materials with predictable surface areas. In order to test the derived Equation (3.1), two "control samples" were synthesized with 50 and 70 mol% KCl, respectively. The predicted values and the experimental values were in agreement showing only minor deviations of 5.0 % and 1.0 % for Glu_50 and Glu_70, respectively (Table S9). Additionally, the shape of the corresponding N_2-isotherms confirmed the continuous pore tuning (Figure S8).

The PXRD data of the samples show the typical pattern expected for amorphous highly porous carbons (Figure S9).[159] Intriguingly, the (002) reflection resulting from the interlayer stacking of graphitic layer is barely observable for the high surface area carbons (Glu_00, Glu_10, and Glu_20). The reflection starts to appear for Glu_30 and grows in intensity with increasing KCl-content. These findings point to an increased stacking number of graphitic carbon layers induced by larger unmixed domains of carbon and salt phase.
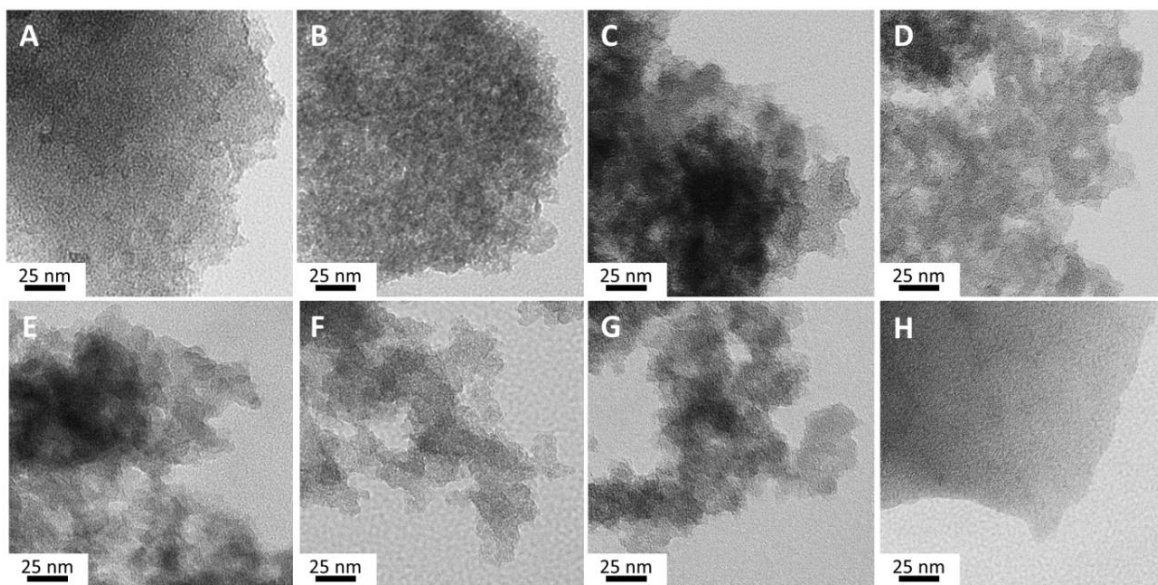
Figure 3.10 TEM images of the glucose derived materials prepared with different KCl-content in the KCl/ZnCl$_2$ mixture. a) Glu_00, b) Glu_10, c) Glu_20, d) Glu_30, e) Glu_40, f) Glu_46, g) Glu_60, h) Glu_80.

Figure 3.10 depicts representative TEM images of the samples. The visible stepwise increase in separation of the primary carbon particles and the widening of the pore system

confirm the N_2-physisorption results. Interestingly, Glu_60 shows a very open structure whereas Glu_80 seems completely dense. Additional SEM studies confirmed the pore tuning observed and further revealed effects concerning macropore formation (Figure 3.11). The sample synthesized with pure $ZnCl_2$ shows a rather smooth and dense surface with almost no visible pores. An increasing KCl-content caused a stronger separation of the primary carbon particles, and pores, in the range of large mesopores, can be observed. Few additional macropores (d > 50nm) are visible in Glu_30. Glu_46, representing the material synthesized with the eutectic, exhibits an open pore structure with a large amount of mesopores and several small macropores (d < 200 nm). The formation of some larger macropores (d > 200 nm) in Glu_60 can be explained by the further enhanced phase separation. However, according to the phase diagram, some of the salt (KCl/K_2ZnCl_4) should stay solid during the isothermal annealing at 350 °C which could result in the presence of additional (hard) macropore templates. Very high amounts of solid salt during the carbon solidification can lead to large macropores (d > 4 μm) as observed for Glu_80.
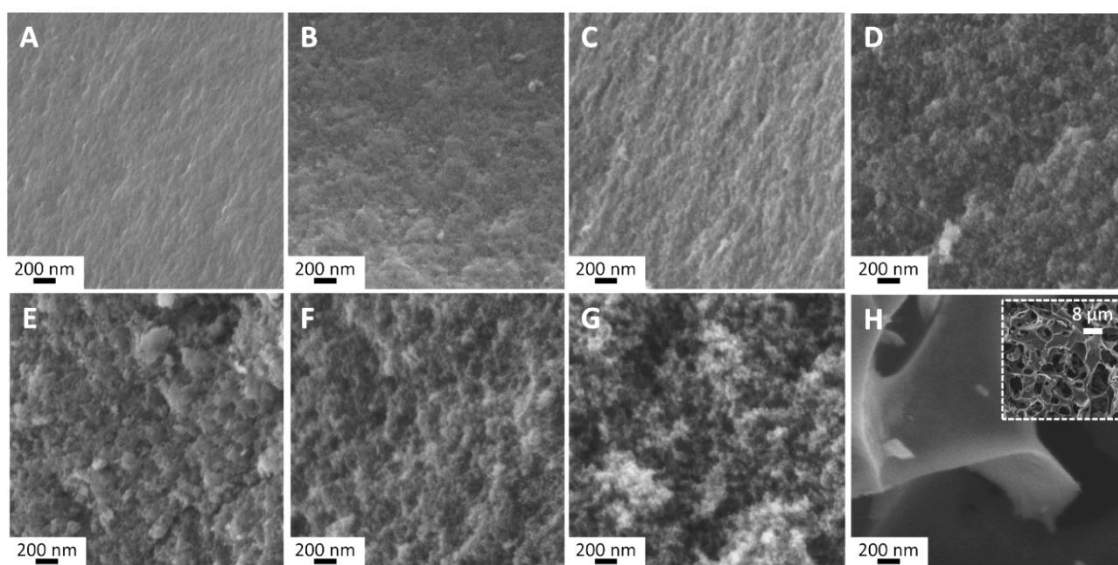
Figure 3.11 SEM images of the glucose derived materials prepared with different KCl-content in the $KCl/ZnCl_2$ mixture. A) Glu_00, B) Glu_10, C) Glu_20, D) Glu_30, E) Glu_40, F) Glu_46, G) Glu_60, H) Glu_80 (inset with lower magnification depicts the macroporous structure).

Additional evaluation of the macroporosity would help to further understand the porogenesis mechanism. Therefore, Hg-intrusion was conducted for Glu_00, Glu_30, Glu_46, Glu_70, Glu_80 (Figure 3.12, Table S10, Figure S10). According to the PSDs, the highest Hg uptake is due to pores with diameters between 100 and 10 μm (Figure 3.12A). These rather large pores are most likely random interstitial pores of the secondary carbon particles. The secondary grain size is defined by the facility of breaking the carbon

particles by grinding. Lower amounts of KCl results in a decreased separation of the primary carbon particles, as observed by TEM, which apparently increases the hardness of the carbon grains. The resulting larger secondary particle size also leads to larger interstitial pores. This explains the observed shift of the pore maxima in the samples prepared with lower KCl-contents. For the presented pore tailoring, the region between 0.004 and 10 μm is more relevant (Figure 3.12B). Nonetheless, also in this region, larger pores (d > 1 μm) might be induced rather by random interstitial pores than by templating effects of the salt. Glu_00 exhibits almost no pores in this region, while Glu_30 possesses meso- and small macropores (d < 100 nm) agreeing with the findings of TEM, SEM and N_2-physiorption. The eutectic sample shows a strongly increased mesopore volume. The mesopore maximum slightly shifts to larger pore diameters in the case of Glu_60. Furthermore, the PSD of Glu_60 exhibits a small maximum at 200 nm, which could imply the aforementioned presence of some solid salt particles during the process of carbon solidification. Interestingly, Glu_70 possesses a defined pore maximum at d = 1 μm, which is not expected for random interstitial pores. The observed maximum shifts to d = 4 μm for Glu_80.
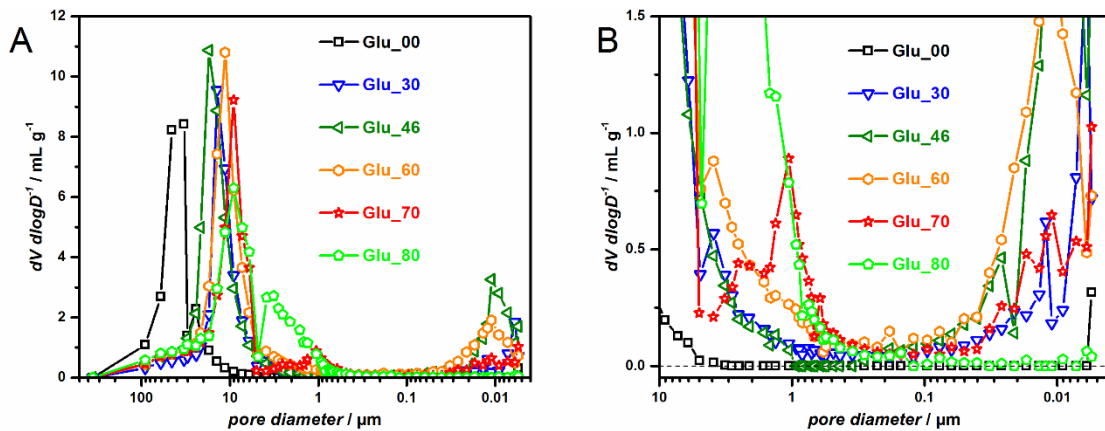
Figure 3.12 a) Overview and b) enlarged region (0.004 - 10 μm) of the pore size distributions derived from mercury intrusion of Glu_00, Glu_30, Glu_46, Glu_60, Glu_70, Glu_80

Additionally, optical microscopy studies at different temperatures were performed on a non-eutectic $KCl/ZnCl_2$ mixture containing 60 mol% of KCl (Figure 3.13). The mixture started to partially melt at the melting point of the eutectic mixture (T = 230 °C). At higher temperatures (T = 320 °C) some dispersed, solid, cubic particles were detected inside the molten salt matrix further demonstrating the presence of additional macrotemplates if KCl rich salt mixtures are used. These findings support the possibility of introducing macroporosity with the remaining solid salt particles. However, it has to be kept in mind that very high KCl-contents can induce inhomogeneities in the material. Generally, Hg-

intrusion and the optical microscopy measurements confirm the described pore forming model.
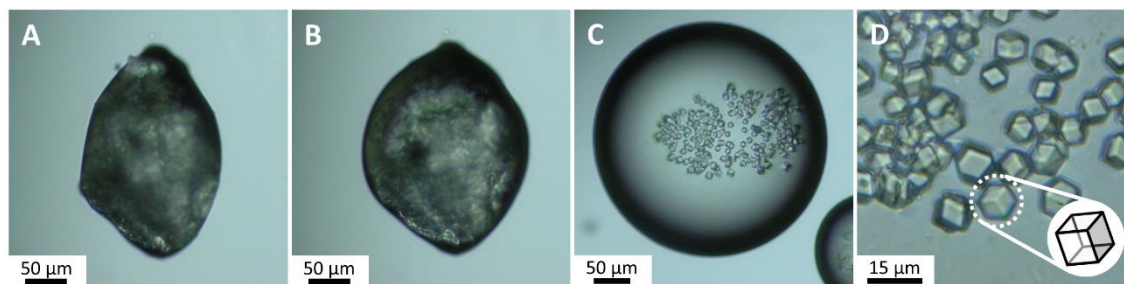
Figure 3.13 Light microscopy of non-eutectic KCl-ZnCl$_2$ mixture containing 60 mol% of KCl at different temperatures. A+B) salt particle during partial melting at 230 °C (melting point of eutectic mixture); C+D) cubic, solid crystals (probably KCl) dispersed in molten salt mixture at 320 °C.

One fact, which still has to be explained, is the drastically increased mesopore and total pore volume of the eutectic mixture. According to the predicted model, the "real" TPV should be almost constant for all samples due to the usage of the same total amount of salt mixture. The different densities of the two salts will lead to a slightly enhanced pore volume for salt mixtures richer in KCl (Figure S11). The volume of the molten salt is ~ 10 % larger for Glu_46 than for Glu_00, which, however, does not explain the increase in TPV by ~ 45 % for the corresponding samples (Figure 3.9A). It has to be considered that the TPV derived from N$_2$-physisorption measurements does not include the volume of larger macropores or the volume of ultramicropores, both not accessible by N$_2$-physi-soprtion measurements. Widening of ultramicropores can explain the slowly rising TPV with increasing KCl-content in the region between 0 and 40 mol% KCl but cannot deliver the explanation for the drastically increased TPV of Glu_46 (Figure 3.9A). Therefore, the explanation has to be the formation of less (not by N$_2$-physisorption accessible) macro-pores in the eutectic mixture compared to the non-eutectic mixtures. Hg-intrusion reveals that Glu_46 does not show any Hg uptake for pores in the range of 0.35 – 1 µm, whereas some pores of this size range are present in Glu_30 (Figure 3.12B). This indicates that, as in higher KCl-content samples, Glu_30 also contains some larger salt domains that remain solid during carbon solidification, which does not occur in the eutectic sample. Hence, different melting models are herein predicted for the melting of eutectic and non-eutectic salt mixtures, as depicted in Figure 3.14.
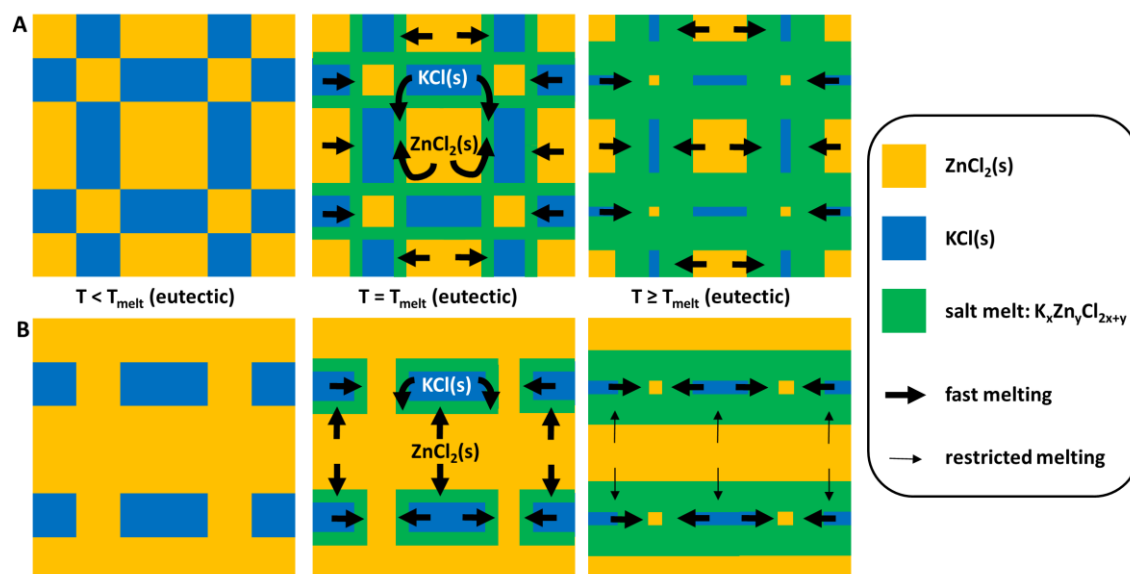
Figure 3.14 Schematic illustration of the melting of A) eutectic and B) non-eutectic salt mixtures.

If a non-eutectic salt mixture is used, the melting process will start at the interface between KCl and $ZnCl_2$ particles when the eutectic melting point is reached, as observed during the optical microscopy measurements. At this stage, both salts show a high tendency to melt (*fast melting*). Upon further melting, the substance not present in excessive amounts (regarding to the eutectic composition) still shows *fast melting* leading to an all-liquid state. Contrarily, the melting of the salt present in in excessive amounts (regarding the eutectic composition) is restricted. Thus, it will stay partially solid. Nevertheless, those solid particles can slowly melt upon a further increase in temperature leading to an all-liquid salt mixture. Apparently, a complete melting of non-eutectics in the present system is rather difficult leading always to smaller TPV. If eutectics are used, the initial melting process does not change, but both salts show *fast melting* throughout the whole melting process. This leads to more homogeneous reaction conditions thereby creating more pores in the accessible range of N_2-physisorption measurements. Intriguingly, the TPV of Glu_46 is only ~ 15 % smaller than the volume of the corresponding molten salt (Figure S11). This supports the suggested melting model and, moreover, confirms that pores are mainly created due to "salt templating" instead of activation.

3.3.2 Influence of the Porosity on the Supercapacitor Performance

The supercapacitor performance is strongly influenced by the porosity characteristics of the electrode material as described in section 1.3.1. The herein synthesized carbons possess very different porosity (SSA, present pore sizes) but can be regarded as chemically

equivalent allowing the study of porosity-performance relations. The SC performance of Glu_00, Glu_10, Glu_30, Glu_46 and Glu_60 was characterized by cyclic voltammetry measurements in a two electrode set-up using 1 M sulfuric acid as electrolyte and polyvinylidene difluoride as binder. The specific capacitance at low scan rates (5 mV s^{-1}) increased with increasing SSA (Figure 3.15A). The highest value (206 F g^{-1}) is obtained for Glu_00. However, the values of Glu_00 drop at faster scan rates indicating mass transport limitations. Glu_10 and Glu_30, showing an open pore system and still reasonable SSA, exhibit 6.1 % and 4.3 % higher capacitances than Glu_00 at the fastest scan rate applied (200 mV s^{-1}). These findings highlight the importance of transport (meso-) pores for high power applications.
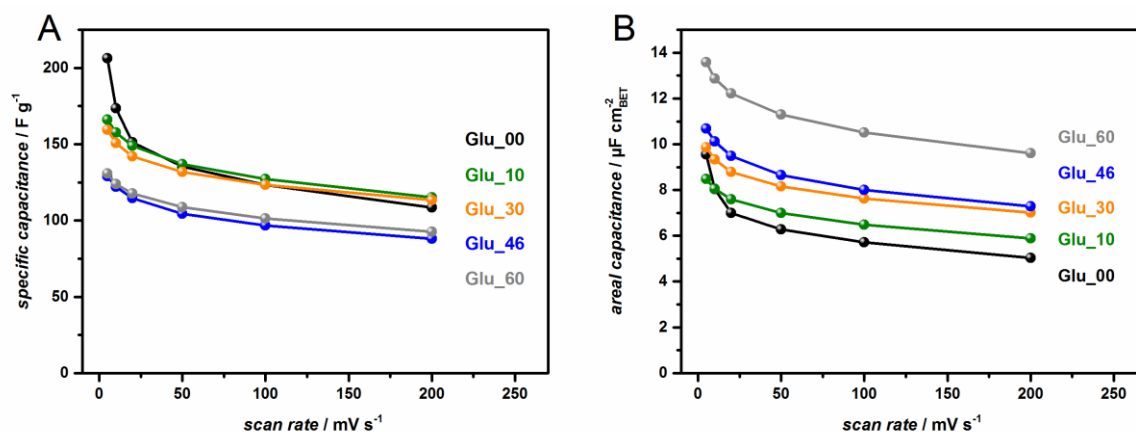
Figure 3.15 A) Specific capacitance and B) areal capacitance of the different samples obtained by cyclic voltammetry measurements with varied scan rate in 1 M sulfuric acid.

More insights are obtained by studying the decay of the specific capacitance with respect to the scan rate (Figure S12). Glu_00 exhibits the largest decay and the absolute values decrease with increasing KCl-content according to Glu_10 > Glu_30 > Gl_46 > Glu_60. Obviously, samples with higher SSA have higher double-layer capacitance. Normalization of the capacitance with respect to the corresponding SSA can deliver more insights regarding the influence of the different pore systems. An opening of the pore system causes improved areal capacities over the whole range of applied scan rates (Figure 3.15B). Glu_60 delivers the largest value of 13.6 F g^{-1} cm$^{-2}_{BET}$ at a scan rate of 2 mV s^{-1}. The areal capacitance obtained at 20 mV s^{-1} is increased by 8.6 %, 25.6 %, 35.6 % and 74.7 % (in comparison to Glu_00) for Glu_10, Glu_30, Gl_46 and Glu_60, respectively. This strong enhancement at higher KCl-contents points to the enhanced accessibility/usage of the surface sites caused by an opening of the pore system, which supports the structural characteristics of the materials. Moreover, the total porosity of the different samples is

rather similar according to the porogenesis mechanism. Hence, the total amount of electrolyte inside the different electrodes can be regarded as constant allowing the elimination of any effects which are related to the total electrolyte volume.

The studied effect of changed molar composition of the used salt mixture on the porosity of ionothermal carbons is highly interesting regarding the synthesis of pore tailored materials and will be expanded in section 3.4.

3.4 Adenine Derived Nitrogen Doped Carbons with Tailored Porosity

The variation of the molar composition of the salt mixture was introduced as a new pore tuning tool for ionothermal carbon materials in chapter 3.3. The present chapter will discuss the extension of the pore tailoring to a different salt system and precursor. Adenine will be used as precursor and $NaCl/ZnCl_2$ as the combined solvent/porogen, leading to highly porous nitrogen doped carbons as already discussed in section 3.2.2. Thus, the general applicability of the developed pore tool can be proven. Moreover, the application field of the pore tailored materials can be enlarged towards the oxygen reduction reaction. The weight ratio of precursor and salt will be kept constant at 1:10 and the influence of a rising NaCl-content in the salt mixture on the porosity will be studied.[112] The general sample preparation and the heat treatment was conducted as described for the nucleobase derived samples in section 3.2.2. In continuation of the aforementioned nomination of the glucose derived, pore tailored carbons, the different adenine derived samples are named Ade_XX, where XX stands for the molar amount of NaCl present in the $NaCl/ZnCl_2$ mixture. In chapter 3.4.1 the influence of a rising NaCl-content will be elaborately investigated by N_2-physisorption, SEM, TEM, X-ray photoelectron spectroscopy (XPS), and PXRD and in section 3.4.2 the ORR performance with respect to of the pore system will be discussed.

3.4.1 Pore Tailored Nitrogen Doped Carbons Synthesized with Non-Eutectic $NaCl/ZnCl_2$-Mixtures

Adenine derived nitrogen doped carbon showed promising porosities if a $NaCl/ZnCl_2$ (42 mol% NaCl) salt mixture was used (cf. chapter 3.2.2, Figure 3.5). However, a relatively high salt to precursor ratio of 14:1 had to be applied to achieve an opening of the pore system, leading to the transport porosity needed for electrochemical applications.

Reduction of the total and relative amounts of the corrosive and volatile $ZnCl_2$, seems highly desirable from an industrial point of view. NaCl on the other side is harmless, cost-efficient, relatively abundant, non-volatile, and inert towards carbon up to very high temperatures. Therefore, it is of high interest to investigate NaCl rich salt mixtures, especially in the context of upscaling.

As revealed by the phase diagram in Figure 3.16, the eutectic $NaCl/ZnCl_2$ mixture melts at 250 °C whereby adenine only decomposes (sublimes) at temperatures higher than 360 °C.[147] The overlay of the phase diagram of $NaCl/ZnCl_2$ and the TGA curve of adenine reveals a relatively large region of $Na_xZn_yCl_{(x+2y)}$ melts with differed compositions, all of them allowing carbon solidification in a homogenous all liquid salt phase (Figure 3.16). The $ZnCl_2$ present could change the reactivity of adenine. Nonetheless, it is believed that the formed oligomeric moieties will be able to dissolve leading to the desired all liquid reaction mixture. This is supported by the observations made during the heating of guanine hydrochloride and $KCl/ZnCl_2$ in a quartz flask (section 3.2.2).
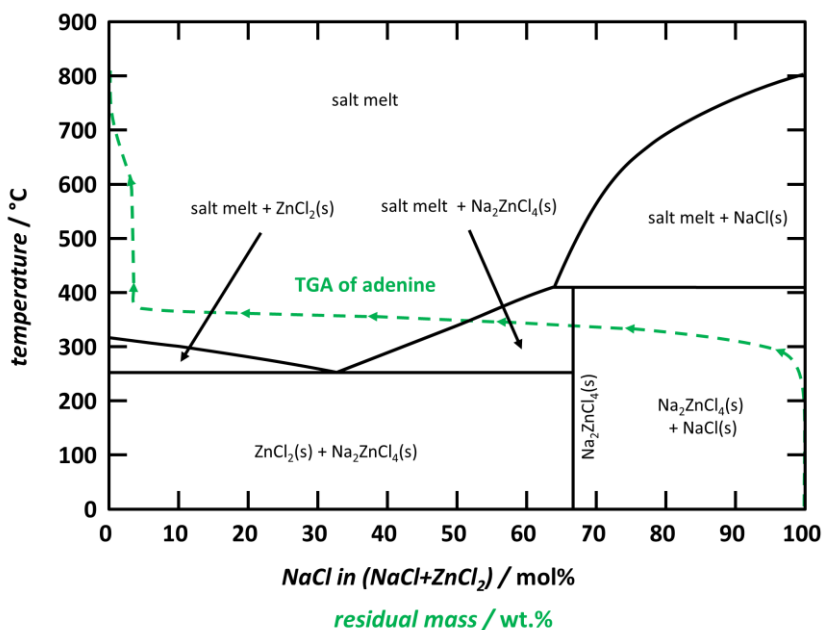
Figure 3.16 Schematic overlap of the measured TGA of adenine and the phase diagram of $NaCl/ZnCl_2$.[147]

The NaCl-content was varied between 33 and 100 mol% and the obtained samples were first characterized by N_2-physisorption (Figure 3.17, Figure 3.18, Table S11). The application of the eutectic mixture (33 mol% NaCl) resulted in an ultrahigh SSA of 2900 m^2 g^{-1} and a very high TPV of 3.0 cm^3 g^{-1}. These values indicate a great miscibility of adenine and eutectic $NaCl/ZnCl_2$ throughout the carbonization. Ade_33 can be described

as an "all-surface-area" nitrogen doped carbon, considering the theoretical surface area of graphene is 2965 m^2 g^{-1}.[17] A rising NaCl-content caused a continuous decrease in SSA. Nevertheless, even 90 mol% NaCl still led to a high SSA of 1770 m^2 g^{-1} whereas 100 mol% NaCl resulted in negligible SSA and porosity. Interestingly, all samples synthesized with a ZnCl$_2$-containing salt mixture showed a rather constant (and high) carbon yield of ~ 60 % (Table S11). Hence, the strong SSA dependence on the NaCl content cannot be caused by a varied activation effect due to different absolute amounts of ZnCl$_2$ present (e.g., by means of carbon etching). The same effect was seen for the glucose derived, pore tailored materials discussed in section 3.3.1.
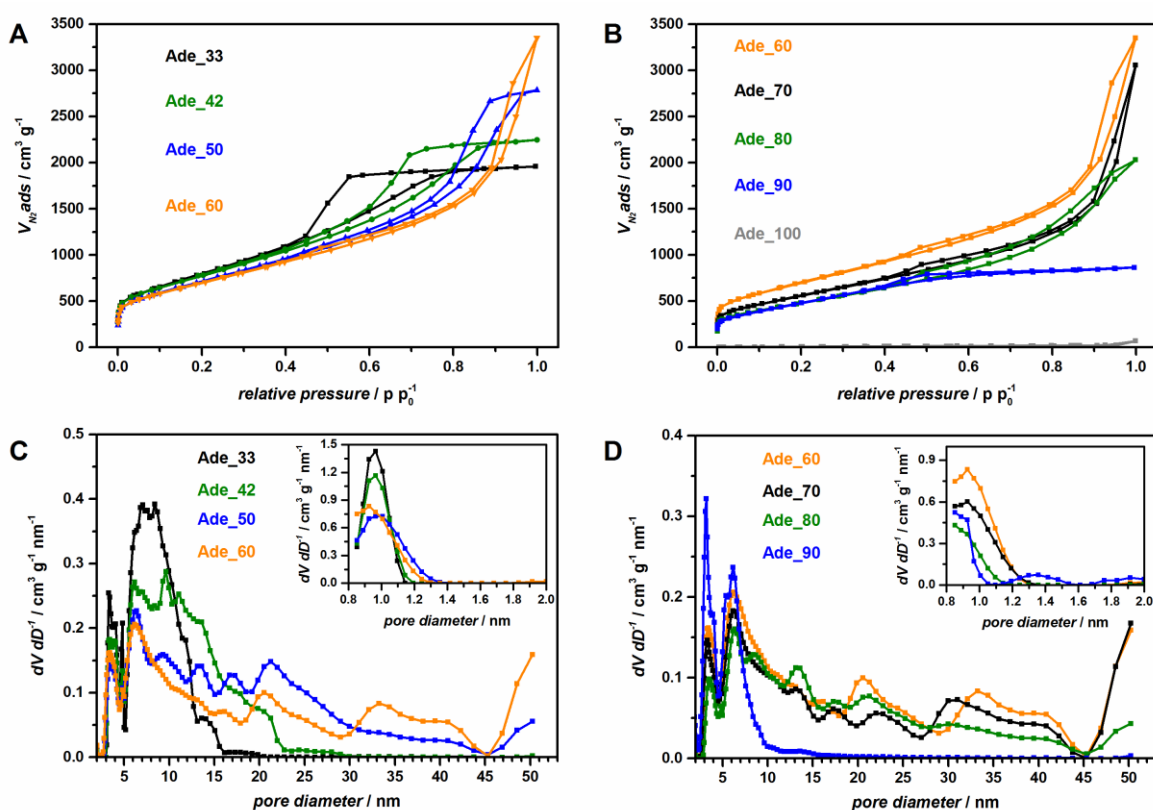
Figure 3.17 A+B) N$_2$-physisorption isotherms and C+D) mesopore and micropore (inset) size distribution of the adenine derived NDCs prepared with different amounts of NaCl in the NaCl/ZnCl$_2$ mixture.

The isotherm shape of the samples obtained with NaCl-contents between 33 and 80 mol% can be generally described as a type IV indicating the presence of mesopores. The hysteresis type and position are clearly influenced by the salt composition as also discussed for the glucose derived samples (section 3.2.1). Ade_33 exhibits a H2 hysteresis implying the presence of bottleneck pores. The very steep desorption branch in the range 0.4 < p p$_0^{-1}$ < 0.5 indicates that pore emptying is mainly induced by cavitation allowing for no conclusion regarding the diameter of the bottlenecks. Ade_42 possesses larger

mesopores as seen by the hysteresis shift to higher pressures. The hysteresis shape still points to the presence of bottleneck pores with neck diameters in the range of $4.0 - 5.5$ nm as derived from the PSD of the desorption branch (Figure 3.6A). A further increased NaCl-content not only causes a hysteresis shift to higher pressures but also results in parallel hysteresis branches indicating a further widening of the mesopores and the elimination of the bottlenecks. However, the highest investigated NaCl-content of 90 mol% predominantly results in micro- and small mesopores, as implied by the type I(b) isotherm, combined with almost no observable hysteresis. The corresponding PSDs clearly depict the loss of micropores and the increasing diameter of the mesopores with rising NaCl-content (Figure 3.17C+D). The high uptake at pressures close to $p\,p_0^{-1} = 1.0$ and the steeply increasing PSD at $d > 45$ nm indicate the presence of additional macropores in the samples obtained with $50 - 80$ mol% NaCl. Basically, the observed effects led to the presence of different sized pores being representative for each sample. Overall, the N_2-physisorption measurements show a stepwise widening of the pore system with increased NaCl-content which is in agreement with the effect of an increasing KCl-content in the KCl/ZnCl$_2$ mixture as presented in chapter 3.3.

The SSA, TPV and the N-content in regards to the applied NaCl-content is depicted in Figure 3.17. The chemical composition of the samples prepared with different NaCl/ZnCl$_2$ ratios are very similar, all showing high nitrogen contents from 5.9 to 7.7 wt.%, and similar oxygen contents of ~ 7 wt.% (Table S12).[X] Interestingly, the TPV increases with rising mesopore size, reaches a maximum of 5.2 cm^2 g^{-1} for Ade_60, and decreases again for higher NaCl-contents. The TPV of Ade_60 is 5-times higher than the typical value for activated carbons of 1 cm^3 g^{-1}.[27,158] The rising TPV most probably results from the opening of ultramicropores, which are not accessible by N_2-physisorption, and the NaCl-dependent increase of the salt volume, as described for the glucose derived samples in section 3.3.1 (Figure S13).[XI] The presence of non-accessible pores for the samples prepared with very low NaCl-contents is supported by the non-linear trend of the SSA in this region (Figure 3.18). Furthermore, very small pores tend to shrink/disappear during work-up due to high Laplace pressures inside the pores. An additional explanation for the high TPV augmentation of 73 %, if Ade_33 is compared with Ade_60, could possibly lie

---

[X] The oxygen present in the samples (synthesized with oxygen free substances) either points to oxygen impurities in the inert gas stream during the pyrolysis or could be the result of post-synthesis oxidation of the carbon materials occurring at ambient conditions due to their very high SSA.

[XI] The maximum TPVs of the adenine derived NDCs even exceed the volume of the molten salt pointing to the presence of an additional porogenic effect. Presumably, the additional porosity is introduced due to removal of nitrogen sites from the carbon framework by "nitrothermal" reduction at high temperatures.

in a density change of the salt if it is very close to the carbon surface or confined in very small pores (ultramicropores). Both effects result in a decreased salt volume (ergo TPV), and are intensified for materials with small pores and high SSA.
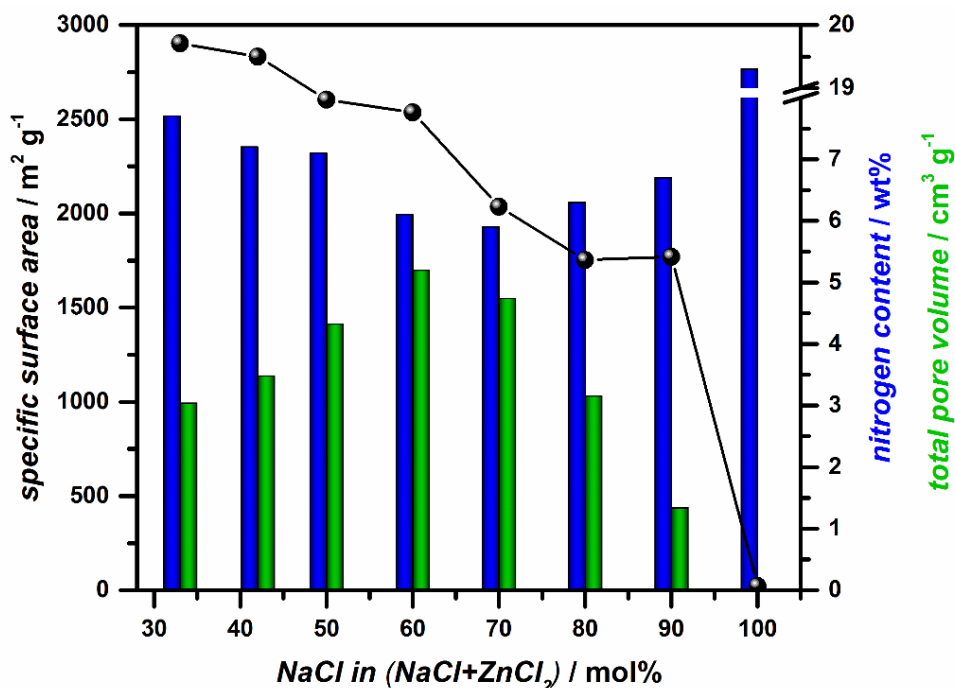
Figure 3.18 Influence of the amount of NaCl used in the NaCl/ZnCl$_2$ mixture on the specific surface area, nitrogen content and total pore volume of the obtained catalysts.

Another interesting factor is the increased macroscopic volume of the carbons with rising NaCl-content (Figure S14), showing almost the same trend as the TPV. This effect could be due to the aforementioned rising total volume of the salt mixture with increasing NaCl-contents and the shrinkage/instability of very small pores during work-up. The N-content shows a trend opposite to the TPV (Figure 3.18). Typically, a succeeding nitrogen loss takes place with increasing synthesis temperature caused by the formation of volatile N-species.[160,161] Apparently, a high TPV and an open pore system promotes the volatilization leading to lower N-contents in the final carbon. The same effect is the reason for the very high N-content (19.3 wt.%) of the non-porous Ade_100. The accomplished N-contents (5.9 − 7.7 wt.%) represent relatively high nitrogen contents in comparison to the literature, especially for such highly porous systems. This points to the high stability of the N-sites throughout the whole synthesis. For electrochemical applications, not just the total amount of nitrogen is of importance, but also the specific type of nitrogen present. Therefore, XPS measurements were performed to gain deeper knowledge of the chemical state of the elements. The survey spectra of all samples show the presence of carbon, nitrogen, oxygen and minor amounts of residual ZnCl$_2$ which is probably captured in non-

accessible pores (Table S12). Interestingly, the molar ratio of Zn to Cl is approximately 1:1 indicating the additional presence of other Zn-sites than $ZnCl_2$. Probably, residual Zn is also coordinated as (single atom) Zn^{2+} to N-sites which is supported by HRTEM measurements of an adenine derived NDC synthesized with a $KCl/ZnCl_2$ salt mixture (Figure S15). Considering earlier reports, a direct influence of the Zn-content on the electrochemical performance can be neglected.[116] Nevertheless, some doubts about the influence of the residual Zn on the ORR-performance remain, which will be addressed in more detail in chapter 5 (section 5.3.2). The high resolution N 1s spectra reveals the presence of pyridinic (398.5 eV), pyrollic (399.9 eV), graphitic (401.3 eV) and oxidizied N-sites (403.3 eV) in all samples (Figure S17). According to the quantification of the different N-sites, the amount of NaCl present in the $NaCl/ZnCl_2$ has no significant influence on the nitrogen type obtained in the final carbon. In conclusion, all materials obtained with $NaCl/ZnCl_2$ exhibit qualitatively and quantitatively very similar N-sites, but show distinct differences in SSA and pore size (Figure S18).
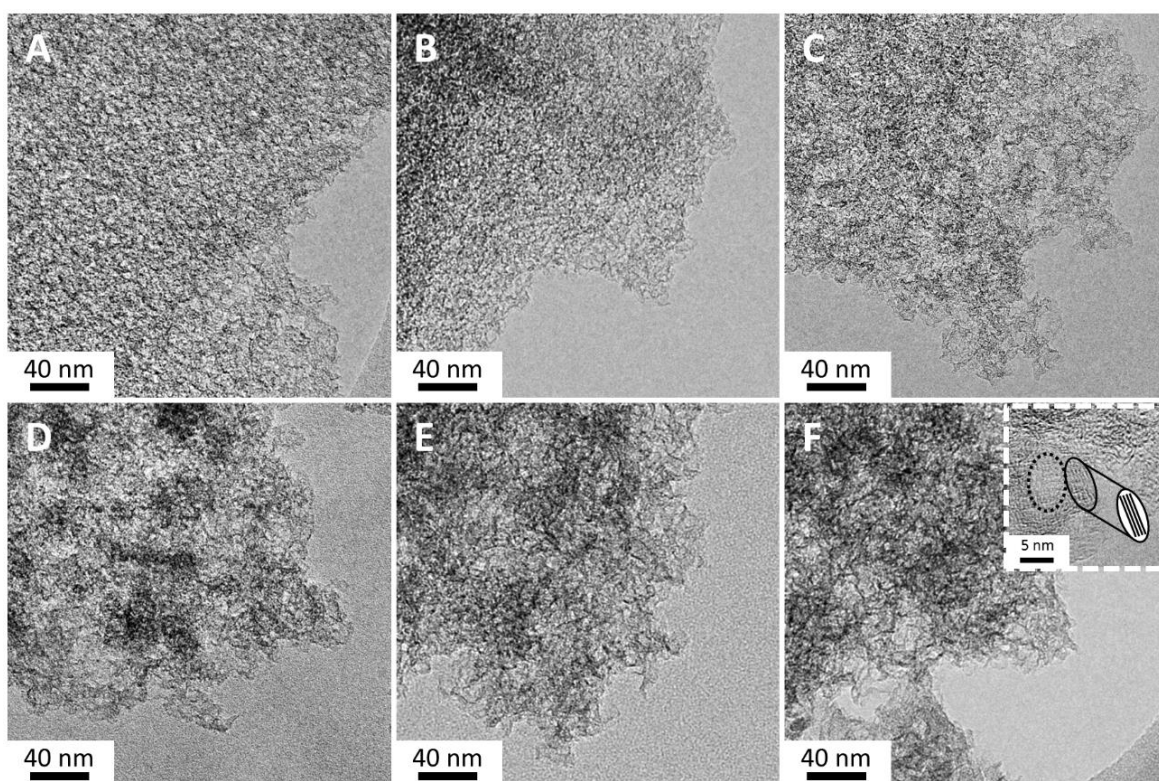
Figure 3.19 TEM images of the adenine derived samples prepared with different NaCl-content in the $NaCl/ZnCl_2$ mixture. A) Ade_33, B) Ade_42, C) Ade_50, D) Ade_60, E) Ade_70, F) Ade_80 (HRTEM inset with indicated mesopore and 'thick' pore wall.

(HR)TEM images confirm the stepwise opening of the pore system (Figure 3.19). Ade_33 shows small, spherical mesopores pointing to porogenesis caused by salt droplet templating. The mesopores grow with rising NaCl-contents but appear less uniform in size.

Furthermore, the number of stacked carbon layers increases representing the "wall thickness" of the carbon matrix. The sample prepared with 80 mol% NaCl exhibits relatively "thicker walls" with increased graphitic stacking (inset Figure 3.19F). The increased number of stacked carbon layers with higher NaCl-content goes along well with the PXRD results (Figure S19). The interlayer reflection (002) is not visible for the high SSA materials, but appears as a shoulder in Ade_80 and Ade_90. Furthermore, the angle of the (002) reflection is shifted to lower angles (~ 23°), as compared to graphite (26.3°), pointing to a larger interlayer distance due to porosity and disorder (0.39 nm vs. 0.34 nm). Stereoscopic TEM images allow an improved visualization of the 3D-structure and porosity of the different materials (Figure S16). SEM images confirm the stronger separation of primary carbon particles with rising NaCl fractions (Figure 3.20). Ade_33 and Ade_42 still appear rather dense, whereas Ade_50 and Ade_60 exhibit an open pore system. Ade_70 and Ade_80 surpass a microseparation maximum resulting in additional macroporosity. The usage of very high amounts of NaCl (90 mol%) lead again to a rather dense material. The application of pure NaCl results in carbon solidification on the surface of salt particles before the event of melting, as depicted by the sheet like morphology with extended lateral dimensions.
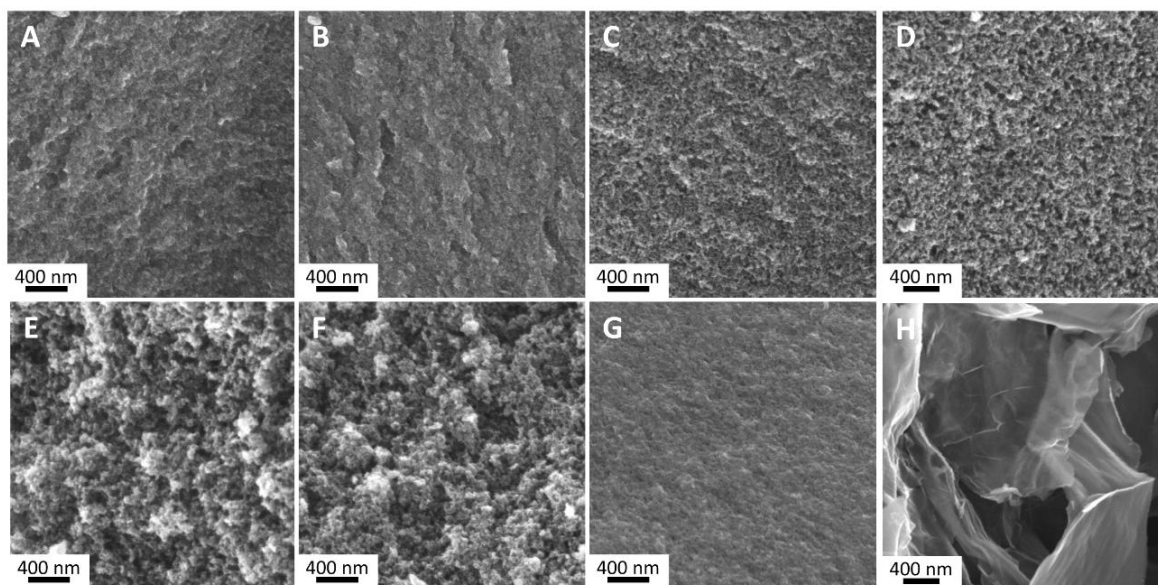
Figure 3.20 SEM images of the adenine derived samples prepared with different NaCl-content in the NaCl/ZnCl₂ mixture. A) Ade_33, B) Ade_42, C) Ade_50, D) Ade_60, E) Ade_70, F) Ade_80, G) Ade_90, H) Ade_100.

Interestingly, electron microscopy shows that throughout the synthesis carbon forms the dispersing phase, although the salt fraction is much higher. This stands in contrast to the glucose derived carbons synthesized herein and to the typically observed results in

literature, especially for high salt to carbon ratios, which usually indicate colloidal carbonization.[95,116] Furthermore, a TPV value of $5 \, cm^3 \, g^{-1}$, created by salt templating, corresponds to a carbon to (molten) salt volume ratio of 1:10 (assuming a carbon density of $2 \, g \, cm^{-3}$). Thus, the synthesis of adenine derived NDCs obtained with $NaCl/ZnCl_2$ may be regarded as a high internal salt phase ionothermal carbonization.

All these results clearly depict a progressive pore tuning if the NaCl fraction is enlarged in a $NaCl/ZnCl_2$ melt. It has to be pointed out that Ade_33 combines an ultrahigh SSA ($2900 \, m^2 \, g^{-1}$) with a rather dense appearance (regarding SEM and TEM), and a high nitrogen content of 7.7 wt.%. Hence, Ade_33 can be described as a 3D textured framework built up from nanographenes and that most of the nitrogen/carbon atoms should be accessible from two sides. As aforementioned, rising NaCl fractions lead to steadily changed properties of the melt which causes a continuous increase of the pore size, thereby leading to larger mesopores and an open hierarchical pore system. Larger pores are mainly formed at the expense of smaller pores which indicates coalescence of small salt droplets throughout the porogenesis. Furthermore, distinct morphology changes, as seen by SEM images, can be directly connected to the phase diagram (Figure 3.16). At NaCl fractions above 67 mol%, i.e. across the binodal curve of the phase diagram, the coexistence of liquid melt and solid NaCl is expected, even throughout carbon solidification at high temperatures. This implies that the more open porous morphology of Ade_70 and Ade_80, clearly observed by SEM (Figure 3.20E+F), not only results from the NaCl enriched $NaCl/ZnCl_2$ salt mixture but is also caused by additional macrotemplating by solid NaCl particles dispersed in the liquid reaction mixture. The effect is in line with the macrotemplating of glucose derived carbons synthesized with KCl rich $KCl/ZnCl_2$ mixtures, as described in section 3.3.1. A very low volume fraction of the molten salt kinetically hinders the coalescence of the salt droplets, resulting only in smaller pores (d < 10 nm), which is the case for Ade_90 (Figure 3.17D). Accordingly, the quantity of small pores of Ade_90 is again higher in comparison to Ade_80. The pore formation model is depicted in the schematic illustration in Figure 3.21.
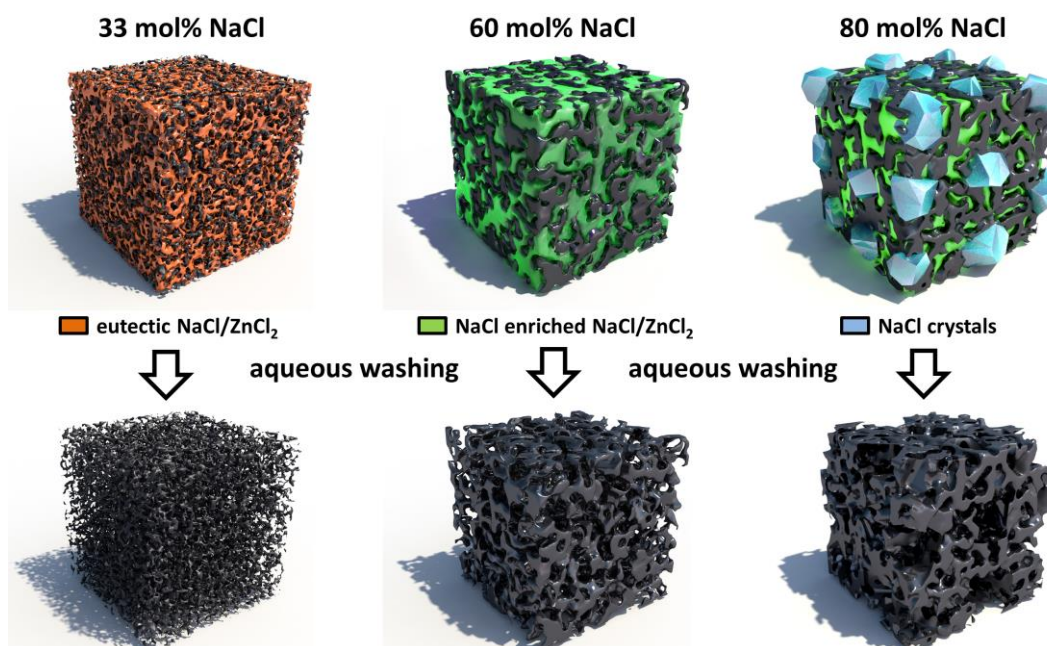
Figure 3.21 Schematic illustration of the pore formation depending on the amount of NaCl present in the NaCl/ZnCl$_2$ mixture.

Generally, it was shown that the variation of the molar fraction of NaCl in a NaCl/ZnCl$_2$ mixture can be used to tailor the porosity of NDCs without changing the chemical composition. It has to be emphasized that the materials can be prepared with high reproducibility, thereby allowing fine pore tuning with minimal molar changes of the salt mixtures (Figure S20). This is seen by the isotherms of two additional samples prepared with 78 and 82 mol% NaCl, respectively (Figure S21). The porosity characteristics of the obtained NDCs are very appealing for electrochemical applications, and their ORR-performance will be presented in the following section 3.4.2.

3.4.2   Influence of the Porosity on the Oxygen Reduction Reaction

In order to study the porosity-activity relation, the ORR performance of the obtained NDCs was investigated by RDE and RRDE measurements under alkaline conditions. All samples are active towards the ORR, as indicated by the polarization curves in Figure 3.22A+B. At high overpotentials, all samples deliver constant current densities indicating no kinetic limitations. The values of the limiting currents are in the range of the theoretical Levich current for the aimed four electron mechanism within the experimental error of ~ 10 %.[111] These results coincide well with the similarity of the chemical composition and N-sites of these NDCs. However, the catalysts show clear and surprising differences in the kinetically limited region at low overpotentials.

To gain a better understanding of the present catalysts, the catalytic activity (onset potential) and the kinetics (current trend dependent on the overpotential) will be discussed separately. The respective porosity characteristics obviously have a strong influence on the catalyst kinetics. The $E_{1/2}$ shifts from 820 mV to 880 mV if Ade_33 is compared with Ade_70 (or Ade_80). The maximum $E_{1/2}$ values are approaching the best (Fe-)NDC materials reported so far.[162,163] The performance of Ade_80 in comparison to other benchmark, non-precious metal catalysts from literature is depicted in Figure 3.22D. The exact descriptions of the reference catalysts and the corresponding measurement conditions are summarized in Table S13.[91,98,113,116,164-167] Apparently, an additional potential dependent factor exists, as indicated by the sometimes ill-shaped LSV curves. Therefore, the kinetics are mainly discussed in terms of the overpotential needed to reach a certain percentage of the limiting current ($E_{1/2}$, $E_{4/5}$, $E_{9/10}$), instead of the Tafel slopes (Figure 3.22C).
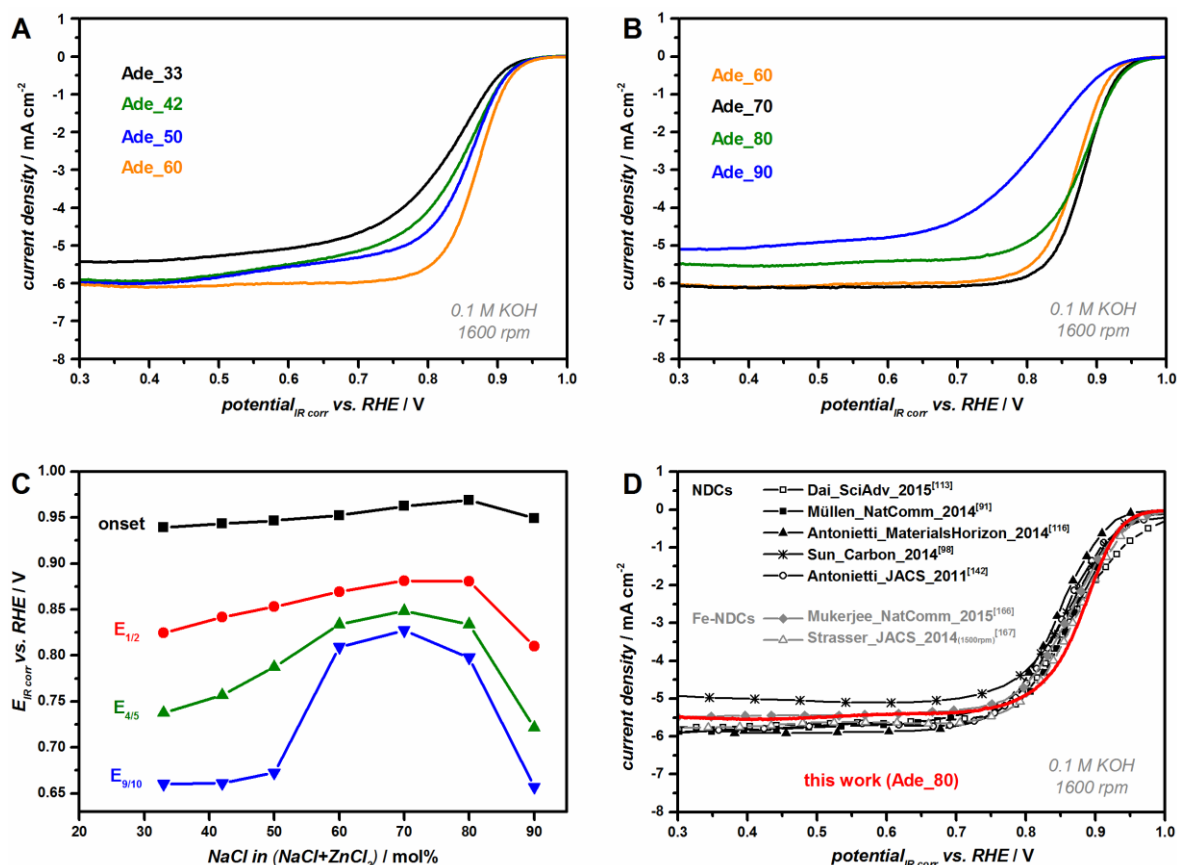
Figure 3.22 A+B) RDE polarization curves of the adenine derived NDCs prepared with different amounts of NaCl in the NaCl/ZnCl$_2$ mixture in O$_2$-saturated 0.1 M KOH with a sweep rate of 5 mV s^{-1}, 1600 rpm. C) Influence of the amount of NaCl used in the NaCl/ZnCl$_2$ mixture on onset, $E_{1/2}$, $E_{4/5}$ and $E_{9/10}$ of the catalysts obtained. d) Comparison with RDE polarization curves of different literature benchmark, non-noble metal catalysts (alkaline solution).

From a general point of view, a higher SSA should result in a larger interface between NDC and electrolyte, thereby also leading to an increased electrochemical active surface area (EASA) which is coupled with the catalytic activity. Ade_70 exhibits a 30 % smaller SSA than Ade_33. However, the former distinctly outperforms the latter in electrocatalysis. The material synthesized with 80 mol% of NaCl exhibits only 60 % of the SSA of Ade_33, nevertheless it still shows a very high ORR activity. These findings point towards a non-linear correlation between SSA and EASA. This is supported by Figure S22 revealing the kinetically controlled region of the RDE polarization curves normalized to the respective SSA. Furthermore, in the present set of NDCs, a higher nitrogen fraction of the catalysts cannot be directly linked to an increased ORR performance, as indicated by the comparison of NDC_33 and NDC_70 which exhibit a N-content of 7.7 wt.% and 5.9 wt.%, respectively. Several literature results already highlighted the importance of a hierarchical open pore system to achieve fast kinetics.[91,168,169] Wei *et al.* showed that larger mesopores (d = 22 nm) lead to a higher activity than smaller pores (d = 7 nm).[169] Nonetheless, the development of an open pore system was usually accompanied by an increase of the SSA, allowing a different/opposing explanation of the observed activity shift. Zhang *et al.* introduced an additional pore dependent parameter based on reduced limiting currents which, however, are not observed for the current set of materials.[160] Concurrent to the present work, Ferrero *et al.* even discussed the positive influence of present mesopores on the ORR performance studying catalysts exhibiting similar SSA but different pore sizes.[170] Apparently, the activity at high performance, represented by $E_{9/10}$, shows the strongest dependence on the present pore system, as indicated by the large shift of ~ 160 mV from Ade_33 to Ade_70. Interestingly, the catalytic performance coincides well with the stepwise opening of bottleneck pores (Ade_33) towards highly open pores (Ade_70), as presented in section 3.4.1. Presumably, bottleneck pores not only hinder nitrogen desorption in N_2-physisorption experiments, but also the mass transport of oxygen towards the active centers in the electrocatalytic reduction of oxygen, resulting in the inefficient use of surface area (EASA < SSA) and poor ORR kinetics. In contrast, an open pore system allows the full usage of the active centers (EASA = SSA), and leads to fast kinetics (Figure 3.23). Of course, to reach the best performance both aspects have to be present, meaning a high SSA and an open pore system. High NaCl-fractions result in smaller amounts of liquid porogen due to NaCl precipitation causing reduced SSA. This explains why Ade_80, exhibiting an open pore system, showed the same $E_{1/2}$ than Ade_70, however a slightly reduced $E_{4/5}$. The very low amount of liquid porogen for Ade_90 leads

to a closed pore system. Therefore, while the SSAs of Ade_80 and Ade_90 are almost the same, a much lower activity is seen for Ade_90. All these findings point to the strong influence of the pore system on the ORR performance. Apparently, bottleneck pores can limit the activity strongly by restricting the effective EASA. In conclusion, the variation/optimization of the pore system is an effective tool to enhance the catalytic activity. Moreover, the results reveal that N_2-physisorption, being a facile and widely accessible tool, may be used for the prediction and thus optimization of the electrochemical activity.
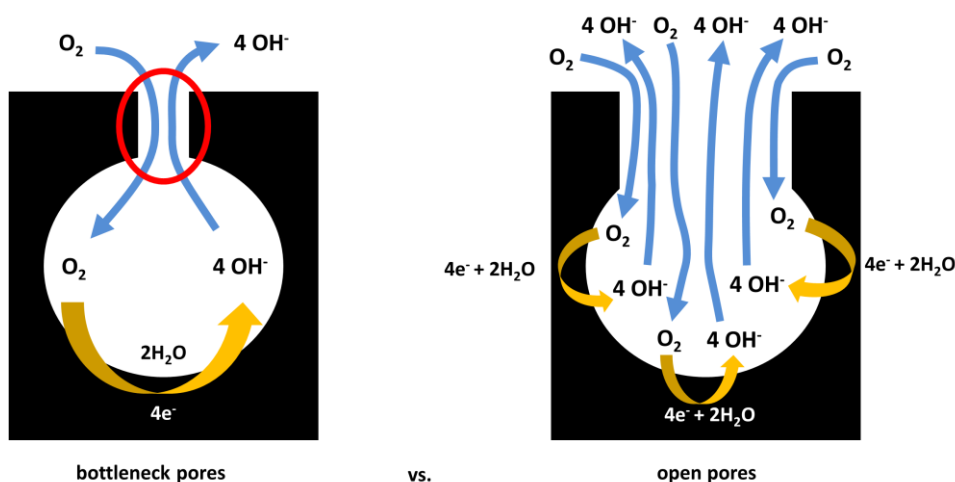
Figure 3.23 Schematic illustration of the ORR-kinetics in bottleneck pores and open pores. Bottleneck pores hinder the transport of educts as well as of (intermediate, side) products leading to poor kinetics and unused SSA (active centers), whereas open pores result in fast kinetics and allow more effective usage of the SSA.

Intriguingly, the chemically similar materials show a slightly different trend for the onset potentials (Figure 3.22C). Despite the fact that high amounts of NaCl led to a reduced SSA, the highest value of $E_{onset} = 0.97\,V$ was obtained for Ade_80. The most obvious difference of Ade_80, in comparison to the other samples, is the increased width of the carbon domains as shown by PXRD and HRTEM. It can be suggested that the exchange current densities are smaller for very thin carbon domains due to a lower local density of electronic states. An effective ORR requires a high density of electronic states due to the four electrons needed per molecule of oxygen. At low overpotentials, Ade_80 indeed shows the highest current densities, even though the Tafel plots reveal very similar rate limiting steps for Ade_42 to Ade_80 with slopes close to 45 mV/dec (Figure S23). Another explanation could be that the macroscopic resistivity of the catalyst film increases with increased SSA of the NDCs. To differ between the two factors, additional experiments were conducted with the Ade_50 sample. The macroscopic conductivity was increased by adding 10 wt.% conductive Carbon Black (Printex®XE2, *Degussa*) during the ink

preparation. The carbon domain thickness was influenced by adding thermally reduced graphene oxide (TRGO) in the initial adenine – salt mixture (10 wt.% in respect to the typical NDC yield). The aim herein was the formation of the NDC on top of the TRGO, combining the high SSA of Ade_50 with a larger carbon backbone. The LSVs at 1600 rpm are depicted in Figure 3.24A.
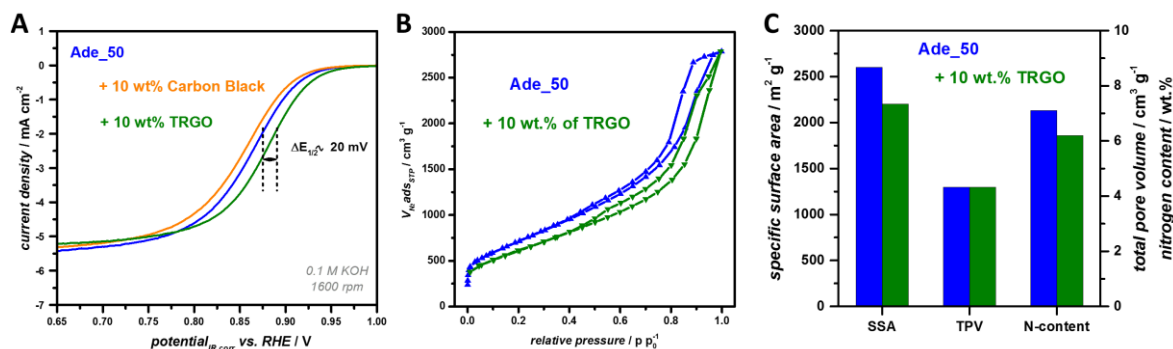
Figure 3.24 A) RDE polarization curves (O$_2$-saturated 0.1 M KOH; 5 mV s^{-1}; 1600 rpm), B) nitrogen physisorption isotherms, and C) SSA, TPV, and N-Content of pristine and modified (with carbon black or TRGO) Ade_50.

Increasing the macroscopic density does not improve the activity. Actually, a minor activity decrease was observed due to the reduced amount of active material present in the catalyst mixture. Therefore, it can be concluded that in the present case the macroscopic conductivity is not the reason for the different performances obtained. Interestingly, adding TRGO resulted in a clear shift of the whole LSV curve to higher potentials, however, it did not change the general curve shape. This is in line with the very similar N$_2$-isotherms, SSAs, and chemical composition of the two materials (Figure 3.24B+C, Table S14). The findings support the suggested increase of the electronic states due to larger carbon domains.

Regarding the general aim to replace platinum as the catalyst for the ORR reaction, the material Ade_80 shows very promising electrocatalytic features (Figure 3.25). Furthermore, the application of 80 mol% NaCl strongly improves the ionothermal process in perspective of Green Chemistry. The ORR-overpotential of Ade_80 is only negatively shifted by ~ 9 % when compared to the ORR-overpotential of the commercial Pt/C catalyst (with a relatively high Pt loading of 60 µg$_{Pt}$ cm^{-2}) measured under optimized conditions for Pt.[111] Furthermore, the stability of Ade_80 was determined by chronoamperometric measurements, resulting in a low current drop of 8.5 % after 12h. The initial stability was

even better, and the final current drop very similar when compared to Pt/C with the high loading of 60 μg_{Pt} cm^{-2} which showed 7.8 % of the initial current value after 12h.[XII]
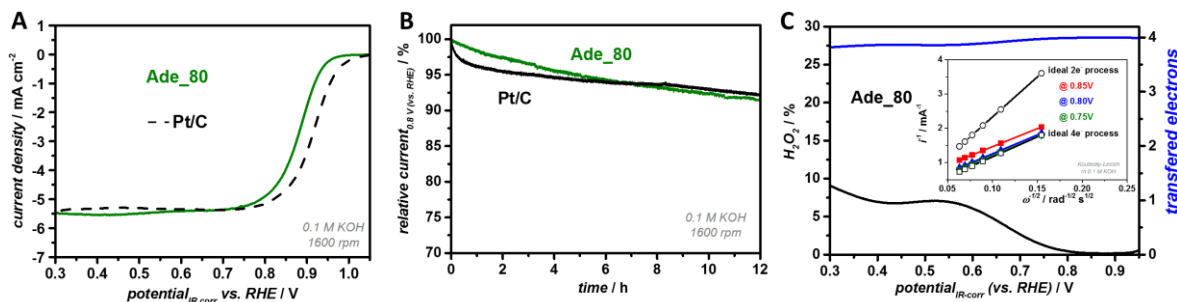
Figure 3.25 A) RDE polarization curves of Ade_80 and of Pt/C (Pt-loading = 60 μg cm^{-2}) in O$_2$-saturated 0.1 M KOH with a sweep rate of 5 mV s^{-1}, 1600 rpm. B) Chronoamperometric measurements at 0.8 V (vs. RHE) of Ade_80 and the commercial Pt/C catalyst in O$_2$-saturated 0.1 M KOH with rotating rate of 1600 rpm. C) Number of transferred electrons and hydrogen peroxide yield of Ade_80 obtained by RRDE-measurements in O$_2$-saturated 0.1 M KOH with a sweep rate of 5 mV s^{-1}, 1600 rpm. The inset shows the Koutecky-Levich-plots at different potentials derived from RDE-measurements with different rotating rates confirming the high selectivity towards the 4 electron process.

Additional RRDE measurements, as a directly experimental proof compared to KL-analysis, reveal a high selectivity towards the aimed four electron process delivering a very low hydrogen peroxide (H$_2$O$_2$) yield of smaller than 0.5 % at a potential of 0.8 V (vs. RHE). The selectivity was confirmed by KL-studies at different potentials, calculated from the polarization curves at different rotation rates.

One drawback of NDCs and noble-metal free ORR-catalysts in general is the large activity decrease when switching from alkaline to acidic medium. Although the research interest in alkaline fuel cells is a growing field, the main industrial applications are still concentrating on the acidic medium. Hence, the design of active and stable noble metal-free catalysts under acidic conditions is of high importance. One of the main issues restricting the targeted design of a catalyst for acidic applications is the missing knowledge about the exact mechanism of the ORR. Actually, the ORR-mechanism in both mediums (alkaline and acidic) is still widely debated. To tackle the missing understanding, a new approach to gain more insights into the ORR-mechanism, the so called "hydrogen peroxide crossover test", will be introduced and discussed in chapter 4.

[XII] In literature, stability measurements of Pt/C are often carried out with Ag/AgCl reference electrodes that slowly poison the Pt/C catalyst, leading to lower stabilities. The stability tests herein were conducted with a salt bridge separating the electrolyte and the Ag/AgCl$_{sat}$ reference electrodes.
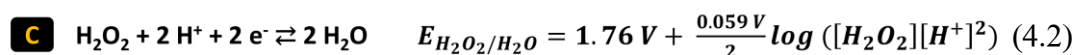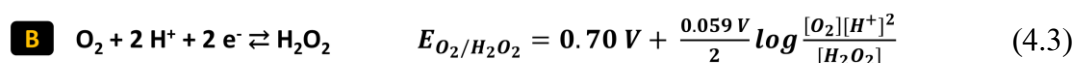
4 Hydrogen Peroxide Crossover Test

4.1 Background and State-of-the-Art

In the last decade, metal and noble metal free catalysts have been developed that show greatly improved activity towards the ORR.[171,172] In particular, iron containing NDCs (Fe-NDCs) show the possibility of replacing Pt as the cathodic catalyst in the acidic medium of proton exchange membrane fuel cells (PEMFCs).[96,173] Different approaches how to synthesize Fe-NDC materials will be discussed in more detail in chapter 5 (section 5.3.2). The present chapter is focused on the ORR-mechanism, the unraveling of which is still proving to be a major challenge. The reaction scheme of the ORR is rather complicated due to the involvement of several elementary steps and different possible reaction intermediates.[174] Moreover, the catalytic pathways are most likely pH-dependent. In the following, the presented reactions will mainly concentrate on the acidic conditions representing the current commercial standard. Furthermore, the focus is put on Fe-NDCs due to their promising activity in acidic conditions.

The most commonly used (simplified) reaction scheme is the one developed by Wroblawa *et al.* which consists of two pathways, A) the "four electron" or "direct" pathway (herein abbreviated as *4e*) and B) the "two plus two electron" or "series" pathway (*2e+2e*).[175] During the *4e,* (adsorbed) oxygen is directly reduced to water without the formation of detectable intermediates as presented in Equation (4.1). The respective standard potential ($E^{\circ}_{O_2/H_2O}$) of 1.23 V represents the theoretical onset potential of the ORR. The *2e+2e* first leads to the formation of H_2O_2 ($E^{\circ}_{O_2/H_2O_2} = 0.70$ V) which is electrochemically directly further reduced to water driven by the large standard potential of the corresponding reaction ($E^{\circ}_{H_2O_2/H_2O} = 1.76$ V), as presented in Equation (4.3) and (4.2). Hence, both pathways, *4e* and *2e+2e*, result in 4 transferred electrons overall per oxygen molecule. However, the H_2O_2 formed can also diffuse into the bulk solution, resulting in a "pure" two electron process (*2e*), or can disproportionate in a non-electrochemical reaction forming oxygen and water. The oxygen formed in the latter case could be reduced again to H_2O_2 as well leading overall to four transferred electrons per oxygen. This "false series" pathway, involving the first step of the *2e+2e* and the disproportionation of H_2O_2, will be discussed as *2e+DP*. The challenge lies in the instability/high reactivity of the possibly formed H_2O_2 close to the catalyst surface preventing its detection at the ring in an RRDE set-up, as described in section 1.3.2. The different reactions are summarized in Figure 4.1

and show the complexity of the system. It has to be mentioned that the real mechanism is, of course, more complex, e.g., the exact position of the adsorbed intermediates leading to the dissociative or the associative mechanism or the involvement of radical/superoxide species.[174] Furthermore, the actual structure of the active site (mainly discussed as a Fe-N site), which adsorbs the oxygen or the reaction intermediates, is strongly debated but beyond the scope of the present chapter.[176-179]

$$A \quad O_2 + 4\,H^+ + 4\,e^- \rightleftarrows 2\,H_2O \qquad E_{O_2/H_2O} = 1.23\,V + \frac{0.059\,V}{4}log\big([O_2][H^+]^4\big) \qquad (4.1)$$

$$B \quad O_2 + 2\,H^+ + 2\,e^- \rightleftarrows H_2O_2 \qquad E_{O_2/H_2O_2} = 0.70\,V + \frac{0.059\,V}{2}log\frac{[O_2][H^+]^2}{[H_2O_2]} \qquad (4.3)$$

$$C \quad H_2O_2 + 2\,H^+ + 2\,e^- \rightleftarrows 2\,H_2O \qquad E_{H_2O_2/H_2O} = 1.76\,V + \frac{0.059\,V}{2}log\big([H_2O_2][H^+]^2\big) \qquad (4.2)$$
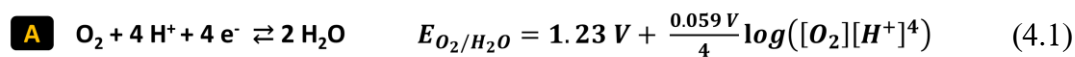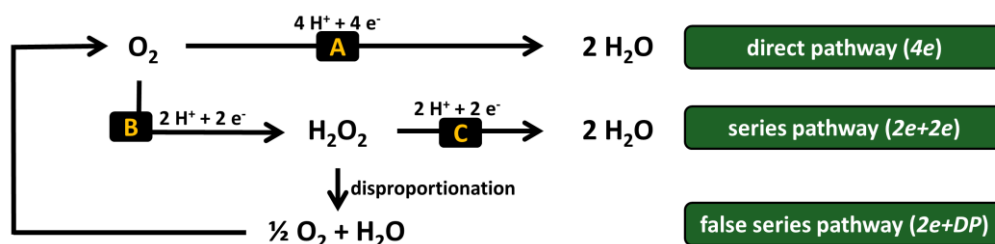
Figure 4.1 Schematic illustration of the different ORR pathways and of the therein occurring reactions. Additionally, the corresponding Nernst equations are shown (for T = 25 °C).[XIII]

The three main pathways presented (*4e, 2e+2e, 2e+DP*) can all result in four transferred electrons per oxygen molecule. Thus, KL-analysis and also RRDE measurements cannot be (directly) used to differentiate between them. Nonetheless, the unraveling of the pathway is very important because H_2O_2 can strongly decrease the PEMFC performance.[89] Additionally, more knowledge about the ORR mechanism could help to understand (and minimize) the typically observed strong decrease in activity when changing from alkaline to acidic conditions.[95,167,180]

In the context of mechanistic discussions, it needs to be considered that the catalyst loading can influence the electron transfer number determined by RRDE measurements, like studied by Bonakdarpour *et al.*[89] For their Fe-NDC catalyst, the amount of H_2O_2 detected strongly increased with lower loadings. It was concluded that the catalyst reduces O_2 mainly *via 2e+2e* and that higher loadings (ergo thicker catalyst layers) hinder the diffusion of the formed H_2O_2 into the bulk solution. Thus, the interaction time between catalyst and H_2O_2 is prolonged enhancing the successive reactions (electrochemical reduction and/or the disproportionation) leading to the observed *4e* during the RRDE

[XIII] Concentrations are identified by box brackets, e.g., [O_2] stands for the concentration of O_2.
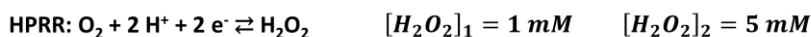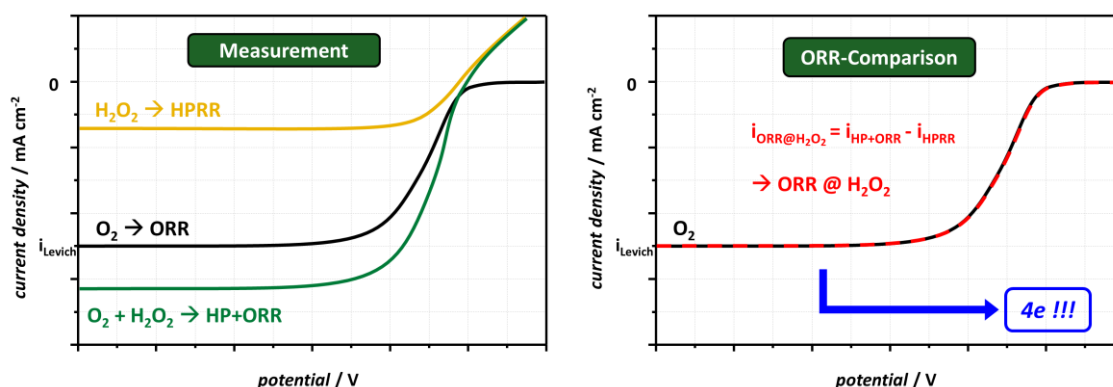
measurement. However, from a practical point of view, the preparation of homogenous catalyst layers with very low loadings is rather difficult and the investigations of multiple loadings is time consuming. Moreover, in a later study, Jaouen *et al.* presented a Fe-NDC catalyst for which the detectable H_2O_2 amount (in a RRDE set-up) was hardly influenced by the loading.[181]

Another approach, which can overcome the detection of intermediately formed H_2O_2, is the separate investigation of the catalytic activity towards the ORR and towards the hydrogen peroxide reduction reaction (HPRR). The subsequent comparison of the ORR and the HPRR activity allows conclusions towards the pathway present, as already shown in literature.[174,181,182] However, the results are contradicting which could be either caused by the different catalysts studied or by the rather complex and thereby error-prone analysis method.[181,182] Nevertheless, the comparison between the acidic and alkaline HPRR conducted by Ramaswamy *et al.* is highly interesting. In alkaline media, the HPRR of the investigated Fe-NDC shows a very high onset (1.01 V vs. RHE) which clearly is more positive than the acidic HPRR value (0.80 V vs. RHE), and even 60 mV positively shifted in comparison to the alkaline ORR onset. Thus, any formed H_2O_2 during alkaline ORR could be immediately further reduced to water pointing to the *2e+2e*. Moreover, this indicates that the superior performance of (Fe-)NDCs in alkaline conditions compared to acidic media could be caused by the kinetically favored alkaline HPRR which shifts the ORR to higher potentials.

It should also be mentioned that RRDE measurements are a powerful and comparably straight forward tool for kinetic studies allowing statements regarding the preferred mechanism.[183] Nonetheless, the theoretical model used is rather complex and the inherent assumptions require optimal conditions (e.g., layer thickness) and precisely reproducible results which are rather difficult to achieve for the typically used dropcasted RDE/RRDE electrode layers. Hence, a facile approach to study the ORR mechanism, that can be implemented by materials chemists, is very interesting.

The idea herein is to first study the ORR activity in an O_2-saturated electrolyte and the HPRR in a (N_2-saturated) H_2O_2 containing electrolyte solution, similar to the literature studies.[182,184] The next step is to investigate the ORR activity in an O_2-saturated electrolyte in the presence of H_2O_2 (HP+ORR). This test allows the direct investigation of the influence of H_2O_2 (in the bulk) on the occurring reactions on the catalyst surface. Thus, the approach will be called herein hydrogen peroxide crossover test. In case of the *2e+2e* and

of the *2e+DP*, the potential of the overall reaction should be mainly determined by the potential of the initial reaction, e.g., the reduction of O_2 to H_2O_2 due to its relatively low standard potential of $E^{\circ}_{O_2/H_2O_2} = 0.70$ V. The presence of H_2O_2 should influence this initial step negatively, according to the Le Châtelier's principle (Equation (4.3)).[12] Moreover, the employment of different H_2O_2 concentrations (e.g, 1 mM and 5 mM) allows a mathematical prediction of the potential shift using the Nernst equation as presented in Equation (4.4). Contrarily, the *4e* should be independent on the amount of H_2O_2. Thus, it should be possible to easily differentiate between the *4e* and mechanisms intermediately forming H_2O_2. Figure 4.2 shows the principle of the H_2O_2 crossover test and the theoretically expected curves for a *4e*.

Shift of HPRR in Dependence of the Present Amount of H_2O_2

HPRR: $O_2 + 2\,H^+ + 2\,e^- \rightleftarrows H_2O_2$ $[H_2O_2]_1 = 1\,mM$ $[H_2O_2]_2 = 5\,mM$

$$\Delta E_{O_2/H_2O_2} = E_2 - E_1 = \left(0.70\,V + \frac{0.059\,V}{2}log\frac{[O_2][H^+]^2}{[H_2O_2]_2}\right) - \left(0.70\,V + \frac{0.059\,V}{2}log\frac{[O_2][H^+]^2}{[H_2O_2]_1}\right)$$

$$\Delta E_{O_2/H_2O_2} = \frac{0.059\,V}{2}log\frac{[H_2O_2]_1}{[H_2O_2]_2} = \frac{0.059\,V}{2}log\frac{5\,mmol\,l^{-1}}{1\,mmol\,l^{-1}} = 21\,mV \tag{4.4}$$

Figure 4.2 Schematic illustration of the different curves obtained during the H_2O_2 crossover test and the comparison of the measured ORR and the calculated ORR in the presence of H_2O_2. The results depict the behavior expected for a *4e*. Additionally, the calculation, according to the Nernst equation, of the potential shift of the HPRR, when increasing the H_2O_2 concentration from 1 mM to 5 mM, is presented (T = 25 °C).

It can be assumed that the current of the HP+ORR (i_{HP+ORR}) is the superposition of the ORR current, appearing in the presence of H_2O_2 ($i_{ORR@H_2O_2}$), and the HPRR current (i_{HPRR}). The HPPR should not be influenced by the presence of O_2 according to the Nernst equation (Equation (4.2)). Thus, the difference between i_{HP+ORR} and i_{HPR} (determined under N_2 atmosphere) allows for the calculation of $i_{ORR@H_2O_2}$ which can be directly compared to the ORR current (i_{ORR}). If i_{ORR} and $i_{ORR@H_2O_2}$ are superimposed, H_2O_2 does not influence the ORR mechanism pointing to the favored *4e*. The H_2O_2 crossover test was developed in a

collaboration with the Gasteiger group at the Technical University of Munich (TUM) where also some of the measurements were conducted.[XIV]

In section 4.2, the different catalysts used for the H_2O_2 crossover test and their ORR performances will be presented. Section 4.3 concentrates on the results in acidic media that indicate that H_2O_2 influences the ORR activity of the commercial Pt/C catalyst as well as the activity of the studied Fe-NDCs. However, the strong effect in the latter case is mainly caused by instability of the Fe-NDCs catalysts towards H_2O_2. Nonetheless, the results point towards a *2e+2e* in acidic media for all of the catalysts. Section 4.4 will discuss the alkaline H_2O_2 crossover test. Intriguingly, the herein synthesized ionothermal Fe-NDC is highly stable vs. H_2O_2 in alkaline conditions and shows a HPRR activity which clearly differs from the one previously obtained by Ramaswamy *et al.*[182] The findings indicate a clear *4e* for the ionothermal Fe-NDC.

4.2   Studied Catalysts

Three different catalysts were selected to study the H_2O_2 crossover test: A) the commercial Pt/C as reference material, B) a Fe-NDC material prepared at the TUM in a very similar procedure as the high performing catalyst presented by Lefèvre *et al.* (abbreviated as Fe-NDC_lit), and C) a Fe-NDC prepared by the ionothermal approach using GuaHCl as precursor (Fe-NDC_GuaHCl).[96]

The GuaHCl derived catalyst was synthesized with a $NaCl/ZnCl_2$ (42 mol%) salt mixture in a precursor to salt wt.-ratio of 1:10, according to the method presented in section 3.2.2. To achieve an additional iron doping, 2.2 wt.% of iron(III) chloride (in respect to GuaHCl) was added in the initial salt mixture. The general sample preparation and the heat treatment were conducted as described for the nucleobase derived samples in section 3.2.2. The final catalyst was analyzed by inductively coupled plasma optical emission spectrometry (ICP-OES) revealing an Fe-content of 2.1 wt.%. The Fe-NDC_GuaHCl was analyzed by N_2-physisorption, PXRD, SEM and TEM showing very similar results as the non-doped catalyst (Figure S24). Thus, the additional presence of the iron salt does not seem to influence the porogenesis during the ionothermal synthesis. The iron of the X-ray amorphous Fe-NDC_GuaHCl is located in $Fe-N_4$ sites (with a relative

---

[XIV] The results may be presented in a different context in the thesis of Thomas Mittermeier (TUM).

abundance of 18 %) and in amorphous iron oxide nanoparticles as indicated by Mößbauer measurements (Figure S25).[XV]

    Figure 4.3A shows the anodic branch of the CVs (corrected for the capacitive currents, 10 mV s^{-1}) at 1600 rpm for the two Fe-NDCs in 0.05 M sulfuric acid (H$_2$SO$_4$) and for Pt/C in 0.1 M perchloric acid (HClO$_4$).[XVI] Due to the aforementioned influence of the thickness of the catalyst layer, low loadings of 100 μg cm^{-2} were used for Pt/C and Fe-NDC_GuaHCl. However, a loading of 300 μg cm^{-2} was necessary for Fe-NDC_lit to ensure a sufficient activity. The activity in acidic conditions (according to E$_{1/2}$) can be ranked as Pt/C ≫ Fe-NDC_GuaHCl > Fe-NDC_lit (high loading) ≫ Fe-NDC_lit (low loading). The basic medium is especially interesting for non-noble metal catalysts due to their particularly high alkaline activity. Thus, all alkaline studies focus on the Fe-NDC materials. Both catalysts delivered sufficient performance at the low loading of 100 μg cm^{-2} and the E$_{1/2}$ follow the order of Fe-NDC_GuaHCl > Fe-NDC_lit (Figure 4.3B). Moreover, all catalysts, independent of the electrolyte, show limiting currents in the range of the experimental error for the Levich current of a four electron process of 6.0 mA cm^{-2}, 5.6 mA cm^{-2} and 5.7 mA cm^{-2} for 0.05 M H$_2$SO$_4$, 0.1 M HClO$_4$ and 0.1 M KOH, respectively.[111]
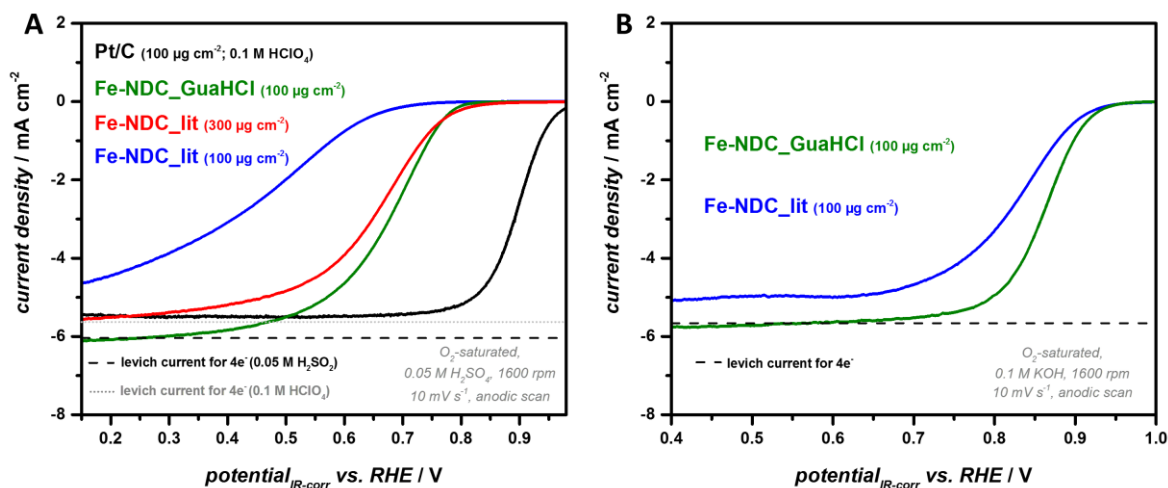
Figure 4.3 ORR performance (1600 rpm, anodic scan, 10 mV s^{-1}) of the different catalysts in A) acidic conditions and B) alkaline conditions.

Interestingly, the ionothermal Fe-NDC synthesized in this work reaches a slightly enhanced activity, at only 33 % of the loadings, as the high performing literature catalyst

---

(Fe-NDC_lit) in acidic conditions and a clearly improved activity, at the same loading, in alkaline conditions. Hence, GuaHCl derived Fe-NDCs, showing promising activities in acidic electrolyte, can be synthesized by simply adding an iron salt to the initial precursor/salt mixture, which is in line with IL-derived Fe-NDCs in literature, and indicates the general feasibility to obtain Fe-NDCs *via* the ionothermal approach.[95]

4.3 Hydrogen Peroxide Crossover Test in Acidic Media

The performances of the three catalysts with respect to the different reactions were studied at different rotation rates by means of CV measurements ($10\ mV\ s^{-1}$) according to the following order: i) ORR, ii) HPRR ($\sim 1\ mM\ H_2O_2$), iii) HP+ORR ($\sim 1\ mM\ H_2O_2$), iv) HPRR ($\sim 5\ mM\ H_2O_2$), and v) HP+ORR ($\sim 5\ mM\ H_2O_2$).[XVII] All of the depicted curves represent the anodic scan at 1600 rpm and are corrected for the capacitive current measured in N_2-saturated electrolyte. Moreover, the ORR performance in presence of the H_2O_2 was obtained by subtracting the HPRR curve from the HP+ORR curve. The Pt/C catalysts and the Fe-NDCs were investigated in $0.1\ M\ HClO_4$ and $0.05\ M\ H_2SO_4$, respectively.
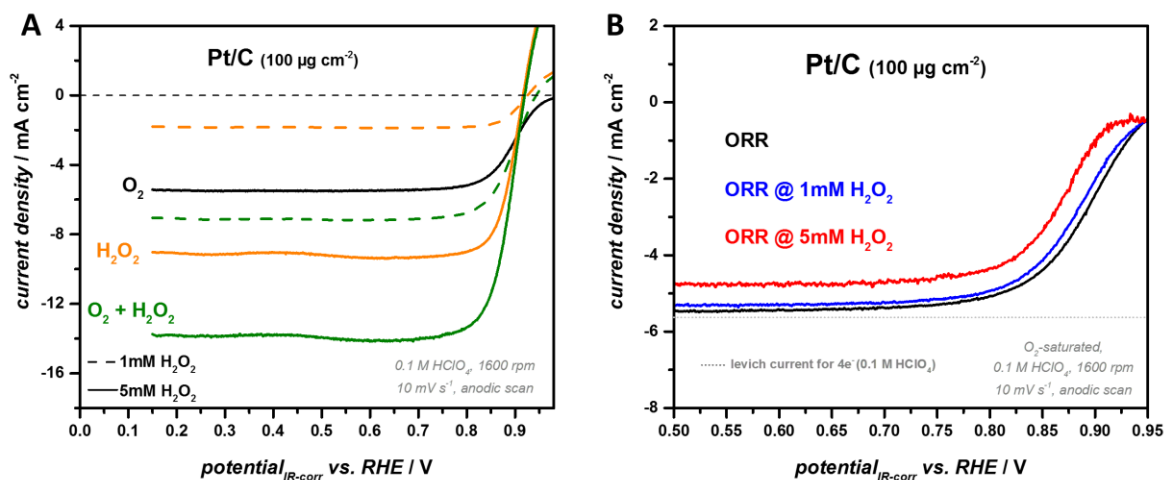
Figure 4.4 A) ORR, HPRR and HP+ORR of the Pt/C catalyst in acidic media (1600 rpm, anodic scan, $10\ mV\ s^{-1}$). B) Comparison of the measured ORR performance of Pt/C and the calculated ORR curves in presence of H_2O_2 (H_2O_2 crossover test).

Figure 4.4A shows the performance of the Pt/C catalyst towards the different reactions. The HPRR reaches diffusion limitation approaching the theoretical limiting currents of $2.3\ mA\ cm^{-2}$ and $11.4\ mA\ cm^{-2}$, for a H_2O_2 concentration of 1 mM and 5 mM, respectively.

[XVII] H_2O_2 is thermodynamically instable for $[H_2O_2] > 0.87 \cdot 10^{-18}\ mol\ l^{-1}$ and will slowly disproportionate. Thus, the exact concentrations could be slightly lower than the stated ones.[174]

This shows the high HPRR activity of Pt/C. Moreover, at high potentials (> 0.92 V vs. RHE) Pt/C is very active towards the oxidation of H_2O_2. Hence, any intermediately formed H_2O_2 from the ORR would be immediately further reduced to H_2O or oxidized to O_2. These results are in line with the literature and indicate that disproportionation of H_2O_2 plays only a minor role for the Pt/C catalyst.[174] Interestingly, the calculation of the H_2O_2 dependent ORR curves reveals a clear shift of the $E_{1/2}$ to lower potentials as expected for a mechanism intermediately forming H_2O_2 (Figure 4.4B). The increase of the H_2O_2 concentration from 1 mM to 5 mM causes a ORR potential shift of -15 mV which is close to the theoretical value of -21 mV. Moreover, the slopes of the ORR curves (measured and calculated) are very similar indicating that the general ORR mechanism does not change in the presence of H_2O_2. Thus, it can be concluded that the Pt/C reduces (at least partially) O_2 according to the *2e+2e*.[XVIII] However, no H_2O_2 is released into the bulk electrolyte due to the high HPRR activity, which is in line with the classical literature predicting a *4e* at potentials higher than 0.3 V (vs. RHE).[186]

The H_2O_2 crossover test of the Fe-NDC_lit is depicted in Figure 4.5A. The HPRR activity is relatively poor and remains under kinetic control in the applied potential range showing a clearly reduced activity compared to the Pt/C catalyst. However, the onsets of the HPRR and the ORR for Fe-NDC_lit overlap indicating similar initial steps for both reactions. The presence of 1 mM H_2O_2 strongly influences the ORR leading to a cathodic shift of the mixed kinetic-diffusion controlled region of the HP+ORR (0.55 V > E > 0.75 V) which is even more negative than the ORR curve. The discussed potential region is further negatively shifted for the HP+ORR curve in the presence of 5 mM H_2O_2, although the HPRR currents are generally larger for the higher concentration. The strong influence of H_2O_2 on the ORR is clearly depicted by the calculated ORR curves in Figure 4.5B. However, the H_2O_2 crossover test of non-noble metal catalysts has to be analyzed with care due to the known instability of those materials towards H_2O_2 and oxidative conditions.[180,187,188] Thus, an additional step was introduced to analyze the degradation during the H_2O_2 crossover test. After conducting the whole test, the catalyst layer was cleaned by rotating in the respective electrolyte to remove H_2O_2 and the ORR activity was measured again in a new electrolyte solution. The resulting ORR curves are also depicted in Figure 4.5 and identified by the suffix "after testing". The literature catalyst reveals a strongly reduced ORR activity after the H_2O_2 crossover test with a $\Delta E_{1/2}$ of ~ 47 mV (Figure 4.5). Moreover, the ORR curve after testing is slightly negatively

---

[XVIII] To ensure the validity of the results, the ORR-activity of the Pt/C catalyst after the H_2O_2 crossover test should be investigated in the future and compared to the initial ORR-activity.

shifted when compared to the ORR curve in 1 mM H_2O_2 pointing to a stronger degradation for higher H_2O_2 concentration.[XIX] The results indicate the non-comparability of the curves obtained with different H_2O_2 concentrations due to the unknown effect of the concurrent degradation.
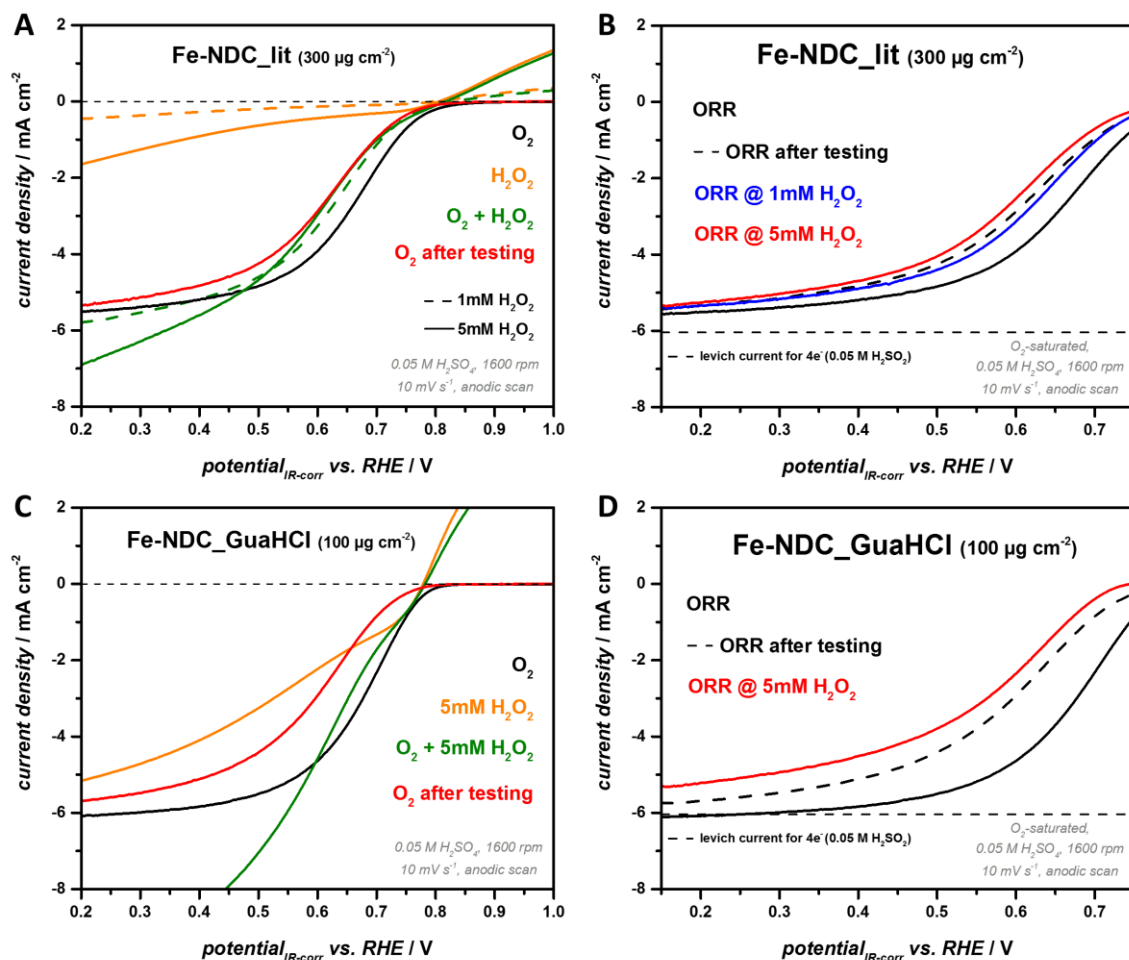
Figure 4.5 A+C) ORR, HPRR and HP+ORR of the Fe-NDC catalysts in acidic media (1600 rpm, anodic scan, 10 mV s⁻¹). B+D) Comparison of the measured ORR performance of the Fe-NDCs and the calculated ORR curves in presence of H_2O_2 (H_2O_2 crossover test). Additionally, the ORR performance after the H_2O_2 crossover test is depicted for the respective catalyst.

Nonetheless, the ORR in presence of 5 mM H_2O_2 can be compared to the ORR after testing revealing a negatively shifted activity ($\Delta E_{1/2} \sim 18$ mV) of the former. This indicates that the Fe-NDC_lit catalyst (or at least the active sites which are stable in 5 mM H_2O_2) partially reduces the O_2 *via 2e+2e* or *2e+DP*. However, the shift is smaller than the difference in $E_{1/2}$ of the ORR and the ORR in the presence of 5 mM H_2O_2 for the Pt/C catalyst ($\Delta E_{1/2} \sim 23$ mV) indicating that the Fe-NDC can also reduce O_2 according to *4e*.

[XIX] Additional tests were conducted to minimize the degradation. However, the catalyst showed also a strong degradation after conducting the H_2O_2 crossover test in 1 mM H_2O_2. Moreover, different acidic electrolytes were used (0.1 M HClO₄, 0.1 M HCl) but the degradation was always observed (results not shown).

Interestingly, the limiting currents of the different ORR curves are close to the theoretical value for the four electron process pointing (also for the degraded catalyst) to a minor occurrence of the *2e*.

The H_2O_2 peroxide crossover test was also conducted with the ionothermal Fe-NDC (Fe-NDC_GuaHCl) showing a behavior very similar to the Fe-NDC_lit (Figure 4.5C+D).[XX] Both catalysts give a value of ~ 18 mV for the $E_{1/2}$ shift of the ORR curve after testing and the ORR curve in the presence of 5 mM H_2O_2 pointing to very similar ORR mechanisms (at least at the stable active sites). The biggest difference is the generally enhanced, however, still kinetically controlled, HPRR activity of the ionothermal Fe-NDC when compared to the literature catalyst. The enhanced HPRR activity of the former, when coupled with a *2e+2e* mechanism, can also explain the initially higher ORR activity of the ionothermal Fe-NDC. However, the more active catalyst degrades more ($\Delta E_{1/2}$ of ~ 74 mV vs. ~ 47 mV) indicating the general problem that a higher activity is very often coupled with a lower stability. The exact differentiation between the *2e+2e* and the 2e+DP should be addressed in more detail in the future (e.g., by determination of the H_2O_2 disproportionation constant). This is, nonetheless, rather difficult with the two Fe-NDCs investigated due to the degradation in the presence of H_2O_2. However, the developed H_2O_2 crossover test could be used to identify a Fe-NDC material which is stable towards H_2O_2 allowing a more detailed mechanism study, and would be a valuable standard tool in eletrocatalyst characterization. The results in acidic conditions are very interesting and H_2O_2 crossover test will be expanded to the alkaline media in the following section 4.4.

4.4 Hydrogen Peroxide Crossover Test in Alkaline Media

The H_2O_2 crossover test in alkaline media was conducted with the Fe-NDCs using the same protocol (including the analysis of the ORR activity after conducting the H_2O_2 crossover test) presented in section 4.4. The ORR curves as well as the HPRR and HP+ORR curves obtained in the presence of 5 mM H_2O_2 at 1600 rpm are summarized in Figure 4.6. For the sake of completeness, it is necessary to mention that the dominant species of hydrogen peroxide in alkaline media is actually HO_2^- according to the first acid dissociation constant of H_2O_2 ($pk_{s1} = 11.6$).[189] The feasibility of the H_2O_2 crossover test is independent of which H_2O_2 species is present, and, for simplification, the term H_2O_2 will be also used for alkaline conditions.

[XX] The curves for 1 mM H_2O_2 are not shown due to the non-evaluated degradation of the catalyst in 1 mM H_2O_2.
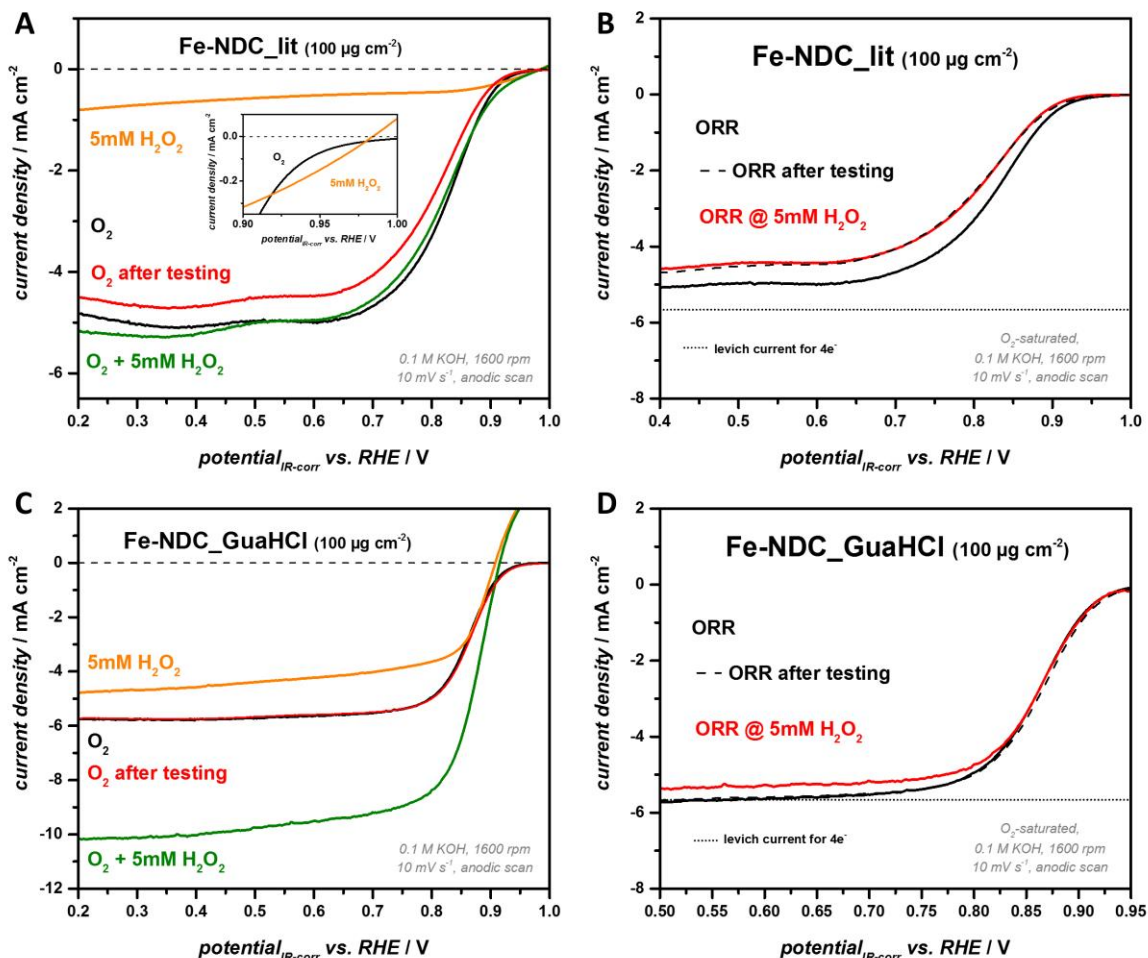
Figure 4.6 A+C) ORR, HPRR and HP+ORR of the Fe-NDC catalysts in alkaline media (1600 rpm, anodic scan, 10 mV s^{-1}). The inset in A) shows the mixed kinetic-diffusion controlled region of the HPRR. B+D) Comparison of the measured ORR performance of the Fe-NDCs and the calculated ORR curves in presence of H$_2$O$_2$ (H$_2$O$_2$ crossover test). Additionally, the ORR performance after the H$_2$O$_2$ crossover test is depicted for the respective catalyst.

The Fe-NDC_lit shows a strongly enhanced alkaline HPRR when compared to the acidic media regarding onset and the reached current densities ($E_{onset,acidic}$ = 0.79 V vs. $E_{onset,alkaline}$ = 0.96 V). In alkaline media, the mixed kinetic-diffusion limited range of the HPRR (0.92 V > E > 0.97 V vs. RHE) is even cathodically shifted in respect to the corresponding ORR curve in the same potential region, which is in line with the results of Ramaswamy *et al.* (inset Figure 4.6A).[182] Hence, it could be assumed that the Fe-NDC_lit can reduce any intermediately formed H$_2$O$_2$ to water pointing to the *2e+2e*. The Fe-NDC_lit catalyst is relatively stable towards H$_2$O$_2$ in the alkaline electrolyte showing a small $\Delta E_{1/2}$ of ~ 14 mV for the ORR curves before and after the test protocol (Figure 4.6B). The value is clearly improved compared to the strong shift in $E_{1/2}$ of ~ 47 mV obtained in acidic media. The most interesting fact is the almost perfect overlap of the ORR curve measured after the testing and the one calculated in the presence of 5 mM H$_2$O$_2$

(Figure 4.6B). Thus, the ORR of the Fe-NDC_lit does not involve H_2O_2 as an intermediate in alkaline media and the ORR-mechanism can be regarded a *4e*. Nonetheless, due to the occurring degradation, the statement is only valid for the stable active sites.

The HPRR currents reached at low potentials for Fe-NDC_GuaHCl are clearly improved but the HPRR onset is negatively shifted when compared to the values for Fe-NDC_lit (Figure 4.6C). The alkaline HPRR onset (E_{onset} = 0.91 V) of the ionothermal Fe-NDC is even more negative than the respective ORR onset (E_{onset} = 0.95 V). These results strongly contradict the results for the Fe-NDC_lit catalyst as well as the literature data for Fe-NDCs in alkaline conditions.[182] Moreover, the ionothermal Fe-NDC is highly stable towards H_2O_2 showing no degradation after the test protocol (Figure 4.6D). As seen for Fe-NDC_lit, the calculated ORR curve in the presence of 5 mM H_2O_2 perfectly overlaps (except a slightly lower limiting current) with the measured ORR curve in the absence of H_2O_2. This result is highly interesting and shows that the ionothermal catalyst reduces O_2 *via* (the favored) *4e* in alkaline media. Speculatively, the sites active towards the ORR do not adsorb H_2O_2 thus being stable against H_2O_2-induced degradation. Generally, the results indicate that Fe-NDCs are rather stable against peroxide species in alkaline conditions but are strongly degraded by intermediately formed H_2O_2 in acidic conditions. These findings should be further investigated in the future, especially, regarding a possible influence of the dissociation state of the peroxide species, i.e., H_2O_2 or HO_2^-, on the stability.

The results of the H_2O_2 crossover test in alkaline media are highly intriguing showing that both Fe-NDC catalysts reduce oxygen *via* the *4e*. The conclusion that H_2O_2 is not intermediately formed is supported by the fact that both Fe-NDCs show similar ORR onset potentials (~ 0.95 V) but very different HPRR activities. Furthermore, the reason for the generally higher alkaline activity compared to acidic activity of Fe-NDCs cannot generally be connected to the improved HPRR activity as stated by Ramaswamy *et al.*[182] An alternative explanation could be that the first electron transfer is an outer sphere process creating an $O_2^{\bullet-}$ species which is then adsorbed on the catalyst's surface.[190,191] Contrary to the ORR, the outer sphere electron transfer mechanism is pH-independent and its potential is strongly shifted in the anodic direction for higher pH values.[192] Thus, the overall reaction can be shifted towards more anodic potentials at higher pHs as shown in the modified Pourbaix diagram (Figure S26).

Figure 4.7. depicts the overall results of the investigated catalysts (in alkaline and acidic conditions), by means of $E_{1/2}$ values of the measured and calculated ORR curves, as well as

the conclusions. The test reveals that all investigated catalysts (also Pt/C) form intermediately H_2O_2 under acidic conditions pointing to the (partially) presence of the *2e+2e*. Contrarily, both Fe-NDCs catalyze the ORR according to *4e* in alkaline media. Generally, the herein developed H_2O_2 crossover test is as a quick method to analyze if H_2O_2 is formed as an intermediate or not. Moreover, the procedure could be understood as a fast degradation test for Fe-NDCs. Generally, the occurring degradation points to the great importance of analyzing the ORR activity after testing HPRR activities to avoid false inferences.
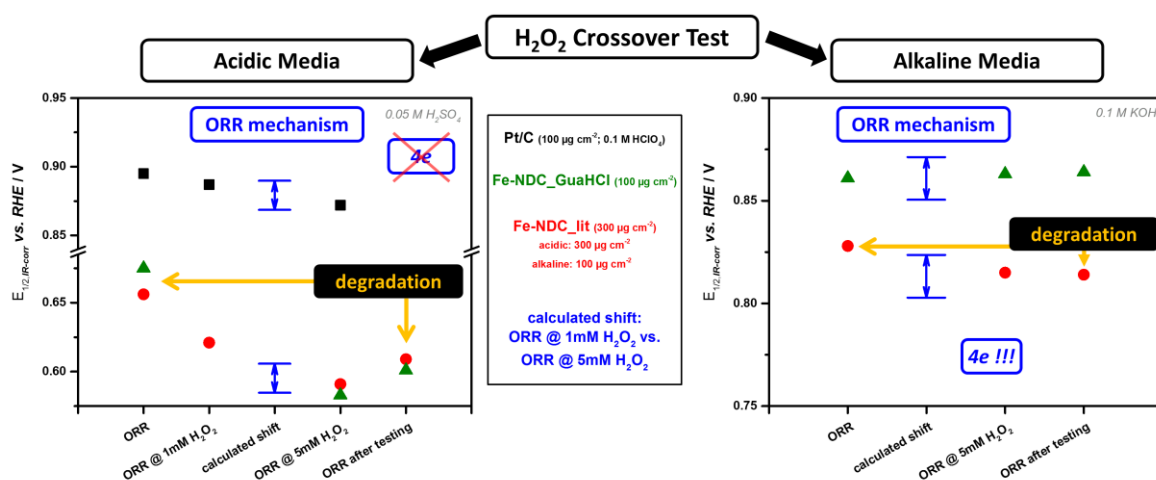
Figure 4.7 Halfwave potentials of the different catalysts (acidic and alkaline media) obtained from the measured ORR and the calculated ORR curves in presence of H_2O_2. The results can be used to analyze the catalyst degradation and the occurring ORR mechanism.

The results presented in this section revealed not only different ORR activities, but also different ORR mechanisms, when comparing the acidic and alkaline media (Figure 4.7). One drawback of the studied ionothermal catalyst, hindering conclusions regarding the active site, is the variety of present functional sites, i.e., different N-sites, Fe-N sites, nanoparticular iron oxide, and maybe even non-detectable elemental iron. The presence of multiple iron species is a general limitation in today's catalyst syntheses and can be connected to the typically used synthesis methods for Fe-NDCs involving a high temperature treatment, in which all elements (Fe, N, C) are present, which gives rise to unwanted reactions, e.g., the carbothermal reduction of iron. The following Chapter 5 will address this issue, firstly, by extending the ionothermal synthesis of NDCs to (ZnCl$_2$-free) salt hydrates, and secondly, by investigating the possibility of introducing active Fe-N sites in the obtained highly porous NDC by a facile, low-temperature metalation approach.

5 Extended Ionothermal Synthesis

5.1 Background and State-of-the-Art

The in chapter 3 discussed sol-gel type ionothermal carbonization with molecular carbon precursors and high salt volume fractions can be regarded as a dispersion of the solidifying carbonizing phase in the liquid salt phase. A special case represents the dispersion of vast liquid salt amounts inside the solidifying carbonizing phase as observed for the adenine derived pore tailored NDCs that may be compared as a high internal salt phase ionothermal carbonization. Typically, the dispersions were desired to be homogeneous throughout the carbonization process. As described earlier the carbonization of nucleobases is exceptional as the carbonizing phase intermediately forms a dense solid and subsequent liquefication generates homogeneous dispersions at higher temperatures (cf. section 3.2.2). This does not only shine light on the potential to obtain homogeneous carbons with high porosity from complex biomass by intermediate biomass liquefication, but also brings up the question if intermediate solid phases cannot be used to introduce certain morphologies and thereby extend ionothermal carbonization by another mechanistic structuration pathway. What if the dispersing salt phase would undergo intermediate solidification/crystallization throughout the carbonization process?

In fact, a number of salts show melting points only above the onset of pyrolysis, however have hydrated forms that melt at lower temperatures, below pyrolysis conditions. Throughout thermal treatment, the dehydration of the molten salt hydrate can lead to intermediate crystallization followed by another melting process. Calcium and magnesium chloride show melting points of 772 °C and 708 °C, respectively.[12] Calcium dihydrate ($CaCl_2 \cdot 2\,H_2O$) melts at 175 °C and can also form the monohydrate by dehydration that has a melting point at 260 °C.[193] Thus, the polymerization/carbonization before pyrolysis could start homogeneously, in a liquid molten salt hydrate. It has to be considered that melting and decomposition (meaning the elimination of crystal water) of salt hydrates are superimposed leading to a complex mechanistic pathway.[194] This could lead to the dynamic formation/depletion of solid salt acting as secondary hard template for the carbonizing phase. A similar situation is expected for magnesium chloride. The hexahydrate ($MgCl_2 \cdot 6\,H_2O$) is a promising precursor due to the low melting point and its ability to melt/decompose in multiple steps.[189] However, the thermal decomposition of $MgCl_2 \cdot 6\,H_2O$ is rather complex. Next to dehydration, it can decompose by elimination of

hydrochloric acid (HCl) resulting in magnesium oxyhydrochloride (Mg(OH)Cl). At higher temperatures, Mg(OH)Cl will decompose to magnesium oxide (MgO). The whole system is further complicated by the fact that MgOHCl can exist in different hydration states. Sugimoto *et al.* studied the thermal decomposition of $MgCl_2 \cdot 6\,H_2O$ in detail using *in-situ* synchrotron powder pattern date recorded in a dry helium gas stream.[195] The thereby obtained different decomposition reactions of $MgCl_2 \cdot 6\,H_2O$ are presented together with the corresponding transition temperature in Equation (5.1) to (5.7).

$$MgCl_2 \cdot 6\,H_2O \rightleftarrows MgCl_2 \cdot 4\,H_2O + 2\,H_2O \qquad T = 96\,°C \qquad (5.1)$$

$$MgCl_2 \cdot 4\,H_2O \rightleftarrows MgCl_2 \cdot 2\,H_2O + 2\,H_2O \qquad T = 107\,°C \qquad (5.2)$$

$$MgCl_2 \cdot 2\,H_2O \rightleftarrows MgCl_2 \cdot H_2O + H_2O \qquad T = 153\,°C \qquad (5.3)$$

$$MgCl_2 \cdot 2\,H_2O \rightleftarrows Mg(OH)Cl \cdot n\,H_2O + HCl + (1-n)\,H_2O \qquad T = 193\,°C \qquad (5.4)$$
$$(0 \leq n \leq 0.3)$$

$$Mg(OH)Cl \cdot 0.3\,H_2O \rightleftarrows Mg(OH)Cl + 0.3\,H_2O \qquad T = 339\,°C \qquad (5.5)$$

$$2\,Mg(OH)Cl \rightleftarrows MgO + MgCl_2 + H_2O \qquad T = 398\,°C \qquad (5.6)$$

$$MgCl_2 + H_2O \rightleftarrows MgO + HCl \qquad T = 441\,°C \qquad (5.7)$$
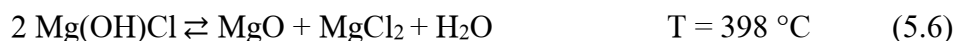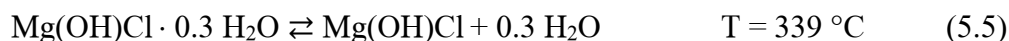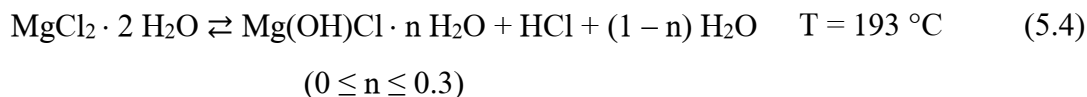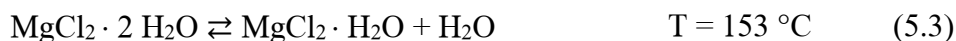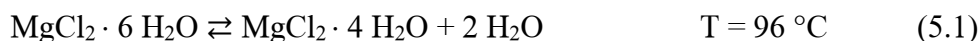
The actual phase transitions/reactions will strongly depend on the chosen reaction conditions, e.g., heating rate and applied gas stream. If water cannot immediately evaporate throughout the dehydration, a hydrate melt will form instead of the occurrence of a solid-solid phase transition. Important in this context is that also crystallization of lower hydrates from liquid phase is to be expected and can strongly modify the ionothermal carbonization mechanism by introducing a secondary templating effect that is the in-situ formation of hard templates.

There are already few reports in literature introducing the use of metal chlorides such as $CaCl_2$ and $MgCl_2$ for biomass activation.[196-201] The use of $CaCl_2$ as mesopore template was shown by Huang *et al.* in 2011.[202] An aqueous $CaCl_2$ solution was used as solvent for the polymerization of a melamine formaldehyde resin. Subsequent drying and heat treatment of the salt containing resin resulted in a nitrogen doped material with incorporated $CaCl_2$ particles showing diameters smaller than 5 nm. Aqueous salt removal gave a micro- and mesoporous nitrogen doped carbon with a SSA of ~ 1300 $m^2\,g^{-1}$. The possibility to obtain hierarchical NDCs with $CaCl_2$ from biomass was shown by Liu *et al.* concurrently to the

present work.[203] Bagasse was impregnated with an aqueous solution of $CaCl_2$ and urea (as nitrogen source) yielding a hierarchical porous NDC material after pyrolysis and work-up.

Although $MgCl_2$ is discussed in context with metal chloride "activation" agents, there are almost no detailed articles about the porosity/morphology obtained.[201,204,205] Valix *et al.* obtained a porous carbon material pyrolizing bagasse at 500 °C which was wet-impregnated with $MgCl_2$.[201] The largest SSA obtained was relatively low only showing a value of 200 $m^2\,g^{-1}$. Mise *et al.* obtained higher SSAs up to 620 m^2 at a pyrolysis temperature of 850 °C using fruit shells as precursors.[205] However, the mentioned literature neither discusses N_2-isotherms (and the corresponding PSDs) nor shows SEM/TEM images.

Currently the role assigned to $CaCl_2$ and $MgCl_2$ is to act as dehydrating agent enhancing the crosslinking reaction of the biomass causing higher yields. The mechanism of the porogenesis, however, is hardly discussed, while the term activating agent suggests leaching of carbon matrix. Thermodynamically carbon etching connected to carbothermal reduction of possibly formed metal oxides requires temperatures higher than 1500 °C clearly exceeding the applied reaction temperatures.[206] The melting points of the single salts are also too high to act as molten solvent/porogen like possible in the case of $ZnCl_2$. However, impregnation of aqueous salt solutions and the thermal dehydration of biomass give rise to quantities of water that allow formation of the respective metal hydrate melts. Hence, the molten state gives the explanation of the successful formation of internal surface area and porosity reported in literature.

In the present chapter it will be investigated if hydrated $CaCl_2$ and $MgCl_2$ may be used as porogens for the synthesis of hierarchical porous NDCs. Adenine will be chosen as small molecular precursor as it showed very promising features in the conventional ionothermal synthesis using $ZnCl_2$ containing salt mixtures (chapter 3.2.2). First, the porosity obtained with anhydrous $CaCl_2$ and $CaCl_2$ dihydrate ($CaCl_2DH$) will be discussed and compared in section 5.2. The experimental results reveal strongly improved yields using $CaCl_2DH$, but giving in both cases a morphology indicative of carbonization on the surface of solid salt particles rather than conventional sol-gel carbonization. Intriguingly, the employment of $CaCl_2DH$ indeed results in a very interesting secondary templating effect. This secondary templating effect is even more pronounced if $MgCl_2$ hexahydrate ($MgCl_2HH$) is used as salt phase leading to highly porous NDCs with very interesting morphology features (section 5.3). The morphology and porosity in dependence of the synthesis temperature

will be analyzed by N_2-physisorption, SEM and TEM. Those results in combination with the salt phase(s) present after the synthesis, as analyzed by PXRD, give further insights on the secondary templating effect. The thermal decomposition of $MgCl_2HH$ leads to multiple phases, complicating the unraveling of the morphology formation. Nevertheless, the materials are highly interesting and show reasonable ORR activities under alkaline conditions (section 5.3.2). Additionally, the possibility to greatly enhance the initially poor acidic ORR performance by simple metalation with iron ions will be presented. The metalation experiments were conducted in a collaboration with Dr. Asad Mehmood (Korea Institute of Science and Technology) and exploit that NDCs can be used as solid ligands for iron ions for the first time in the context of ORR.

5.2   Anhydrous CaCl₂ vs. CaCl₂ Dihydrate: "New" Reaction Mediums for the Synthesis of Adenine Derived Nitrogen Doped Carbons

Different groups already discussed $CaCl_2$ as alternative salt to $ZnCl_2$ for the synthesis of porous carbon materials aiming towards a greener process.[196-199,201] As discussed in section 5.1, the typically used wet-impregnation will lead to the formation of hydrated $CaCl_2$ showing a distinctly different melting point than anhydrous $CaCl_2$. It can be assumed that $CaCl_2DH$, showing a melting point of 260 °C, is the phase present before the pyrolysis treatment at high temperatures.[193] Thus, the carbon formation could take place in a liquid molten salt.

The influence of hydrated and non-hydrated state of $CaCl_2$ on the materials porosity is investigated in the following. Adenine and anhydrous $CaCl_2$ and $CaCl_2DH$, respectively, were mixed by thorough grinding in a 1:10 wt.-ratio in a glove box. The obtained white powder was heated in an inert gas atmosphere with 2.5 K min^{-1} to 900 °C and the final temperature was kept for 1 hour. Residual salt was removed by aqueous washing yielding the nitrogen doped carbon material. The obtained samples are specified as Ade-CaCl₂ and Ade-CaCl₂DH. The materials were first analyzed by N_2-physisorption and elemental analysis (Figure 5.1, Table S16). Interestingly, both salts ($CaCl_2DH$ and $CaCl_2$) yield porous nitrogen doped carbon materials with SSAs higher than 1500 m^2 g^{-1} and TPVs larger than 1.6 cm^3 g^{-1}. Additionally, the shape and the position of the N_2 isotherms are very alike. The nitrogen content of both samples is very similar showing values of 5.8 wt.% and 5.6 wt.% for $CaCl_2$ and $CaCl_2DH$, respectively. Apparently the porosity, measurable by N_2-physisorption, does not strongly depend on the hydration state of $CaCl_2$. Nevertheless, a closer look on the isotherms reveals small differences. $CaCl_2$ results in a

composite isotherm of type I(b) and type III coupled with a small H3 hysteresis pointing to micropores and a high amount of large interstitial pores. Contrarily, the isotherm of Ade-$CaCl_2DH$ can be described as type I(b) with a H4 hysteresis showing less N_2 uptake at high pressures. This indicates that the application of $CaCl_2DH$ promotes the general miscibility of adenine and salt phase leading to smaller pores which can also explain the ~ 10 % higher SSA in the case of the hydrated salt.
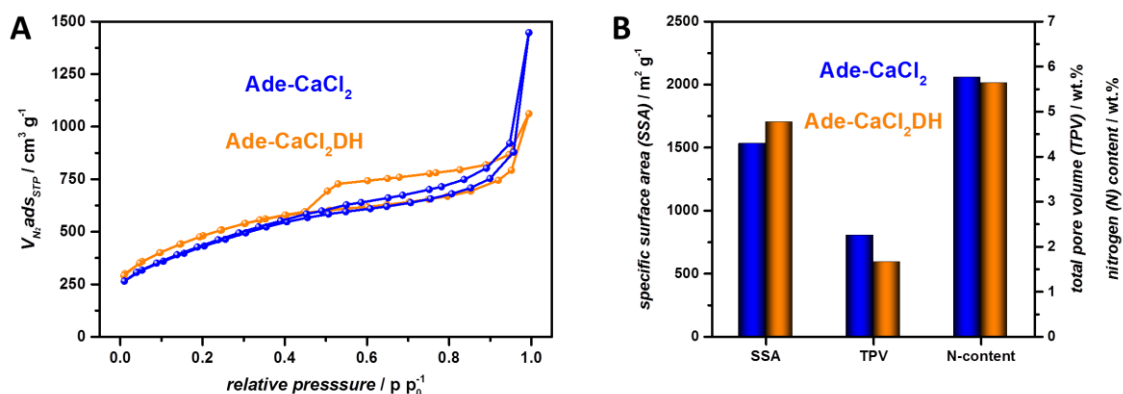
Figure 5.1 A) Nitrogen physisorption isotherm and B) SSA, TPV, and N-content of adenine derived NDCs using either CaCl2 or CaCl2DH as salt. The precursor to salt wt.-ratio was fixed to 1:10 in both cases.

A clear influence of the hydration state of $CaCl_2$ on the carbonization of adenine is reflected by the carbon yields. Anhydrous $CaCl_2$ yields only 15.6 wt.% carbon whereas $CaCl_2DH$ results in a carbon yield of 25.7 wt.% (Table S16). Apparently, $CaCl_2DH$ supports the fixation of gaseous decomposition products of adenine which points to a molten state of the salt during initial adenine crosslinking. The results are in line with the adenine derived NDCs discussed in section 3.4.1. Therein, the employment of low-melting $NaCl/ZnCl_2$ mixtures resulted in a three times increased carbon yield when compared to the value for the material carbonized in the presence of pristine NaCl. The very low carbon yield of the Ade-$CaCl_2$ points to adenine decomposition in manner of a solid-state reaction. Hence, the carbonization takes place on the surface of the solid $CaCl_2$ particles which goes along with the graphene like morphology observed by SEM and TEM (Figure 5.2A+B). Pure adenine starts to sublime/decompose at $T \sim 320\,°C$ according to the TGA-measurements (Figure S4). In the presence of $CaCl_2$, volatile species can be trapped on the surface of the salt particles, and undergo crosslinking reactions probably promoted by the ability of $CaCl_2$ to form complexes with NH_3 representing a possible leaving group of adenine condensation.[207] Thus, complete evaporation, as observed in the TGA measurements, is prevented. The high salt to precursor ratio ensures a thin character of the

crosslinked precursor domains which leads to the formation of graphene like nitrogen doped carbon.
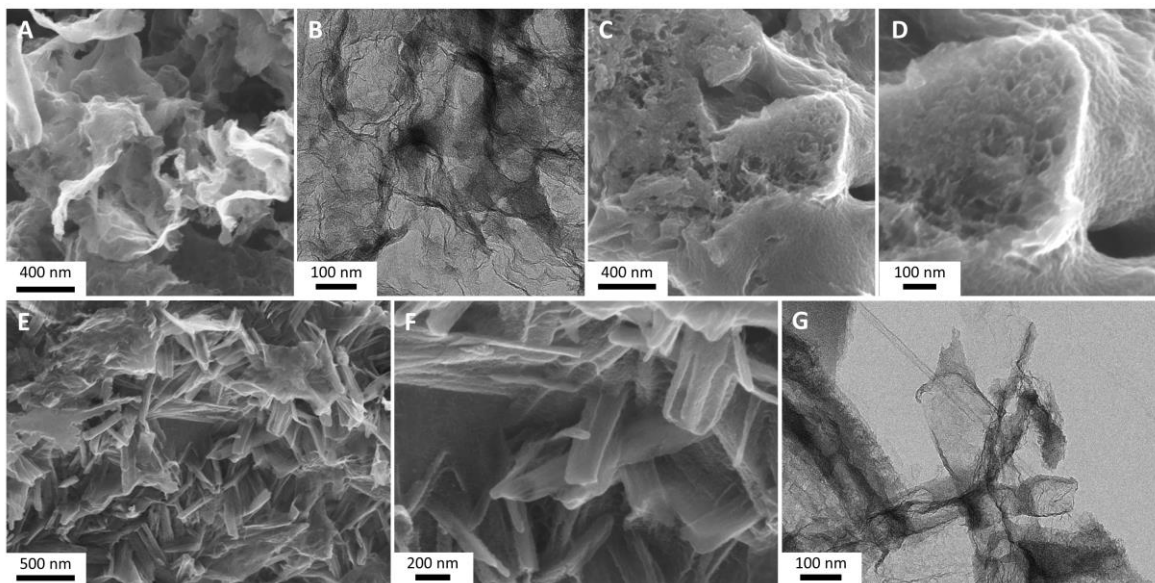
Figure 5.2 A) SEM and B) TEM image of the adenine derived material using $CaCl_2$ as reaction medium. C+D+E+F) SEM and G) TEM images of the adenine derived samples using $CaCl_2DH$ as reaction medium. The precursor to salt wt.-ratio was fixed to 1:10 in both cases.

Contrarily, SEM images of the $CaCl_2DH$ sample reveal a rather dense but still porous structure indicating that the precursor interacts with the liquid salt phase (Figure 5.2C+D). However, the morphology obtained, consisting of small, interconnected carbon sheets, does not represent the typical sol-gel structure. Intriguingly, the SEM images of the $CaCl_2DH$ also show the presence of rod-like shaped carbon domains indicating a herein desired secondary templating effect (Figure 5.2E+F+G). The liquid (intermediate) state of $CaCl_2DH$ supports the general mixing of adenine and salt phase. However, the continuous dehydration of the salt phase causes its resolidification. Presumably, adenine stays at the interface between liquid and solid phase thereby partially hindering the formation of large salt domains. Thus, adenine is either in contact with the solid and the liquid phase, or confined in between two solid salt particles during carbonization both promoting the fixation of volatile decomposition products of adenine. Those regions, consisting of small salt particles separated by adenine, probably lead to the rather dense carbon structure observed by SEM (Figure 5.2D). In contrast, larger salt domains lead to actual recrystallization of $CaCl_2$. The larger crystals are nevertheless covered with adenine and can act as mold (template) yielding a hollow rod-like carbon morphologies in the final product (Figure 5.2E+F+G).

Regarding the porosity characteristics, $CaCl_2DH$ (instead of anhydrous $CaCl_2$) supports the initial mixing of adenine and salt due to the liquid intermediate state. Thus, the interface between adenine and salt is enlarged supporting the fixation of volatile products which explains the largely enhanced yield by 65 %. However, the improved carbon yields of 25.7 wt.% are still rather low when compared to 50 – 60 % carbon yield of the adenine derived samples prepared with $ZnCl_2$-containing salt mixture (chapter 3.2.2). The low yields combined with the sheet like carbon structure, which is present for $CaCl_2$ and $CaCl_2DH$ (although in different dimensions), point to the fact that the final carbonization rather takes place on the surface of solid salt particles than in molten salt. The SSAs achieved are relatively large indicating the microporous nature of the sheet (graphene) like carbon domains. Microporosity connected to a low carbon yield is often explained by etched (activated) carbon, however thermodynamically this is not expected. Considering that anhydrous $CaCl_2$ melts at 772 °C, liquid $CaCl_2$ may penetrate the carbon structure thereby introducing microporosity by means of salt templating.

The adenine derived NDCs synthesized in $ZnCl_2$-containing salt mixtures showed very promising ORR-activities (cf. section 3.4.2). Thus, it is very interesting to investigate the ORR-performance of the also adenine derived materials of the present section synthesized with $CaCl_2$ or $CaCl_2DH$, especially, regarding their Zn-free character. The electrocatalytic activity towards the ORR was tested in alkaline conditions using a RDE set-up (Figure 5.3).
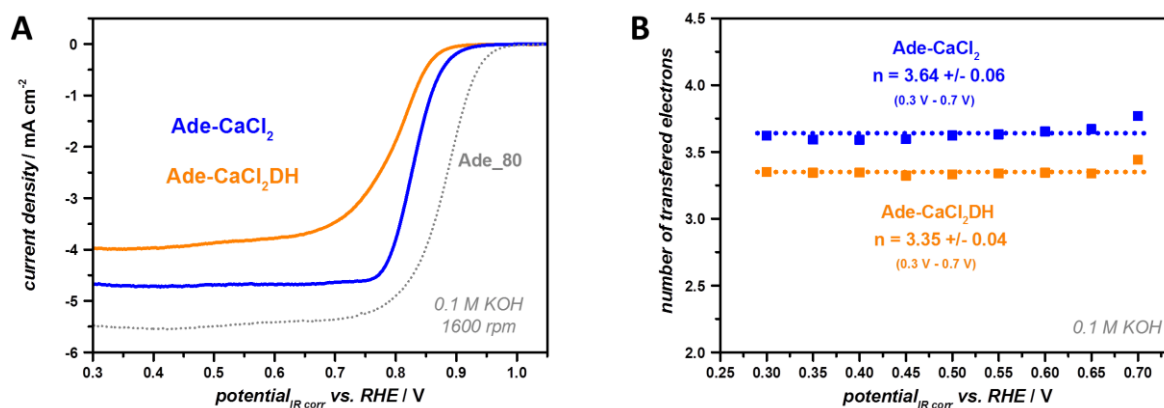
Figure 5.3 A) RDE polarization curves of Ade-$CaCl_2$ and Ade-$CaCl_2DH$ in O_2-saturated 0.1 M KOH with a sweep rate of 5 mV s^{-1}, 1600 rpm. For comparison, the LSV obtained of Ade_80 is also depicted (section 3.4.2). B) Number of transferred electrons (at different potentials) calculated from KL-plots at different potentials derived from RDE-measurements with different rotating rates.

Ade-$CaCl_2$ generally shows a better performance than Ade-$CaCl_2DH$. The former exhibits an onset potential of ~ 0.92 V (vs. RHE) and a $E_{1/2}$ of ~ 0.83 V (vs. RHE) reflecting a positive shift of ~ 20 mV and ~ 35 mV, respectively, when compared to Ade-$CaCl_2DH$.

According to KL-analysis at different potentials, Ade-CaCl$_2$ also possesses a higher electron transfer number (3.64 vs. 3.35) which is close to the desired four electron process. Although both samples exhibit similar chemical composition and SSA, their catalytic activity is quite different, pointing to the importance of the "right" porosity for the ORR as already discussed in chapter 3.4.2. The higher performance of Ade-CaCl$_2$ could be linked to the accessibility of the surface sites due to its sheet like structure when compared to the more closed structure of Ade-CaCl$_2$DH. Generally, the performance is worse compared to the materials synthesized in ZnCl$_2$-containing salt mixtures either pointing to the relevance of ZnCl$_2$ in forming the active sites or the presence of residual Zn itself.

Generally, the application of hydrated salts as reaction medium for the extended ionothermal synthesis using adenine is very promising due to the enhanced yield (compared with pristine CaCl$_2$) and the possibility to structure carbon materials by secondary templating. The approach will be discussed in more detail in the following section 5.3 applying MgCl$_2$HH as reaction medium.

5.3 MgCl$_2$ Hexahydrate as Reaction Medium for the Synthesis of Adenine Derived "Fibrous" Nitrogen Doped Carbons: Secondary Templating Effect and Electrochemical Application

The present section addresses the employment of MgCl$_2$HH as reaction medium for the extended ionothermal synthesis of adenine derived NDCs. The salt was chosen due its low melting point of 117 °C and its ability to melt/decompose in multiple steps.[189] The possibly formed MgCl$_2$ dihydrate decomposes at 300 °C representing a temperature close to the onset of adenine decomposition.[12] Section 5.3.1 will focus on the possibility of introducing a secondary templating effect leading to fibrous highly porous NDCs with SSAs up to 2780 m^2 g^{-1} and TPVs up to 3.68 cm^3 g^{-1}. The importance of a high salt to precursor will be highlighted and the influence of the synthesis temperature will be discussed. PXRD will be used to gain further insights on the mechanism of the secondary templating. In the second part (section 5.3.2), the electrocatalytic activity in alkaline and acidic conditions will be presented briefly. In alkaline electrolyte, the materials are active (Zn-free) ORR-catalysts. The initially poor performance in acidic conditions can be strongly enhanced by simple metalation, i.e., solid-state coordination. The results show that NDCs can be used as solid ligands for, e.g., iron ions to obtain active and stable ORR catalysts. Thus, the ligand

optimization (NDC) can be decoupled from the introduction of iron ions, which can bypass the parasitic carbothermal reduction of iron-based active sites at high temperatures.

Adenine was mixed with $MgCl_2HH$ in different salt to precursor ratios and the obtained solid mixture was pyrolized at various temperatures. The general sample preparation and the heat treatment were conducted as described for the samples synthesized with $CaCl_2$ in section 5.2. However, to remove magnesium hydroxide ($Mg(OH)_2$), formed upon aqueous washing, the samples were washed with 2 M hydrochloric acid (HCl) and then neutralized again with deionized water. The samples names are given as Ade-Mg-X-Y where X represents the adenine to $MgCl_2HH$ wt.-ratio (1:X) and Y the final pyrolysis temperature.

5.3.1 The MgCl₂HH-Induced Secondary Templating Effect During the Synthesis of Adenine Derived Highly Porous Nitrogen Doped Carbon Materials

Motivated by the interesting morphologies obtained with the adenine-$CaCl_2DH$ system (section 5.2), the reaction medium was changed to $MgCl_2HH$ and three different adenine to salt ratios were studied (1:1, 1:5, and 1:10). The synthesized materials were investigated by SEM, N_2-physisorption and elemental analysis (Figure 5.4, Table S17). Ade-Mg-1-900 consists of secondary particles in the size range of 50 - 200 μm in diameter, showing a macroporous structure of differently shaped pores (Figure 5.4A). The mainly microporous material shows a medium SSA and TPV of 980 m^2 g^{-1} and 0.61 cm^3 g^{-1}, respectively. An increased salt to precursor ratio of 5:1 clearly enhances the separation of the formed (nitrogen doped) carbon domains resulting in smaller secondary particles (Figure 5.4B-1). Furthermore, the SEM images with higher magnification reveal the presence of channel like linear macropores. The porogenesis is likely to be linked to a secondary templating effect as observed for $CaCl_2DH$ in section 5.2. Ade-Mg-5-900 shows a largely enhanced SSA (vs. Ade-Mg-1-900) leading to a very high value of 2780 m^2 g^{-1}. Therefore, it can be concluded that adenine and its oligomeric decomposition products can mix well with the initially liquid $MgCl_2HH$ salt phase, also emphasizing the expected precursor sensitivity. Throughout the process of salt resolidification, the carbonizing phase apparently acts as surfactant and prevents the formation of large salt domains leading to a high interface between the carbonizing precursor and the salt, ergo to a high SSA of the final material. Thus, $MgCl_2HH$ appears to be a very interesting reaction medium to synthesize highly porous nitrogen doped carbon as further supported by the N-content and TPV of Ade-Mg-5-900 showing values of 2.3 wt.% and large 2.83 cm^3 g^{-1}, respectively. However,

the relatively low carbon yield of 25.6 % indicates that the final carbonization takes rather place in a solid reaction mixture than in a liquid salt phase (Table S17). These findings are in line with the results observed for the adenine derived materials synthesized with $CaCl_2DH$ (section 5.2).
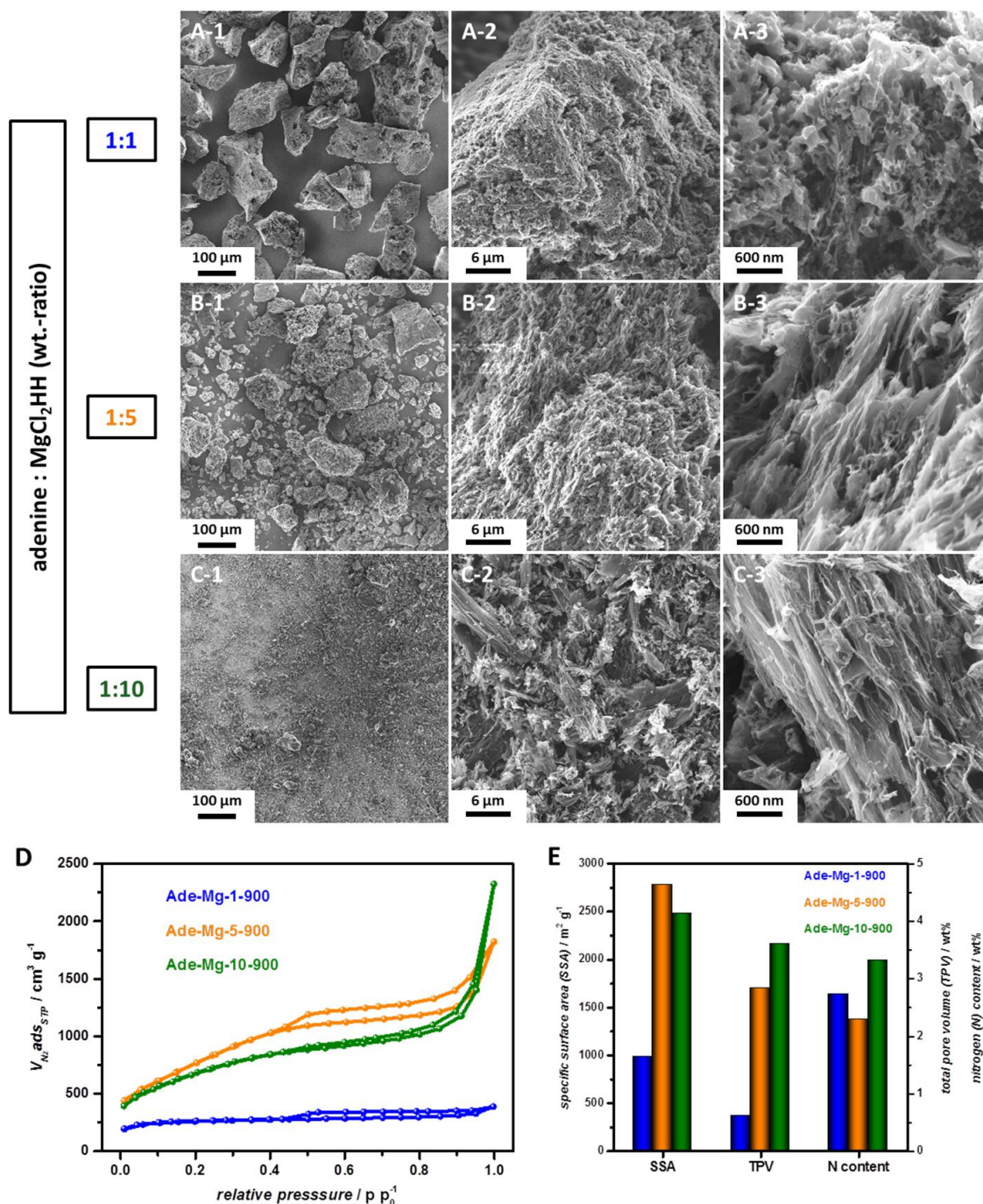
Figure 5.4 SEM images with different magnifications of A) Ade-Mg-1-900, B) Ade-Mg-5-900, and C) Ade-Mg-10-900. D) Nitrogen physisorption isotherms and B) SSA, TPV, and N-content of the corresponding samples.

Moreover, the N-content is clearly decreased compared to the ~ 7 wt.% N of the adenine derived samples synthesized (at the same temperature) with $ZnCl_2$-containg salt melts (section 3.2.2). This indicates that the liquid state of the salt and/or the presence of $ZnCl_2$

has a positive effect on nitrogen fixation during the carbonization. Interestingly, Ade-Mg-1-900 shows a lower carbon yield (17.0 %) than Ade-Mg-5-900 implying that the almost threefold increased SSA of the latter sample is indeed caused by a templating effect and not by a promoted carbon leaching (activation) mechanism. The statement is confirmed by the very similar carbon yield (26.4 %) of the sample obtained with a further enlarged salt to precursor ratio of 10:1. The large excess of salt in the case of Ade-Mg-10-900 causes even higher separation of the formed carbon domains resulting in a very large TPV of 3.60 cm^3 g^{-1} and a slightly decreased SSA of 2480 m^2 g^{-1}. These findings are in line with the typically observed effects of salt templating investigated with $ZnCl_2$-containing salt melts.[116] Intriguingly, the secondary templating effect is even more pronounced for Ade-Mg-10-900 leading to very interesting morphology features depicted in Figure 5.4C-3. The majority of the NDC sample seems to be made up of parallel ordered fiber-like carbon domains. The fibers show a width of ~ 30 nm and lengths up to ~ 4 μm leading to an aspect of ~ 1:130. However, it has to be mentioned that the fiber like structure is not always aligned as depicted in Figure 5.5C+D and Figure S27. Generally, the observed templating is very interesting and many parameters such as the size and shape homogeneity of the precursor salt particles are still potentially to be optimized. The very high SSA points either to very thin NDC layers forming those structures and/or to the internal microporosity of the materials. The material prepared with the highest salt content combines high SSA, high TPV with an open pore structure, which should allow a high accessibility of the surface sites. These features are interesting for electrochemical applications which will be further discussed in section 5.3.2.

As mentioned before, the decomposition of $MgCl_2HH$ is a complicated multistep procedure complicating the unraveling of the reason for the second templating effect. According to Equation (5.6) and (5.7), *in-situ* formed MgO could be the substance present during carbon solidification and act as template. From literature, it is known that MgO can be used as hard template to obtain hollow nitrogen doped carbon materials.[208] Furthermore, Jung *et al.* showed the possibility to obtain porous carbon nanofibers by electrospinning a solution made up of polyacrylonitrile and $MgCl_2$.[209] PXRD results revealed that the $MgCl_2$ was *in-situ* transformed in MgO during the heat treatment and the porous structure was obtained after removing the as hard template acting MgO by acidic washing.

In order to gain more insights regarding the morphology formation different Ade-Mg-10 samples were synthesized at different temperatures. The N_2-physisorption

isotherms, SSA, carbon yield and N-content in dependence on the synthesis temperature (500 – 1000 °C) are depicted in Figure 5.5A+B and more details are given in Table S18.
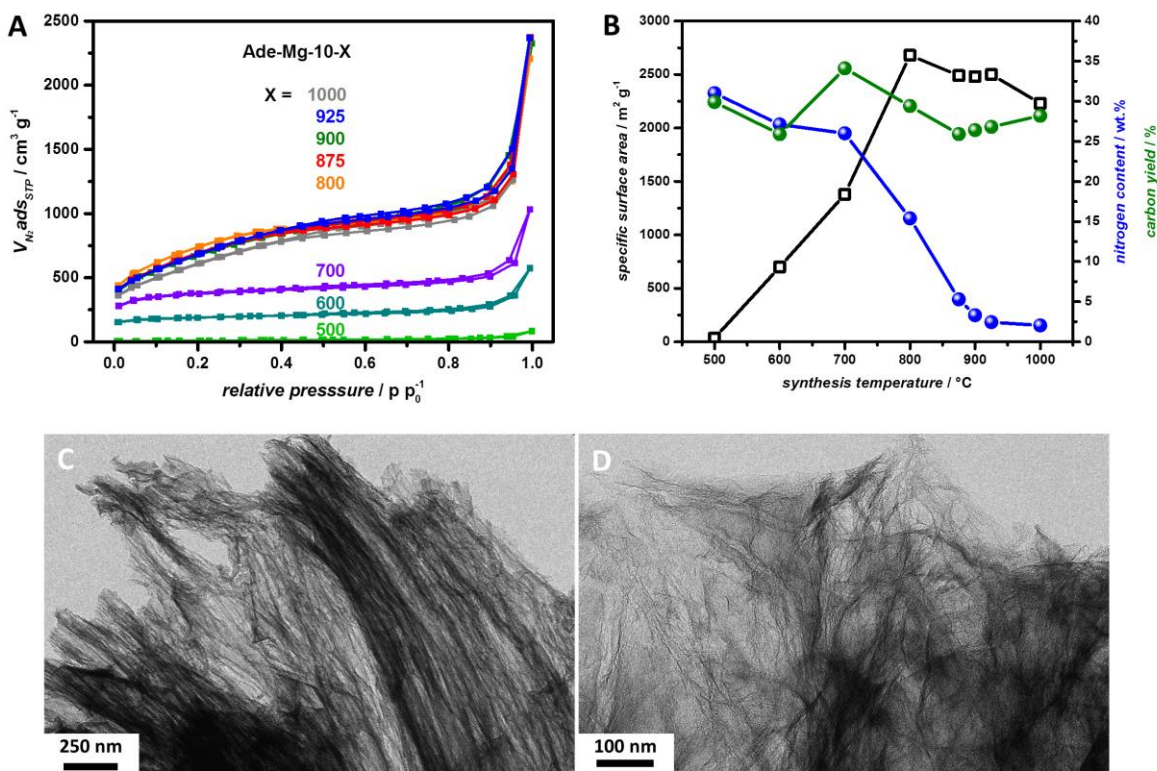
Figure 5.5 A) Nitrogen physisorption isotherms of the Ade-Mg-10 samples prepared at different synthesis temperatures. B) SSA, N-content. and carbon yield of the different Ade-Mg-10 samples with respect to the synthesis temperature applied. C+D) TEM images of Ade-Mg-10-900 depicting its fiber-like structure.

The sample prepared at 500 °C shows only negligible SSA. Higher synthesis temperatures lead to an almost linear increase of the SSA which reaches an outstanding maximum value of 2680 m^2 g^{-1} at 800 °C. Further increased temperatures cause a small decrease in SSA. However, the general porosity accessible by N$_2$-physisoprtion (SSA, PSD and TPV) hardly changes between temperatures of 800 °C and 1000 °C as indicated by the very similar isotherms (Figure 5.5A, Table S18). Considering that the chemical composition, such as the quality and quantity of heteroatom dopants is changing with temperature this will give the possibility to study chemical effects independent of the porosity in topical applications such as lithium sulfur batteries and capacitive desalination. Furthermore, the fibrous carbon domains are present in all samples as revealed by SEM and TEM images (Figure S28). Exemplarily, the TEM images of Ade-Mg-10-900 are depicted in Figure 5.5C+D. The sample is made up of fiber-like carbon domains which can be aligned but also assemble in a more random structure. Intriguingly, the carbon yield stays almost constant during the whole set of experiments indicating that the high porosity is not related to

carbon etching. However, the porosity could be triggered by the elimination (etching) of nitrogen functionalities which are released throughout crosslinking of the adenine domains. This explanation is in line with the gain in SSA accompanied by a large loss in nitrogen between 700 and 800 °C. However, distinct nitrogen loss also occurs between 800 and 900 °C whereas the SSA decreases in this region. The porosity could be also induced by liquid $MgCl_2$ (T_{melt}=708 °C) via salt templating at higher temperatures.[12] Presumably, the salt domains are separated into small (nano)-clusters by the adenine. Hence, the melting point can be strongly reduced which could explain the porosity already develops at lower temperatures than 700 °C.[210] Moreover, at lower temperatures the high nitrogen content that is connected to termination sites in the carbon framework accounts for a rather weakly crosslinked carbon network. Hence, small pores could be simply collapse during the (aqueous and acidic) work-up due to high LaPlace pressures inside the pores. Certainly an interplay of the three factors described is realistic.

Furthermore, the unwashed samples were analyzed by PXRD allowing assumptions regarding the present salt phase(s) during the synthesis. The PXRD result of the unwashed Ade-Mg-10-900 reveals that at 900 °C $MgCl_2$ and MgO is present (Figure S29A). This does not reflect the aforementioned salt phase transitions described by Sugimoto *et al.* pointing to large differences depending on the reaction conditions.[195] Any influence of the work-up on the morphology can be excluded as SEM reveals the fibrous domains already in the unwashed material (Figure S29C). Interestingly, PXRD and SEM of the sample only treated in deionized water discloses that aqueous washing causes the formation of stacked magnesium hydroxide ($Mg(OH)_2$) nanoplatelets formed by the reaction between MgO and water.[189] All (crystalline) inorganic species are completely removed during the final washing in 2 M HCl (Figure S29B). Higher synthesis temperatures support the formation of MgO according to the studies conducted by Sugimoto *et al.*[195] Hence, the templating effect should be more dominant at higher temperature if MgO is the critical templating phase. However, also in the unwashed sample prepared at 700 °C both features, the MgO reflections in the PXRD and the fibrous carbon domains (SEM), are already present (Figure S30). Thus, a clear role of the formed MgO cannot be concluded.

Moreover, energy dispersive X-ray (EDX) was conducted on the unwashed Ade-Mg-10-700 (Figure 5.6). An area was selected which showed both the fibrous but also spherical-like morphology. Elemental mapping reveals that the fiber like structure contains chlorine, magnesium and oxygen. Contrarily the spherical particles consist mainly out of magnesium and oxygen (no chlorine). Those results point to a sphere like morphology of

the MgO detected by PXRD and to a chlorine containing fibrous templating phase. The N-signal is homogeneously distributed throughout the material indicating a homogenous nitrogen doping.
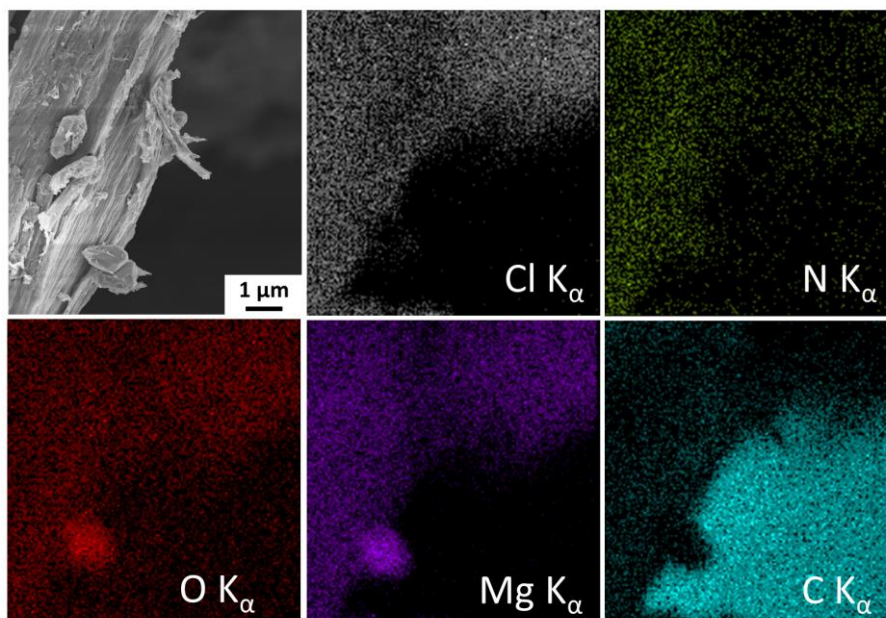
Figure 5.6 EDX analysis (elemental mapping) of the unwashed Ade-Mg-10-700. The inverse contrast of the C K_α-signal is caused by the carbon tape of the SEM holder.

The previous paragraph revealed that MgO may not act as fibrous templating phase. In respect to the studied system, the general question arises if I) $MgCl_2HH$ forms the fibrous templating phase itself or II) adenine is involved in the growth of the fiber-like structures indicating a cooperative mechanism. According to the decomposition reactions of $MgCl_2HH$, presented in in Equation (5.1) to (5.7), the templating could either be caused by $MgCl_2$ in different hydrated states (mainly the tetrahydrate or the dihydrate) or by magnesium oxyhydrochlorides. Interestingly, Huang *et al.* obtained a fiber-like Mg(OH)Cl structure by the decomposition of $MgCl_2HH$.[211] The exact composition was described as $Mg_3Cl_2(OH)_4 \cdot 4\,H_2O$. However, the phase only formed after dehydration in HCl atmosphere at 203 °C and subsequent hydration at the same temperature. Nonetheless, these findings point to the possibility to obtain fiber like structures without the presence of adenine. To further discuss the cases I) and II), more detailed studies were conducted at low temperatures between 300 and 600 °C. The adenine derived materials prepared as such low temperatures are certainly organic materials rather than carbons considering the very high heteroatom contents (Table S18). Hence, those materials will be discussed as pre-NDCs. Additionally, blank samples derived only from $MgCl_2HH$ were synthesized at the according temperatures. Those samples are specified by Mg-X where X indicates the final

annealing temperature. SEM studies were conducted on the acid washed pre-NDC materials and compared with the $MgCl_2HH$-derived materials (Figure 5.7A). Furthermore, all materials were analyzed by PXRD directly after the synthesis (Figure 5.7B).
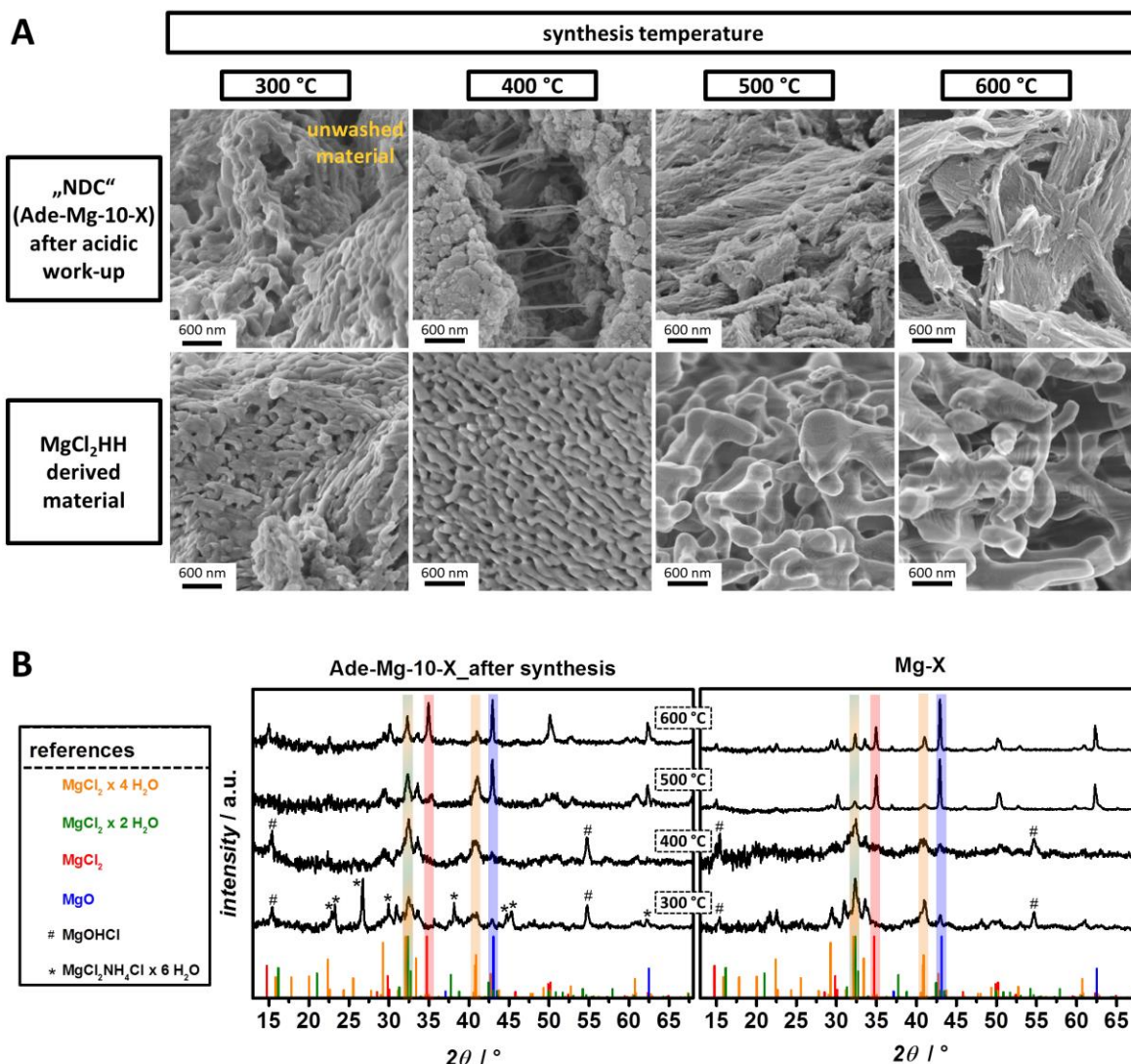
Figure 5.7 A) SEM images of the Ade-Mg-10 samples (upper row) and of the $MgCl_2HH$ derived materials (bottom row) synthesized at different temperatures (300 – 600 °C). B) Normalized PXRD diffractograms of the corresponding unwashed materials (the ICDD numbers of the references are given in Table S3).

According to PXRD, the $MgCl_2HH$ derived material synthesized at 300 °C contains $MgCl_2$ tetrahydrate ($MgCl_2 \cdot 4\,H_2O$), $MgCl_2$ dihydrate ($MgCl_2 \cdot 2\,H_2O$) and MgOHCl. The morphology of Mg-300 shows irregularly shaped, interconnected particles with interstitial pores in the macropore range. Ade-Mg-10-300 dissolved completely during the acidic work-up indicating that only small or instable adenine crosslinked pre-NDC domains were formed at such a low temperature. Hence, only the SEM of the unwashed material is shown depicting, however, a very similar morphology as Mg-300. Interestingly, the PXRD of the unwashed material reveals the presence of $MgCl_2NH_4Cl \cdot 6\,H_2O$. Thus, adenine

starts already to decompose/crosslink under NH_3 elimination at $T \leq 300\,°C$.[XXI] The N containing salt phase vanishes completely when the temperature is increased to $400\,°C$ probably *via* the elimination of NH_3 and HCl. The SEM image of Ade-Mg-10-400 reveals the formation of some fiber-like pre-NDC domains but also completely amorphous areas are present. The latter could be caused by the precipitation of only weakly crosslinked adenine domains during the acidic work-up. At this temperature the PXRD does not show any MgO supporting the former statement that MgO is unlikely to be the fibrous templating phase. The PXRD of the reference Mg-400 is very similar to the adenine containing material. The SEM of Ade-400 shows worm-like, partially parallel aligned particles. However, the dimensions of the particles are distinctly larger than the fiber-like structures obtained in the presence of adenine. Higher temperatures (500 and $600\,°C$) cause a growth of the worm-like particles resulting in irregular shaped but still interconnected salt crystals. Contrarily, the adenine derived materials show a well-developed fiber structure in this temperature range clearly indicating that adenine plays an important role for the development of the overall morphology. Hence, the case II) scenario is confirmed meaning that adenine is involved in the growth of the fiber-like structures indicating a cooperative templating mechanism. The PXRD results show that the MgOHCl phase completely vanishes and MgO is formed at $500\,°C$, independently on the presence of adenine. Thus, MgOHCl can be probably excluded as fibrous templating phase. Intriguingly, the intensity ratios between MgO and the (hydrated) $MgCl_2$ phases indicate that adenine hinders the formation of MgO. The effect is also present for the samples prepared at $600\,°C$. Moreover, adenine seems to restrict the elimination of crystal water of the hydrated $MgCl_2$ phases. In Mg-500 the main chlorine containing phase is anhydrous $MgCl_2$ whereas in Ade-Mg-10-500 large amounts of $MgCl_2 \cdot 4\,H_2O$ and $MgCl_2 \cdot 2\,H_2O$ are present.[XXII]

In conclusion, the materials synthesized at low temperatures support the theory that the fibrous morphology of the NDCs is not caused by MgO particles. Moreover, it can be believed that adenine supports the morphology development. Nonetheless, the obtained results do not allow a clear statement about the exact fibrous templating phase. Adenine seems to function as a structure-directing agent restricting/directing the crystal growth of the salt phase. A preferential crystal growth should be detectable by XRD. However, the

---

[XXI] NH_3 as leaving group fits to the aforementioned possibility of a crosslinking similar to the Gattermann-reaction (cf. section 3.2.2).

[XXII] The presence of different hydration phases should be handled with care because the samples were only protected by scotch tape during the PXRD measurement minimizing but probably not preventing hydration

co-existence of multiple phases with overlapping reflections in the present system does not allow for unambigous analysis. Intriguingly, it was shown in literature that adenine can form a crystalline phase with $MgCl_2HH$.[212] The system is stabilized *via* hydrogen bonds between the electron accepting hydrogen groups of $MgCl_2HH$ and the free electron pair of the nitrogen atoms present in adenine. This fact combined with the detailed study of the intermediate phases during $MgCl_2HH$ decomposition conducted by Sugimoto *et al.* leads to the (speculative) explanation of the observed secondary templating effect which is presented in the next paragraph and summarized in Figure 5.8.[195]
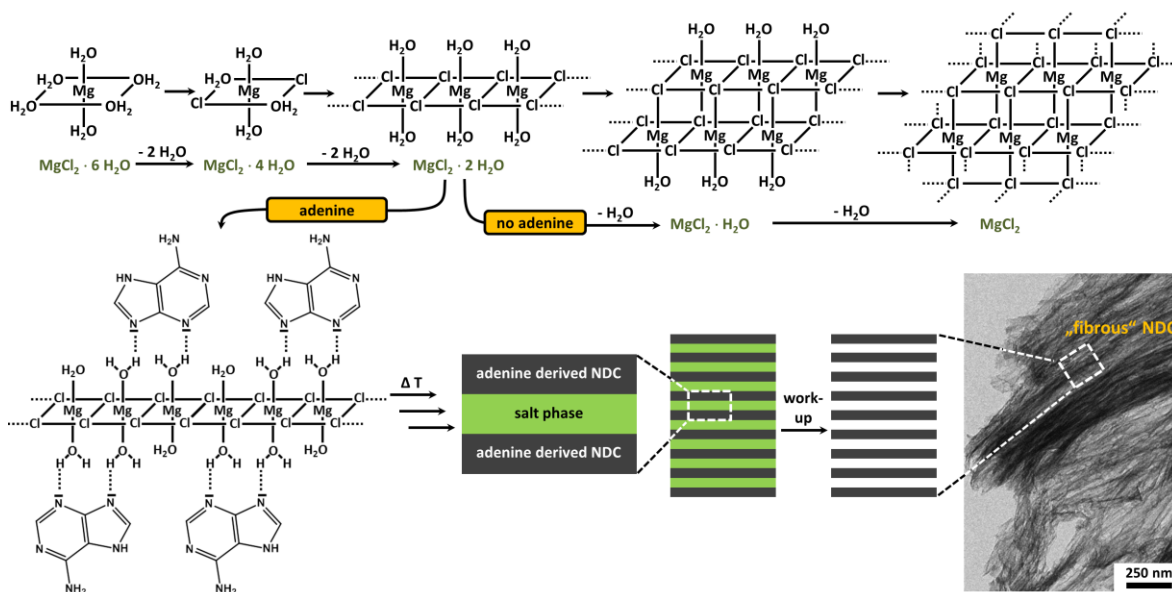
Figure 5.8 Schematic illustration of the (cooperative) secondary templating during the synthesis of adenine derived NDCs obtained with $MgCl_2HH$ as reaction medium. The reactions occurring in the absence of adenine are adapted from[195].

Adenine dissolves first in the liquid $MgCl_2HH$ which consists of isolated $Mg(H_2O)_6^{2+}$ octahedra and Cl^- anions. The elimination of water will lead to the recrystallization of $MgCl_2 \cdot 4\,H_2O$ made up of isolated and disordered $Mg(H_2O)_4Cl_2$ octahedra with two chloride ions in trans-equatorial position. At this stage adenine can assemble on the solid-liquid interface and bond to the water atoms of $MgCl_2 \cdot 4\,H_2O$ *via* hydrogen bonding thus influencing (restricting) the further decomposition. Interestingly, the $MgCl_2 \cdot 2\,H_2O$ formed upon further elimination of water consist of infinite single chains formed by $Mg(H_2O)_2Cl_4$ octahedra in which chlorine atoms occupy all the equatorial positions. It can be assumed that adenine interacts with the water molecules located in the axial positions thereby promoting the growth of linear crystals. Further water elimination leads to the formation of "infinite" double chains composed of $Mg(H_2O)Cl_5$ octahedra. The remaining water molecules are pointing away from the chain allowing further interaction with

adenine. The elimination of the last water molecule would lead to the sheet structure of $MgCl_2$. Moreover, the composition involves the intermediate formation of different Mg(OH)Cl phases and the final decomposition into MgO. However, the crosslinked adenine domains sitting on the crystal surface during $MgCl_2 \cdot X\,H_2O$ decomposition can conserve the linear shape of the intermediate phases which finally leads to "structured" highly porous NDC materials. Hence, the "structured" NDC is obtained by a cooperative templating mechanism of adenine and $MgCl_2HH$.

As aforementioned, it should be possible to improve the degree of "structuring" (i.e., appearance and size of the carbon domains consisting of parallel aligned fibers) by carefully adjusting the synthesis conditions. This hypothesis was supported by the synthesis of an additional Ade-Mg-10-900 sample obtained with a slightly modified procedure. During the usual heat treatment, an additional dwelling step at 400 °C for 10 h was introduced. The resulting material possessed "structered" NDC domains (particles) consisting of parallel aligned fibrous NDC in the range of up to 60 μm corresponding to a width-length aspect ratio larger than 1:1000 (Figure S31).

The porosity of the herein synthesized NDCs combines high SSA with an open pore structure speculatively promoting the accessibility of the surface sites which is very important regarding electrochemical applications. Therefore, the ORR-performance of the NDCs synthesized with $MgCl_2HH$ will be further discussed in section 5.3.2.

5.3.2 Boosting the Acidic Electrocatalytic Activity of Nitrogen Doped Carbons by Facile Metalation with Iron Ions

First, the electrocatalytic activity of Ade-Mg-10-900 was studied towards the ORR in alkaline conditions to obtain a general statement about the performance of NDCs synthesized with $MgCl_2HH$. Furthermore, this allows the direct comparison to the activity of the samples synthesized with $CaCl_2$ under very similar conditions. The $MgCl_2HH$ "templated" material is less active towards the ORR than Ade-$CaCl_2$ in terms of onset and $E_{1/2}$ (Figure 5.9A). This could be related to the lower nitrogen content of the former (3.3 wt.%) when compared to the latter (5.8 wt.%). Intriguingly, the in section 3.4.2 discussed Ade_80 has an even higher nitrogen content of 6.3 % and shows a further improved ORR-activity. Speculatively, higher N-contents will lead to an increase in Fermi level due to the electron donation character of the N-atoms.[73] A higher Fermi level (i.e., reduced work function) facilitates the first electron transfer from the NDC to the oxygen thereby reducing the overpotential.[70,190] This is especially valid if an outer-sphere electron

transfer is regarded as the first step of the ORR-mechanism in alkaline condition, as discussed in chapter 4. To gain further insights, the ORR-performance of Ade-Mg-10-900 was analyzed under acidic condition using 0.05 M sulfuric acid (H_2SO_4) as electrolyte. The performance is strongly impaired as depicted by the large shift of the LSV curve to lower potentials (Figure 5.9A). Moreover, the strong pH-dependence of the ORR-activity is confirmed by the ORR-performance of Ade-CaCl$_2$ in acidic and alkaline media (Figure 5.9A). This is in line with the commonly observed largely decreased ORR-activity in acidic milieu in comparison to alkaline milieu, as already discussed in chapter 4.

It is known that the (poor) acidic performance of NDCs can be enhanced by introducing non-noble metal ions such as iron or cobalt.[173] The research towards non-noble metal catalysts was greatly promoted by the groundbreaking results obtained by Lefèvre *et al.* in 2009.[96] A porous activated carbon was used as conductive backbone and mixed with phenanthroline as nitrogen and iron(II) acetate as iron source. After heat treatment, first in inert and second in NH_3-atmosphere, a very active ORR-catalyst for acidic medium was obtained. It is broadly accepted that the active site involves a porphyrine-like structure where iron is bond to nitrogen of the NDC-framework. Nonetheless, the exact structure of the active site as well as the detailed ORR-mechanism are still strongly debated and beyond the scope of the present chapter (mechanistic considerations can be found in chapter 4). Thus, the structure will be simply described as Fe-N site herein. Based on the work of Lefèvre *et al.*, various methods were developed to obtain Fe-NDCs.[173,180,182,213] The exact synthesis procedures are quite different ranging from the rather simple carbonization of iron porphyrins (already containing the supposed active site) in the presence of carbon black to complex multistep procedures applying different precursors for carbon, nitrogen and iron, respectively.[182,213] However, all methods usually involve a final treatment at high temperature in which all three elements of the active site (iron, carbon and nitrogen) are present. The final annealing conditions (temperature, atmosphere and time) play an important role regarding the activity obtained and the iron-site present.[96,176,182] Higher temperatures usually improve the conductivity of the materials promoting the ORR activity. Contrarily, an increased temperature will support the carbothermal reduction of iron ions to elemental iron (Fe^0) reducing the number of Fe-N sites. Moreover, carbothermal reduction occurs the earlier, the higher the iron concentration.[95] Thus, concurrent pyrolysis of Fe, N, and C also limits the concentration of active sites. The formed elemental iron can be covered by a thin carbon layer. Thus, it is even stable during the acidic work-up and can be present in the final catalyst.[180]

Furthermore, the process can also lead to the formation of iron oxides introducing another possible active site (cf. section 4.2). The role of the formed Fe^0, however, is controversially discussed. Tylus *et al.* showed that (for their Fe-NDC) the iron particles served as secondary catalytic site ensuring a four electron process.[180] In contrast, Zitolo *et. al.* was able to synthesize a Fe^0-free material by carefully adjusting the synthesis conditions, which clearly showed a four electron process.[176] Overall, the occurrence of the carbothermal reduction clearly complicates unambigous conclusions regarding the relation between the synthesis temperature applied and the activity obtained. Therefore, the possibility to decouple the synthesis of the nitrogen doped carbon framework from the introduction of the metal center is highly interesting. The idea herein is to introduce the Fe-N site by simple metalation at low temperatures of a pre-formed solid NDC completely preventing carbothermal reduction (Figure 5.9B). Thus, the solid NDC ligand can be synthesized/optimized independently allowing a precise investigation of the relation between the properties of the NDC and the ORR-activity obtained.
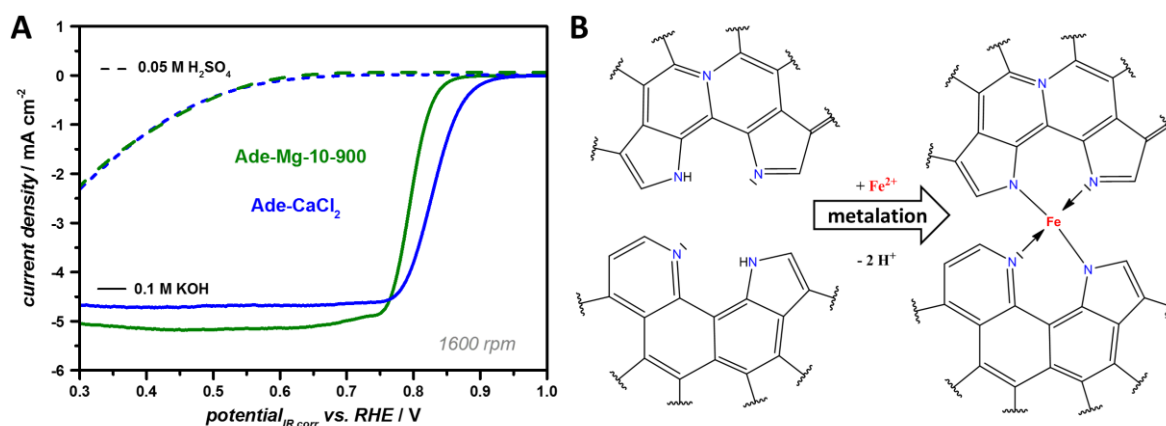
Figure 5.9 A) RDE polarization curves of Ade-Mg-10-900 in 0.1 M KOH and 0.05 M H_2SO_4 (O_2-saturated, 5 mV s^{-1}, 1600 rpm). Additionally, the performance of Ade-$CaCl_2$ in both electrolytes is shown for comparison. B) Schematic illustration of the metalation of a (hypothetical) N_4 unit with an iron ion..

The NDC should possess a high SSA and, even more importantly, very accessible surface sites to allow a successful metalation. According to the porosity/morpholgy analysis presented in section 5.3.1, Ade-Mg-10-900 can fulfill those requirements. Hence, it was chosen as the solid ligand and metalated by facile stirring with an iron(II) chloride tetrahydrate ($FeCl_2 \cdot 4 H_2O$, 50 mM) solution in methanol (MeOH) under reflux conditions for 24 h. The sample obtained was washed in 0.5 M H_2SO_4 to remove physisorbed iron ions, neutralized by aqueous washing, and its ORR activity was analyzed by RDE measurements. The metalated sample is identified by the suffix "_Fe". The LSV in acidic conditions of Ade-Mg-10-900_Fe shows a great activity increase when compared to the

non-metalated sample as reflected by a magnificent onset shift of ~ 240 mV (Figure 5.10A). It is necessary to mention that the porosity, elemental composition and morphology were hardly influenced by the metalation treatment (Figure S32). These results indicate that the active center can be introduced by a simple metalation reaction.[XXIII] The amount of iron present in the metalated material was analyzed by inductively coupled plasma optical emission spectrometry revealing the presence of 0.46 wt.% iron (Figure 5.10B, Table S19).[XXIV]

The metalation was repeated with the Ade-Mg-10 materials synthesized at different temperatures (800 – 1000 °C) and the ORR-activity was studied, allowing a direct correlation between the chemical state of the solid ligand and the activity obtained. It has to be considered that the materials synthesized in this temperature range show very similar porosity features such as SSA and TPV (Figure 5.5, Table S18, Table S19). The obtained LSVs show the system's sensitivity to the synthesis temperature of the NDC (Figure 5.10A). The activity increases if the synthesis temperature is raised from 800 °C to 875 °C and decreases again at higher temperatures. The activity can be linked to the optimization of the ligand "quality" of the NDC which, however, is hard to distinguish in its physochemical properties (Figure 5.10B). Apparently, higher N-content allows a higher degree of metalation leading to the introduction of more active sites. Hence, the materials synthesized at lower temperatures contain more iron and show a positively shifted onset potential. However, if the synthesis temperature is too low (800 °C), the activity, especially the kinetic performance, is decreased, which is probably caused by the very high N-content of 15.4 wt.% shifting the electronic properties of the NDC more in the direction of a semiconductor. Among the investigated synthesis temperatures, 875 °C results in the best performing catalyst showing an $E_{1/2}$ of ~ 0.76 V (vs. RHE). This value is close to the range of previously reported "high-performing" ORR-catalysts in acidic conditions.[166,180,214-217] Nonetheless, there are reported Fe-N catalysts which show even higher activities with values of $E_{1/2}$ up to ~ 0.84 V (vs. RHE).[213] Additionally, the commercial Pt/C catalyst shows distinctly better activities with an $E_{1/2}$ of ~ 0.90 V (vs. RHE) measured under optimized conditions (cf. section 4.3).

[XXIII] The effect could be linked to an enlarged Fermi level of the material caused by the introduction of iron which is, however, unlikely. Nevertheless, Mößbauer measurements should be conducted in the future to proof the presence of Fe-N sites.

[XXIV] Interestingly, the measurement of the non-metalated sample revealed the presence of 0.02 wt.% iron. However, the poor catalytic performance of Ade-Mg-10-900 in acidic media indicates that the value comes either from the sample preparation for the ICP-OES and/or can be regarded as "non-active" iron. Moreover, the iron amount is very low and accounts for one iron atom per ~ 20000 carbon atoms.
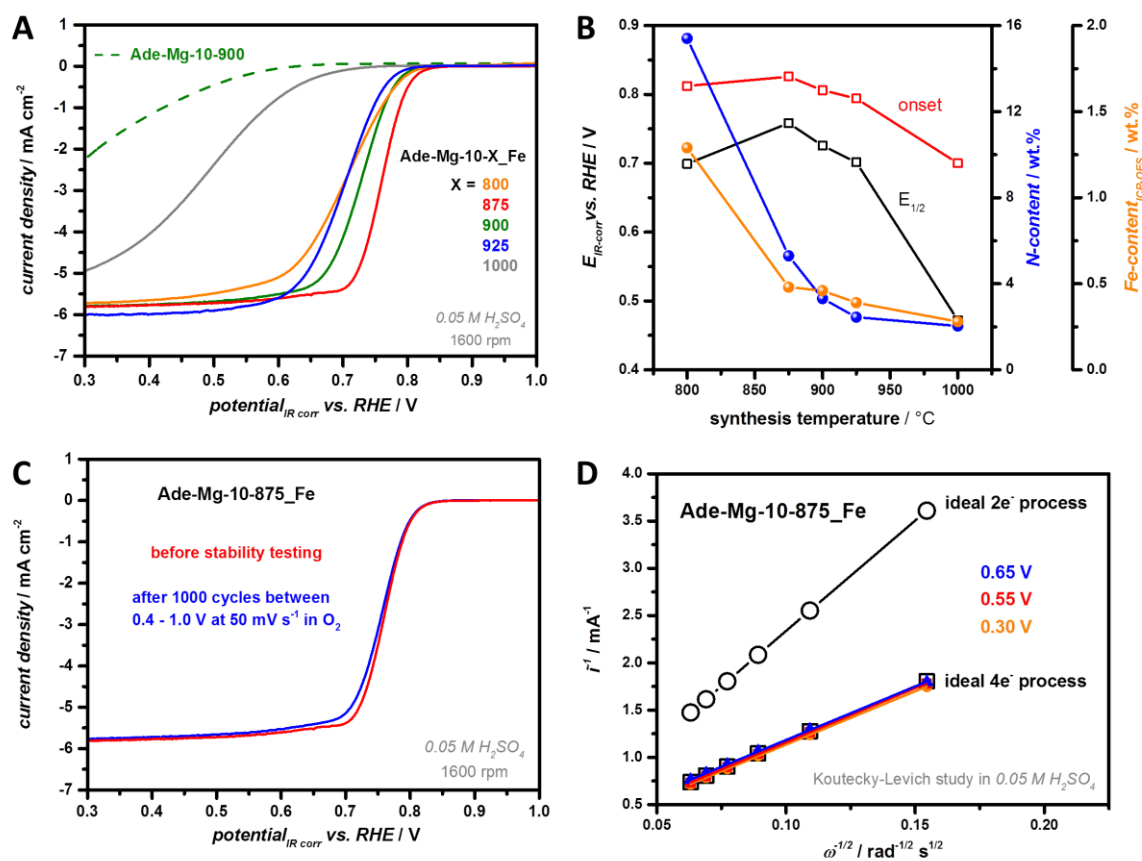
Figure 5.10 A) RDE polarization curves of the metalated Ade-Mg-10 samples synthesized at different temperatures in 0.05 M H_2SO_4 (O_2-saturated, 5 mV s^{-1}, 1600 rpm). For comparison, the activity of the non-metalated Ade-Mg-10-900 is also shown. B) Onset potential, $E_{1/2}$, and iron content of the metalated samples with respect to the applied synthesis temperature. Furthermore, the N-content of the initial (non-metalated materials) is shown. C) Stability measurement and D) KL-analysis at different potentials of the best performing material (Ade-Mg-10-875_Fe) in acidic conditions.

The best performing material of the catalysts prepared in this section was further evaluated regarding its stability and selectivity. KL-studies at different potentials reveal an almost ideal four electron process and the catalysts show only very low degradation ($\Delta E_{1/2} = 5$ mV) after 1000 cycles in O_2-saturated electrolyte (Figure 5.10C+D).[XXV] Those values not only show the desired selectivity, but also reveal the stability of the active sites introduced by facile metalation at low temperatures.

Ionothermal carbons synthesized with $ZnCl_2$-containing show very promising ORR-activities as shown in section 3.4.2 and in literature.[95,116] However, the obtained materials always contain residual zinc which is even stable in strong acidic conditions. Thus, it has been difficult to exclude a possible influence of the remaining zinc on the ORR performance as already briefly addressed in chapter 3 (section 3.4.2). Contrarily, the herein developed metalation approach allows to directly investigate the influence of zinc

---

[XXV] It is important to determine the stability of ORR-catalysts in the presence of oxygen to guarantee realistic stability values of (Fe-)NDCs materials.

on the ORR performance. Interestingly, the with Zn-metalated material (Ade-Mg-10-900_Zn; 0.18 wt.% Zn) shows almost the same activity as Ade-Mg-10-900 (Figure S33A). Hence, a direct involvement of Zn-ions in the ORR under acidic conditions is highly unlikely. Moreover, the activity of the Zn-containing and Zn-free sample are also very alike in alkaline conditions supporting the inactivity of the remaining Zn-sites towards the ORR (Figure S33B).[XXVI] Nonetheless, the presence of zinc or $ZnCl_2$ may play a crucial role for the formation of the active sites.

The general procedure was repeated with Ade-CaCl$_2$ confirming the possibility of introducing acidic active ORR-sites by facile metalation reaction. The Ade-CaCl$_2$_Fe sample showed an improved onset potential of ~ 135 mV when compared to Ade-CaCl$_2$ (Figure S34A). Interestingly, the metalation only slightly enhanced the activity in alkaline conditions (in contrast to the large improvement in acidic conditions) when comparing the activity of Ade-Mg-10-900 and the corresponding Fe-metalated material (Figure S34B). The findings point to the presence of different active sites (at least in the case of the investigated catalyst) for the ORR in alkaline conditions and acidic conditions.[XXVII] The statement is supported by the different ORR-pathways as revealed by the H_2O_2 crossover test conducted in chapter 4. Speculatively, Fe-N sites need to be present to catalyze the reaction in acidic milieu while metal-free N-sites can fulfill the reaction under alkaline conditions. Alternatively, the activity could be linked to pH-dependent protonation of the N-sites which, probably, loose their activity upon protonation. Hence, the active site is naturally present in alkaline media but needs to be protected (e.g., by coordination to iron) under acidic conditions.

[XXVI] Remaining Zn-sites may act as sacrificial sites enhancing the stability during ORR measurements.

[XXVII] The statement is only valid, if adsorption to active sites is actually relevant for the ORR-activity. Especially, in alkaline conditions, the ORR may be initiated by an outer sphere electron transfer. Hence, the work function could be one of the main factors dictating the activity in alkaline media.

6 Summary, Conclusions, and Perspectives

The basic motivation of the thesis on hand is to contribute to the development of energy storage and conversion devices for a sustainable future. Porous carbon materials play a major role in many of those devices. Among different characteristics, distinct porosity features, e.g., specific surface area (SSA), total pore volume (TPV), and the pore size distribution (PSD), are important to maximize the performance in the final device. In order to approach the aim to synthesize porous carbon materials in a sustainable fashion, the present thesis focused on biomass-derived precursors employing and developing the ionothermal carbonization. Three main topics were investigated which can be all related to the advanced synthesis of ionothermal carbon materials and their electrochemical application.

The first topic (chapter 3) addressed the possibility to precisely tailor the porosity of ionothermal carbon materials by an experimentally simple variation of the molar composition of the binary salt mixture employed as combined solvent/porogen. Different molar ratios lead to varied solvent properties which influence the mixing/demixing behavior of the liquid salt and the solidifying precursor phase. A decreased polarity of the salt leads to stronger demixing, yielding materials with lower SSA but larger pores. These effects can be used to introduce desirable transport porosity and/or to synthesize carbon materials with tunable SSAs. Moreover, the pore tailored materials can be regarded as chemically equivalent allowing the precise investigation of porosity dependent effects.

In section 3.3, the porosity of glucose derived carbon was tailored by changing the molar KCl-content present in KCl/ZnCl$_2$. The ionothermal carbons exhibit high TPV and SSA with values up to 1.73 cm^3 g^{-1} and 2160 m^2 g^{-1}, respectively. A steadily increased KCl-content led to the formation of larger pores on cost of smaller pores accompanied by a continuous widening of the pore system and a steady decrease in SSA. The largest TPV, that was ~ 50 % higher than the value of commercial activated carbons, was reached for the eutectic composition which was related to different melting kinetics for eutectic compared to non-eutectic salt mixtures. Interestingly, the SSA linearly depends on the relative amount of KCl present in the salt mixture giving a quantitative relation as a recipe for the fabrication of carbons with predictable SSAs in the range of ~ 900 to ~ 2100 m^2 g^{-1}. As all carbons are derived from the same precursor system, major influence on chemical properties of the carbon surface can be neglected. Moreover, the almost equal overall

macroscopic porosity allows reduction to only two parameters. In this regard, variations of electrochemical performances can be assigned to a trade-off between the SSA and the pore size range present. In a first proof of principle, the materials were applied as supercapacitor electrodes. Normalization on the SSA clearly showed the advantageous effect of the presence of larger pores, i.e., mass transport porosity, on the areal capacitance of the devices. Additionally, larger pores clearly lead to enhanced capacitance retentions.

In section 3.4, the developed pore tuning tool was expanded to nitrogen doped carbons employing the nucleobase adenine as precursor and adequate $NaCl/ZnCl_2$ salt mixtures as combined solvent/porogen. The results not only showed that the developed pore tailoring tool for ionothermal carbons can be employed for different salts and precursors, but also led to the exploration that pore tuning has a strong influence on the electrocatalytic activity towards the oxygen reduction reaction (ORR) which is the crucial reaction in fuel cells. The application of adenine as biomass derived precursor and the eutectic $NaCl/ZnCl_2$ as combined solvent/porogen led to highly porous nitrogen doped carbons (NDCs) with outstanding SSAs of 2900 m^2 g^{-1} rendering the material as an "all-surface-area" NDC. The changed molar amount of NaCl present in the salt mixture led to an opening of the pore system but again hardly influenced the chemical nature of the obtained materials. Both effects are in line with the results discussed for the glucose derived materials. Intriguingly, for the adenine derived carbons, the eutectic salt melt does not lead to the TPV maximum, further confirming that the porosity tailoring is caused by the alteration of the properties (polarities) of the liquid salt phase. Moreover, the material synthesized with 60 mol% NaCl combines outstanding porosity features with a SSA and TPV of 2540 m^2 g^{-1} and 5.19 cm^3 g^{-1}, respectively. The TPV is $4-5$ times higher than the typical value of commercial activated carbons, and implies a volume ratio of $\sim 1:10$ between carbon and molten salt. Interestingly, electron microscopy data indicated that the carbon forms the dispersing phase throughout the synthesis leading to the expression of a high internal salt phase ionothermal carbonization. Presumably, the developed pore tuning tool is neither restricted to a specific precursor, nor to a specific salt mixture. Furthermore, the porosity tailoring seems to be independent of which component, i.e., salt (glucose derived system) or carbon (adenine derived system), forms the dispersing phase. The porosity of the adenine derived NDCs had a strong influence on the electrocatalytic performance as shown by ORR-experiments in alkaline medium revealing that tailoring of open pores as compared to bottle-neck pores strongly enhances the performance (section 3.4.2). The material with the optimized pore system, despite possessing a

relatively low SSA, was selective towards the desired four electron ORR-process, showed good stability, and revealed a half-wave potential ($E_{1/2}$) of ~ 0.88 V (vs. RHE). The achieved $E_{1/2}$ implies an electrochemical efficiency of ~ 72 % at 50 % current density, one of the best values reported for biomass based NDCs so far. Furthermore, these findings indicate that it may be interesting to revise previously reported porous ORR-catalysts regarding an optimization of the pore properties. Moreover, the pore shape dependent activities render N_2-physisoption as a facile and widely accessible tool to predict/optimize the porosity of NDCs regarding their ORR-performance.

Generally, a variation of the molar ratio is facile and can be conducted precisely, allowing the synthesis of fine pore tuned materials in the mesopore region. Furthermore, the ionothermal synthesis is a one-step approach only requiring aqueous washing as a post-treatment, and a possible recycling of the salt. This demonstrates great advantages of ionothermal pore tuning compared to other porogenic carbonization methods.

The second topic (chapter 4) addressed the investigation of the not-yet unraveled mechanism of the oxygen reduction reaction. The herein developed H_2O_2 crossover test can be regarded as a quick method to analyze if H_2O_2 is formed as an intermediate or not using a simple half-cell test by means of the rotating disc electrode. Furthermore, the procedure displays an accelerated stability test for the catalyst materials although the exact degradation mechanism is still under debate.

The tests were conducted with a commercial platinum catalyst (Pt/C), a high performance iron doped NDC (Fe-NDC) known from literature, and a herein synthesized nucleobase derived Fe-NDC. In acidic media, mechanistic studies with both Fe-NDC catalysts were rather difficult due to the concurrent degradation of the catalysts induced by the present H_2O_2. Nonetheless, the measurements pointed to intermediately formed H_2O_2 for the Fe-NDCs which explains the usually observed strong degradation of those materials when tested under acidic conditions. Although preliminary, the results also pointed to an involved intermediate H_2O_2 in case of Pt/C that is against common believe. Contrarily, the results in alkaline media clearly showed that both Fe-NDC catalysts catalyze the ORR according to the favored direct four electron pathway. Hence, the ORR for (the studied) Fe-NDCs followed a different pathway in acidic than in alkaline media which may be connected to different involved active sites, respectively. Moreover, the results revealed that the strongly improved ORR-activity of (Fe-)NDCs in alkaline media (when compared to acidic media) cannot be explained by a strongly improved H_2O_2 in alkaline media as

stated by Ramaswamy *et al.* Presumably, the large difference is caused by different adsorbing species, i.e., O_2 in acidic media and $O_2^{\cdot-}$ in alkaline media.

The third topic (chapter 5) addressed the expansion of the used salts for the ionothermal approach towards hydrated calcium and magnesium chloride. Adenine was used as molecular precursor yielding highly porous NDC materials. The most interesting fact of the so-called extended ionothermal synthesis is the possibility to create a secondary templating effect due to intermediate salt recrystallization. Herein, the ionothermal approach is a combination of liquid templating by means of sol-gel synthesis with an *in-situ* formed solid scaffold. Moreover, the concept of active site implementation by a facile low-temperature metalation employing the obtained NDCs as solid ligands could be shown for the first time in the context of ORR.

The employment of calcium chloride dihydrate (CaCl$_2$DH) strongly enhanced the yield and changed the product morphology when compared to the NDC synthesized with pristine CaCl$_2$. Both effects can be linked to the initial liquid state of the hydrated salt. Apparently, the presence of H_2O is crucial. Previously coming from polycondensation reactions and neglected, it enhances the yield and allows for porogenesis due to the formation of low melting hydrates. Moreover, the unique morphology locally observed for the adenine derived NDC synthesized with CaCl$_2$DH could be linked to the desired secondary templating effect induced by the salt hydrate. The secondary templating effect was even more pronounced when employing hydrated magnesium chloride as discussed in the following paragraph.

The study conducted with adenine as precursor and different amounts of magnesium chloride hexahydrate (MgCl$_2$HH) as salt revealed the possibility to alter the porosity by simply changing the precursor to salt ratio (section 5.3.1), just like for the "classical" ionothermal approach employing ZnCl$_2$-containing salt mixtures (first topic, section 3.2.2). It comes to an extended ionothermal porogenesis due to *in-situ* crystallization of a solid salt templating phase. A major difference is that the final carbonization takes probably place in an all solid reaction mixture. In comparison to the materials synthesized with CaCl$_2$DH, the secondary templating effect was more pronounced and observed in the whole NDC material, especially if high MgCl$_2$HH to adenine ratios were employed. The obtained materials can be regarded as "fibrous" NDCs and show very promising porosity characteristics with SSAs and TPVs up to 2780 m^2 g^{-1} and 3.86 cm^3 g^{-1}, respectively. The investigation of the generation of the fibrous structure

points to a cooperative effect between the *in-situ* formed, solid hydrate phases and the decomposing (crosslinking) adenine. In a preliminary experiment, it could be shown that the introduction of an additional isothermal heating step can increase the size of the parallel aligned fibrous domains leading to a length-width aspect ratio of the NDC-fibers exceeding 1000:1.

The high SSA, TPV, and fiber-like structure of the adenine derived material synthesized in a 1:10 wt.-ratio with $MgCl_2HH$ points to a high accessibility of the present surface sites which should support the kinetics of the ORR. Indeed, the analysis of the ORR-activity in alkaline media revealed very fast kinetics, however, a relatively high ORR-overpotential (section 5.3.2). The activity strongly decreased when changing to the acidic media. Nonetheless, the high accessibility of the surface sites made those NDCs appealing for metalation experiments with iron at low temperature. The obtained metalated material showed a strongly improved acidic (and also a slightly improved alkaline) activity. The findings showed that the metalation approach can decouple the ligand, i.e., NDC, optimization from the introduction of iron ions, which can bypass the parasitic carbothermal reduction of iron-based active sites at high temperatures. The carbothermal reduction is currently one of the main factors limiting the accessibility of well-defined Fe-N sites, especially, at high active site concentrations. The optimized catalyst showed a promising $E_{1/2}$ of ~ 0.76 V (vs. RHE) standing for an electrochemical efficiency of ~ 62 % at 50 % current density. This value is close to the range of previously reported "high-performing" ORR-catalysts in acidic conditions. Moreover, the results indicate that different active centers are responsible for the ORR in alkaline conditions than in acidic conditions. Presumably, metal-free N-sites can fulfill the reaction under alkaline conditions whereas Fe-N sites need to be present to run the reaction in acidic milieu. Furthermore, the results are in line with the pH-dependent ORR-pathway as revealed during the aforementioned mechanistic studies conducted herein (second topic, chapter 4). Intriguingly, the metalated NDC with the highest activity showed almost no degradation during the stability measurement under operating conditions. The high stability coupled with the presence of distinct iron sites (or at least the absence of elemental iron and iron oxides) refers to the metalated Fe-NDC as very interesting candidate for the herein developed H_2O_2 crossover test.

In conclusion, the topics investigated in the thesis on hand underline the great potential of the ionothermal approach for the synthesis of highly porous (N-doped) carbon materials

with pore tailored and/or even structured porosities. In order to put the achieved porosities in literature context, the SSAs and TPVs of selected herein synthesized materials compared to reference carbon materials are depicted in Figure 6.1 (detailed information of the reference material can be found in Table S5 and Table S7).
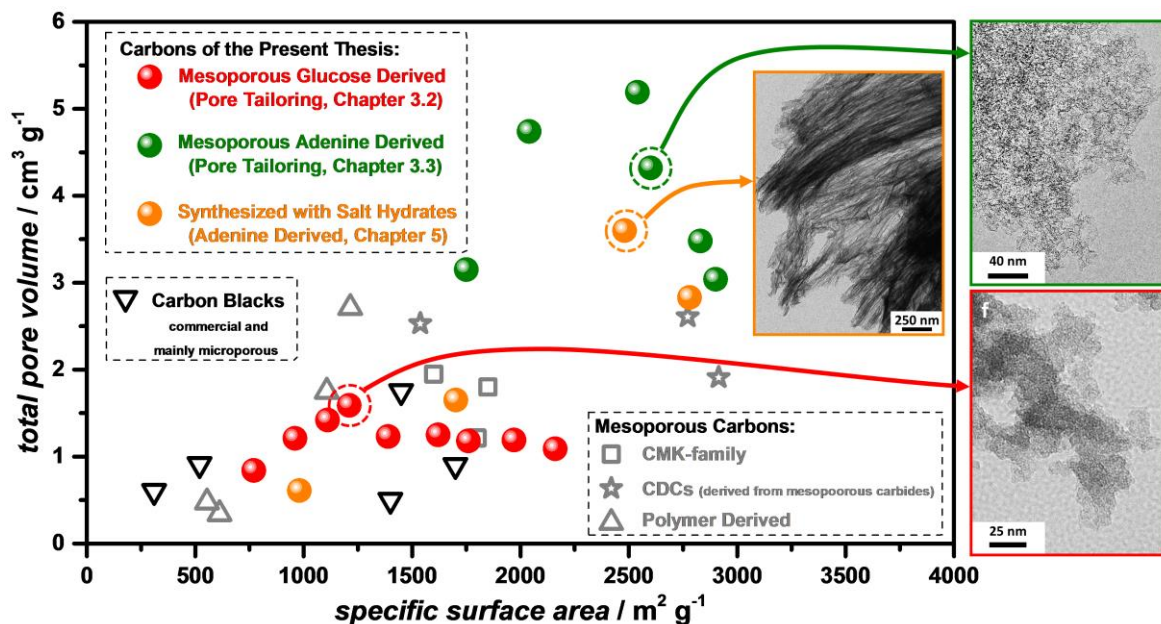
Figure 6.1 SSAs and TPVs (calculated from N_2-physisorption measurements) of selected ionothermal carbon materials prepared in the present thesis, mesoporous carbons from literature (including CMK-materials as well as micro- and mesoporous CDCs), and commercially available activated carbons (Carbon Blacks). Additionally, TEM images of selected ionothermal carbons are depicted showing the variety in structure/morphology of the obtained materials.

It has to be highlighted that the depicted pore tailored glucose derived carbons (red circles) and adenine derived NDCs (green circles), respectively, can be regarded as chemically equivalent. This indicates the large porosity range (by means of SSA and TPV) which can be covered by the facile pore tailoring tool developed in the present thesis, and point to the aforementioned possibility to employ the system for the investigation of porosity dependent effects in multiple application fields, e.g., capacitive deionization, lithium-sulfur batteries, and gas adsorption as well as in the herein already presented fields of supercapacitors and the oxygen reduction reaction. Moreover, all precursors applied are biomass derived being in line with a sustainable synthesis. Additionally, the ionothermal approach is scalable as demonstrated in the thesis on hand realizing batch sizes up to 130 g NDC. However, the presented pore tailoring methodology always led to larger pores at the cost of smaller pores. Thus, the SSA and pore size of the materials could not be tailored independently. If the already known salt to precursor ratio is added (investigated) as an additional parameter, it should be possible to gain a 3D diagram of SSA and present pore

sizes depending on the salt to precursor ratio and the salt composition. Thus, allowing the synthesis of porous (heteroatom doped) carbon material with independently predictable SSA and pore size. The extension of the ionothermal synthesis towards the employment of hydrates salt melts lead to highly porous NDCs with very interesting morphologies induced by a secondary templating effect (orange circles, Figure 6.1). Nonetheless, further investigations are necessary to gain deeper insights on the templating mechanism. Among different techniques, *in-situ* XRD could be used to follow the phase formation precisely. Furthermore, other precursor (N-containing and N-free) should be used to gain more insights on the importance of present N-functionalities in the precursor. Generally, the secondary templating effect is highly interesting, especially, regarding the possibility to obtain ordered structures in the future by the careful adjustment of the synthesis conditions. In context of electrochemical applications, new insights were gained in the present thesis regarding the porosity dependent ORR and the general ORR-mechanism. Generally, the herein developed H_2O_2 crossover test is highly interesting and should be studied by the application to more catalysts, ideally ones possessing a distinct active site, in the future. Furthermore, the involvement of H_2O_2 as an intermediate in the reaction pathway of all catalysts investigated in acidic conditions (even Pt/C) but its clear absence during the alkaline ORR points to the increasing relevance of the alkaline fuel cell sector in the future, especially, for the application of Pt-free catalysts. Indeed, the application of the adenine derived ionothermal carbon synthesized with a NaCl/ZnCl₂ mixture (80 mol% NaCl) as a cathode catalyst in a direct methanol fuel cell (operated under alkaline conditions) delivered very promising preliminary results. The experiments were conducted in a collaboration with the Fraunhofer Institute for Chemical Technology (Pfinztal, Germany) and showed that the NDC-based cathode can deliver ~ 40 % of the maximum power output when compared to the reference cathode which contained the same mass of platinum (in respect to the mass of NDC). However, the still rather poor stability of the NDC-based electrode needs to be improved in the future by optimizing the cathode ink formulation and the operation conditions of the fuel cell.

Overall, the thesis may pave the way towards highly porous carbon with tailor-made porosity materials prepared by an inexpensive and sustainable pathway, which can be applied in energy related field thereby supporting the needed expansion of the renewable energy sector.

7 References

(1) United Nations, *Department of Economic and Social Affairs, Population Division (2015)*, "World Population Prospects: The 2015 Revision".

(2) U.S. Energy Information Administration, *Center for Strategic and International Studies*, "International Energy Outlook 2016".

(3) Deane, J. P.; Ó Gallachóir, B. P.; McKeogh, E. J. *Renewable and Sustainable Energy Reviews* **2010**, *14*, 1293.

(4) Bundesverband der Energie- und Wasserwirtschaft (BDEW), *Foliensatz:* "Erneuerbare Energien und das EEG: Zahlen, Fakten, Grafiken (2016)", Germany (Berlin).

(5) Ibrahim, H.; Ilinca, A.; Perron, J. *Renewable and Sustainable Energy Reviews* **2008**, *12*, 1221.

(6) Bundesverband der Energie- und Wasserwirtschaft (BDEW), *Anhang zur BDEW-Presseinformation - "Im Januar wird am meisten Strom verbraucht" (vom 28. Januar 2010)*, "Durchschnittlicher Stromverbrauch von Januar bis Dezember", Germany (Berlin).

(7) Tzimas, E.; Filiou, C.; Peteves, S. D.; Veyret, J. B., "Hydrogen storage: state-of-the-art and future perspective", *Netherlands: European Cimmunities*, 2003.

(8) Schlögl, R. *ChemSusChem* **2010**, *3*, 209.

(9) Chu, S.; Majumdar, A. *Nature* **2012**, *488*, 294.

(10) Greenwood, N. N.; Earnshaw, A., "Chemistry of the Elements", *Elsevier Science*, 2012.

(11) Sicius, H., "Kohlenstoffgruppe: Elemente der vierten Hauptgruppe: Eine Reise durch das Periodensystem", *Springer Fachmedien Wiesbaden*, 2015.

(12) Riedel, E.; Janiak, C., "Anorganische Chemie", *De Gruyter*, 2011.

(13) Geim, A. K.; Novoselov, K. S. *Nature materials* **2007**, *6*, 183.

(14) Lu, A.-H.; Hao, G.-P.; Sun, Q.; Zhang, X.-Q.; Li, W.-C. *Macromolecular Chemistry and Physics* **2012**, *213*, 1107.

(15) Taylor, R.; Walton, D. R. M. *Nature* **1993**, *363*, 685.

(16) Thostenson, E. T.; Ren, Z.; Chou, T.-W. *Composites Science and Technology* **2001**, *61*, 1899.

(17) Chae, H. K.; Siberio-Perez, D. Y.; Kim, J.; Go, Y.; Eddaoudi, M.; Matzger, A. J.; O'Keeffe, M.; Yaghi, O. M. *Nature* **2004**, *427*, 523.

(18) Borchardt, L.; Oschatz, M.; Kaskel, S. *Materials Horizons* **2014**, *1*, 157.

(19) Dai, L.; Chang, D. W.; Baek, J.-B.; Lu, W. *Small* **2012**, *8*, 1130.

(20) Joo, S. H.; Choi, S. J.; Oh, I.; Kwak, J.; Liu, Z.; Terasaki, O.; Ryoo, R. *Nature* **2001**, *412*, 169.

(21) Liang, C.; Li, Z.; Dai, S. *Angewandte Chemie International Edition* **2008**, *47*, 3696.

(22) Morris, R. E.; Wheatley, P. S. *Angewandte Chemie International Edition* **2008**, *47*, 4966.

(23) Wei, L.; Sevilla, M.; Fuertes, A. B.; Mokaya, R.; Yushin, G. *Advanced Energy Materials* **2011**, *1*, 356.

(24) Zhang, P.; Yuan, J.; Fellinger, T.-P.; Antonietti, M.; Li, H.; Wang, Y. *Angewandte Chemie International Edition* **2013**, *52*, 6028.

(25) Holst, J. R.; Cooper, A. I. *Advanced Materials* **2010**, *22*, 5212.

(26) Thommes, M.; Kaneko, K.; Neimark Alexander, V.; Olivier James, P.; Rodriguez-Reinoso, F.; Rouquerol, J.; Sing Kenneth, S. W. *pac* **2015**, *87*, 1051.

(27) Ahmadpour, A.; Do, D. D. *Carbon* **1996**, *34*, 471.

(28) Rodríguez-Reinoso, F., "Production and Applications of Activated Carbons" in "Handbook of Porous Solids", *Wiley-VCH Verlag GmbH*, 2008.

(29) Caturla, F.; Molina-Sabio, M.; Rodríguez-Reinoso, F. *Carbon* **1991**, *29*, 999.

(30) Otowa, T.; Tanibata, R.; Itoh, M. *Gas Separation & Purification* **1993**, *7*, 241.

(31) Molina-Sabio, M.; RodRíguez-Reinoso, F.; Caturla, F.; Sellés, M. J. *Carbon* **1995**, *33*, 1105.

(32) Wang, J.; Kaskel, S. *Journal of Materials Chemistry* **2012**, *22*, 23710.

(33) Marsh, H.; Reinoso, F. R., "Activated Carbon", *Elsevier Science*, 2006.

(34) Kaneko, K. *Journal of Membrane Science* **1994**, *96*, 59.

(35) Kyotani, T. *Carbon* **2000**, *38*, 269.

(36) Schüth, F. *Angewandte Chemie International Edition* **2003**, *42*, 3604.

(37) Kresge, C. T.; Leonowicz, M. E.; Roth, W. J.; Vartuli, J. C.; Beck, J. S. *Nature* **1992**, *359*, 710.

(38) Kleitz, F.; Hei Choi, S.; Ryoo, R. *Chemical Communications* **2003**, 2136.

(39) Zhao, D.; Huo, Q.; Feng, J.; Chmelka, B. F.; Stucky, G. D. *Journal of the American Chemical Society* **1998**, *120*, 6024.

(40) Attard, G. S.; Glyde, J. C.; Goltner, C. G. *Nature* **1995**, *378*, 366.

(41) Huo, Q.; Margolese, D. I.; Ciesla, U.; Demuth, D. G.; Feng, P.; Gier, T. E.; Sieger, P.; Firouzi, A.; Chmelka, B. F. *Chemistry of Materials* **1994**, *6*, 1176.

(42) Moriguchi, I.; Ozono, A.; Mikuriya, K.; Teraoka, Y.; Kagawa, S.; Kodama, M. *Chemistry Letters* **1999**, *28*, 1171.

(43) Chuenchom, L.; Kraehnert, R.; Smarsly, B. M. *Soft Matter* **2012**, *8*, 10801.

(44) Lu, A. H.; Schüth, F. *Advanced Materials* **2006**, *18*, 1793.

(45) Gilbert, M. T.; Knox, J. H.; Kaur, B. *Chromatographia* **1982**, *16*, 138.

(46) Ryoo, R.; Joo, S. H.; Jun, S. *The Journal of Physical Chemistry B* **1999**, *103*, 7743.

(47) Jun, S.; Joo, S. H.; Ryoo, R.; Kruk, M.; Jaroniec, M.; Liu, Z.; Ohsuna, T.; Terasaki, O. *Journal of the American Chemical Society* **2000**, *122*, 10712.

(48) Lu, A. H.; Zhao, D.; Wan, Y., "Nanocasting: A Versatile Strategy for Creating Nanostructured Porous Materials", *Royal Society of Chemistry*, 2010.

(49) Stein, A. *Microporous and Mesoporous Materials* **2001**, *44–45*, 227.

(50) White, R. J.; Tauer, K.; Antonietti, M.; Titirici, M.-M. *Journal of the American Chemical Society* **2010**, *132*, 17360.

(51) Gogotsi, Y.; Nikitin, A.; Ye, H.; Zhou, W.; Fischer, J. E.; Yi, B.; Foley, H. C.; Barsoum, M. W. *Nature materials* **2003**, *2*, 591.

(52) Presser, V.; Heon, M.; Gogotsi, Y. *Advanced Functional Materials* **2011**, *21*, 810.

(53) Krawiec, P.; Kockrick, E.; Borchardt, L.; Geiger, D.; Corma, A.; Kaskel, S. *The Journal of Physical Chemistry C* **2009**, *113*, 7755.

(54) Oschatz, M.; Kockrick, E.; Rose, M.; Borchardt, L.; Klein, N.; Senkovska, I.; Freudenberg, T.; Korenblit, Y.; Yushin, G.; Kaskel, S. *Carbon* **2010**, *48*, 3987.

(55) Fechler, N.; Fellinger, T.-P.; Antonietti, M. *Advanced Materials* **2013**, *25*, 75.

(56) Rogers, R. D.; Seddon, K. R. *Science* **2003**, *302*, 792.

(57) Morris, R. E. *Chemical Communications* **2009**, 2990.

(58) Abbott, A. P.; Boothby, D.; Capper, G.; Davies, D. L.; Rasheed, R. K. *Journal of the American Chemical Society* **2004**, *126*, 9142.

(59) Abbott, A. P.; Capper, G.; Davies, D. L.; Rasheed, R. K.; Tambyrajah, V. *Chemical Communications* **2003**, 70.

(60) Yin, Y.; Alivisatos, A. P. *Nature* **2005**, *437*, 664.

(61) Cushing, B. L.; Kolesnichenko, V. L.; O'Connor, C. J. *Chemical Reviews* **2004**, *104*, 3893.

(62) Park, J.; Joo, J.; Kwon, S. G.; Jang, Y.; Hyeon, T. *Angewandte Chemie International Edition* **2007**, *46*, 4630.

(63) Liu, X.; Fechler, N.; Antonietti, M. *Chemical Society Reviews* **2013**, *42*, 8237.

(64) Liu, X.; Giordano, C.; Antonietti, M. *Small* **2014**, *10*, 193.

(65)   Liu, X.; Antonietti, M. *Advanced Materials* **2013**, *25*, 6284.

(66)   Liu, X.; Antonietti, M. *Carbon* **2014**, *69*, 460.

(67)   Liu, X.; Fechler, N.; Antonietti, M.; Willinger, M. G.; Schlogl, R. *Materials Horizons* **2016**, *3*, 214.

(68)   Gong, K.; Du, F.; Xia, Z.; Durstock, M.; Dai, L. *Science* **2009**, *323*, 760.

(69)   Kang, K. Y.; Lee, B. I.; Lee, J. S. *Carbon* **2009**, *47*, 1171.

(70)   Cheon, J. Y.; Kim, J. H.; Kim, J. H.; Goddeti, K. C.; Park, J. Y.; Joo, S. H. *Journal of the American Chemical Society* **2014**, *136*, 8875.

(71)   Paraknowitsch, J. P.; Thomas, A. *Macromolecular Chemistry and Physics* **2012**, *213*, 1132.

(72)   Czerw, R.; Terrones, M.; Charlier, J. C.; Blase, X.; Foley, B.; Kamalakaran, R.; Grobert, N.; Terrones, H.; Tekleab, D.; Ajayan, P. M.; Blau, W.; Rühle, M.; Carroll, D. L. *Nano Letters* **2001**, *1*, 457.

(73)   Li, X.-H.; Antonietti, M. *Chemical Society Reviews* **2013**, *42*, 6593.

(74)   Frackowiak, E. *Physical Chemistry Chemical Physics* **2007**, *9*, 1774.

(75)   Manthiram, A.; Fu, Y.; Su, Y.-S. *Accounts of Chemical Research* **2013**, *46*, 1125.

(76)   Karden, E.; Ploumen, S.; Fricke, B.; Miller, T.; Snyder, K. *Journal of Power Sources* **2007**, *168*, 2.

(77)   Debe, M. K. *Nature* **2012**, *486*, 43.

(78)   Gu, W.; Yushin, G. *Wiley Interdisciplinary Reviews: Energy and Environment* **2014**, *3*, 424.

(79)   Frackowiak, E.; Abbas, Q.; Béguin, F. *Journal of Energy Chemistry* **2013**, *22*, 226.

(80)   Simon, P.; Gogotsi, Y. *Nature materials* **2008**, *7*, 845.

(81)   Boukhalfa, S.; Evanoff, K.; Yushin, G. *Energy & Environmental Science* **2012**, *5*, 6872.

(82)   Pinkert, K.; Giebeler, L.; Herklotz, M.; Oswald, S.; Thomas, J.; Meier, A.; Borchardt, L.; Kaskel, S.; Ehrenberg, H.; Eckert, J. *Journal of Materials Chemistry A* **2013**, *1*, 4904.

(83)   Hu, Y.; Liu, H.; Ke, Q.; Wang, J. *Journal of Materials Chemistry A* **2014**, *2*, 11753.

(84)   Atlhues, H., "Anorganische Materialien für elektrische Energiespeicherung", *lecture manuscript - TU Dresden*, SS 2013.

(85)   Béguin, F.; Presser, V.; Balducci, A.; Frackowiak, E. *Advanced Materials* **2014**, *26*, 2219.

(86)   Zhang, L.; Yang, X.; Zhang, F.; Long, G.; Zhang, T.; Leng, K.; Zhang, Y.; Huang, Y.; Ma, Y.; Zhang, M.; Chen, Y. *Journal of the American Chemical Society* **2013**, *135*, 5921.

(87)   Wang, D.-W.; Li, F.; Liu, M.; Lu, G. Q.; Cheng, H.-M. *Angewandte Chemie International Edition* **2008**, *47*, 373.

(88)   Frackowiak, E.; Béguin, F. *Carbon* **2001**, *39*, 937.

(89)   Bonakdarpour, A.; Lefevre, M.; Yang, R.; Jaouen, F.; Dahn, T.; Dodelet, J.-P.; Dahn, J. R. *Electrochemical and Solid-State Letters* **2008**, *11*, B105.

(90)   Bing, Y.; Liu, H.; Zhang, L.; Ghosh, D.; Zhang, J. *Chemical Society Reviews* **2010**, *39*, 2184.

(91)   Liang, H. W.; Zhuang, X.; Bruller, S.; Feng, X.; Mullen, K. *Nature Communications* **2014**, *5*, 4973.

(92)   Duan, J.; Chen, S.; Jaroniec, M.; Qiao, S. Z. *ACS Catalysis* **2015**, *5*, 5207.

(93)   Jiao, Y.; Zheng, Y.; Jaroniec, M.; Qiao, S. Z. *Chemical Society Reviews* **2015**, *44*, 2060.

(94)   Wang, D.-W.; Su, D. *Energy & Environmental Science* **2014**, *7*, 576.

(95)   Elumeeva, K.; Ren, J. W.; Antonietti, M.; Fellinger, T. P. *Chemelectrochem* **2015**, *2*, 584.

(96) Lefèvre, M.; Proietti, E.; Jaouen, F.; Dodelet, J.-P. *Science* **2009**, *324*, 71.

(97) He, W.; Jiang, C.; Wang, J.; Lu, L. *Angewandte Chemie International Edition* **2014**, *53*, 9503.

(98) Ning, R.; Ge, C.; Liu, Q.; Tian, J.; Asiri, A. M.; Alamry, K. A.; Li, C. M.; Sun, X. *Carbon* **2014**, *78*, 60.

(99) Eisenberg, D.; Stroek, W.; Geels, N. J.; Tanase, S.; Ferbinteanu, M.; Teat, S. J.; Mettraux, P.; Yan, N.; Rothenberg, G. *Physical Chemistry Chemical Physics* **2016**, *18*, 20778.

(100) Zhang, Y.; Ge, J.; Wang, L.; Wang, D.; Ding, F.; Tao, X.; Chen, W. *Scientific Reports* **2013**, *3*, 2771.

(101) Geng, D.; Chen, Y.; Chen, Y.; Li, Y.; Li, R.; Sun, X.; Ye, S.; Knights, S. *Energy & Environmental Science* **2011**, *4*, 760.

(102) Lai, L.; Potts, J. R.; Zhan, D.; Wang, L.; Poh, C. K.; Tang, C.; Gong, H.; Shen, Z.; Lin, J.; Ruoff, R. S. *Energy & Environmental Science* **2012**, *5*, 7936.

(103) Lin, Z.; Waller, G. H.; Liu, Y.; Liu, M.; Wong, C.-p. *Nano Energy* **2013**, *2*, 241.

(104) Park, M.; Lee, T.; Kim, B.-S. *Nanoscale* **2013**, *5*, 12255.

(105) Yasuda, S.; Yu, L.; Kim, J.; Murakoshi, K. *Chemical Communications* **2013**, *49*, 9627.

(106) Guo, D.; Shibuya, R.; Akiba, C.; Saji, S.; Kondo, T.; Nakamura, J. *Science* **2016**, *351*, 361.

(107) Bard, A. J.; Faulkner, L. R., "Electrochemical Methods: Fundamentals and Applications", *Wiley*, 2000.

(108) Bruckenstein, S.; Miller, B. *Accounts of Chemical Research* **1977**, *10*, 54.

(109) Treimer, S.; Tang, A.; Johnson, D. C. *Electroanalysis* **2002**, *14*, 165.

(110) Levich, V. G., "Physicochemical Hydrodynamics", *Prentice-Hall*, 1962.

(111) Mayrhofer, K. J. J.; Strmcnik, D.; Blizanac, B. B.; Stamenkovic, V.; Arenz, M.; Markovic, N. M. *Electrochimica Acta* **2008**, *53*, 3181.

(112) Pampel, J.; Fellinger, T.-P. *Advanced Energy Materials* **2016**, *6*, 1502389.

(113) Shui, J.; Wang, M.; Du, F.; Dai, L. *Science Advances* **2015**, *1*, e1400129.

(114) Albery, W. J.; Hitchman, M. L., "Ring-disc electrodes", *Clarendon Press*, 1971.

(115) Fechler, N., *PhD thesis (2012)*, "Salts as highly diverse porogens: functional ionic liquid-derived carbons and carbon-based composites for energy-related applications"

(116) Elumeeva, K.; Fechler, N.; Fellinger, T. P.; Antonietti, M. *Materials Horizons* **2014**, *1*, 588.

(117) Antonietti, M.; Fechler, N.; Fellinger, T.-P. *Chemistry of Materials* **2014**, *26*, 196.

(118) Fellinger, T.-P., *Journal of Sol-Gel Science and Technology* **2016**, *published online*, doi: 10.1007/s10971-016-4115-z.

(119) Pekala, R. W. *Journal of Materials Science* **1989**, *24*, 3221.

(120) Pekala, R. W.; Alviso, C. T.; Kong, F. M.; Hulsey, S. S. *Journal of Non-Crystalline Solids* **1992**, *145*, 90.

(121) Tamon, H.; Ishizaka, H.; Mikami, M.; Okazaki, M. *Carbon* **1997**, *35*, 791.

(122) LaMer, V. K.; Dinegar, R. H. *Journal of the American Chemical Society* **1950**, *72*, 4847.

(123) Antonietti, M.; Titirici, M.-M. *Comptes Rendus Chimie* **2010**, *13*, 167.

(124) Titirici, M.-M.; Antonietti, M.; Baccile, N. *Green Chemistry* **2008**, *10*, 1204.

(125) Baccile, N.; Antonietti, M.; Titirici, M.-M. *ChemSusChem* **2010**, *3*, 246.

(126) Fellinger, T.-P.; White, R. J.; Titirici, M.-M.; Antonietti, M. *Advanced Functional Materials* **2012**, *22*, 3254.

(127) White, R. J.; Yoshizawa, N.; Antonietti, M.; Titirici, M.-M. *Green Chemistry* **2011**, *13*, 2428.

(128) Fechler, N.; Wohlgemuth, S.-A.; Jaker, P.; Antonietti, M. *Journal of Materials Chemistry A* **2013**, *1*, 9418.

(129) Schipper, F., *PhD thesis (2014)*, "Biomass derived carbon for new energy storage technologies".

(130) Anastas, P. T.; Warner, J. C., "Green Chemistry: Theory and Practice", *Oxford University Press*, 2000.

(131) Porada, S.; Schipper, F.; Aslan, M.; Antonietti, M.; Presser, V.; Fellinger, T.-P. *ChemSusChem* **2015**, *8*, 1867.

(132) Schipper, F.; Vizintin, A.; Ren, J.; Dominko, R.; Fellinger, T. P. *ChemSusChem* **2015**, *8*, 3077.

(133) Ullmann, F.; Gerhartz, W.; Yamamoto, Y. S.; Campbell, F. T.; Pfefferkorn, R.; Rounsaville, J. F., "Ullmann's Encyclopedia of industrial chemistry", *VCH*, 1995.

(134) Ma, Z.; Zhang, H.; Yang, Z.; Zhang, Y.; Yu, B.; Liu, Z. *Journal of Materials Chemistry A* **2014**, *2*, 19324.

(135) Bazuła, P. A.; Lu, A.-H.; Nitz, J.-J.; Schüth, F. *Microporous and Mesoporous Materials* **2008**, *108*, 266.

(136) Deng, Y.; Yu, T.; Wan, Y.; Shi, Y.; Meng, Y.; Gu, D.; Zhang, L.; Huang, Y.; Liu, C.; Wu, X.; Zhao, D. *Journal of the American Chemical Society* **2007**, *129*, 1690.

(137) Kang, M.; Yi, S. H.; Lee, H. I.; Yie, J. E.; Kim, J. M. *Chemical Communications* **2002**, 1944.

(138) Kruk, M.; Jaroniec, M.; Bereznitski, Y. *Journal of Colloid and Interface Science* **1996**, *182*, 282.

(139) Tamon, H.; Ishizaka, H.; Yamamoto, T.; Suzuki, T. *Carbon* **1999**, *37*, 2049.

(140) Wu, D.; Liang, Y.; Yang, X.; Zou, C.; Li, Z.; Lv, G.; Zeng, X.; Fu, R. *Langmuir* **2008**, *24*, 2967.

(141) Vižintin, A., *PhD thesis (2016)*, "Surface Modified Materials for Lithium Sulfur Batteries".

(142) Yang, W.; Fellinger, T.-P.; Antonietti, M. *Journal of the American Chemical Society* **2011**, *133*, 206.

(143) Maruyama, J.; Fukui, N.; Kawaguchi, M.; Abe, I. *Journal of Power Sources* **2009**, *194*, 655.

(144) Shen, M.; Zheng, L.-R.; He, W.; Ruan, C.; Jiang, C.; Ai, K.; Lu, L. *Nano Energy* **2015**, *17*, 120.

(145) Robelin, C.; Chartrand, P. *The Journal of Chemical Thermodynamics* **2011**, *43*, 377.

(146) Janz, G. J., "Molten salts handbook", *Academic Press*, 1967.

(147) Shaw, S. J.; Perry, G. S. *Thermochimica Acta* **1990**, *157*, 329.

(148) Gattermann, L. *Justus Liebigs Annalen der Chemie* **1906**, *347*, 347.

(149) Borchardt, L.; Oschatz, M.; Lohe, M.; Presser, V.; Gogotsi, Y.; Kaskel, S. *Carbon* **2012**, *50*, 3987.

(150) Oschatz, M.; Borchardt, L.; Pinkert, K.; Thieme, S.; Lohe, M. R.; Hoffmann, C.; Benusch, M.; Wisser, F. M.; Ziegler, C.; Giebeler, L.; Rümmeli, M. H.; Eckert, J.; Eychmüller, A.; Kaskel, S. *Advanced Energy Materials* **2014**, *4*, 1300645.

(151) Reichardt, C.; Welton, T., "Solvents and Solvent Effects in Organic Chemistry", *Wiley*, 2011.

(152) Behrendt, F.; Neubauer, Y.; Oevermann, M.; Wilmes, B.; Zobel, N. *Chemical Engineering & Technology* **2008**, *31*, 667.

(153) Graglia, M.; Pampel, J.; Hantke, T.; Fellinger, T. P.; Esposito, D. *ACS Nano* **2016**, *10*, 4364.

(154) Zakzeski, J.; Bruijnincx, P. C. A.; Jongerius, A. L.; Weckhuysen, B. M. *Chemical Reviews* **2010**, *110*, 3552.

(155) Pampel, J.; Denton, C.; Fellinger, T.-P. *Carbon* **2016**, *107*, 288.

(156) Fischer, S.; Leipner, H.; Thümmler, K.; Brendler, E.; Peters, J. *Cellulose* **2003**, *10*, 227.

(157) Molina-Sabio, M.; Rodríguez-Reinoso, F. *Colloids and Surfaces A: Physicochemical and Engineering Aspects* **2004**, *241*, 15.

(158) Ahmadpour, A.; Do, D. D. *Carbon* **1997**, *35*, 1723.

(159) Ji, Y.; Li, T.; Zhu, L.; Wang, X.; Lin, Q. *Applied Surface Science* **2007**, *254*, 506.

(160) Zhang, Z.; Veith, G. M.; Brown, G. M.; Fulvio, P. F.; Hillesheim, P. C.; Dai, S.; Overbury, S. H. *Chemical Communications* **2014**, *50*, 1469.

(161) Fellinger, T.-P.; Su, D. S.; Engenhorst, M.; Gautam, D.; Schlogl, R.; Antonietti, M. *Journal of Materials Chemistry* **2012**, *22*, 23996.

(162) Chung, H. T.; Won, J. H.; Zelenay, P. *Nature Communications* **2013**, *4*, 1922.

(163) Liu, J.; Sun, X.; Song, P.; Zhang, Y.; Xing, W.; Xu, W. *Advanced Materials* **2013**, *25*, 6879.

(164) Liu, X.; Zhou, Y.; Zhou, W.; Li, L.; Huang, S.; Chen, S. *Nanoscale* **2015**, *7*, 6136.

(165) Fellinger, T.-P.; Hasché, F.; Strasser, P.; Antonietti, M. *Journal of the American Chemical Society* **2012**, *134*, 4072.

(166) Strickland, K.; Miner, E.; Jia, Q.; Tylus, U.; Ramaswamy, N.; Liang, W.; Sougrati, M.-T.; Jaouen, F.; Mukerjee, S. *Nature Communications* **2015**, *6*.

(167) Ranjbar Sahraie, N.; Paraknowitsch, J. P.; Göbel, C.; Thomas, A.; Strasser, P. *Journal of the American Chemical Society* **2014**, *136*, 14486.

(168) Liang, J.; Zheng, Y.; Chen, J.; Liu, J.; Hulicova-Jurcakova, D.; Jaroniec, M.; Qiao, S. Z. *Angewandte Chemie International Edition* **2012**, *51*, 3892.

(169) Wei, W.; Liang, H.; Parvez, K.; Zhuang, X.; Feng, X.; Müllen, K. *Angewandte Chemie International Edition* **2014**, *53*, 1570.

(170) Ferrero, G. A.; Preuss, K.; Fuertes, A. B.; Sevilla, M.; Titirici, M. M. *Journal of Materials Chemistry A* **2016**.

(171) Wu, K.-H.; Wang, D.-W.; Su, D.-S.; Gentle, I. R. *ChemSusChem* **2015**, *8*, 2772.

(172) Dai, L.; Xue, Y.; Qu, L.; Choi, H. J.; Baek, J. B. *Chemical Reviews* **2015**, *115*, 4823.

(173) Jaouen, F.; Proietti, E.; Lefevre, M.; Chenitz, R.; Dodelet, J.-P.; Wu, G.; Chung, H. T.; Johnston, C. M.; Zelenay, P. *Energy & Environmental Science* **2011**, *4*, 114.

(174) Katsounaros, I.; Schneider, W. B.; Meier, J. C.; Benedikt, U.; Biedermann, P. U.; Auer, A. A.; Mayrhofer, K. J. J. *Physical Chemistry Chemical Physics* **2012**, *14*, 7384.

(175) Wroblowa, H. S.; Yen Chi, P.; Razumney, G. *Journal of Electroanalytical Chemistry and Interfacial Electrochemistry* **1976**, *69*, 195.

(176) Zitolo, A.; Goellner, V.; Armel, V.; Sougrati, M. T.; Mineva, T.; Stievano, L.; Fonda, E.; Jaouen, F. *Nature materials* **2015**, *14*, 937.

(177) Jia, Q.; Ramaswamy, N.; Hafiz, H.; Tylus, U.; Strickland, K.; Wu, G.; Barbiellini, B.; Bansil, A.; Holby, E. F.; Zelenay, P.; Mukerjee, S. *ACS Nano* **2015**, *9*, 12496.

(178) Jia, Q.; Ramaswamy, N.; Tylus, U.; Strickland, K.; Li, J.; Serov, A.; Artyushkova, K.; Atanassov, P.; Anibal, J.; Gumeci, C.; Barton, S. C.; Sougrati, M.-T.; Jaouen, F.; Halevi, B.; Mukerjee, S., *Nano Energy* **2016**, *published online*, doi: 10.1016/j.nanoen.2016.03.025.

(179) Holby, E. F.; Zelenay, P., *Nano Energy* **2016**, *published online*, doi: 10.1016/j.nanoen.2016.05.025.

(180) Tylus, U.; Jia, Q.; Strickland, K.; Ramaswamy, N.; Serov, A.; Atanassov, P.; Mukerjee, S. *The Journal of Physical Chemistry C* **2014**, *118*, 8999.

(181) Jaouen, F.; Dodelet, J.-P. *The Journal of Physical Chemistry C* **2009**, *113*, 15422.

(182) Ramaswamy, N.; Mukerjee, S. *Advances in Physical Chemistry* **2012**, *2012*, 17.

(183) Muthukrishnan, A.; Nabae, Y.; Okajima, T.; Ohsaka, T. *ACS Catalysis* **2015**, *5*, 5194.

(184) Jaouen, F.; Goellner, V.; Lefèvre, M.; Herranz, J.; Proietti, E.; Dodelet, J. P. *Electrochimica Acta* **2013**, *87*, 619.

(185) Jiang, J.; Yi, B. *Journal of Electroanalytical Chemistry* **2005**, *577*, 107.

(186) Damjanovic, A.; Genshaw, M. A.; Bockris, J. O. M. *Journal of The Electrochemical Society* **1967**, *114*, 466.

(187) Goellner, V.; Armel, V.; Zitolo, A.; Fonda, E.; Jaouen, F. *Journal of The Electrochemical Society* **2015**, *162*, H403.

(188) Choi, C. H.; Baldizzone, C.; Grote, J. P.; Schuppert, A. K.; Jaouen, F.; Mayrhofer, K. J. *Angewandte Chemie International Edition* **2015**, *54*, 12753.

(189) Wiberg, E.; Wiberg, N., "Inorganic Chemistry", *Academic Press*, 2001.

(190) Choi, C. H.; Lim, H.-K.; Chung, M. W.; Park, J. C.; Shin, H.; Kim, H.; Woo, S. I. *Journal of the American Chemical Society* **2014**, *136*, 9070.

(191) Marcus, R. A. *The Journal of Chemical Physics* **1956**, *24*, 966.

(192) Blizanac, B. B.; Ross, P. N.; Markovic, N. M. *Electrochimica Acta* **2007**, *52*, 2264.

(193) Lannung, A. *Zeitschrift für anorganische und allgemeine Chemie* **1936**, *228*, 1.

(194) van Essen, V. M.; Cot Gores, J.; Bleijendaal, L. P. J.; Zondag, H. A.; Schuitema, R.; Bakker, M.; van Helden, W. G. J. *ASME 2009 3rd International Conference on Energy Sustainability* **2009**, *2*, 825.

(195) Sugimoto, K.; Dinnebier, R. E.; Hanson, J. C. *Acta Crystallographica Section B* **2007**, *63*, 235.

(196) da Silva Lacerda, V.; López-Sotelo, J. B.; Correa-Guimarães, A.; Hernández-Navarro, S.; Sánchez-Báscones, M.; Navas-Gracia, L. M.; Martín-Ramos, P.; Martín-Gil, J. *Journal of Environmental Management* **2015**, *155*, 67.

(197) Kim, J.-W.; Sohn, M.-H.; Kim, D.-S.; Sohn, S.-M.; Kwon, Y.-S. *Journal of Hazardous Materials* **2001**, *85*, 301.

(198) Sahira, J.; Mandira, A.; Prasad, P. B.; Ram, P. R. *Research Journal of Chemical Sciences* **2013**, *3*, 19.

(199) Karthikeyan, S.; Sivakumar, P.; Palanisamy, P. N. *E-Journal of Chemistry* **2008**, *5*, 409.

(200) Gumus, R. H.; Okpeku, I. *Advances in Chemical Engineering and Science* **2015**, *5*, 51.

(201) Valix, M.; Cheung, W. H.; McKay, G. *Langmuir* **2006**, *22*, 4574.

(202) Huang, Y. a.; Yang, F.; Xu, Z.; Shen, J. *Journal of Colloid and Interface Science* **2011**, *363*, 193.

(203) Liu, J.; Deng, Y.; Li, X.; Wang, L. *ACS Sustainable Chemistry & Engineering* **2016**, *4*, 177.

(204) Bansal, R. C.; Donnet, J. B.; Stoeckli, F., "Active Carbon", *Taylor & Francis*, 1988.

(205) Mise, S. R. *Journal of the IPHE* **2008**, *4*, 5.

(206) Ellingham, H. J. T. *Journal of the Society of Chemical Industry* **1944**, *63*, 125.

(207) Sharonov, E. V.; Aristov, I. Y. *Reaction Kinetics and Catalysis Letters* **2005**, *85*, 183.

(208) Savilov, S. V.; Arkhipova, E. A.; Ivanov, A. S.; Maslakov, K. I.; Shen, Z.; Aldoshin, S. M.; Lunin, V. V. *Materials Research Bulletin* **2015**, *69*, 7.

(209) Jung, M.-J.; Im Ji, S.; Jeong, E.; Jin, H.; Lee, Y.-S. *Carbon letters* **2009**, *10*, 217.

(210) Sun, J.; Simon, S. L. *Thermochimica Acta* **2007**, *463*, 32.

(211) Huang, Q.; Lu, G.; Wang, J.; Yu, J. *Journal of Analytical and Applied Pyrolysis* **2011**, *91*, 159.

(212) Mastropietro, T. F.; Armentano, D.; Marino, N.; De Munno, G. *Polyhedron* **2007**, *26*, 4945.

(213) Sahraie, N. R.; Kramm, U. I.; Steinberg, J.; Zhang, Y.; Thomas, A.; Reier, T.; Paraknowitsch, J. P.; Strasser, P. *Nature Communications* **2015**, *6*, 8618.

(214) Serov, A.; Artyushkova, K.; Niangar, E.; Wang, C.; Dale, N.; Jaouen, F.; Sougrati, M.-T.; Jia, Q.; Mukerjee, S.; Atanassov, P. *Nano Energy* **2015**, *16*, 293.

(215) Zhao, D.; Shui, J.-L.; Grabstanowicz, L. R.; Chen, C.; Commet, S. M.; Xu, T.; Lu, J.; Liu, D.-J. *Advanced Materials* **2014**, *26*, 1093.

(216) Yuan, S.; Shui, J.-L.; Grabstanowicz, L.; Chen, C.; Commet, S.; Reprogle, B.; Xu, T.; Yu, L.; Liu, D.-J. *Angewandte Chemie International Edition* **2013**, *52*, 8349.

(217) Kramm, U. I.; Herrmann-Geppert, I.; Behrends, J.; Lips, K.; Fiechter, S.; Bogdanoff, P. *Journal of the American Chemical Society* **2016**, *138*, 635.

(218) Sing, K. S. W. *pac* **1985**, *57*, 603

(219) Giesche, H., "Mercury Porosimetry" in "Handbook of Porous Solids", *Wiley-VCH Verlag GmbH*, 2008.

(220) Thompson, M.; Walsh, J. N., "Handbook of inductively coupled plasma spectrometry", *Blackie*, 1989.

(221) Long, G. J., "Basic Concepts of Mössbauer Spectroscopy" in "Mössbauer Spectroscopy Applied to Inorganic Chemistry", *Springer US*, 1984.

(222) Cornell, R. M.; Schwertmann, U., "The Iron Oxides: Structure, Properties, Reactions, Occurrences and Uses", *Wiley*, 2006.

I Appendix

I.I Abbreviations

(HR)TEM	-	(high resolution) transmission electron microscopy
$CaCl_2DH$	-	calcium chloride dihydrate
CV	-	cyclovoltammetry
EtOH	-	ethanol
GuaHCl	-	guanine hydrochloride
HAADF	-	high-angular annular-dark field
HPRR	-	hydrogen peroxide reduction reaction
KAIST	-	Korea Advanced Institute of Science and Technology
LSV	-	linear sweep voltammetry
MeOH	-	methanol
$MgCl_2HH$	-	magnesium chloride hexahydrate
ORR	-	oxygen reduction reaction
PSD	-	pore size distribution
PXRD	-	powder X-ray diffraction
QSDFT	-	quenched solid density functional theory
RDE	-	rotating disc electrode
RHE	-	reversible hydrogen electrode
RRDE	-	rotating ring-disc electrode
SC	-	supercapacitor
SEM	-	scanning electron microscopy
SSA	-	specific surface area
STEM	-	scanning transmission electron microscopy
TPV	-	total pore volume
TRGO	-	thermally reduced graphene oxide
TUM	-	Technical University of Munich

I.II Applied Methods

Nitrogen Physisorption

Nitrogen physisorption is a widely employed and powerful tool to characterize the porosity characteristics of a specimen. The method delivers information regarding the specific surface area (SSA), the total pore volume (TPV), and the pore size distribution (PSD) of the sample. Generally, the adsorbed volume of the adsorbate (N_2) on the adsorbent (herein carbon materials) is measured in respect to the relative pressure ($p\,p_0^{-1}$) of the adsorptive. In order to ensure the equilibrium conditions for N_2-gas, the measurements are typically conducted at 77 K and ambient pressure. Thus, only weak interactions, i.e., Van der Waals interaction, occur between the adsorbate and the adsorbent rendering the process as physisorption and leading to multilayer adsorption. Typically, nitrogen is dosed in small portions into the measurement cell containing the sample and the adsorbed volume is detected in respect to the relative pressure. The pressure is first increased till $p\,p_0^{-1} \sim 1.0$. The thereby recorded points represent the adsorption branch of the isotherm. Usually, the pressure is also lowered again to measure the desorption behavior of the sample. Due to the types of pores present, the desorption can be shifted to lower pressures giving rise to a hysteresis. The shape of the adsorption isotherm generally represents the interactions of the adsorbate with the adsorbent and is further influenced by the pore size and pore shape. In 1985, the IUPAC introduced the widely employed concept to distinguish pores by their internal diameter (*d*) into three types: micropores (d < 2 nm), mesopores (2 nm < d < 50 nm), and macropores (d > 50 nm).[218] Moreover, they published six types of isotherm which, however, were revised, and extended to eight isotherm types in 2015 (Figure S1).[26]
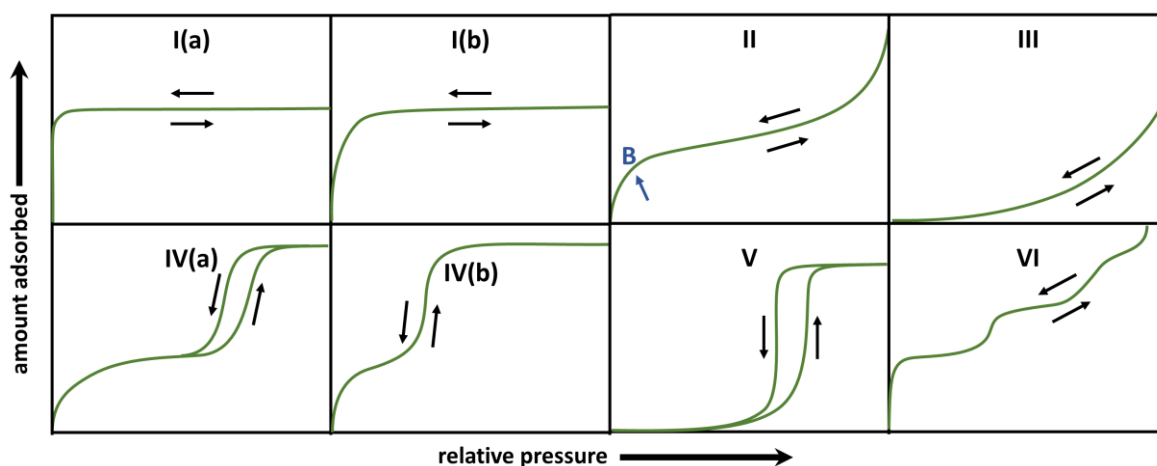
Figure S1 Classification of physisorption isotherms according to IUPAC (adapted from[26]).

A reversible type I isotherm is observed for microporous solids with almost no external surface. The very steep uptake at low pressures can be related to the enhanced nitrogen adsorption due to the presence of narrow micropores, and the limiting value of the adsorbed volume at higher pressures to the complete filling of the present pores. Type I(a) represents materials possessing mainly pores with diameters of $d < \sim 1nm$. Contrarily, type I(b) indicates the presence of larger micropores and even some small mesopores with diameters smaller than ~ 2.5 nm. A reversible type II isotherm points to a non-porous or solely macroporous specimen. The shape is based on unrestricted monolayer-multilayer adsorption over the whole pressure range. A sharp knee (point B) can be connected to the completion of the monolayer coverage. A type III isotherm indicates the presence of a non-porous or macroporous sample coupled with very weak adsorbate-adsorbent interactions. Hence, the adsorbate molecules are clustered around the most favorable adsorption site and no point B exits. A type IV isotherm is representative for mesoporous materials. Here, the shape is determined by the adsorbate-adsorbent interactions and by the interactions between the adsorptive molecules in the condensed state. The initial adsorption proceeds similar to a type II isotherm but at higher pressures pore condensation (inside the mesopores) occurs. Pore condensation implies that a gas condenses inside a pore at pressures lower than the bulk liquid's saturation pressure (p_0). If the pores exceed a critical size ($d > \sim 4$ nm), capillary condensation is coupled with the formation of a hysteresis, giving rise to a type IV(a) isotherm. If the present mesopores are smaller, a reversible type IV(b) isotherm is observed. At high pressures, the adsorbed volume for a type IV isotherm generally reaches a saturation plateau. Type V and type VI isotherms are rather uncommon, and characteristic for a porous sample with weak adsorbent-adsorbate interactions and for a layer-by-layer adsorption on a non-porous specimen, respectively.

Generally, it is to consider that the different isotherm types (and also the various hysteresis types discussed in the following paragraph) are idealized and "real" materials possess very often intermediate or combined shapes of different isotherm types. The shape and the pressure range of the hysteresis can be related to the (meso-)pore size, the pore shape, and the pore connectivity. According to IUPAC, the hysteresis loops can be classified into six different types (Figure S2).[26]
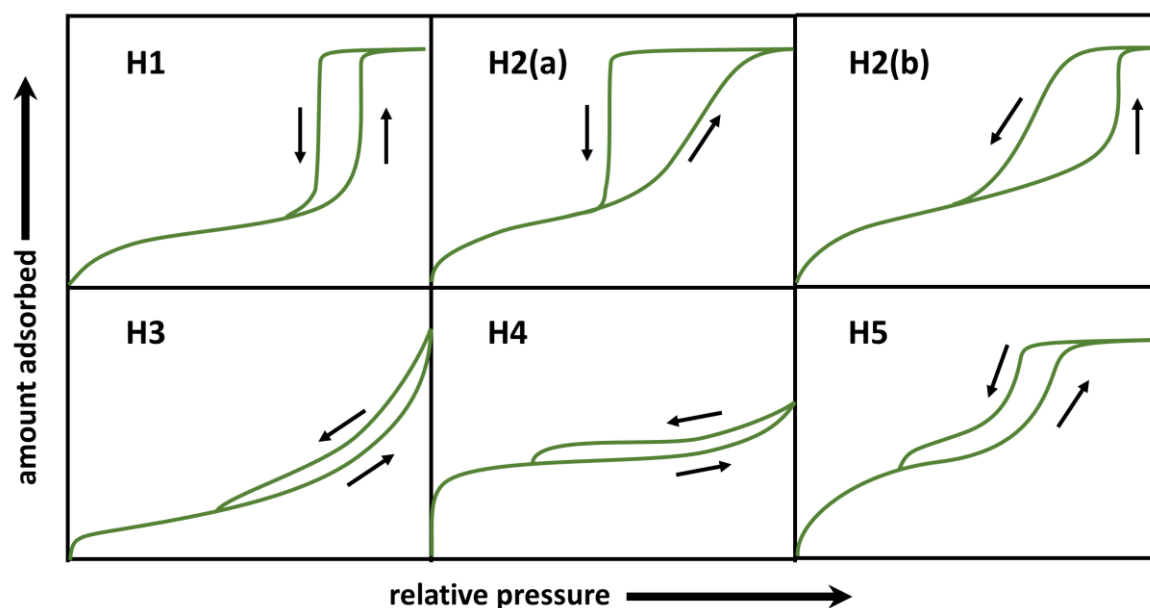
Figure S2 Classification of physisorption hysteresis loops according to IUPAC (adapted from[26]).

A very steep uptake due to pore condensation, a delayed desorption, and parallel adsorption and desorption branches are characteristic for a H1 hysteresis loop indicating the presence of a narrow range of uniform mesopores. Contrarily, a H2 hysteresis loop points to the presence of more complex structures and pore connectivity effects. Generally, a H2 loop indicates pores (or pore networks) possessing a different pore diameter when compared to the diameter of the poreneck. A H2(a) loop implies the presence of different sized mesopores as reflected by a condensation spread over a relatively large pressure range during the adsorption. Contrarily, the desorption branch, occurring at lower pressures, is very steep, and non-parallel when compared to the adsorption branch. Depending on the relative pressure range of the desorption branch, a H2(a) loop can either be connected to cavitation induced pore emptying (p p_0^{-1} ~ 0.4 – 0.5) or to pore-blocking in a narrow range of porenecks (p p_0^{-1} > 0.5). Generally, the poreneck is smaller than the pore diameter giving rise to the expression of bottleneck-pores (cf. section 3.4.1). A H(2)b loop (classically, described as an inverse H2 hysteresis) is also connected to pore-blocking, but, all (meso-)pores possess very similar pore diameters coupled with different sized porenecks. A classical H3 hysteresis exhibits an adsorption branch of a type II isotherm and a cavitation induced lower limit of the desorption branch. This points either to the presence of non-rigid aggregates of plate-like particles or to macropores which are not completely filled at high pressures. The H4 loop is very similar to the H3 loop. However, in a H4 loop the adsorption branch represents rather a combined type I – type II isotherm indicating the presence of micro- and mesopores. The H5 type is rather uncommon but

exhibits a distinct shape which can be connected to the co-existence of open- and blocked mesopores.

Moreover, the points recorded during a N_2-phyisisorption measurement allow the calculation of the SSA by the employment of different models. Generally, the adsorbed volume can be related to the thickness of the adsorbed mono- or multilayer and thus to the area covered (ergo, the surface area of the specimen). The most commonly employed method nowadays is the one developed by Brunauer, Emmett, and Teller (BET-theory). Furthermore, various models with distinct approximations allow the calculation of the pore size distribution as also briefly discussed in section 3.2.2.

N_2-physisorption measurements were performed on a Quantachrome Quadrasorb SI porosimeter. Prior to the measurements, the samples were degassed in vacuum at 150 °C for 20 h. The SSA was determined according to the multipoint Brunauer-Emmett-Teller (BET) model using the data points suggested by the *micropore BET assistant* of the software (however, not exceeding the range $p\ p_0^{-1} > 0.30$). The quenched solid density functional theory (QSDFT) model for slit shaped, spherical and cylindrical pores, provided by Quantachrome data reduction software QuadraWin Version 5.11, served for the calculation of the pore size distributions (PSDs) using the adsorption branch. The TPV was calculated at $p\ p_0^{-1} = 0.99$.

Mercury Porosimetry (Intrusion)

Mercury porosimetry is a useful method to collect information about the porosity characteristics (e.g., volume, and size distribution) and the bulk-density of a specimen. In contrast to N_2-physisorption pores of larger sizes are accessible with diameters in the range of ~ 0.005 to $\sim 300\ \mu m$. Generally, porosimetry is based on the pressure dependent intrusion of a non-wetting liquid in the pores of a sample. Mercury is especially qualified due to its non-wetting character, high surface tension, and large contact angle. Due to these characteristics, mercury only penetrates pores if it is forced by an employed pressure.[219] The pressure needed to force mercury to penetrate a certain pore size is inversely proportional to the size of the pore. Hence, larger pores are penetrated at low mercury pressures whereas large pressures are needed to fill small pores. The Washburn equation connects the pressure applied (p) with the pore size (d_{pore}) penetrated (Equation (S-1)).

$$d_{pore} = 2d\sin\frac{-4\,\sigma cos\theta}{p} \qquad\qquad \text{(S-1)}$$

Here, σ and Θ stand for the surface tension and the contact angle of mercury, respectively. The measurement of the volume of mercury which intrudes into the specimen at a certain pressure allows the determination of the volume of pores possessing the corresponding diameter.

Mercury intrusion experiments were performed at the Department of Chemistry, Graduate School of Science, Kyoto University (Japan) on a Micromeritics AutoPore IV 9500 in a mercury pressure range between 0.035 and 227 MPa reflecting a pore radius between 335 and 0.0055 µm.

Light Microscopy

Light microscopy allows the visualization of objects which are too small for the resolution range of the human eye. In a classical light microscope, the image is formed through a series of lenses. The often employed bright-field mode implies that the light of a bright source is directed to a lens (the condenser) which is located beneath the stage. The subsequent light path goes through the sample, through an objective lens, and finally to the eye through another magnifying lens (the ocular). The contrast of the recorded image is based on the different absorption of light mainly caused by pigmentation and/or the thickness of the sample. Moreover, specially designed microscope stages, e.g., temperature controlled stages, allow the direct visual recording of ongoing changes of the specimen.

Light microscopy studies were performed on an Olympus BX41TF combined with a Linkam THMS600 temperature controlled stage under N2-atmosphere.

Scanning Electron Microscopy / (Scanning) Transmission Electron Microscopy

Scanning electron microscopy (SEM) and (scanning) transmission electron microscopy ((S)TEM,) are both based on interactions of electrons with the specimen. Generally, electrons are generated by an electron gun, accelerated by an electromagnetic field, and vertically directed (as well as focused) towards the sample by electromagnetic lenses.

SEM is based on the detection of different radiations created in the specimen upon interaction with the incident electron beam. Thus, information about the morphology and

the chemical properties of the specimen can be gathered. Due to collisions between the incident electron beam and valence electrons of the sample, secondary electrons are created. Those electrons possess relatively low energy and can only escape the specimen if they are generated close to the surface. Local curvatures (e.g., edges or plates) facilitate the release of electrons. Hence, the quantity of created electrons depends on the morphology of the sample which leads to an intensity contrast in the recorded image representing topological information of the specimen's surface. Furthermore, incident electrons are directly scattered on the nucleus and radiated in all spatial directions. The so-called backscattered electrons possess larger energy than secondary electrons. Hence, the can escape the sample from much higher depth. The quantity of created backscattered electrons depends on the atomic number of the elements. Heavier elements will create more electrons, thus, appearing brighter than light elements in the detected image. The obtained image represents the so-called material-contrast of the specimen. Qualitative information about the sample can be obtained by energy-dispersive X-ray (EDX). Here, the incident electron beam excites an electron from an inner shell of an atom. The electron is ejected thus generating an electron hole in the inner shell. Subsequently, an electron from an outer shell occupies the generated electron hole. The difference in energy between the inner- and outer shell is released in the form of X-rays. The X-ray wavelength is specific for each element leading to qualitative information. The X-ray intensities of the different elements present in a sample allow conclusions regarding the quantitative occurrence of the elements. Moreover, EDX-mapping can be used to study the local distribution of elements in the sample.

SEM measurements were conducted on a LEO 1550-Gemini system from Zeiss (acceleration voltage: 0.1 to 30 kV). Non-conductive samples were sputtered with Au/Pd prior to the measurement.

In **TEM** the electrons transmitting a very thin sample are detected leading even to higher resolution when compared to SEM. The resolution can be adjusted by the acceleration voltage where larger voltage generally allows higher resolutions. The contrast of the detected image depends on the thickness and the elemental composition of the specimen. In the typically applied bright field mode, the non-scattered (or only slightly scattered) electrons are detected. Thus, thicker regions appear darker than thinner domains, and low-scattering (lighter) elements appear brighter than heavier elements. The STEM-mode allows high-angular annular-dark field (HAADF) imaging where the scattered electrons are

detected. Thus, the contrast is reversed when compared to bright field imaging, and one can clearly differentiate between lighter and heavier elements.

TEM measurements were conducted at the Technical University Berlin (Germany) with a TEM type Zeiss EM 912Ω operated at 120 kV acceleration voltage. HRTEM imaging was performed on a FEI Tecnai G² 20 S-TWIN equipped with a LaB6 cathode operated at 200 kV. HAADF imaging was performed at the National Institute of Chemistry Slovenia using a HR(S)TEM type Joel ARM 200 CF.

Powder X-Ray Diffraction

X-ray diffraction (XRD) is a widely employed method to characterize crystalline substances. XRD is based on the interaction between an X-ray beam and the electrons of the atoms in the specimen. The X-ray beam is generated by high-energy electrons which hit a material and are thereby deaccelerated. The therein occurring processes result in the radiation of a continuous X-ray spectrum and in a for each element specific line-spectrum of X-rays. The individual X-rays of the line-spectrum are monochromatic and are used for the X-ray diffraction experiment.

If the monochromatic X-ray hits the specimen, elastic and inelastic interactions occur. Inelastic effects cause coherent scattering representing the basis for all diffraction experiments. Generally, diffraction occurs if the wavelength of the radiation is in the same range as the distance of the diffraction lattice. Since the atom distances in crystals are in the same range as the wavelength of X-rays, crystalline materials represent a three-dimensional diffraction lattice during a XRD experiment. It is to consider that constructive interference only occurs if the optical path difference (Δ) is an integral multiple of the wavelength (λ). Hence, positive interference exits only for specific diffraction angles (Θ). The mathematical description between the interlayer spacing (d) of the atomic planes and λ (in respect to Θ) is given by Bragg's Law (Equation (S-2)).

$$\Delta = n\lambda = 2d\sin(\Theta) \quad (n \in N) \quad\quad\quad (S-2)$$

Positive interferences lead to reflections in the recorded diffractogram revealing the characteristic diffraction pattern of the investigated specimen.

X-ray diffraction (XRD) measurements were conducted on a Bruker D8 Advance device (equipped with a scintillator detector) between 3.0° and 70.0° 2θ applying a step of 0.05° and a measurement time of 2 s per step using Cu-Kα radiation ($\lambda = 1.5418$ Å). The

ICDD PDF 4+ was used as reference data base, and the corresponding ICDD numbers of the employed reference patterns can be found in Table S3.

Elemental Analysis and Inductively Coupled Plasma Optical Emission Spectrometry

Elemental microanalysis is a facile combustion method for quantifying the elemental composition in terms of carbon, nitrogen, hydrogen, and sulfur content. The specimens are catalytically burnt in an O_2-atmosphere at temperatures over 1000 °C. The formed gaseous products (CO_2, H_2O, SO_2, and N_2) are separated and precisely quantified by heat conductance detectors. Inductively coupled plasma optical emission spectrometry (ICP-OES) is based on the element-specific emission of electromagnetic radiations of excited atoms. Typically, the specimen is injected as an aerosol into an argon plasma. Hence, atomization takes place and the formed atoms are excited and ionized. The intensity of the elemental-specific radiation allows the direct quantification of the corresponding element when compared with calibration solutions.[220]

Elemental analysis (C, H, N, S) was conducted by combustion analysis using a Vario El Micro device. ICP-OES measurements were performed on a ICP-OES Optima 2100 DV from Perkin Elmer. Prior to the measurement, acidic chemical digestion for 12 h at 40 °C was conducted with the specimens for solubilisation.

X-Ray Photoelectron Spectroscopy

X-ray photoelectron spectroscopy (XPS) is a surface sensible, ultra-high vacuum technique allowing the quantitative investigation of the elemental composition and the electronic state of the elements. The specimens are irradiated with X-rays photons in the energy range of 100 to 10,000 eV. The high energy mainly leads to the release of core-level electrons whose kinetic energy (E_{kin}) is measured. The difference between the (known) energy of the incident photon (E_{phot}) and the detected E_{kin} corresponds to the binding energy (E_{bind}). Due to the conversation of energy, E_{bind} can be calculated according to Equation (S-3).

$$E_{bind} = E_{phot} - E_{kin} \qquad \text{(S-3)}$$

E_{bind} is characteristic for each element leading to qualitative and quantitative inferences. Furthermore, the fine structure of the signal of one element depends on its surrounding allowing conclusions regarding specific binding motifs.

XPS measurements were conducted at the University of Vigo (Spain) on a Thermo-VG Scientific ESCALAB 250 X-ray photoelectron spectrometer (Thermo Electron, U.K.) using Al Kα X-ray source (1486.6 eV) and the carbon peak as internal reference. In order to quantify the different N-sites, high resolution N1 s spectra were measured and the experimental error was obtained by the signal to noise ratio. The corresponding noise of the different N1s scans was calculated by the standard variation of the raw signal in a region where no N-peaks occur (390 - 395 eV). The program XPSPEAK 4.1 was used for deconvolution of the N1s-spectra in four different N-species: pyridinic-N (398.5 eV); pyrrolic-N (399.9 eV); graphitic-N (401.3 eV), oxidized-N (403.3 eV).

Mößbauer Spectroscopy

Mößbauer spectroscopy is based on the Mößbauer and the Doppler effect. Typically, a solid sample is exposed to gamma-rays and the intensity of the transmitted radiation is detected. Hereby, the atoms of the gamma-ray source have to be of the same isotope as the element absorbing the radiation (ergo, the element of interest). Hence, only some elements (precisely, some isotopes) can be investigated by Mößbauer experiments, among which ^{57}Fe is by far the most studied one. The emitting (source) nuclei and the absorbing one have different energy levels caused by a different chemical environment. Due to the extremely narrow spectral linewidth of gamma-rays, those rather small energy differences result in a largely changed absorption behavior. In order to bring the two nuclei again in resonance, the energy of the incident gamma-ray has to be precisely adjusted. This can be realized by the Doppler effect induced by the acceleration of the emitting source through a range of different velocities. The obtained spectrum depicts the gamma ray intensity in respect to the source velocity. Velocities which represent a resonant energy of the specimen cause adsorption of the gamma-rays resulting in a dip in the spectrum. The amount, positions, and intensities of the dips allow conclusions regarding the electronic surrounding of the investigated element, such as, the oxidation state, the spin state, and the electronegativity of the ligands.[221]

^{57}Fe Transmission Mößbauer spectra were measured at the Institute Charles Gerhardt Montpellier (France) with a source of ^{57}Co in rhodium metal. During all

measurements, the source was kept at ambient temperature (300 K). The sample was either kept at room temperature, or cooled down to 5 K using a liquid helium flow cryostat. The spectrometer was operated in the constant acceleration mode with a triangular velocity waveform. The velocity scale was calibrated with the magnetically split sextet spectrum of a high-purity α-Fe foil as the reference absorber at room temperature.

Thermogravimetric Analysis

Thermogravimetric analysis (TGA) allows to monitor different thermodynamic events such as phase transition, thermal stability as well as the adsorption and desorption of gases. Usually, the temperature- and time dependent mass loss of a specimen is recorded.

Thermogravimetric analysis was performed on a Netzsch TG 209 F1 device under constant N_2-flow applying a heating rate of 10 K min^{-1}.

Eletrochemical Methods

The employment of the **rotating (ring-)disc electrode** (RDE/RRDE) to investigate the oxygen reduction reaction of a catalyst as well as the corresponding equations were introduced in section 1.3.2. Moreover, the principles of cyclicvoltammetry (CV) and linear sweep voltammetry (LSV) were presented. In the thesis on hand, RDE/RRDE measurements were conducted at a three electrode rotating disk/ring-disk electrode set up (Gamry Instruments). A graphite rod (diameter, 6 mm) and Ag/AgCl$_{sat}$ were used as counter and reference electrode, respectively. All the potentials were converted to the RHE scale and corrected to the internal resistance (IR) according to Equation (S-**4**).

$$E_{IR-corr} = (E_{applied} - i \cdot IR) + 0.198\,V + pH \cdot 0.059\,V \qquad (S\text{-}4)$$

Here, $E_{IR\text{-}corr}$ and $E_{applied}$ represent the real potential at the working electrode (vs. RHE) and the applied potential (vs. Ag/AgCl$_{sat}$), respectively. Furthermore, i is the absolute current measured and pH stands for pH of the electrolyte. The IR value includes the solution-, wire- and/or substrate-resistance and was determined by impedance measurements at high frequencies prior to the measurement. In order to obtain stable CVs, the samples were first cycled for 10 cycles between 0.0 and 1.0 V (vs. RHE) in O_2-saturated electrolyte. If not mentioned elsewise, CVs were received with a sweep rate 50 mV s^{-1} and LSVs with 5 mv s^{-1}, respectively. Before each measurement the working electrode was kept at the

starting potential for 5 s. As mentioned in section 1.3.2, LSVs were corrected to the double layer capacitance by subtracting the LSV obtained in N_2-saturated solution. Typically, the limiting current and the onset potential were determined from the LSV (recorded with a rotation rate of 1600 rpm) at 0.3 V (vs. RHE) and at 100 $\mu A\ cm^{-2}$, respectively. The collection efficiency of the RRDE set-up was determined as 36 % by the use of LSVs at different rotation rates in 10 mmol potassium ferrocyanide solution. During RRDE measurements the ring current was kept at 1.5 V (vs. RHE) to oxidize possibly formed H_2O_2.

For catalyst ink preparation, 5 mg of the ball-milled catalyst was typically dispersed in 350 µl of absolute ethanol and 95 µl of Nafion® solution. The ink was sonicated for 30 min to assure a homogenous dispersion and dropcasted onto the well-polished glassy carbon electrodes. For RDE-electrodes (diameter, 5.0 mm) 5 µl and for RRDE-electrodes (diameter, 5.7 mm) 6.5 µl were employed resulting in a catalyst loading of ~ 290 $\mu g\ cm^{-2}$ for both cases. If not stated elsewise, the reference experiments were conducted with a commercial 20 wt.% Pt on carbon (Pt/C; Alfa Aesar) with a Pt/C loading of ~ 290 $\mu g\ cm^{-2}$. If a different loading should be investigated, all the parameters (e.g., nafion to carbon ratio and volume of dropcasted ink) were kept constant and only the amount of ethanol present in the ink was varied.

The LSVs obtained at different rotation rates (400, 800, 1200, 1600, and 2000 rpm) were used to determine the number of transferred electrons according to the Koutecky-Levich analysis (cf. Equation (1.17)). Therein, the faradaic constant (F) and the geometric area of the RDE electrode (A) are 96,485 As mol^{-1} and 0.196 cm^2, respectively. The values of the other constant (however, electrolyte dependent) parameters are summarized in Table S1. The same parameters were also used to calculate the corresponding Levich currents of a four electron process (cf. Equation (1.16)).

Table S1 Values of the electrolyte-dependent parameters for the calculation of the Levich current and the number of transferred electrons according to the Koutecky-Levich analysis: saturated oxygen concentration (c_o), kinematic viscosity of oxygen (v), and diffusion coefficient of oxygen (D_F).

electrolyte	c_o / mol m^3	v / m^2 s^{-1}	D_F / m^2 s^{-1}
0.1 M KOH	1.21	$1.008 \cdot 10^{-6}$	$1.86 \cdot 10^{-9}$
0.05 M H_2SO_4	1.26	$1.009 \cdot 10^{-6}$	$1.93 \cdot 10^{-9}$
0.1 M $HClO_4$	1.18	$8.93 \cdot 10^{-7}$	$1.86 \cdot 10^{-9}$

The principle of **supercapacitors** as well as the corresponding equations were introduced in section 1.3.1. In the thesis on hand, the supercapacitor performance was tested in a two electrode Swagelok-cell and recorded on a Biologic VMP3. Two electrodes were prepared for one measurement. Typically, a freshly prepared and sonicated suspension of 5 wt.% polyvinylidenefluoride and 95 wt.% sample in 100 µl acetone was dropcasted on a platinum disk (d = 1 cm) to achieve a mass loading of 5 mg cm^{-2} per electrode. The suspension was first dried in air and further dried in a vacuum oven at 60 °C for 60 min. Two carbon electrodes and a filter paper separator were assembled sandwich like in Swagelok-cell using 40 µl of 1 M sulfuric acid as electrolyte. The cyclovoltammetry tests were conducted with varied sweep rates in a voltage window of 1 V. The specific capacitances (C_{sp}) of the investigated carbons were obtained from the recorded cyclovoltammograms according to Equation (S-5).

$$C_{Sp} = 2 \frac{\int i \cdot dt}{m_e \Delta V v_s} \quad\quad\quad\quad \text{(S-5)}$$

Here, i and t represent current and time, respectively. ΔV stands for the potential range, m_e is the mass of a single electrode and v_s represents the scan rate.

I.III Experimental Part

Chemicals

Table S2 Employed chemicals in the thesis on hand.

substance	*chemical formula*	*purity grade*	*supplier*
1-10 phenanthroline	$C_{12}H_8N_2$	$\geq 99\ \%$	Aldrich
absolute ethanol	CH_3CH_2OH	$\geq 99.8\ \%$	Sigma Aldrich
adenine	$C_5H_5N_5$	$\geq 99\ \%$	Sigma Aldrich
calcium chloride	$CaCl_2$	$96\ \%$	Acros Organics
calcium chloride dihydrate	$CaCl_2 \cdot 2\ H_2O$	$99.5\ \%$	AppliChem
D-glucosamine hydrochloride	$C_6H_{13}NO_5 \cdot HCl$	$\geq 98+\ \%$	Alfa Aesar
D-glucose	$C_6H_{12}O_6$	$> 99.5\ \%$	Roth
guanine hydrochloride	$C_5H_5N_5O \cdot HCl$	$99\ \%$	Alfa Aesar
hydrogen peroxide solution	$H_2O_2\ (30\ wt.\%)$	Emsure®	Merck
iron (II) acetate	$Fe(CH_3COO)_2$	$\geq 99.99\ \%$	Aldrich
iron (II) chloride tetrahydrate	$FeCl_2 \cdot 4\ H_2O$	$\geq 99.0\ \%$	Sigma Aldrich
iron (III) chloride	$FeCl_3$	$> 97\ \%$	VWR
lithium chloride	$LiCl$	$98+\ \%$	Alfa Aesar
magnesium chloride hexahydrate	$MgCl_2 \cdot 6\ H_2O$	$98+\ \%$	Acros Organics
methanol	CH_3OH	$> 99.9\ \%$	Merck
Nafion® solution	-	5 wt.% in lower aliphatic alcohols and water	Sigma Aldrich
potassium chloride	KCl	$> 99.5\ \%$	Roth
potassium hydroxide solution	$0.1\ M\ KOH$	Titripur®	Merck
sodium chloride	$NaCl$	$\geq 99.8\ \%$	Sigma Aldrich
sulfuric acid solution	$0.05\ M\ H_2SO_4$	Titripur®	Merck
zinc chloride	$ZnCl_2$	$98+\ \%$	Alfa Aesar

ICDD Numbers of Reference PXRD Patterns

Table S3 ICDD numbers of the PXRD reference patterns used in the present thesis.

substance	*ICDD number*
graphite	00-056-0159
MgO	04-016-6275
$Mg(OH)_2$	00-007-0239
$MgCl_2$	04-008-7748
$MgCl_2 \cdot 2\ H_2O$	00-061-0221
$MgCl_2 \cdot 4\ H_2O$	04-015-2200
$MgCl_2 \cdot 6\ H_2O$	04-010-1481
$Mg(OH)Cl$	00-003-0100
$MgCl_2NH_4Cl \cdot 6\ H_2O$	01-080-5969

3.2 Precursor Systems

3.2.1 Glucose and Glucosamine Derived Ionothermal Carbons

Synthesis

Prior to the experiments the salt mixture of $KCl/ZnCl_2$ (eutectic, 46 mol% KCl) was freshly prepared by through grinding in a glove box. Typically, 800 mg of precursor, D-glucose or glucosamine hydrochloride, were mixed with the according mass of the eutectic $KCl/ZnCl_2$ mixture to achieve the aimed precursor to salt wt.-ratio. The resulting mixture was transferred in a ceramic crucible (50 ml; VWR) and heat treated under nitrogen atmosphere. The sample was ramped with 2.5 K min^{-1} to 900 °C and the final dwelling was conducted for 1 h at 900 °C. After cooling to RT, the mostly black monolithic structure was carefully grinded, washed twice with 1 L of deionized water and dried in vacuum at 60 °C overnight.

3.2.2 Nucleobase Derived Ionothermal Carbons

Synthesis

The salt mixtures of $KCl/ZnCl_2$ (nearly eutectic, 50 mol% KCl), $LiCl/ZnCl_2$ (eutectic, 22 mol% LiCl) and $NaCl/ZnCl_2$ (nearly eutectic, 42 mol% NaCl) were prepared by carefully grinding the respective salts in the glove box. Typically, 800 mg of the

nucleobases (guanine hydrochloride or adenine) were thoroughly mixed with 8000 mg of the respective salt mixture. The heat treatment and work-up of the samples was conducted as described in the experimental part for 3.2.1.

3.3 Glucose Derived Carbons with Tailored Porosity

Synthesis

Prior to the experiments the salt mixture of KCl/ZnCl$_2$ with varied KCl-content was freshly prepared by through grinding in a glove box. Typically, 800 mg D-glucose were carefully mixed with 4000 mg salt mixture. The heat treatment and the work-up of the samples was conducted as described in the experimental part for 3.2.1. However, an additional isothermal annealing for 2 h at 350 °C was introduced during the typical heating procedure (except for the samples identified by the suffix L).

Electrochemical Measurements (Supercapacitor)

The ink- and electrode preparation as well as the measurement procedure were conducted as described in section I.II (electrochemical methods).

3.4 Adenine Derived Nitrogen Doped Carbons with Tailored Porosity

Synthesis

Prior to the experiments the salt mixture of NaCl/ZnCl$_2$ with varied NaCl-content was freshly prepared by through grinding in a glove box. Typically, 800 mg adenine were carefully mixed with 8000 mg salt mixture. The heat treatment and the work-up of the samples were conducted as described in the experimental part for 3.2.1.

Electrochemical Measurements (Oxygen Reduction Reaction)

The ink- and electrode preparation as well as the measurement procedure were conducted as described in section I.II (electrochemical methods). The stability was evaluated by chronoamperometric measurements in O$_2$-saturated electrolyte at 0.8 V (vs. RHE) for 12 h employing a rotation rate of 1600 rpm.

4 Hydrogen Peroxide Crossover Test

Synthesis of Fe-NDC_lit[XXVIII]

The synthesis of the Fe-NDC_lit material was conducted as described in the work of Jaouen *et al.*[184] Briefly, 31 mg iron (II) acetate was mixed with 500 mg 1-10 phenanthroline and 469 mg Black Pearls (B-type, *Tanaka Kikinzoku Kogyo*). The obtained powder was ball-milled for 3 h at 400 rpm. Heat treatment was first conducted in argon atmosphere for 60 min at 1000 °C. The material was treated a second time under NH_3-atmosphere for 60 min at 950 °C yielding the final Fe-NDC material.

Synthesis of Fe-NDC_GuaHCl

To synthesize the ionothermal Fe-NDC, 2.2 wt.% $FeCl_3$ (in respect to GuaHCl) was added to the initial GuaHCl/salt mixture. The general procedure (sample preparation, heat treatment, and work-up) was conducted as described for the GuaHCl derived sample with $NaCl/ZnCl_2$ (42 mol% NaCl, GuaHCl to salt ratio = 1:10 wt.%) in the experimental part for 3.2.2.

Electrochemical Measurements (H_2O_2 Crossover Test) in Alkaline and Acidic Media

The ink- and electrode preparation as well as the measurement procedure were generally conducted as described in section I.II (electrochemical methods). However, the volume of ethanol used for the ink-preparation was adjusted to yield the respective electrode loading (100 or 300 µg cm^{-2}). Additionally, the ratio between Nafion solution and catalyst was lowered from 95 µl Nafion solution vs. 5 mg catalyst to 50 µl vs. 5 mg.

To obtain the date needed for the H_2O_2 crossover test, the catalyst's electrochemical response was investigated by cyclovoltammetry under different conditions employing the following order: i) O_2-saturated electrolyte, ii) N_2-saturated electrolyte, iii) N_2-saturated electrolyte in the presence of 1 mM H_2O_2, iv) O_2-saturated electrolyte in the presence of 1 mM H_2O_2, v) N_2-saturated electrolyte in the presence of 5 mM H_2O_2, and vi) O_2-saturated electrolyte in the presence of 5 mM H_2O_2. The initial electrolyte volume was set to 150 ml. The aimed H_2O_2 concentration was achieved by adding the respective amount of H_2O_2 (30 wt.%) solution into the electrolyte. Furthermore, the electrode was rotated for 10 min at 1600 rpm after adding the respective volume of H_2O_2 solution to ensure a homogenous H_2O_2 concentration. For each condition, three rotation rates were studied (400, 900, and 1600 rpm), and for each rotation rate three CVs were recorded (sweep rate 10 mV s^{-1}) between 0.05 V and 1.0 V (vs. RHE). In all cases, the anodic branch of the

---

[XXVIII] The synthesis of Fe-NDC_lit was conducted by Thomas Mittermeier at the TUM.

second CV was used for analysis. After the whole measurement procedure, the electrode was first washed by thorough rinsing with the respective electrolyte and, secondly, by rotating the electrode in the respective electrolyte for 10 min at 1600 rpm. Then, the electrocatalytic performance of the catalyst was again investigated in O_2-saturated electrolyte in the same manner as conducted initially (indicated as "ORR after testing").

5 Extended Ionothermal Synthesis

5.2 Anhydrous CaCl2 vs. CaCl2 Dihydrate: "New" Reaction Mediums for the Synthesis of Adenine Derived Nitrogen Doped Carbons

Synthesis

Typically, 800 mg adenine was thoroughly grinded with 8000 mg of the salt ($CaCl_2$ or $CaCl_2 \cdot 2\,H_2O$) in a glove box. The heat treatment and the work-up of the samples were conducted as described in the experimental part for 3.2.1.

Electrochemical Measurements (Oxygen Reduction Reaction)

The ink- and electrode preparation as well as the measurement procedure were generally conducted as described in section I.II (electrochemical methods). However, the thoroughly grinded samples could be directly used for ink-preparation (without additional ball-milling) due to their facile dispersibility. Additionally, the ratio between Nafion solution and catalyst was lowered from 95 µl Nafion solution vs. 5 mg catalyst to 50 µl vs. 5 mg. Moreover, the total ink-volume was doubled by adjusting the amount of ethanol, in order to achieve a viscosity suitable for dropcasting. Thus, 10 µl of the obtained ink was used for dropcasting resulting in the herein usually investigated loading of ~ 290 µg cm^{-2}.

5.3 MgCl2 Hexahydrate as Reaction Medium for the Synthesis of Adenine Derived "Fibrous" Nitrogen Doped Carbons: Secondary Templating Effect and Electrochemical Application

Synthesis

Typically, 800 mg of adenine was thoroughly grinded (in a glove box) with the according mass of $MgCl_2 \cdot 6\,H_2O$ to achieve the aimed precursor to salt wt.-ratio. The heat treatment and the work-up of the samples were conducted as described in the experimental part for section 3.2.1. However, the final annealing temperature was adjusted to the respective

temperature. Furthermore, the materials were additionally washed in 1 L of 2 M HCl and neutralized again with deionized water before drying. The reference samples, just containing salt, were prepared in the same fashion as the adenine containing samples, however, without any washing steps.

Metalation Procedure

Metalation of the NDCs with iron ions was conducted by stirring ~ 30 mg NDC in 50 ml MeOH containing 50 mM $FeCl_2 \cdot 4 H_2O$ under reflux conditions for 24 h. The sample obtained was thoroughly washed with 0.5 M H_2SO_4 to remove physisorbed iron ions, neutralized by aqueous washing, and dried in vacuum at 60 °C overnight. In order to metalate the NDC with zinc ions, the same procedure was used, however, employing a 50 mM $ZnCl_2$ solution in MeOH.

Electrochemical Measurements (Oxygen Reduction Reaction)

The ink- and electrode preparation as well as the measurement procedure were generally conducted as described in section I.II (electrochemical methods). However, the ink-preparation and the dropcasted ink-volume was slightly adjusted in the same way as described for the materials synthesized with $CaCl_2$ (experimental part for section 5.2). For stability measurements, the LSVs at 1600 rpm before and after 1000 CVs in O_2-saturated electrolyte were recorded. Herein, the potential region of the CVs was set between 0.4 and 1.0 V (vs. RHE), and a sweep rate of 50 mV s^{-1} was employed.

I.IV Supporting Figures and Tables

3 Ionothermal Carbons with Tailored Porosity

3.2 Precursor Systems

Table S4 Different characteristics of Glu-3, Glu-5, GluNH$_2$-3, GluNH$_2$-3_bigbatch, and GluNH$_2$-4_bigbatch: specific surface area and total pore volume (obtained from nitrogen physisorption), elemental composition (C, H, N) obtained by combustion analysis, and calculated carbon yield as well as total yield.

sample	SSA_{BET} / m^2 g^{-1}	$TPV_{p/po = 0.99}$ / cm^3 g^{-1}	C – content / wt.%	H – content / wt.%	N – content / wt.%	carbon yield / %	total yield / %
Glu-3	975	1.31	92.8	1.1	-	64.0	31.1
Glu-5	1180	1.55	87.9	1.3	-	66.5	31.4
GluNH$_2$-3	1120	1.45	74.0	2.3	4.7	66.4	27.9
GluNH$_2$-3 _bigbatch	790	1.34	79.5	1.7	3.2	-	-
GluNH$_2$-4 _bigbatch	875	1.61	76.0	1.7	2.9	66.0	29.0

Table S5 SSAs and TPVs (from N2-physisorption literature data or product data sheets) of mesoporous carbons from literature (polymer derived and CMK-materials), and commercially available activated carbons (Carbon Blacks).

material class	detailed sample name or further information	SSA_{BET} / m^2 g^{-1}	$TPV_{N2-physisorption}$ / cm^3 g^{-1}	reference
carbon black (commercial and mainly microporous)	Darco® KB-G	1700	0.90	product data sheet (*Cabot Norit)*
	Cabot BP 2000	1450	1.75	[138]
	Vulcan XC-72	310	0.60	measured
	Ketjenblack® EC-600JD	1400	0.50	product data sheet (*AkzoNobel)*
	Cabot BP 1300	520	0.91	[138]
polymer derived mesoporous carbons	c-fdu-15	612	0.34	[140]
	c-fdu-18-450	554	0.48	[136]
	polymer aerogel	1215	2.7	[139]
	polymer cryogel	1107	1.8	[139]
CMK-materials	CMK-1	1800	1.21	[46]
	CMK-3	1600	1.95	[137]
	CMK-5	1850	1.80	[135]
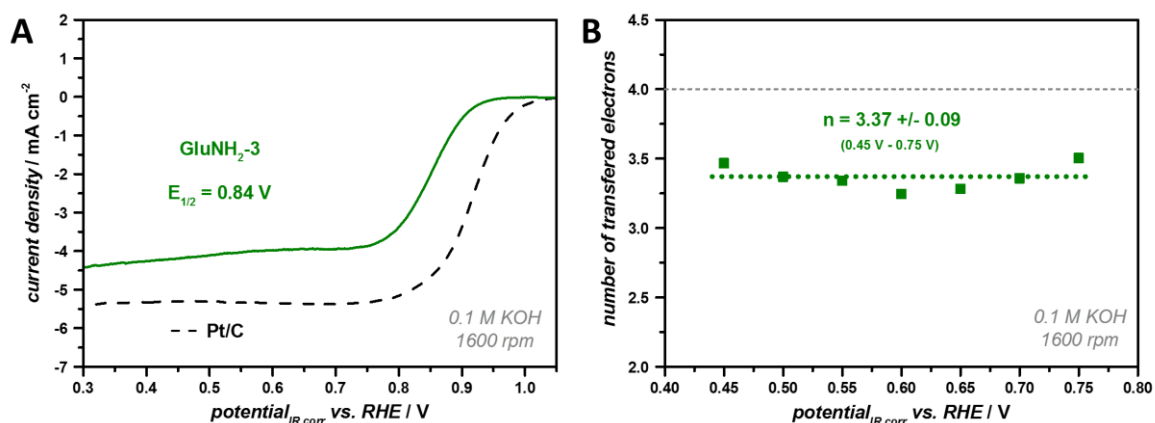
Figure S3 A) RDE polarization curves of GluNH$_2$-3 in O$_2$-saturated 0.1 M KOH with a sweep rate of 5 mV s^{-1}, 1600 rpm. B) Corresponding number of transferred electrons (at different potentials) calculated from KL-plots at different potentials derived from RDE-measurements with different rotating rates.
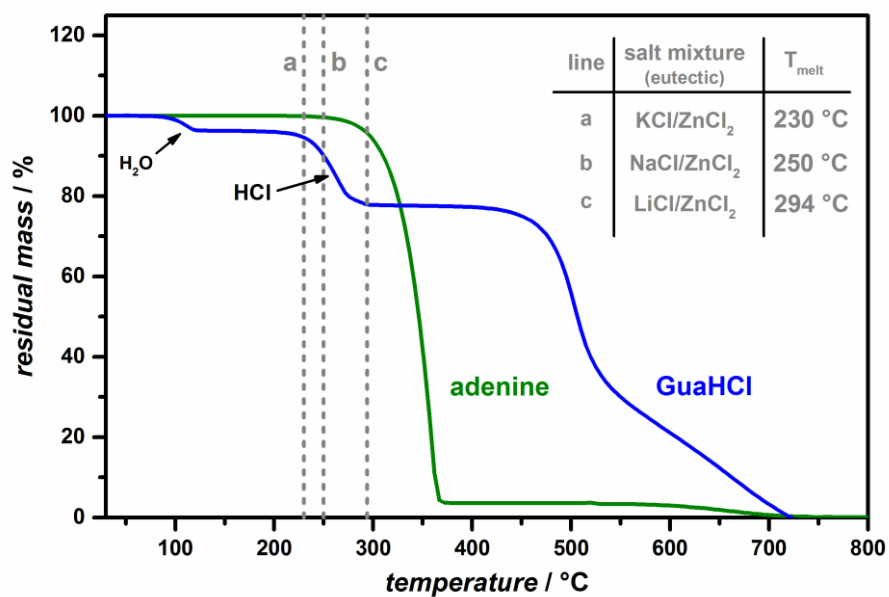

Figure S4 Overlay of the TGA analysis of the nucleobases (adenine and GuaHCl) and the melting points of different eutectic salt mixtures (KCl/ZnCl$_2$, NaCl/ZnCl$_2$, and LiCl/ZnCl$_2$).

Table S6 Different characteristics of GuaHCl and adenine derived ionothermal NDCs with different salt mixtures and various precursor to salt wt.-ratios: specific surface area and total pore volume (at $p/p_0 = 0.99$) obtained from nitrogen physisorption, elemental composition (C, H, N) obtained by combustion analysis, and calculated carbon yield as well as total yield. The used salt mixtures were $LiCl/ZnCl_2$ (22 mol% LiCl), $NaCl/ZnCl_2$ (42 mol% NaCl), and $KCl/ZnCl_2$ (50 mol% KCl).

precursor	salt	precursor to salt wt.-ratio	SSA_{BET} / m² g⁻¹	TPV / cm³ g⁻¹	C − content / wt.%	H − content / wt.%	N − content / wt.%	carbon yield / %	total yield / %
GuaHCl	LiCl/ ZnCl₂	1 : 6	2360	1.72	73.7	1.7	8.4	38.5	16.7
		1 : 10	2320	2.81	64.9	2.0	6.5	35.8	17.7
		1 : 14	1880	2.91	74.4	1.9	7.5	42.6	18.4
GuaHCl	NaCl/ ZnCl₂	1 : 6	2480	3.55	77.3	1.7	6.8	45.3	18.7
		1 : 10	2510	5.29	74.5	1.9	6.9	49.2	21.2
		1 : 14	2530	4.92	74.2	1.8	6.9	46.7	20.2
GuaHCl	KCl/ ZnCl₂	1 : 6	2140	1.35	73.2	1.7	6.7	-	-
		1 : 10	2130	1.41	75.7	1.5	7.2	59.9	25.4
		1 : 14	2150	1.44	75.7	1.6	6.4	42.5	18.0
adenine	NaCl/ ZnCl₂	1 : 6	2690	2.42	77.8	16	7.3	59.5	34.0
		1 : 10	2830	3.48	75.5	1.5	7.2	58.1	34.2
		1 : 14	2740	4.32	75.4	1.6	8.0	58.6	34.5
adenine	KCl/ ZnCl₂	1 : 6	2110	1.50	73.1	2.2	6.5	57.8	35.1
		1 : 10	2350	1.80	73.5	2.1	6.3	57.0	34.5
		1 : 14	2410	1.91	78.9	1.7	6.4	62.3	35.1

Table S7 SSAs and TPVs (from N2-physisorption literature data) of micro- and mesoporous CDCs derived from mesoporous carbides.

| material class	carbide	SSA_{BET} / m² g⁻¹	$TPV_{N2\text{-}physisorption}$ / cm³ g⁻¹	reference
CDCs derived from mesoporous carbides	ordered carbide obtained by hard templating with KIT-6	2910	1.91	[54]
	ordered carbide obtained by soft templating	1540	2.53	[149]
	carbide mesofaom	2770	2.61	[150]
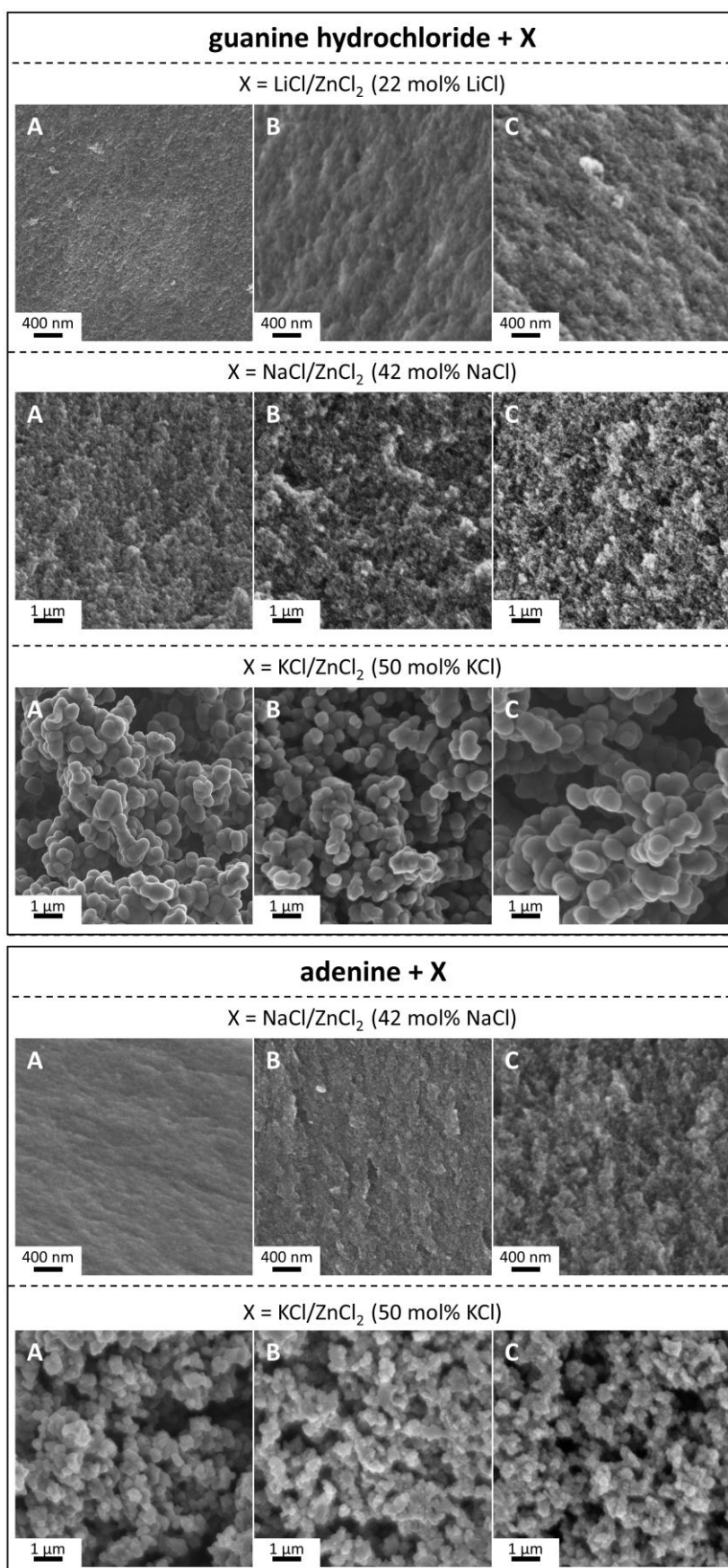
Figure S5 SEM images of the nucleobase derived materials with different salt mixtures and different precursor to salt ratios. The precursor to salt wt.-ratios are A) 1:6, B) 1:10, and C) 1:14.

3.3 Glucose Derived Carbons with Tailored Porosity

Influence of the Heating Procedure on the Obtained Porosity

In the present work, two different salt mixtures (30 mol% and 46 mol%) were chosen in a preliminary experiment. Thereby, the influence of an additional isothermal heating step at a suitable temperature on the obtained pore structure was investigated. The temperature of this step was set to 350 °C, ideally ensuring the homogenization of the non-eutectic mixture. The heating rate was fixed for all experiments to 2.5 K min^{-1} and the final dwelling was conducted for 1 h at 900 °C. The samples synthesized without the additional isothermal heating step are identified by the additional suffix L (standing for linear heating). The porosity of the samples was studied by N$_2$-physisorption (Figure S6).
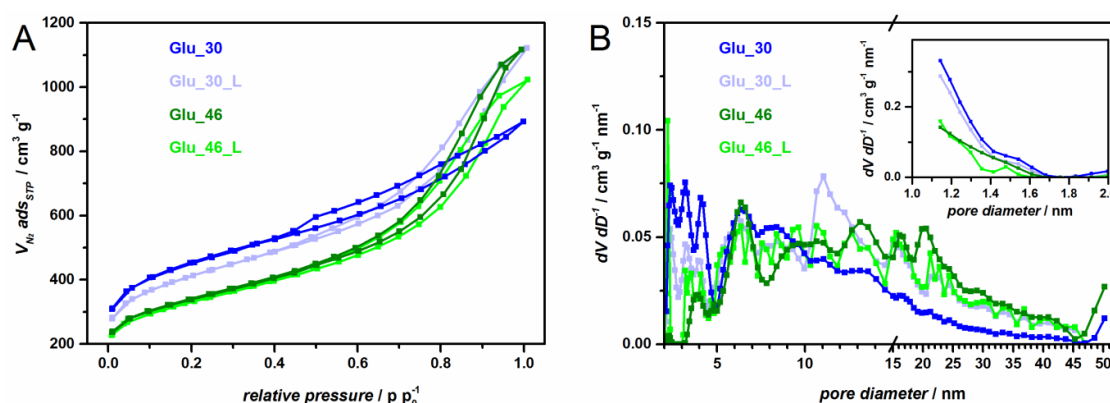
Figure S6 A) Nitrogen physisorption isotherms and B) mesopore and micropore (inset) size distribution of Glu_30, Glu_46, Glu_30_L and Glu-46_L (L…linear heating program – no isothermal heating step).

All four samples possess an open pore structure including micro- and mesoporosity as seen by the type IV isotherm coupled with a H3 hysteresis.[26] An increased molar content of ZnCl$_2$ caused higher SSA regardless of the heating procedure applied (Table S8). However, the pore systems of Glu_30_L and Glu_46_L demonstrate only quantitative differences but are qualitatively very similar as indicated by their almost identical isotherm shape. The corresponding PSDs reveal that Glu_30_L possesses more micropores and slightly more mesopores than Glu_46_L (Figure S6B). On the contrary, the isotherms of Glu_30 and Glu_46 show big differences, especially in the high pressure region (p p$_0^{-1}$ > 0.7). Glu_46 shows a clear augmentation of larger mesopores (d > 10 nm) whereas Glu_30 predominantly contains micro- and small mesopores (d < 15 nm). This indicates that the KCl-content can influence the mixing/demixing behavior of the carbonizing precursor and salt phase. Intriguingly, the additional heating step only had a minor influence on the porosity of the samples synthesized with the eutectic (Glu_46 and Glu_46) but a great influence on the porosity of the samples obtained with 30 mol% KCl. This points to a stronger necessity of an additional heating step if non-eutectic mixtures are used, which can be explained by a relatively delayed complete melting of the salt phase. Additionally, it has to be considered that the properties of the salt mixture can be changed due to the water formation during the polycondensation of glucose. Fischer et. al reported that the solubility of cellulose in ZnCl$_2 \cdot$ X H$_2$O decreases with increasing water content.[51] The additional heating step can enhance the evaporation of the water formed by the polycondensation of the glucose molecules thereby increasing the solubility of precursor (or partially polymerized precursor molecules). Generally, the additional isothermal heating step seems to support the mixing of precursor and salt phase, especially in the case of non-eutectic mixtures.

Table S8 Different characteristics of the glucose derived samples prepared with different KCl-content in the KCl/ZnCl$_2$ mixture: specific surface area and total pore volume obtained from nitrogen physisorption, elemental composition (C, H, O) obtained by combustion analysis (O-content was calculated by difference), and calculated carbon yield as well as total yield. The suffix "_L" identifies the sample synthesized with a simple linear (_L) heating program (no isothermal heating step).

sample	SSA_{BET} / m^2 g^{-1}	$TPV_{p/po = 0.99}$ / cm^3 g^{-1}	$V(meso)_{DFT}$ / cm^3 g^{-1}	C – content / wt.%	H – content / wt.%	O – content / wt.%	carbon yield / %	total yield / %
Glu_00	2160	1.09	0.56	89.8	1.8	8.4	60.1	26.8
Glu_10	1970	1.19	0.72	90.5	1.4	8.1	60.8	26.9
Glu_20	1760	1.18	0.76	89.2	1.3	9.5	64.5	28.9
Glu_30	1620	1.25	0.85	90.2	1.4	8.4	57.5	25.5
Glu_30_L	1472	1.50	1.11	89.5	1.4	9.1	-	-
Glu_40	1390	1.23	0.91	88.8	1.5	9.7	60.4	27.2
Glu_46	1210	1.59	1.33	89.0	1.5	9.5	60.4	27.2
Glu_46_L	1177	1.38	1.14	87.9	1.3	10.8	66.5	31.4
Glu_60	960	1.21	0.97	86.8	1.4	11.8	59.9	27.6
Glu_80	280	0.19	0.10	81.0	1.6	17.4	58.0	28.7
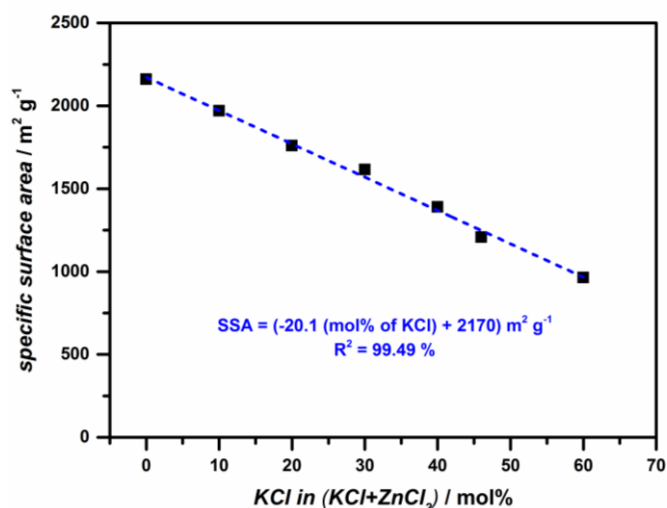
Figure S7 Linear correlation between used molar content of KCl in the KCl-ZnCl$_2$ mixture and the obtained specific surface area (SSA) for the highly porous carbon materials (SSA > 500 m^2 g^{-1}).

Table S9 Nitrogen sorption data of the two "control samples" prepared with 50 mol% (Glu_50) and 70 mol% KCl (Glu_70) in the KCl/ZnCl$_2$ mixture, respectively. Additionally, the calculated values (SSA$_{calculated}$) by use of equation (3.1) are given and the deviation (dev$_{SSA}$) between SSA$_{BET}$ and SSA$_{calculated}$ is included.

sample	TPV$_{p/po = 0.99}$ / cm^3 g^{-1}	SSA$_{BET}$ / m^2 g^{-1}	SSA$_{calculated}$ / m^2 g^{-1}	dev$_{SSA}$ / %
Glu_50	1.42	1110	1165	5.0
Glu_70	0.84	770	763	1.0
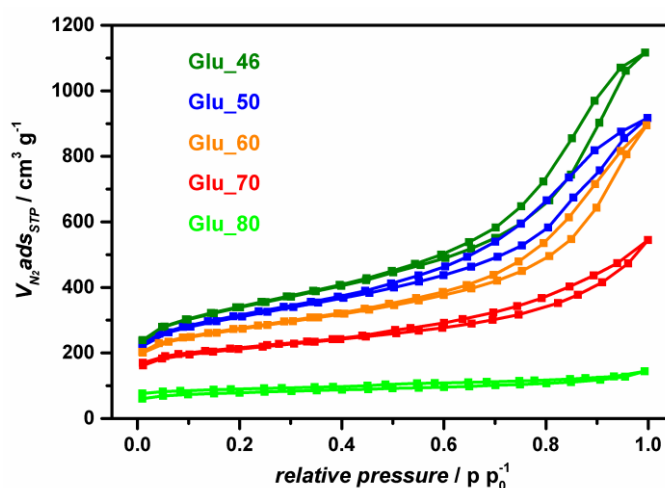
Figure S8 Nitrogen physisorption isotherms of the "control samples" Glu_50 and Glu_70. The isotherms of Glu_46, Glu_60 and Glu_80 are also shown for comparison.
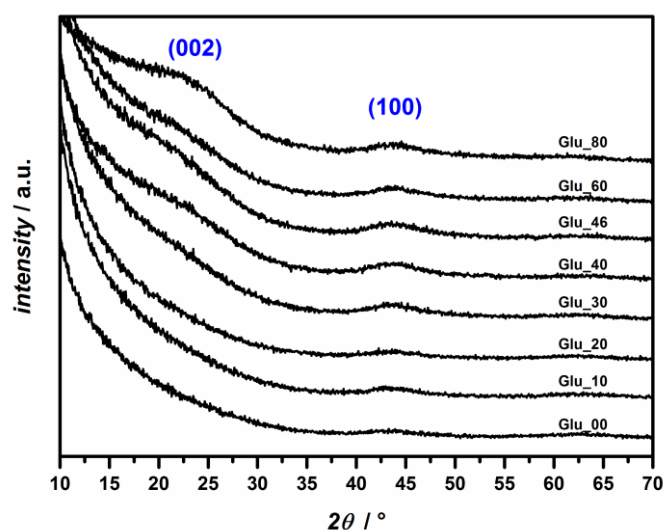
Figure S9 PXRD patterns of the glucose derived samples prepared with different KCl-content in the KCl/ZnCl$_2$ mixture. The reflections present at ~ 23° and ~ 43 can be regarded as the (002) and (100) reflection of the amorphous carbon layers (the ICCD number of the graphite reference can be found in Table S3).

Table S10 Mercury intrusion data of Glu_00, Glu_30, Glu_46, Glu_60, Glu_70 and Glu_80.

sample	total intrusion volume / ml g^{-1}	total pore area / m^2 g^{-1}	porosity / %
Glu_00	3.88	9	66.6
Glu_30	3.60	191	68.4
Glu_46	5.43	447	79.5
Glu_60	5.39	293	80.1
Glu_70	4.16	144	70.6
Glu_80	4.61	10	78.3
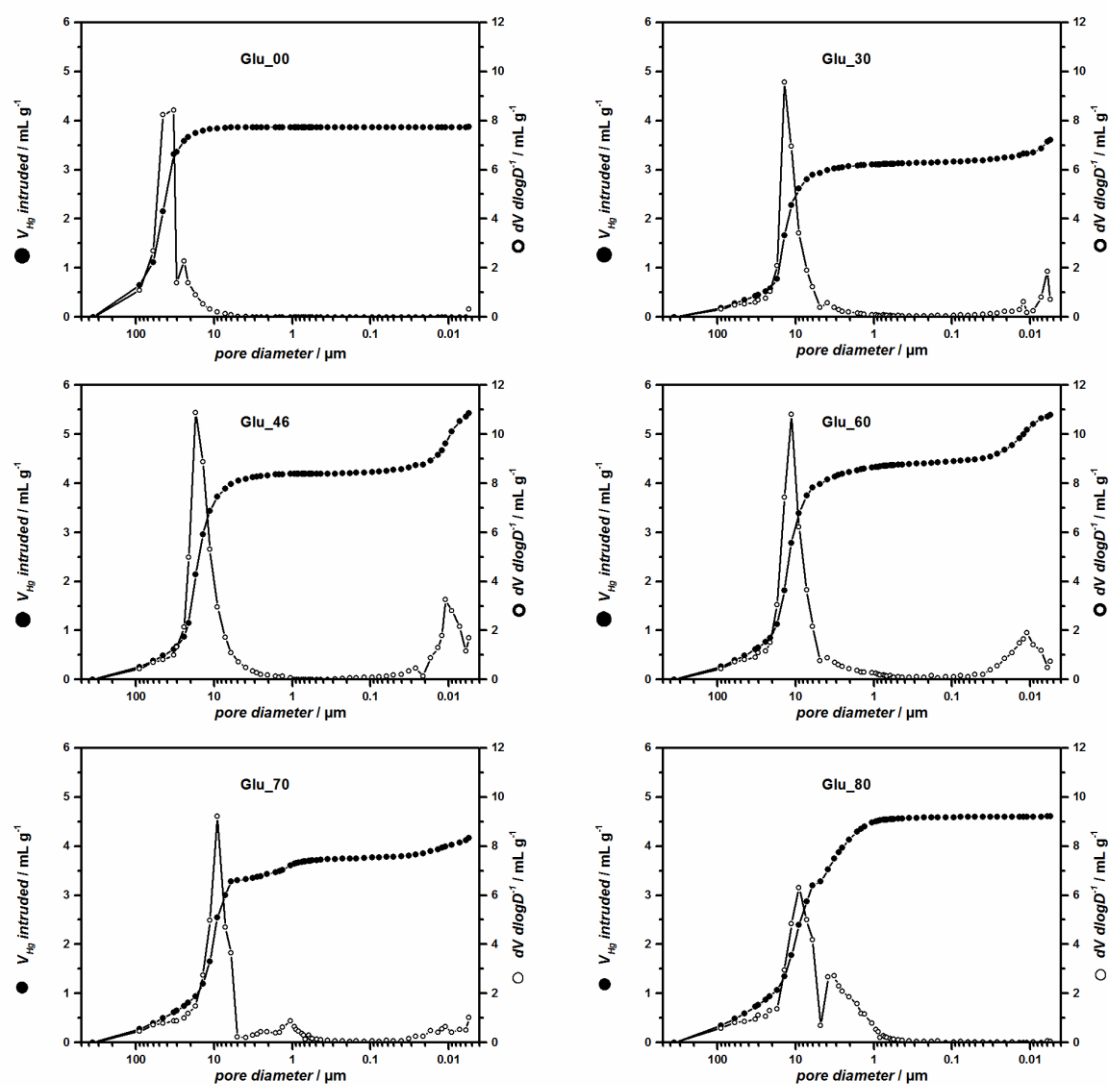
Figure S10 Mercury intrusion results of Glu_00, Glu_30, Glu_46, Glu_60, Glu_70 and Glu_80.
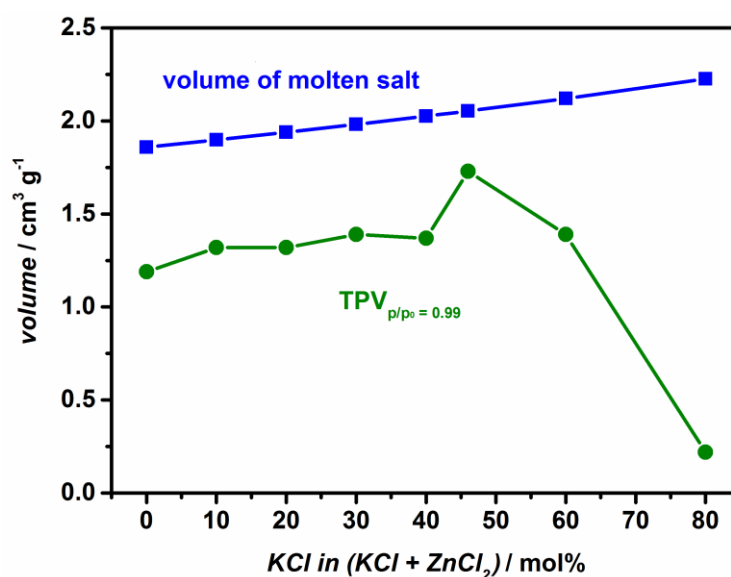
Figure S11 Comparison of the TPV (obtained from N_2-physisorption) of the glucose derived samples with different KCl-content in the $KCl/ZnCl_2$ mixture and the total (molten) volume of the employed salt mixture in respect to the molar KCl-content (calculated from the molar-weighted literature values for the density of the single molten salts[146]).
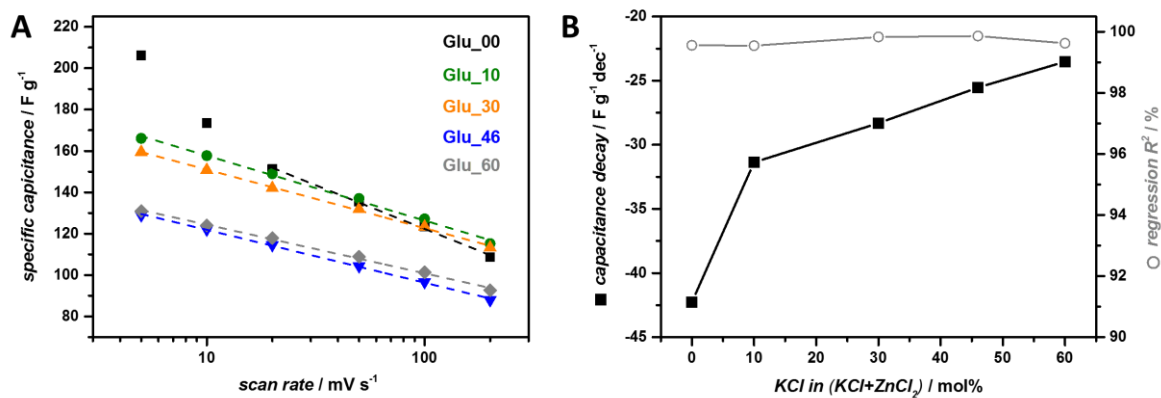
Figure S12 A) Specific capacitance in dependence of the logarithmic scan rate of Glu_00, Glu_10, Glu_30, Glu_46, Glu_60. The dashed lined depicts the linear region which was used for the determination of the capacitance decay. B) Influence of the amount of KCl used in the $KCl/ZnCl_2$ mixture on capacitance decay (filled symbols) and regression (R^2, open symbols) of the corresponding linear correlations.

3.4 Adenine Derived Nitrogen Doped Carbons with Tailored Porosity

Table S11 Nitrogen physisorption data (SSA, TPV, and micro- + mesopore volume), carbon yield, and total yield of the adenine derived samples prepared with different NaCl-content in the NaCl/ZnCl$_2$ mixture.

sample	SSA_{BET} / m^2 g^{-1}	$TPV_{p/po = 0.99}$ / cm^3 g^{-1}	$V(micro)_{DFT}$ / cm^3 g^{-1}	$V(meso)_{DFT}$ / cm^3 g^{-1}	carbon yield / %	total yield / %
Ade_33	2900	3.04	0.68	2.21	62.3	35.3
Ade_42	2830	3.48	0.64	2.79	58.1	34.2
Ade_50	2600	4.32	0.59	3.50	62.0	36.4
Ade_60	2540	5.19	0.62	3.40	56.7	33.0
Ade_70	2040	4.74	0.49	2.74	58.7	33.8
Ade_80	1750	3.15	0.39	2.42	60.7	33.5
Ade_90	1770	1.34	0.52	0.74	55.1	31.5

Table S12 Elemental composition of the adenine derived materials prepared with different NaCl-content in the NaCl/ZnCl$_2$ mixture.

| sample	N - content		C - content		O - content	Zn - content	Cl - content
	combustion analysis / wt.%	XPS / wt.%	combustion analysis / wt.%	XPS / wt.%	XPS / wt.%	XPS / at.%	XPS / at.%
Ade_33	7.7	8.3	78.4	76.0	8.1	1.0	1.0
Ade_42	7.2	7.1	75.5	79.8	7.4	0.7	0.8
Ade_50	7.1	6.7	75.8	80.4	6.6	0.8	0.8
Ade_60	6.1	6.0	76.3	81.2	6.8	0.7	0.9
Ade_70	5.9	5.9	77.1	81.6	7.3	0.5	0.9
Ade_80	6.3	5.6	80.6	83.1	6.0	0.7	0.7
Ade_90	6.7	6.2	77.8	79.2	6.5	1.1	1.0
Ade_100	19.3	-	64.8	-	-	-	-
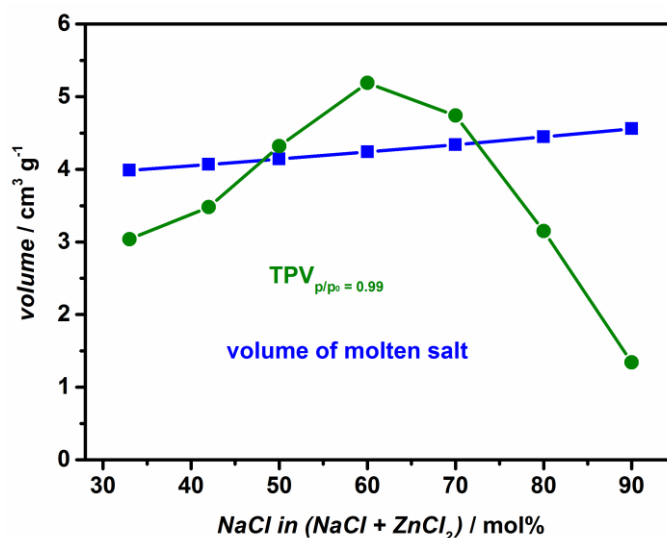
Figure S13 Comparison of the TPV (obtained from N_2-physisorption) of the adenine derived samples with different NaCl-content in the NaCl/ZnCl$_2$ mixture and the total (molten) volume of the employed salt mixture in respect to the molar NaCl-content (calculated from the molar-weighted literature values for the density of the single molten salts[146]).
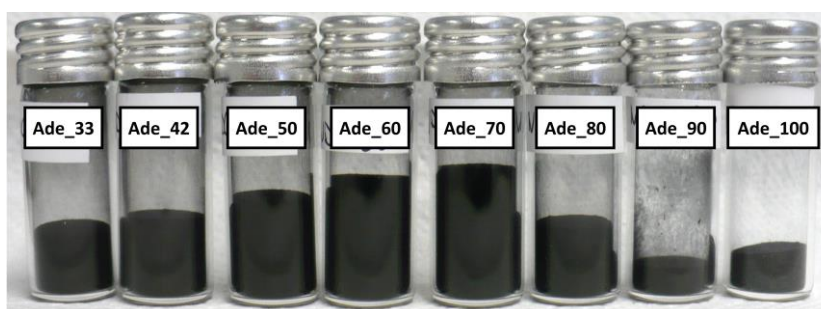

Figure S14 Macroscopic densities of the adenine derived NDCs (40 mg each) prepared with different NaCl-content in the NaCl/ZnCl$_2$ mixture.
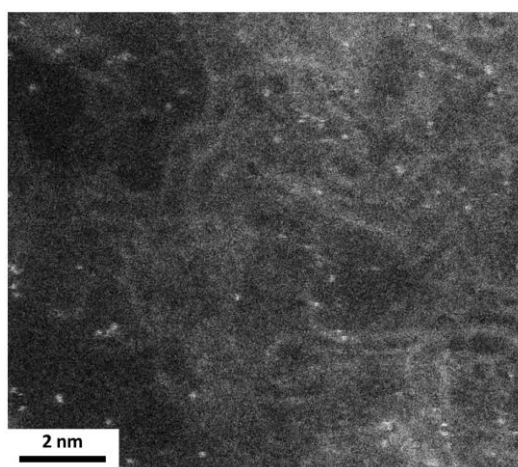
Figure S15 Aberration corrected STEM annular dark field image of an adenine derived NDC synthesized with a KCl/ZnCl$_2$ (50 mol% KCl) mixture (precursor to salt wt.-ratio = 1:10). The bright spots reveal the presence of isolated heavier atoms (probably zinc, Zn^{2+}) in the NDC framework.
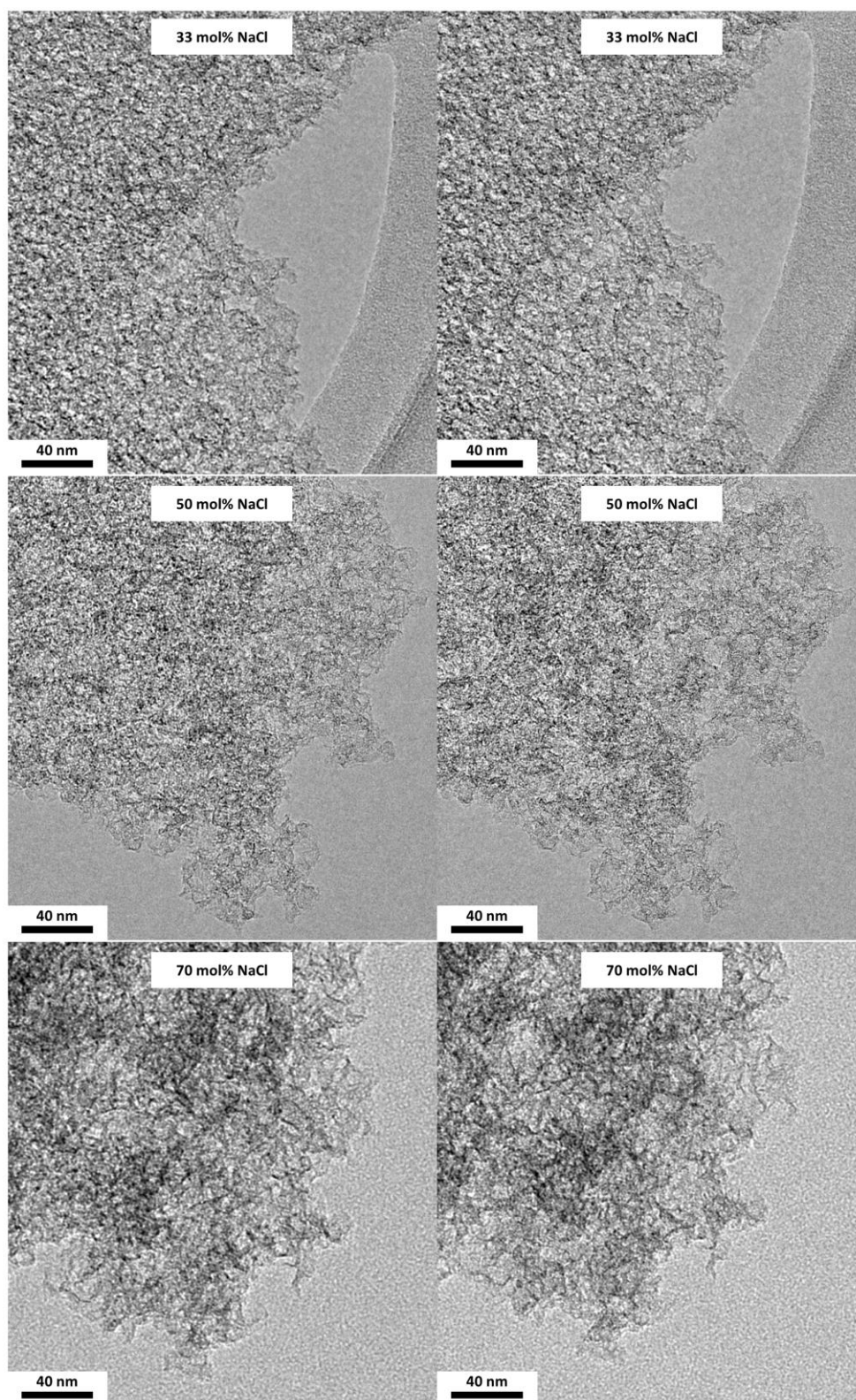
Figure S16 Stereoscopic TEM images of adenine derived NDCs synthesized with different NaCl-content in the NaCl/ZnCl$_2$ mixture.
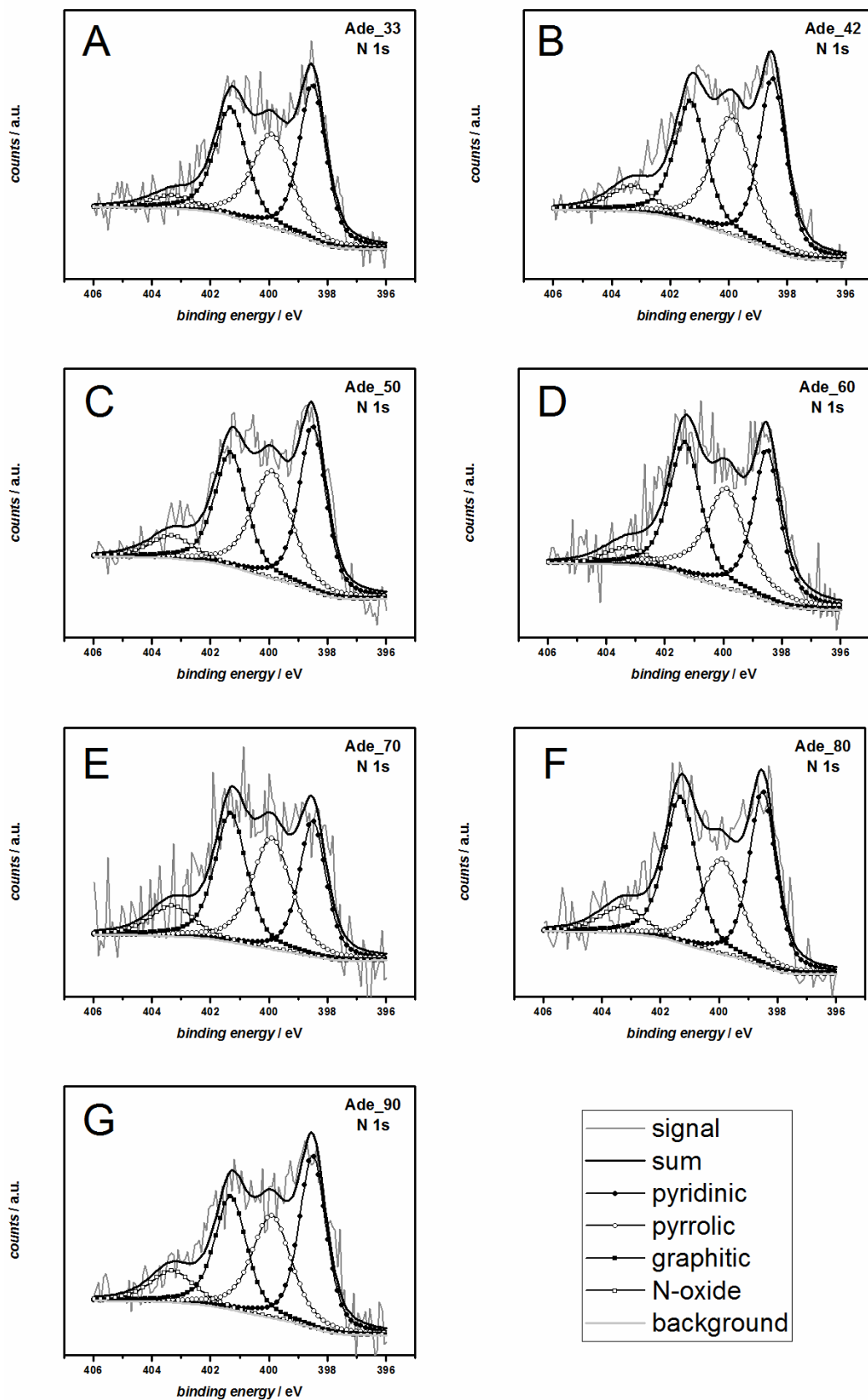
Figure S17 N 1s XPS spectra of the adenine derived materials prepared with different NaCl-content in the NaCl/ZnCl$_2$ mixture. a) NDC_33, b) NDC_42, c) NDC_50, d) NDC_60, e) NDC_70, f) NDC_80, g) NDC_90. Deconvoluted nitrogen peaks: pyridinic-N (398.5 eV); pyrrolic-N (399.9 eV); graphitic-N (401.3 eV), oxidized-N(403.3 eV).
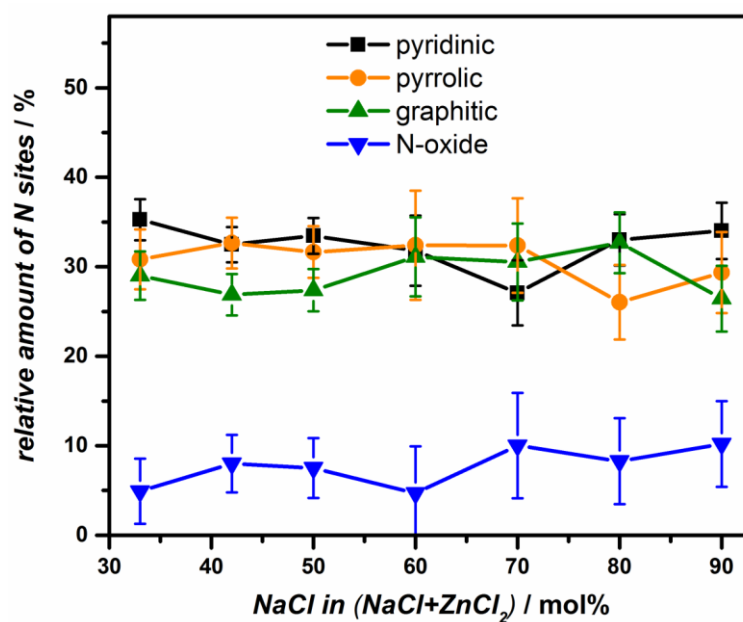
Figure S18 Influence of the amount of NaCl used in the NaCl/ZnCl$_2$ mixture on the type of N-sites present in the adenine derived NDCs (quantified by XPS). The experimental error was obtained by the signal to noise ratio. The corresponding noise of the different N1s scans was calculated by the standard variation of the raw signal in a region where no N peaks occur (390 - 395 eV).
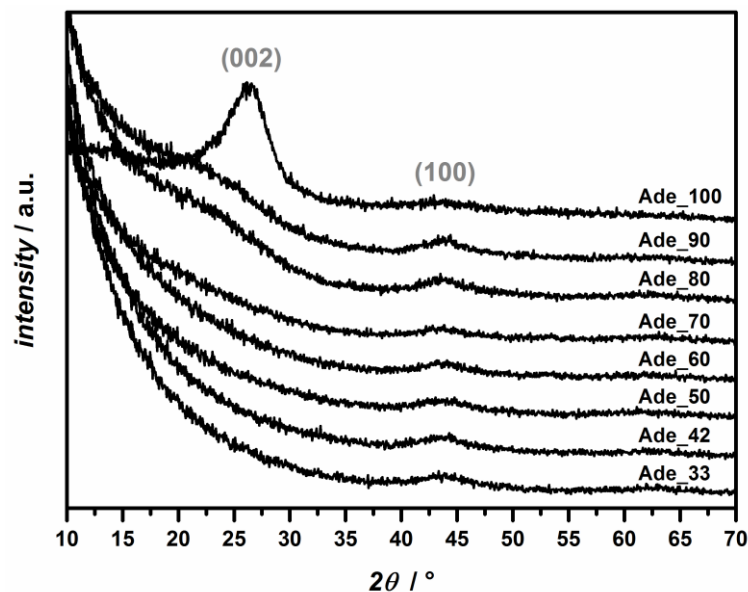

Figure S19 PXRD patterns of the adenine derived samples prepared with different NaCl-content in the NaCl/ZnCl$_2$ mixture. The reflections present at ~ 23° and ~ 43° can be regarded as the (002) and (100) reflection of the amorphous carbon layers (the ICCD number of the graphite reference can be found in Table S3).
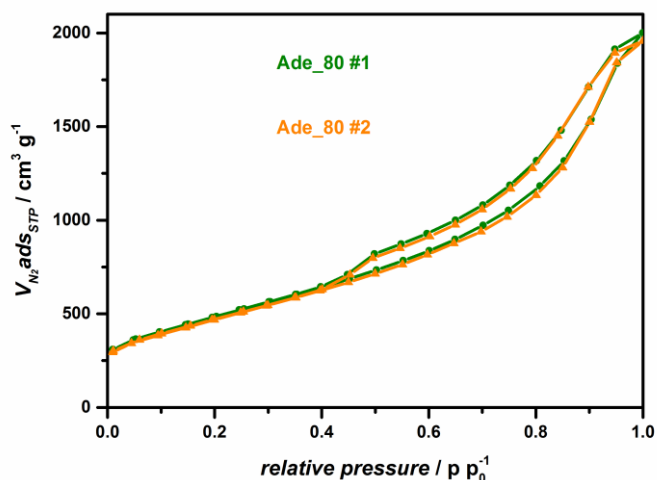
Figure S20 Nitrogen physisorption isotherms of two adenine derived NDCs prepared under the same conditions with 80 mol% NaCl in the NaCl/ZnCl$_2$ mixture.
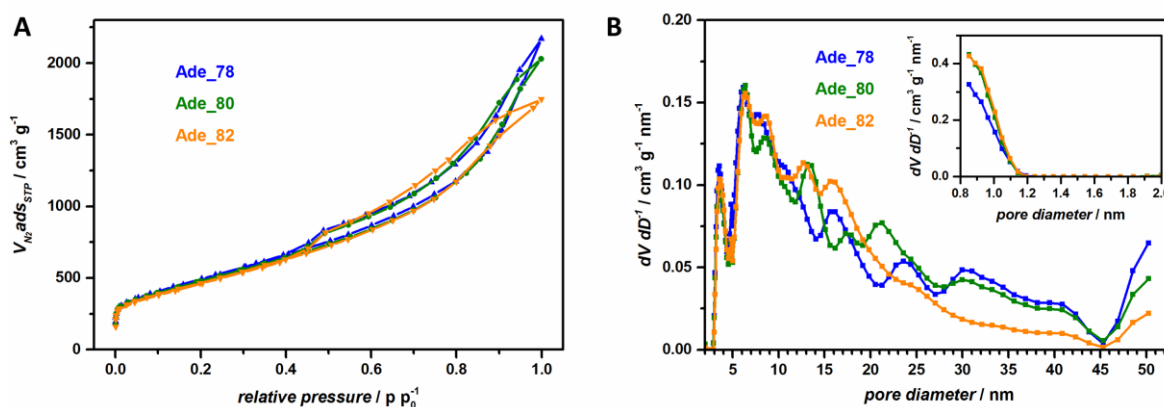

Figure S21 A) Nitrogen physisorption isotherms and B) pore size distribution of the adenine derived NDCs prepared with 78 mol%, 80 mol% and 82 mol% NaCl in the NaCl/ZnCl2 mixture showing the possibility of fine pore tuning.
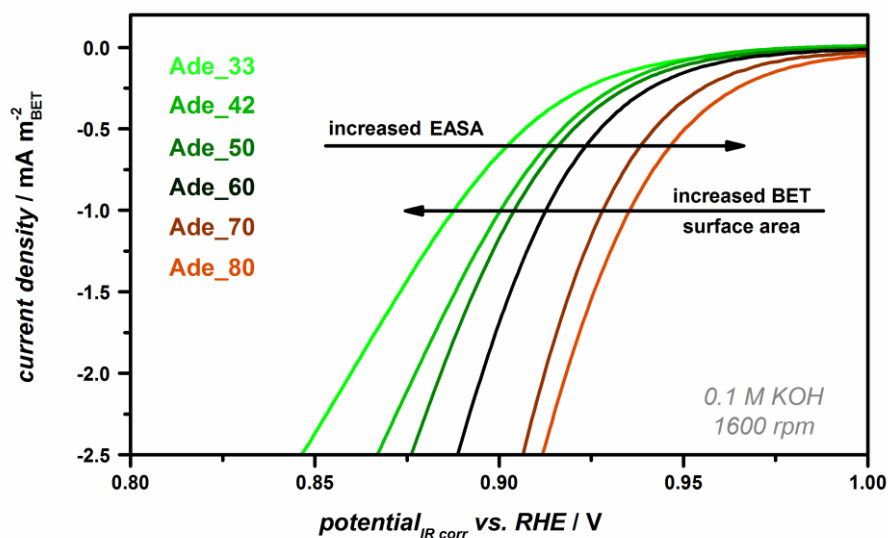
Figure S22 Kinetically controlled region of the RDE polarization curves normalized to the respective BET surface area of the adenine derived NDCs prepared with different amounts of NaCl in the NaCl/ZnCl$_2$ mixture in O$_2$-saturated 0.1 M KOH with a sweep rate of 5 mV s^{-1}, 1600 rpm.

Table S13 ORR-Performance of some benchmark catalysts under alkaline conditions (0.1 M KOH).

catalyst	loading / µg cm^{-2}	$E_{1/2}$ vs. RHE / V	reference
iron doped, MOF derived nitrogen doped carbon	600	0.86	Mukerjee_NatComm_2015 [166]
nitrogen-doped graphene/CNT composite	unknown	0.87	Dai_SciAdv_2015 [113]
hierarchical nitrogen doped carbon derived by hard templating	100	0.85	Müllen_NatComm_2014 [91]
nitrogen doped carbon aerogel derived by ionic liquids	210	0.78	Antonietti_Materials Horizon_2014 [116]
hierarchical nitrogen doped carbon nanoflakes	250	0.87	Sun_Carbon_2014 [98]
sulfur and nitrogen doped carbon derived by functionalization of carbon black with ionic liquids and FeCl$_3$	800	0.87	Strasser_JACS_2014 [167]
iron and nitrogen doped carbon nanotubes/nanoparticles	200 (1000)	0.87 (0.93)	[162]
iron and nitrogen doped carbon derived by functionalization of carbon black	400	0.92	[163]
ionic liquid derived mesoporous nitrogen doped carbon	800	0.85	Antonietti_JACS_2011 [142]
water hyacinth derived nitrogen doped carbon	160	0.83	Chen_Nanoscale_2015 [164]
adenine derived nitrogen doped carbon (Ade_80)	**290**	**0.88**	**this work**
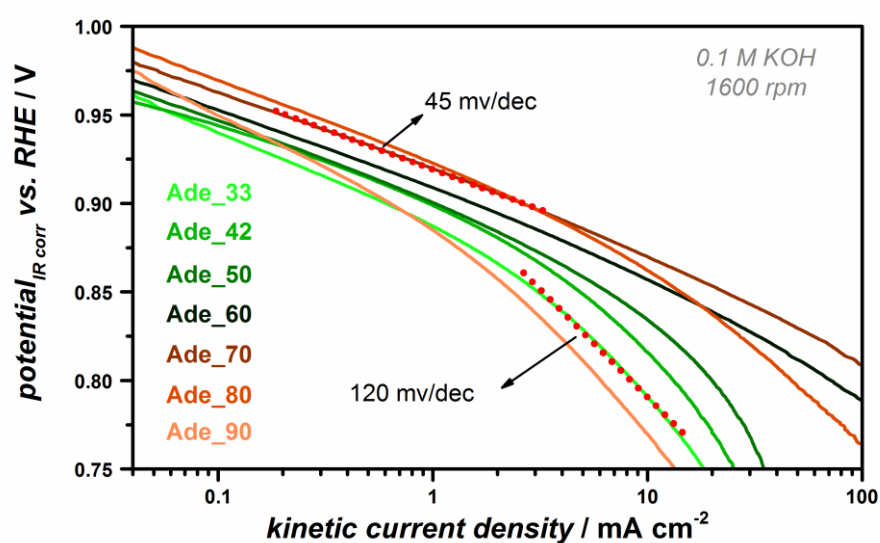
Figure S23 Tafel plots from RDE polarization curves of the adenine derived NDCs prepared with different amounts of NaCl in the NaCl/ZnCl$_2$ mixture in O$_2$-saturated 0.1 M KOH with a sweep rate of 5 mV s^{-1}, 1600 rpm.

Table S14 N$_2$-physisorption data (SSA and TPV) and elemental analysis results (C, H, N) of pristine and with TRGO modified Ade_50.
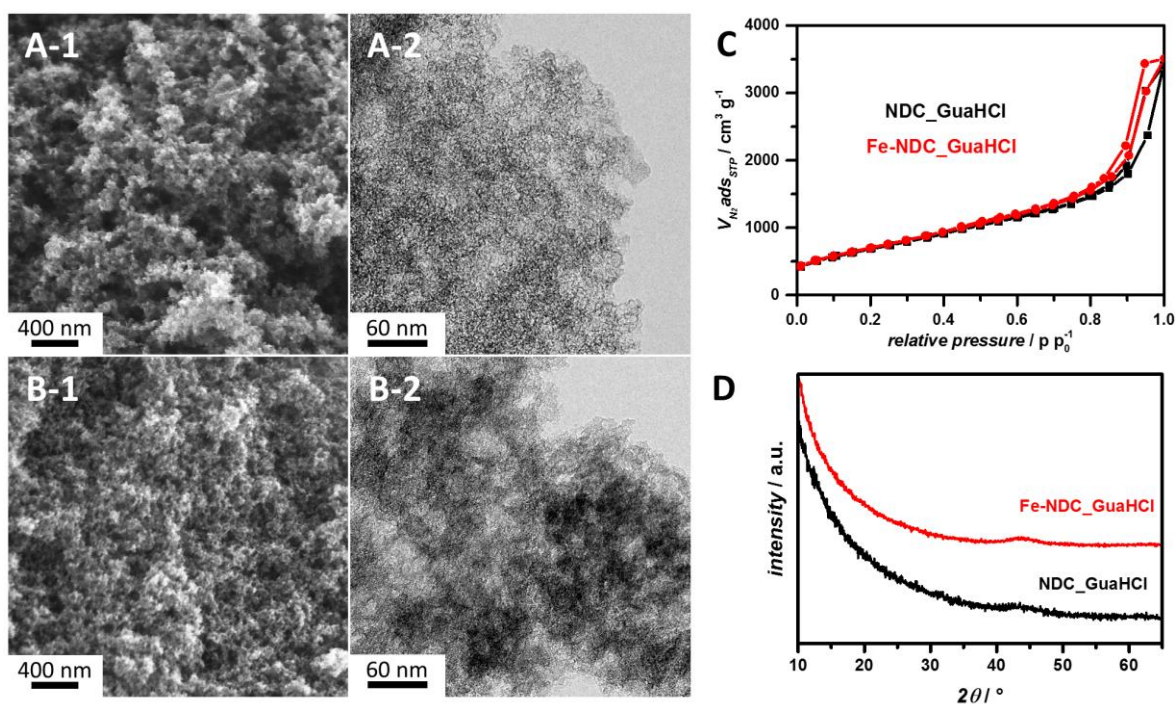
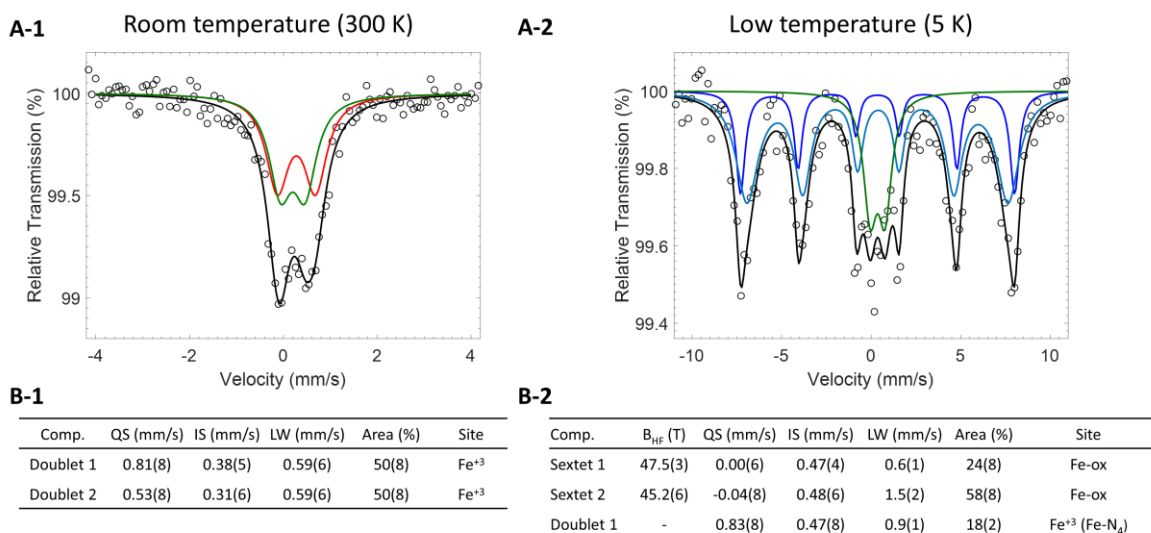| sample	SSA$_{BET}$ / m^2 g^{-1}	TPV$_{p/po = 0.99}$ / cm^3 g^{-1}	C – content / wt.%	H – content / wt.%	N – content / wt.%
Ade_50	2600	4.32	75.8	1.6	7.1
Ade-50 + 10 wt.% TRGO	2200	4.32	58.5	1.2	6.2

4 Hydrogen Peroxide Crossover Test

4.2 Studied Catalyst

Table S15 Different characteristics of Fe-NDC_GuaHCl and of the same sample prepared under the same conditions but without iron(III) chloride in the initial salt mixture (abbreviated with NDC_GuaHCl): specific surface area and total pore volume obtained from nitrogen physisorption, elemental composition (C, H, N) obtained by combustion analysis, and calculated carbon yield.

sample	SSA$_{BET}$ / m^2 g^{-1}	TPV$_{p/po = 0.99}$ / cm^3 g^{-1}	C – content / wt.%	H – content / wt.%	N – content / wt.%	carbon yield / %
Fe-NDC_GuaHCl	2570	5.44	68.5	1.7	6.6	43.0
NDC_GuaHCl	2510	5.39	74.5	1.5	6.9	49.2

Figure S24 Electron microscopy images of A) NDC_GuaHCl and B) Fe-NDC_GuaHCl (X-1: SEM and X-2: TEM). C) N$_2$-physisorption and D) PXRD results of NDC_GuaHCl and Fe-NDC_GuaHCl.

A-1 Room temperature (300 K)   **A-2** Low temperature (5 K)

B-1

Comp.	QS (mm/s)	IS (mm/s)	LW (mm/s)	Area (%)	Site
Doublet 1	0.81(8)	0.38(5)	0.59(6)	50(8)	Fe^{+3}
Doublet 2	0.53(8)	0.31(6)	0.59(6)	50(8)	Fe^{+3}

B-2

Comp.	B_{HF} (T)	QS (mm/s)	IS (mm/s)	LW (mm/s)	Area (%)	Site
Sextet 1	47.5(3)	0.00(6)	0.47(4)	0.6(1)	24(8)	Fe-ox
Sextet 2	45.2(6)	-0.04(8)	0.48(6)	1.5(2)	58(8)	Fe-ox
Doublet 1	-	0.83(8)	0.47(8)	0.9(1)	18(2)	Fe^{+3} (Fe-N_4)

Figure S25 A) Mößbauer spectrum of Fe-NDC_GuaHCl measured at 300 K (A-1) and at 5 K (A-2). The tables in B-X) show the corresponding spectral parameters, i.e., the hyperfine magnetic field (B_{HF}), the quadrupole splitting (QS), the isomer shift (IS) and the relative resonance areas of the different spectral components. The latter correlates to the relative abundance of the fitted iron species.

The spectra were fitted to appropriate combinations of Lorentzian profiles representing hyperfine magnetic sextets and quadrupole doublets by least-squares methods using the program PC-Mos II.[XXIX] In this way, spectral parameters such as the hyperfine magnetic field (BHF), the quadrupole splitting (QS), the isomer shift (IS) and the relative resonance areas of the different spectral components were determined. Isomer shifts are given relative to α-Fe metal.

The room temperature spectrum points to the presence of trivalent iron. It can be fitted with two different species (possible correspondence to two different Fe^{3+} environments) with slightly different isomer shift. The low temperature spectrum depicts a magnetic splitting of the room temperature paramagnetic spectrum, which is in line with the presence of ill-defined or nanosized oxides and/or oxyhydroxides, such as 2-line ferrihydrite, which are known to order magnetically only at low temperature.[222] A significant part of the trivalent iron (18 %), however, remains paramagnetic (green doublet in the middle of the low temperature spectrum) which points to the presence of Fe-N_4 sites.
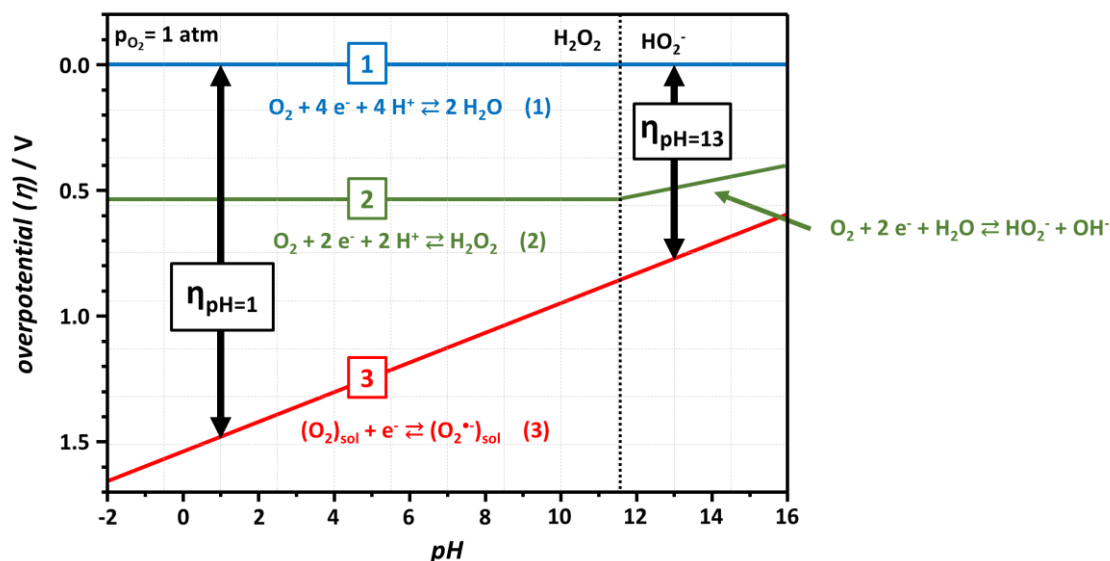
Figure S26 Modified presentation of the Pourbaix diagram (adapted from[192]). All potentials are expressed relative to the equilibrium potential of the ORR according to reaction (1). Line 1: pH dependence of the equilibrium potential of reaction (1) (p_{O2} = 1 atm); line 2: pH dependence of the equilibrium potential of reaction (2) ($\log(p_{O2}/[H_2O_2])$ = 0, $\log(p_{O2}/[HO_2^-])$ = 0); line 3: pH dependence of the equilibrium potential of reaction (3) ($\log(p_{O2}/[O_2^{•-}])$ = 0).

5 Extended Ionothermal Synthesis

5.2 Anhydrous CaCl2 vs. CaCl2 Dihydrate: "New" Reaction Mediums for the Synthesis of Adenine Derived Nitrogen Doped Carbons
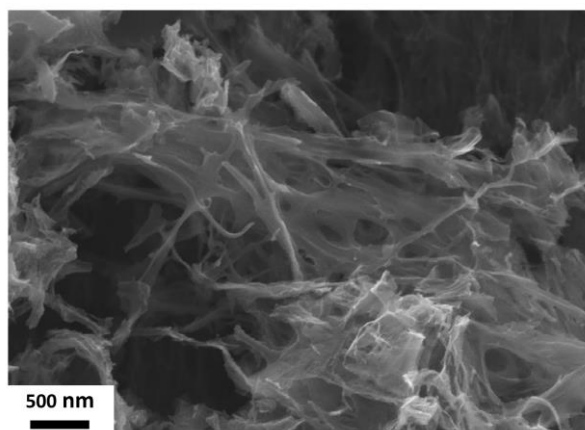
Table S16 Different characteristics of Ade-CaCl$_2$ and Ade-CaCl$_2$DH: specific surface area and total pore volume obtained from nitrogen physisorption, elemental composition (C, H, N) obtained by combustion analysis, and calculated carbon yield as well as total yield.

sample	SSA_{BET} / m^2 g^{-1}	$TPV_{p/po = 0.99}$ / cm^3 g^{-1}	C − content / wt.%	H − content / wt.%	N − content / wt.%	carbon yield / %	total yield / %
Ade-CaCl$_2$	1530	2.24	76.5	1.7	5.8	15.6	9.0
Ade-CaCl$_2$DH	1702	1.65	85.8	1.5	5.6	25.7	13.3

5.3 MgCl2 Hexahydrate as Reaction Medium for the Synthesis of Adenine Derived "Fibrous" Nitrogen Doped Carbons: Secondary Templating Effect and Electrochemical Application

Table S17 Different characteristics of Ade-Mg-1-900, Ade-Mg-5-900, and Ade-Mg-10-900: surface area and total pore volume obtained from nitrogen physisorption, elemental composition (C, H, N) obtained by combustion analysis, and calculated carbon yield as well as total yield.

| sample	SSA_{BET} / $m^2\,g^{-1}$	$TPV_{p/po = 0.99}$ / $cm^3\,g^{-1}$	C – content / wt.%	H – content / wt.%	N – content / wt.%	carbon yield / %	total yield / %
Ade-Mg-1-900	980	0.61	80.0	1.6	2.7	17	10.8
Ade-Mg-5-900	2780	2.83	88.3	1.3	2.3	25.6	13.7
Ade-Mg-10-900	2480	3.6	85.4	1.3	3.3	26.4	13.8

Figure S27 SEM image of Ade-Mg-10-900 depicting a region with non-parallel aligned NDC fibers.

Table S18 Different characteristics of the Ade-Mg-10-X samples (X represents different synthesis temperatures): surface area and total pore volume obtained from nitrogen physisorption, elemental composition (C, H, N) obtained by combustion analysis, and calculated carbon yield as well as total yield.

| sample	SSA_{BET} / m² g⁻¹	$TPV_{p/po = 0.99}$ / cm³ g⁻¹	C – content / wt.%	H – content / wt.%	N – content / wt.%	carbon yield / %	total yield / %
Ade-Mg-10-500	35	0.13	47.6	3.4	31	-	-
Ade-Mg-10-600	700	0.88	49.1	3.3	27.1	-	-
Ade-Mg-10-700	1380	1.60	55.0	2.5	26.0	34.1	29
Ade-Mg-10-800	2680	3.42	68.21	2.4	15.4	29.4	19.2
Ade-Mg-10-875	2490	3.68	83.56	1.5	5.3	25.9	13.8
Ade-Mg-10-900	2480	3.6	85.43	1.3	3.31	26.4	13.8
Ade-Mg-10-925	2500	3.67	86.9	1.5	2.45	26.8	13.7
Ade-Mg-10-1000	2230	3.67	88.17	1.2	2.04	28.2	14.2
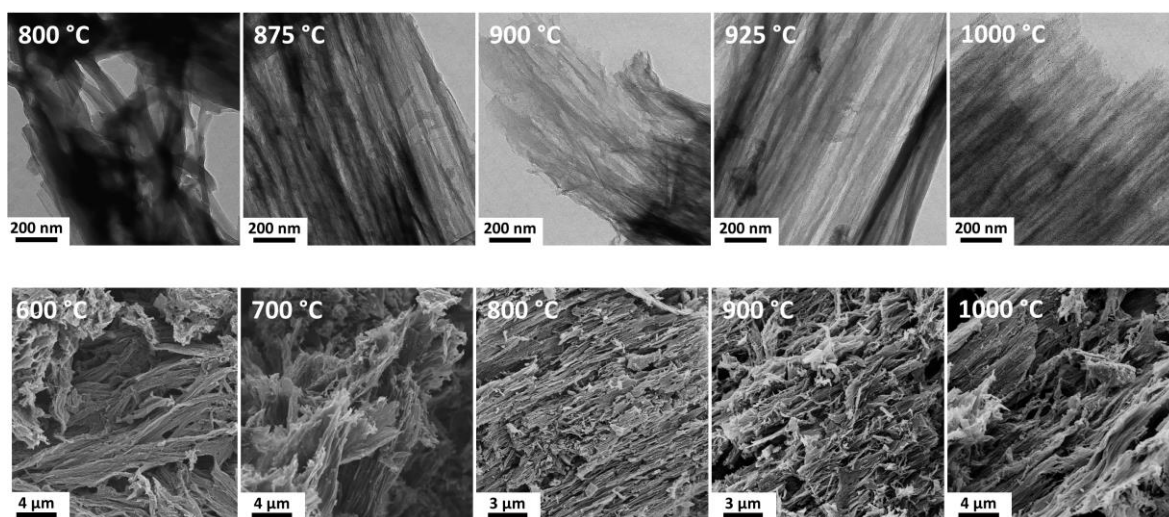
Figure S28 TEM images (upper row) and SEM images (lower row) of the Ade-Mg-10-X samples (X represents the synthesis temperature and is given in the respective image).
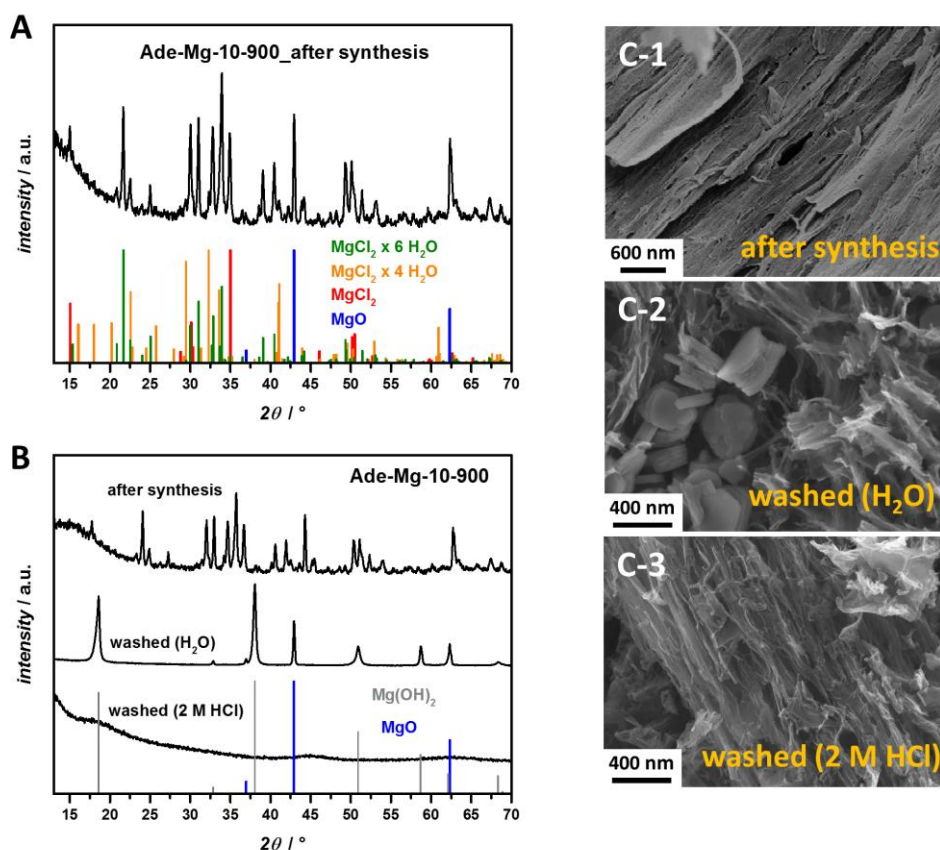
Figure S29 A+B) PXRD of Ade-Mg-10-900 as synthesized (unwashed), after aqueous washing, and after washing with 2 M HCl (the ICDD numbers of the PXRD reference patterns are given in Table S3). C) SEM images of the different work-up states of Ade-Mg-10-900.

It is to consider that MgCl2 is highly hygroscopic causing water uptake during the grinding of the material after the synthesis and during the PXRD measurements under ambient conditions. Therefore, the diffractogram of Ade-Mg-10-900_after synthesis reveals also hydrated phases which should not be present at such a high synthesis temperature. For all further PXRD measurements, the samples were protected with amorphous tape to avoid the hydration during the measurement.
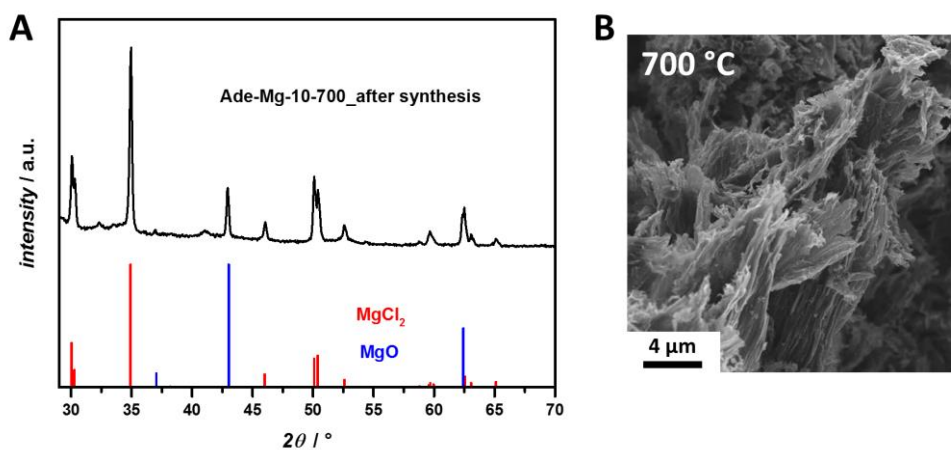
Figure S30 A) PXRD of the unwashed and B) SEM image of the final Ade-Mg-10-700 material (the ICDD numbers of the PXRD reference patterns are given in Table S3).
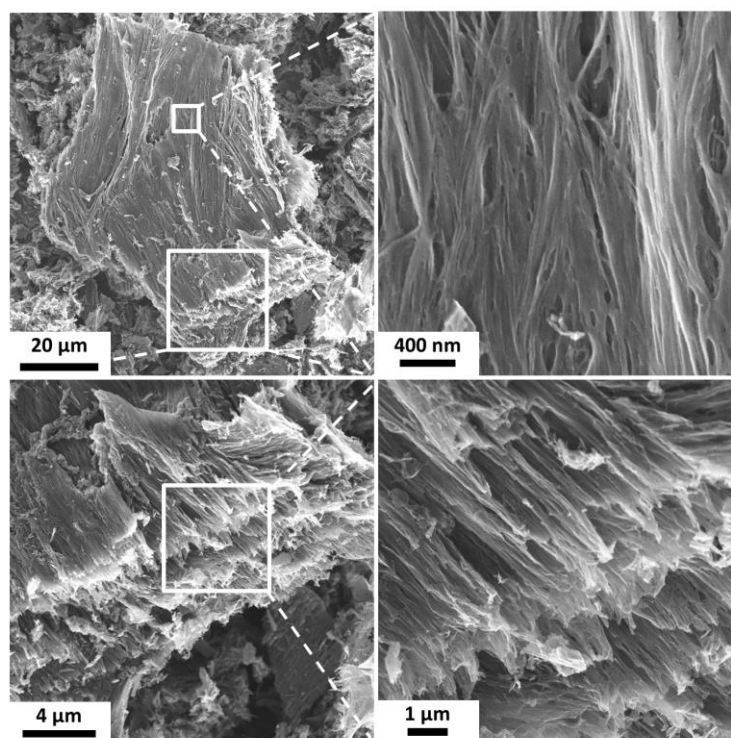
Figure S31 SEM images with different magnifications of the material synthesized in the same fashion as Ade-Mg-10-900 but with an additional isothermal heating at 400 °C for ten hours during the typically used heating procedure. The images show the possibility to obtain large areas of fibrous NDC containing long NDC fibers.
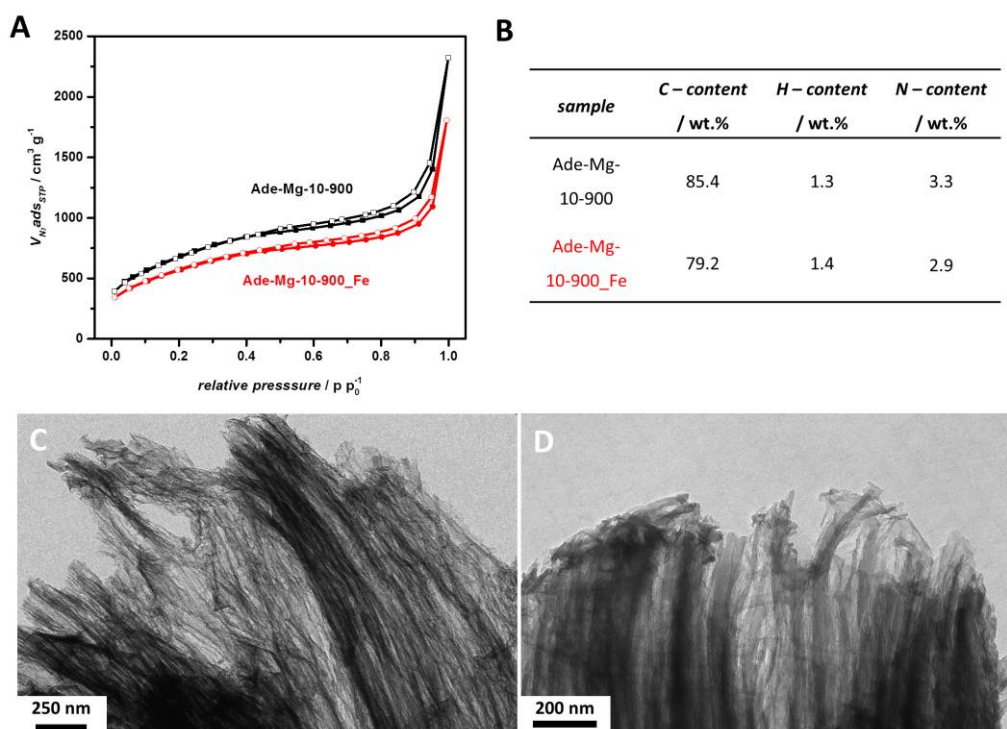

Figure S32 A) N_2-physisorption isotherms, and B) elemental composition (obtained by combustion analysis) of Ade-Mg-10-900 and the metalated Ade-Mg-10-900_Fe. C) TEM image of Ade-Mg-10-900 and D) of Ade-Mg-10-900_Fe.

Table S19 Iron content (determined by ICP-OES) of the different metalated Ade-Mg-10-X. Additionally, the value for the initial Ade-Mg-10-900 sample is given

sample	Fe-content / wt. %
Ade-Mg-10-900	0.02
Ade-Mg-10-800_Fe	1.29
Ade-Mg-10-875_Fe	0.48
Ade-Mg-10-900_Fe	0.46
Ade-Mg-10-925_Fe	0.39
Ade-Mg-10-1000_Fe	0.28
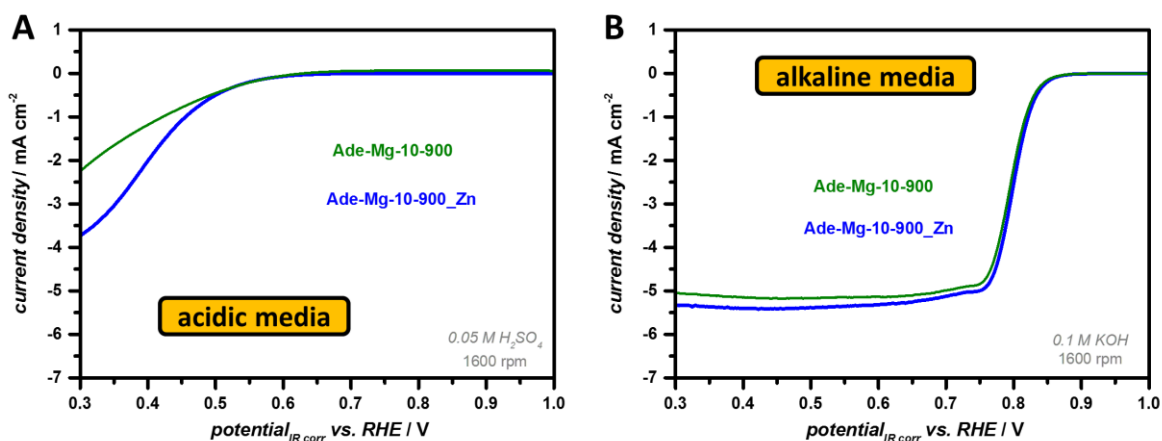
Figure S33 RDE-polarization curves of Ade-Mg-10-900 and Ade-Mg-10-900_Zn measured in A) acidic and B) alkaline media (O$_2$-saturated, 5 mV s^{-1}, 1600 rpm).
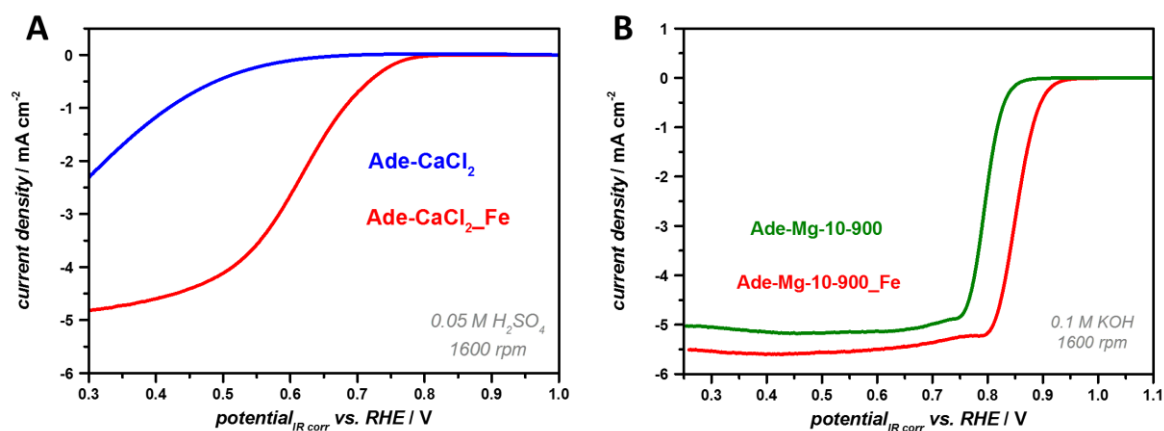
Figure S34 A) RDE-polarization curves of Ade-CaCl$_2$ and Ade-CaCl$_2$_Fe in 0.05 M H$_2$SO$_4$ (O$_2$-saturated, 5 mV s^{-1}, 1600 rpm). B) RDE polarization curves of Ade-Mg-10-900 and Ade-Mg-10-900_Fe in 0.1 M KOH (O$_2$-saturated, 5 mV s^{-1}, 1600 rpm)
.

I.V List of Publications

J. Pampel, C. Denton and T.-P. Fellinger; "Glucose Derived Ionothermal Carbons with Tailor-Made Porosity", *Carbon* **2016**, *107*, 288.

F. Pawlitzek, **J. Pampel**, M. Schmuck, H. Althues, B. Schumm and S. Kaskel, "High-Power Lithium Ion Batteries based on Preorganized Necklace Type $Li_4Ti_5O_{12}$/VACNT Nano-Composites", *Journal of Power Sources* **2016**, *325*, 1.

M. Graglia[XXX], **J. Pampel**[XXX], T. Hantke, T.-P. Fellinger and D. Esposito, "Nitro Lignin Derived Nitrogen Doped Carbon as Efficient and Sustainable Electrocatalyst for the Oxygen Reduction", *ACS Nano* **2016,** *10*, 4363.

J. Pampel and T.-P. Fellinger, "Opening of Bottleneck Pores for the Improvement of Nitrogen Doped Electrocatalysts", *Advanced Energy Materials* **2016**, *6*, 1502389.

G. Teran-Escobar, **J. Pampel**, J. M. Caicedo and M. Lira-Cantú, "Low-Temperature, Solution-Processed, Layered V_2O_5 Hydrate as the Hole-Transport Layer for Stable Organic Solar Cells", *Energy & Environmental Science* **2013**, *6*, 3088.

J. Pampel, A. Mehmood, T.-P. Fellinger and M. Antonietti, "Ionothermal Synthesis of Fibrous Highly Porous Nitrogen Doped Carbons: Secondary Templating Effect and Electrochemical Application", **2016**, *in preparation*.

A. Mehmood, **J. Pampel**, T.-P. Fellinger and M. Antonietti, "Facile Metal-Coordination of Nitrogen Doped Carbons for the Conservative Preparation of Non-Noble Oxygen Reduction Electrocatalysts", **2016**, *in preparation*.

S. Lama, **J. Pampel**, T.-P. Fellinger, V. Molinari and M. Antonietti, "Nickel Nano-particles Deposited on Highly Porous Nitrogen doped Carbon for Lignin Hydro-genolysis", **2016**, *in preparation*.

E. M. Akinoglu, F. E. Kätelhön, **J. Pampel**, T.-P. Fellinger, M. Antonietti, R. G. Compton and M. Giersig, "Vertically Aligned Multi-Walled Carbon Nanotubes on Glassy Carbon: A New Carbon Based Electrode", **2016**, *in preparation*.
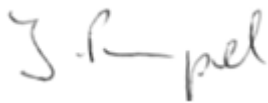

[XXX] shared first authorship

I.VI Declaration

Die vorliegende Dissertation entstand im Zeitraum zwischen Mai 2014 und August 2016 am Max-Planck-Institut für Kolloid und Grenzflächenforschung unter Betreuung von Prof. Dr. Dr. h.c. Markus Antonietti.

Hiermit erkläre ich, dass die vorliegende Arbeit selbstständig angefertigt wurde und keine anderen als die angegebenen Hilfsmittel und Quellen verwendet wurden.

The present work was carried out during the period from May, 2014 to August, 2016 at the Max Planck Institute of Colloids and Interfaces under supervision of Prof. Dr. Dr. h.c. Markus Antonietti.

I declare that I have written this work on my own and used no other than the named aids and references.

Jonas Pampel

Potsdam, 24.08.2016